

0676

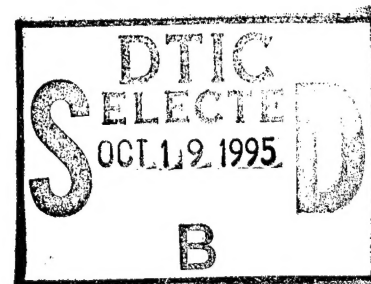
# **PARTICLE-IN-CELL AND MONTE CARLO MODELLING OF ADVANCED PLASMA THRUSTERS**

**R. I. Samanta Roy  
D. E. Hastings**

**Massachusetts Institute of Technology  
Space Power and Propulsion Laboratory  
Department of Aeronautics and Astronautics  
77 Massachusetts Ave.  
Cambridge, MA 02139**

**31 July 1995**

**Final Report**

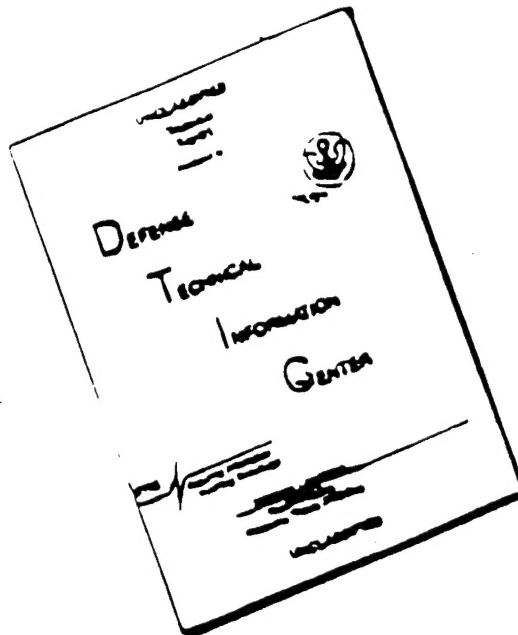


**Approved For Public Release; Distribution Unlimited**

**19951018 015**

**DTIC QUALITY INSPECTED 8**

# DISCLAIMER NOTICE



THIS DOCUMENT IS BEST  
QUALITY AVAILABLE. THE COPY  
FURNISHED TO DTIC CONTAINED  
A SIGNIFICANT NUMBER OF  
PAGES WHICH DO NOT  
REPRODUCE LEGIBLY.

REPORT DOCUMENTATION PAGE			Form Approved OMB No. 0704-0188	
<small>Public reporting burden for this collection of information is estimated to average 1 hour per response, including the time for reviewing instructions, searching existing data sources, gathering and maintaining the data needed, and completing and reviewing the collection of information. Send comments regarding this burden estimate or any other aspect of this collection of information, including suggestions for reducing this burden, to Washington Headquarters Services, Directorate for Information Operations and Reports, 1215 Jefferson Davis Highway, Suite 1204, Arlington, VA 22202-4302, and to the Office of Management and Budget, Paperwork Reduction Project (0704-0188), Washington, DC 20503.</small>				
1. AGENCY USE ONLY (Leave blank)	2. REPORT DATE 31 July 1995	3. REPORT TYPE AND DATES COVERED Final Technical Report (31 Jul 93-31 Jul 95)		
4. TITLE AND SUBTITLE Particle-in-Cell and Monte Carlo Modelling of Advanced Plasma Thrusters		5. FUNDING NUMBERS F49620-93-1-0317		
6. AUTHOR(S) Robie I. Samanta Roy Daniel E. Hastings				
7. PERFORMING ORGANIZATION NAME(S) AND ADDRESS(ES) SpacePower and Propulsion Laboratory Dept. of Aeronautics and Astronautics Massachusetts Institute of Technology 77 Massachusetts Ave. Cambridge, MA 02139		8. PERFORMING ORGANIZATION REPORT NUMBER		
9. SPONSORING/MONITORING AGENCY NAME(S) AND ADDRESS(ES) AFOSR/NA 110 Duncan Ave., Suite B115 Bolling AFB, DC 20332-0001		10. SPONSORING/MONITORING AGENCY REPORT NUMBER		
11. SUPPLEMENTARY NOTES				
12a. DISTRIBUTION/AVAILABILITY STATEMENT Approved for public release; distribution is unlimited.		12b. DISTRIBUTION CODE		
13. ABSTRACT (Maximum 200 words)  In order to accurately assess the backflow contamination potential of electric propulsion thrusters for spacecraft-thruster integration purposes, models of the plumes and backflow are necessary. Both axisymmetric and fully three-dimensional models of the plume and backflow contamination from ion thruster plumes are presented. Components included are primary beam ions, neutral propellant efflux, thermal propellant ions created mainly by charge-exchange (CEX) collisions between primary beam ions and neutral propellant, non-propellant efflux (NPE) sputtered from thruster components, and neutralizing electrons. The plasma hybrid particle-in-cell (PIC) technique is applied to both propellant CEX ions and NPE ions produced in the beam and their transport out of the beam to the regions surrounding a model spacecraft. Simulations are performed for both single and dual thruster operation. Results of plume properties and backflow are compared with data and good agreement is found. Scaling relationships for the backflow are determined, and the levels of NPE deposition are shown to be less than previously thought. In addition, the backflow from multiple thruster operation is found to be non-linear.				
14. SUBJECT TERMS Electric Propulsion, Ion Thrusters, Spacecraft Contamination		15. NUMBER OF PAGES 255		
		16. PRICE CODE		
17. SECURITY CLASSIFICATION OF REPORT UNCLASSIFIED	18. SECURITY CLASSIFICATION OF THIS PAGE UNCLASSIFIED	19. SECURITY CLASSIFICATION OF ABSTRACT UNCLASSIFIED	20. LIMITATION OF ABSTRACT UL	

# **PARTICLE-IN-CELL AND MONTE CARLO MODELLING OF ADVANCED PLASMA THRUSTERS**

by

**Robie I. Samanta Roy  
Daniel E. Hastings**

## **Abstract**

In order to accurately assess the backflow contamination potential of electric propulsion thrusters for spacecraft-thruster integration purposes, models of the plumes and backflow are necessary. The effluents of ion thrusters, Hall or Stationary Plasma Thrusters (SPT), magnetoplasmadynamic (MPD) thrusters, and arcjets are reviewed and the status of electric propulsion contamination is surveyed. A simple analytical analysis of ion thruster contamination is conducted to highlight the deficiencies in current abilities to model backflow contamination. A study is presented of the induced environment produced by an ion thruster, and its interactions with spacecraft. Axisymmetric and fully three-dimensional models of an ion thruster plume are developed and utilized to understand the physical processes involved, as well as to make useful predictions of spacecraft contamination.

A general physical model of an ion thruster plume is developed. Components included are primary beam ions, neutral propellant efflux, slow propellant ions created mainly by charge-exchange (CEX) collisions, non-propellant efflux (NPE) sputtered from thruster components, and neutralizing electrons. The focus of the model is on the creation and transport of both the CEX propellant ions created from the beam ions and neutral propellant, and charged NPE from the thruster plume into the backflow region which is the area greater than  $90^\circ$  to the plume centerline. The role of electron impact ionization in the plume is also examined. A fluid model of the electrons emitted from the ion thruster neutralizer is derived that incorporates the momentum and energy equations. Electron collisions with both ions and neutrals are included, and boundary conditions for the energy equation are addressed.

An axisymmetric numerical model is presented that utilizes the hybrid plasma particle-in-cell (PIC) method to treat the CEX and NPE ions as discrete computational particles that are transported within and out of the plume under the influence of self-consistent electric fields. A volumetric production method is used for creating the CEX ions. Since the electrons are treated as a fluid, the model is time accurate on the ion plasma frequency timescale. A fully three-dimensional numerical model is also presented for plume simulations and contamination assessment of realistic asymmetric spacecraft. Due to the extremely large computational resources required for simulating spatial domains with length scales of up to five meters, parallel computing techniques are required. A fully parallel PIC algorithm is developed and issues regarding multi-computer implementation are discussed.

Axisymmetric plume simulations are performed, and results are compared with ground tests. Computational results of the CEX ion density and flow angles show good qualitative and quantitative agreement with the experimental data. It is shown that the CEX ions created in the beam accelerate outwards and form two distinct energy populations, one with a significant backstreaming component. The effect of the background tank pressure in ground experiments, and the accelerator grid impingement current is examined. The backflow contamination from NASA's current 30 cm xenon ion thruster is investigated over the entire operating envelope of the thruster, and predictions for space operation are made. Scaling relationships for the backflow previously identified are confirmed. Issues



regarding the electron temperature in the plume are explored, and it is shown that the electron temperature plays an important role in the plume, with the backflow increasing with electron temperature. The effect of the spacecraft geometry on the backflow structure in axisymmetric geometry is investigated, and the three-dimensional model is used to investigate the influence of asymmetric spacecraft geometry. Fully three-dimensional results with up to 17.5 million particles are presented and compared with axisymmetric results. It is shown that the spacecraft geometry plays a strong role in the expansion of the CEX plasma. The contamination from the sputtered molybdenum grid material is also examined, and calculations of surface deposition are made that are less than previous estimates based on simple models. The principle of the expanding CEX plasma cloud acting as a plasma bridge for spacecraft potential control is demonstrated. In addition, the use of a plume shield to reduce the plume backflow is simulated and found to be effective. Lastly, the contamination from two thrusters operating simultaneously is examined and the flowfield is found to be highly directional, depending upon thruster separation. EP contamination can present operational hazards to spacecraft, but if taken into account in spacecraft design, it can be avoided to a large extent. Based on the results of the backflow simulation model developed, recommendations regarding spacecraft design and thruster operation are presented.

<b>Accession For</b>	
NTIS GRA&I	<input checked="" type="checkbox"/>
DTIC TAB	<input type="checkbox"/>
Unannounced	<input type="checkbox"/>
Justification	
By	
Distribution/	
Availability Codes	
Dist	Avail and/or Special
A-1	

# Table of Contents

<i>Abstract</i> .....	1
<i>Table of Contents</i> .....	3
<i>List of Figures</i> .....	7
<i>List of Tables</i> .....	14
<i>Nomenclature</i> .....	15
<b>1.0 Introduction</b> .....	<b>17</b>
1.1 Electric Propulsion Contamination - A Review .....	20
1.1.1 Ion Thrusters .....	23
1.1.2 Hall Thrusters .....	30
1.1.3 MPD Thrusters .....	32
1.1.4 Arcjet Thrusters .....	35
1.1.5 Existing Electric Propulsion Contamination Prediction Models .....	36
1.2 Outline of Research Approach .....	39
<b>2.0 Analytical Study of Ion Thruster Contamination</b> .....	<b>43</b>
2.1 Simple CEX Ion Production and Backflow Model .....	43
2.2 Analytical Model Results .....	48
<b>3.0 Physical Model of an Ion Thruster Plume</b> .....	<b>54</b>
3.1 General Description of an Ion Thruster Plume .....	54
3.2 Beam Ion Model .....	54
3.3 Neutral Propellant Model .....	58
3.4 Propellant Charge-Exchange (CEX) Ion Model .....	63
3.5 Non-Propellant Efflux (NPE) Model .....	66
3.6 Electron Fluid Model .....	70
3.6.1 Electron Momentum Equation .....	71

3.6.2	Electron Temperature Equation . . . . .	73
3.7	Collision Models . . . . .	76
3.7.1	Charged-Particle Interactions . . . . .	77
3.7.2	Electron-Neutral Collisions . . . . .	79
3.7.3	Ion-Neutral Collisions . . . . .	81
3.8	Electric Potential Field . . . . .	82
<b>4.0</b>	<b>Numerical Plume Model and Methods (Axisymmetric)</b>	<b>93</b>
4.1	General Backflow Simulation Model . . . . .	93
4.2	Plasma Particle-in-Cell (PIC) Technique . . . . .	94
4.2.1	Non-dimensionalization of Governing Equations . . . . .	95
4.2.2	Various Numerical Aspects of the PIC Technique . . . . .	96
4.3	Computational Grid . . . . .	99
4.4	Poisson's Potential Equation Solution . . . . .	101
4.5	Electron Temperature Equation Solution . . . . .	104
4.6	Spacecraft Floating Potential . . . . .	107
<b>5.0</b>	<b>Two-Dimensional Simulation Results</b>	<b>115</b>
5.1	Preliminary Numerical Comments . . . . .	115
5.2	Comparison of Model with Experiments of <i>Kaufman</i> . . . . .	117
5.2.1	Plasma Density Comparisons . . . . .	118
5.2.2	Plasma Potential Comparisons . . . . .	121
5.2.3	Electron Temperature Comparisons . . . . .	122
5.2.4	Discussion of Variable and Isothermal Temperature Models . . . . .	124
5.2.5	Effect of Tank Background Pressure . . . . .	126
5.2.6	Conclusions from Comparisons with <i>Kaufman's</i> Experiments . . . . .	126
5.3	Comparison of Model with Experiments of <i>Carruth et al</i> . . . . .	127
5.3.1	Flow Angle Comparisons . . . . .	128
5.3.2	Plasma Density Comparisons . . . . .	130
5.3.3	Effect of Tank Background Pressure . . . . .	130
5.3.4	Conclusions from Comparisons with <i>Carruth et al</i> Experiments . . . . .	130
5.4	Investigation of Accel Grid Impingement Current . . . . .	131
5.4.1	Comparison of Model to Computations of <i>Peng et al</i> . . . . .	131
5.4.2	Comparison of Model to Experiments of <i>Monheiser</i> . . . . .	132
5.4.3	Comparison of Model to Experiments of <i>Beattie and Matossian</i> . . . . .	133
5.4.4	Conclusions from Comparisons of Grid Impingement Current . . . . .	134

5.5	NASA 30 cm Xe Ion Thruster Contamination Predictions .....	135
5.5.1	JPL Operating Points .....	136
5.5.2	NASA LeRC Operating Points .....	139
5.6	Effects of Electron Temperature .....	141
5.7	Effects of Geometry .....	143
5.8	Sputtered Grid Material .....	144
5.9	Effect of Thruster Operation on Spacecraft Floating Potential .....	147
5.10	Effect of a Plume Shield to Reduce Backflow .....	148
5.11	Comparison of Numerical Results to Simple Analytical Models .....	149
<b>6.0</b>	<b>Numerical Plume Model and Methods (Three-Dimensional)</b>	<b>199</b>
6.1	Three-Dimensional Additions to Model .....	200
6.2	Parallel Computing Concepts .....	203
6.3	Parallel Implementation of 3-D PIC Model .....	206
<b>7.0</b>	<b>Three-Dimensional Simulation Results</b>	<b>213</b>
7.1	Three-Dimensional Effects .....	213
7.2	Comparison of Two- and Three-Dimensional Results .....	216
<b>8.0</b>	<b>Dual Thruster Simulation Results</b>	<b>226</b>
8.1	Multiple Thruster Issues .....	226
8.2	Dual Thruster Results .....	227
8.2.1	Directional Orientation of Xenon CEX Backflow .....	227
8.2.2	Effect on Grid Impingement Current .....	228
8.2.3	NPE Sputtered Grid Material Backflow .....	228
<b>9.0</b>	<b>Conclusions</b>	<b>235</b>
9.1	Review of Results .....	235
9.1.1	Contributions to Ion Thruster Plume Backflow Modelling .....	235
9.1.2	Contributions to Large-Scale Plasma Simulations .....	238
9.1.3	Contributions to Ion Thruster Backflow Predictions .....	239
9.2	Recommendations for Ion Thruster/Spacecraft Operation .....	240
9.3	Recommendations for Future Research .....	241

<b>Appendix B Parallel Computer Model Flowchart</b>	<b>245</b>
<i>Bibliography</i> .....	246

## List of Figures

1.1	Schematic of EP thruster-spacecraft interactions . . . . .	41
1.2	Schematic of a modern electron bombardment ion thruster . . . . .	41
1.3	Computational results of CEX ion density from PLASIM code compared with experimental data . . . . .	42
2.1	Schematic of geometry for simple CEX models . . . . .	51
2.2	Diagram of CEX velocity components in backflow region . . . . .	51
2.3	Contour plot of mercury CEX ion density for SERT II thruster compared with experimental measurements . . . . .	52
2.4	Plot of molybdenum flux along radial plane at $z=0$ for SERT II thruster . .	53
2.5	Molybdenum desorption flux as a function of temperature . . . . .	53
3.1	Geometry for beam plasma and neutral density models . . . . .	83
3.2	a) Geometry of grid apertures and CEX ion impingement patterns; b) Schematic of potential along aperture centerline through grids . . . . .	83
3.3	Radial cut of model beam ion current density profile showing parabolic core and exponential wing regions . . . . .	84
3.4	Beam ion current density model contours compared to experimental measurements by <i>Monheiser</i> [1991] . . . . .	84
3.5	Radial cut of experimental beam ion current density showing non- uniformities from <i>Monheiser</i> [1991] . . . . .	85
3.6	Comparison of experimental radial ion density profile to parabolic and Gaussian beam models; data from <i>Kaufman</i> [1975] . . . . .	85
3.7	Typical relationship between beam ion cost and propellant utilization efficiency for constant discharge voltage and propellant flow rate for electron bombardment ion thrusters . . . . .	86
3.8	Comparison of exact and far-field neutral density profiles along centerline	86

3.9	a) Computed neutral propellant density contours in plume - simple point source; b) Neutral propellant density contours from detailed numerical model by <i>Monheiser</i> [1991] . . . . .	87
3.10	CEX cross sections for xenon and mercury from <i>Rapp and Francis</i> [1962]	88
3.11	CEX, ionization, and three-body and radiative recombination rates for xenon as a function of electron temperature for densities at thruster exit . .	88
3.12	Computed CEX production contours in plume compared with those of <i>Monheiser</i> [1991] . . . . .	89
3.13	Sputtering yield of Mo bombarded by Xe; averaged data from <i>Weijsenfeld and Hoogendoorn</i> [1961] and <i>Rosenberg and Wehner</i> [1962] . . . . .	89
3.14	CEX, ionization, and three-body and radiative recombination rates for molybdenum as a function of electron temperature for densities at thruster exit . . . . .	90
3.15	Ratio of the electron-ion to electron-neutral collision frequencies for xenon as a function of electron temperature with maximum plume densities . . . .	90
3.16	Electron thermal conductivity of xenon as function of electron temperature with maximum plume densities . . . . .	91
3.17	Axial heat conduction model geometry . . . . .	91
3.18	Elastic electron-neutral collision cross sections for a) Xe and b) Hg . . . .	92
4.1	Schematic of computational domain . . . . .	110
4.2	Comparison of Maxwellian velocity distribution with approximation used for particles . . . . .	110
4.3	Grid cell particle weighting geometry . . . . .	111
4.4	Schematic of leapfrog integration scheme . . . . .	111
4.5	Computational grid . . . . .	112
4.6	Gauss' law in cylindrical coordinates . . . . .	113
4.7	Template for Poisson's equation . . . . .	113
4.8	Comparison of far-field Neumann and Dirichlet boundary conditions on Poisson equation solution . . . . .	114
4.9	Comparison of one-dimensional analytical solution with two-dimensional numerical solution (along a wall) of Poisson's equation at biased wall for various background plasma densities . . . . .	114
5.1	Time history of number of particles in a simulation . . . . .	151
5.2	Time history of backflow current over plane $z=0$ . . . . .	151
5.3	Time history of average total energy of particles in a simulation . . . . .	152



5.4	Dependence of backflow current over plane above thruster exit on total number of particles used in a typical simulation . . . . .	152
5.5	Comparisons between a) unsmoothed and b) smoothed ion density in a typical simulation . . . . .	153
5.6	Contour plot of smoothed total ion density for <i>Kaufman</i> Case A conditions showing variable temperature (gray-scale), isothermal (thin line), and experimental measurements (bold line) . . . . .	154
5.7	Comparison of CEX, ionization, and recombination rates for mercury as a function of electron temperature using densities at thruster exit . . . . .	155
5.8	Ratio of CEX ion density to beam ion density for <i>Kaufman</i> Case A . . . . .	155
5.9	Independence of results on computational domain size. Comparison of the smoothed total ion density in a 0.75 m square domain with a 1.5 m square domain for <i>Kaufman</i> Case A . . . . .	156
5.10	Contour plot of smoothed total ion density for <i>Kaufman</i> Case B conditions showing variable temperature (gray-scale), isothermal (thin line), and experimental measurements (bold line) . . . . .	157
5.11	Radial cut 13 cm downstream of unsmoothed total ion density for variable and constant temperature models for <i>Kaufman</i> Case A . . . . .	158
5.12	Comparison of Figure 5.11 results with data . . . . .	158
5.13	Radial cut 7.5 cm downstream of ion density for <i>Kaufman</i> Case A and comparison with data . . . . .	159
5.14	Radial cut 7.5 cm downstream of ion density for <i>Kaufman</i> Case B and comparison with data . . . . .	159
5.15	Smoothed total ion density along an arc a distance 34 cm from a point 7.5 cm downstream; model results for both variable and constant temperature for <i>Kaufman</i> Case A operating conditions . . . . .	160
5.16	Figure 5.15 model results compared with data . . . . .	160
5.17	Same as Figure 5.15 for <i>Kaufman</i> Case B . . . . .	161
5.18	Same as Figure 5.16 for <i>Kaufman</i> Case B . . . . .	161
5.19	Potential contours for a) variable and b) constant temperature models for <i>Kaufman</i> Case A, overlayed with experimental measurements . . . . .	162
5.20	Same as Figure 5.19 for <i>Kaufman</i> Case B . . . . .	163
5.21	Contours of electron temperature computed for a) Case A and b) Case B . . . . .	164
5.22	Contours of electron thermal conductivity for a) Case A and b) Case B . . . . .	165

5.23	Plasma density vs potential characteristic; comparison with data for <i>Kafuman</i> Case A: a) raw data, b) $\ln(n_i)$ plot for extracting the slope for the electron temperature . . . . .	166
5.24	Same as Figure 5.23 for <i>Kaufman</i> Case B . . . . .	167
5.25	Phase phase plots of CEX ions: radial vs. axial velocity for <i>Kaufman</i> Case A, a) variable and b) constant temperature models . . . . .	168
5.26	Comparison of radial electric fields for Case A from variable temperature and isothermal models . . . . .	169
5.27	Phase phase plots of CEX ions: radial velocity vs. radial position for <i>Kaufman</i> Case A, a) variable temperature and b) isothermal models . . . . .	170
5.28	Phase phase plots of CEX ions: axial velocity vs. axial position for <i>Kaufman</i> Case A, a) variable temperature and b) isothermal models . . . . .	171
5.29	CEX ion current density contours for <i>Kaufman</i> Case A, a) variable temperature and b) isothermal models . . . . .	172
5.30	CEX ion current density at $z=0$ for <i>Kaufman</i> Case A, variable temperature and isothermal model results . . . . .	173
5.31	CEX ion current contours for <i>Kaufman</i> Case A, (isothermal) with background pressure (gray-scale) and without (solid line) . . . . .	173
5.32	CEX ion current density vector field (normalized) . . . . .	174
5.33	Electric field vector plot (normalized) . . . . .	174
5.34	a) Radial potential and b) electric field cuts through the beam 10 cm downstream . . . . .	175
5.35	CEX flow angles at a) 48 cm and b) 66 cm from plume centerline respectively, compared to data . . . . .	176
5.36	Comparison of ion density at 48 cm from the plume centerline . . . . .	177
5.37	Comparison of computational results of CEX plasma flow angle with and without the neutral background pressure . . . . .	177
5.38	Grid impingement current: experimental and model results for <i>Monheiser</i> study . . . . .	178
5.39	Grid impingement current: experimental and model results for <i>Beattie and Matossian</i> study . . . . .	178
5.40	NASA 30 cm xenon ion thruster operating envelope . . . . .	179
5.41	Ratio of backflow current to beam current for 30 cm NASA Xe thruster as a function of thruster power; model results and scaled predictions . . . . .	179

5.42	30 cm NASA Xe thruster CEX density distribution a) Radial ray 100° from centerline from point 10 cm downstream, b) Angular arc 35 cm from point 10 cm downstream; Variable temperature model . . . . .	180
5.43	Same as Figure 5.42, but with CEX ion current density distributions . . . . .	181
5.44	Ratio of accel grid impingement current to beam current for JPL operating points . . . . .	182
5.45	Ratio of backflow current to beam current as a function of beam current for constant beam voltage . . . . .	183
5.46	Ratio of backflow current to beam current as a function of beam voltage for constant beam current and mass flow rate . . . . .	183
5.47	Contours of CEX ion density for a) $T_{eo}=1$ eV, b) $T_{eo}=5$ eV . . . . .	184
5.48	Contours of CEX ion current density for a) $T_{eo}=1$ eV, b) $T_{eo}=5$ eV . . . . .	185
5.49	Contours of potential for a) $T_{eo}=1$ eV, b) $T_{eo}=5$ eV . . . . .	186
5.50	Radial velocity vs. radial position phase plots a) $T_{eo}=1$ eV, b) $T_{eo}=5$ eV . . . . .	187
5.51	Contours of electron temperature for a) $T_{eo}=1$ eV, b) $T_{eo}=5$ eV . . . . .	188
5.52	Radial cuts of electron temperature profiles for a) $T_{eo}=1$ eV, b) $T_{eo}=5$ eV . . . . .	189
5.53	Contours of electron thermal conductivity for a) $T_{eo}=1$ eV, b) $T_{eo}=5$ eV . . . . .	190
5.54	Contours of total electron collision frequency for a) $T_{eo}=1$ eV, b) $T_{eo}=5$ eV . . . . .	191
5.55	Contours of ratio of electron-neutral to electron-ion collision frequency for a) $T_{eo}=1$ eV, b) $T_{eo}=5$ eV . . . . .	192
5.56	CEX ion current density contours for various spacecraft geometries; spacecraft widths: a) 12 cm, b) 24 cm, c) 36 cm . . . . .	193
5.57	Ratio of Mo to Xe CEX ion current density for I3 high ion creation rate case . . . . .	194
5.58	Trajectories of Mo and Xe ions in plume potential field . . . . .	194
5.59	Contour map of Mo deposition for I3 case with high ion creation rate . . . . .	195
5.60	Mo deposition along ray 135° from a point at $z=0.48$ m, $r=0.22$ m . . . . .	195
5.61	Contour map of Mo deposition for I1 case with low ion creation rate . . . . .	196
5.62	Mo deposition as a function of thruster power for NASA 30 cm xenon thruster; high and low ion creation rates along with predicted scaled values . . . . .	196
5.63	Film properties of molybdenum film on solar cell coverglass . . . . .	197
5.64	Radial potential profile on top of spacecraft showing effect of CEX plasma collapsing the sheath around the spacecraft and alleviating extreme negative spacecraft potential . . . . .	197

5.65	Total ion density contours from <i>Kaufman</i> Case A thruster with plume shield at thruster exit plane . . . . .	198
6.1	Three dimensional domain geometry . . . . .	210
6.2	Three dimensional Poisson Equation solver stencil . . . . .	211
6.3	Typical parallel computing performance graph . . . . .	211
6.4	Example of domain decomposition (in a plane) . . . . .	212
6.5	Detail of splitting computational grid between two neighboring blocks . . . . .	212
7.1	Three dimensional simulation results showing potential on $x$ - $y$ and $x$ - $z$ planes, and a potential isosurface . . . . .	219
7.2	Total ion density in $x$ - $y$ plane through plume center ( $z=0$ ) . . . . .	220
7.3	Total ion density in $x$ - $z$ plane through plume center ( $y=0$ ) . . . . .	220
7.4	Comparison of total ion density in $x$ - $y$ and $x$ - $z$ planes along an arc 1.25 m from a point 5 cm in front of the thruster exit . . . . .	221
7.5	Total ion density in $z$ - $y$ plane for $x$ positions a) 3 cm, b) 67 cm, and c) 95 cm upstream of thruster exit plane . . . . .	222
7.6	Comparison of total ion density along an arc in the $z$ - $y$ plane 0.75 m from the plume center in planes 3, 24, and 95 cm upstream of the thruster exit plane . . . . .	223
7.7	Comparison of total ion density from two and three-dimensional models along a cut $90^\circ$ to plume 22 cm downstream from the thruster exit in $x$ - $y$ plane . . . . .	223
7.8	Comparison of total ion density from two and three-dimensional models along a cut $120^\circ$ from plume and from a point 75 cm downstream of thruster exit in $x$ - $y$ plane . . . . .	224
7.9	Comparison of total ion density from two and three-dimensional models along an arc 1.5 m from a point 5 cm in front of the thruster in the $x$ - $y$ plane . . . . .	224
7.10	Comparison of total ion density with and without solar array panel along an arc 1.25 m from a point 5 cm in front of the thruster (Axisymmetric model results) . . . . .	225
7.11	Geometry of a situation where axisymmetric code can be applied with two different dimensions . . . . .	225
8.1	Comparison of propellant CEX ion production rates between beam ion model and beam ion particle injection . . . . .	230
8.2	Three-dimensional domain geometry with dual thrusters . . . . .	230
8.3	CEX ion density in $y$ - $z$ plane 2 cm upstream of thruster exit . . . . .	231

8.4	CEX ion current density along arc 0.2 m from spacecraft center in y-z plane (2 cm upstream) from -y to +y axis .....	231
8.5	Phase plot ( $v_y$ - $v_z$ ) of Xe CEX ions for: a) single thruster, b) dual thrusters	232
8.6	Potential cuts through beam 4 cm down stream along y and z axes .....	233
8.7	Propellant CEX ion current density vector plot in x-y plane ( $z=0$ ) .....	233
8.8	Phase plot ( $v_y$ - $v_z$ ) of Mo CEX ions (dual thrusters) .....	234
8.9	Ratio of Mo to Xe current density along arc 0.2 from spacecraft center in y-z plane (2 cm upstream) from -y to +y axis .....	234

## List of Tables

3.1	Modified SERT II 15 cm ion thruster operating conditions . . . . .	57
3.2	Gyroradii for xenon ions . . . . .	66
3.3	Ionization values for xenon, mercury, and molybdenum . . . . .	80
3.4	Polarizabilities of xenon, mercury, and molybdenum . . . . .	81
5.1	<i>Kaufman</i> SERT II Hg 15 cm ion thruster operating conditions . . . . .	117
5.2	Ratio of backflow current to beam current (variable / constant temperature)	120
5.3	NASA 30 cm xenon thruster: JPL operating points . . . . .	136
5.4	NASA 30 cm xenon thruster: NASA LeRC operating points . . . . .	140
5.5	Lower and Upper limits to backflow contamination for LeRC points . . .	141
5.6	Anticipated accel grid erosion rates in space for NASA 30 cm xenon thruster ( <i>Patterson et al</i> [1993]) . . . . .	144

# Nomenclature

<u>Symbol</u>	<u>Definition (SI Units)</u>
$A_{SC}$	spacecraft current collecting area ( $m^2$ )
$B$	magnetic field (T)
$\bar{C}$	neutral most probable thermal speed (m/s)
$C_s$	ion acoustic speed (m/s)
CEX	charge-exchange
$E$	electric field (V/m)
$F$	thrust (N)
$F_i$	ratio of accel grid impingement current to beam ion current
$I_b$	beam ion current (A)
$I_{bk}$	backflow current (A)
$I_{sp}$	thruster specific impulse (s)
$M$	molecular weight (kg/mole)
$\dot{N}_{cex}$	CEX ion production rate (#/s)
$Q_e$	electron heating/cooling term ( $W/m^3$ )
$R$	spherical radial coordinate (m)
$T_e$	electron temperature (eV)
$T_{eo}$	beam electron temperature at thruster exit (eV)
$T_{e\infty}$	ambient electron temperature (eV)
$T_i$	ion temperature ( $^{\circ}K$ )
$T_w$	thruster wall temperature ( $^{\circ}K$ )
$V_{SC}$	spacecraft velocity for ram current collection (m/s)
$W_p$	macro-particle weighting (no. of real particles for each PIC particle)
$Y$	sputtering yield (atoms/ion)
$Z_k$	number of charges per ion, i.e. $Z_k=1$ for single ions



$e$	electron charge ( $1.6 \times 10^{-19}$ C)
$j_{e,i}$	current density: electron, ion ( $A/m^2$ )
$k$	Boltzmann constant ( $1.38 \times 10^{-23}$ J/°K)
$\dot{m}_{Mo}$	molybdenum sputtered mass loss rate (kg/s)
$m_{e,i,n}$	mass: electron, ion, neutral (kg)
$n_{e,i,n,bio}$	number density: electron, ion, neutral, maximum beam ion ( $m^{-3}$ )
$p_o$	testing chamber background neutral gas pressure ( $N/m^2$ )
$q$	heat flux ( $W/m^2$ )
$r$	cylindrical radial coordinate (m)
$r_T$	thruster radius (m)
$v_{bi}$	beam ion velocity (m/s)
$v_e$	electron drift velocity (m/s)
$v_g$	sputtered grid atom ejection velocity (m/s)
$v_{te,ti}$	electron, ion thermal velocity (m/s)

#### Greek Symbols Definition (SI Units)

$\Delta \Phi$	radial beam potential drop (V)
$\Phi_b$	beam voltage (V)
$\Gamma_s$	sputtered flux from grids ( $\#/m^2/s$ )
$\alpha$	beam divergence angle (degrees)
$\beta$	grid neutral transparency factor
$\eta_p$	propellant utilization efficiency
$\phi$	electric potential (V)
$\phi_{sc}$	spacecraft floating potential (V)
$\gamma$	thrust correction factor
$\kappa_e$	electron thermal conductivity ( $W/m^\circ K$ )
$\lambda_D$	Debye length (m)
$\nu_{ei,en}$	collision frequency: electron-ion, electron-neutral ( $s^{-1}$ )
$\rho$	charge density ( $C/m^3$ )
$\sigma_{cex}$	CEX collision cross section ( $m^2$ )
$\theta$	spherical azimuthal angle (radians)
$\omega_{ce,i}$	cyclotron frequency, electron, ion (rad/s)
$\omega_{pe,i}$	plasma frequency, electron, ion (rad/s)

# Chapter 1

## Introduction

Electric propulsion (EP) is increasingly being considered earnestly for a variety of applications ranging from technology demonstrators to science missions and commercial applications such as station-keeping on geostationary communications satellites [Pollard *et al.*, 1993]. The simple reason is that the mass of propellant consumed, as shown by the well-known rocket equation, scales as  $1 - \exp[-\Delta V/c]$  where  $\Delta V$  is the required mission velocity increment and  $c$  is the exhaust velocity of the propulsive device. State-of-the-art liquid hydrogen/oxygen rockets such as the Space Shuttle Main Engine attain maximum exhaust velocities of approximately 4500 m/s, while in contrast, ion thrusters typically operate with exhaust velocities around 20,000-40,000 m/s. The exhaust velocities of conventional chemical rockets are limited by the thermal energy content of the propellants, while EP thrusters accelerate the propellant via electric or electromagnetic forces, which are only limited by the electrical power supply and the speed of light. The advantage of the high exhaust velocities of EP thrusters on mass savings is significant. For example, the velocity increment required for an orbital transfer from Low Earth Orbit (LEO) to Geosynchronous Earth Orbit (GEO) is 3880 m/s for a chemical thruster that can provide impulsive velocity changes. Since EP thrusters must operate for extended periods of time due to their low thrust, the velocity increment required for a low thrust trajectory is 4630 m/s. Hence, around 58% of the initial mass of a chemically powered spacecraft would be propellant. In contrast, the electrically propelled spacecraft would initially be only about 14% propellant, either yielding substantial payload gains or requiring a smaller launch vehicle. The use of a smaller launch vehicle provides substantial reductions in cost. However, in addition to increased propulsion system performance, spacecraft designers and integrators must also consider the unique and important issues of spacecraft

contamination by EP thruster plume backflow, and how EP thrusters modify the environment surrounding a spacecraft.

Spacecraft contamination is also an important issue for chemical rockets. However, the induced environment in the vicinity of an EP propelled spacecraft is unique consisting of neutral gases, plasmas, and electromagnetic fields as a result of interactions between the ambient environment, thruster effluents, and the spacecraft itself. In comparison to chemical propulsion environments that primarily consist of neutral gases, the plasma plume generated by EP thrusters introduces a new level of complexity to the spacecraft interactions picture.

The evaluation of EP thruster induced environmental effects that could degrade the performance of spacecraft subsystems and sensors is very important. For example, in some thruster plumes, a low-energy plasma is created by charge-exchange (CEX)\* collisions, and can expand around a spacecraft. Many thrusters also emit heavy metal species, both charged and uncharged, due to thruster component erosion. These thruster effluents, in addition to other neutral and plasma species, contribute to the induced environment surrounding a spacecraft and can lead to, or influence, various interactions such as:

- current drain to biased surfaces
- degradation of solar array panels, thermal control surfaces, and optical windows due to effluent deposition
- attenuation and refraction of electromagnetic wave transmission and reception due to enhanced plasma density
- absolute and differential charging of the spacecraft
- interference due to electrostatic and/or electromagnetic noise
- surface phenomena such as spacecraft glow
- modification of spacecraft radiation signature
- alteration of electrical and thermal properties of surfaces

A schematic in Figure 1.1 illustrates a number of these thruster-spacecraft interactions. Most of these interactions are detrimental to spacecraft operation, and surface contamination in particular, can seriously degrade spacecraft performance and decrease the operational lifetime.

In order to understand and predict the thruster induced environment, it is vitally important to understand the plumes of EP thrusters - both the species that are emitted, and

---

\* The term charge-exchange (CEX) will be used throughout this thesis in a number of contexts, such as CEX collisions, CEX ions, or CEX plasma.

their transport mechanisms within and outside of the plume. It is desirable to have a model that will be able to predict the fluxes of potentially contaminating material from the thruster plume onto spacecraft surfaces. It is common practice to call this flow of material from a thruster in directions away from the thrust axis leading to undesirable fluxes to spacecraft surfaces, the *backflow*, a term that will be used throughout this thesis. We will refer to the regions outside of the plume that are at angles greater than  $90^\circ$  to the plume centerline, the *backflow region*.

A review of the literature regarding EP thruster spacecraft interactions, reveals an awareness of many of the above issues from early on in the development of EP thrusters. However, accurate measurement and prediction of thruster effluents were hampered by both experimental and numerical limitations. Due to experimental facility effects, many ground results are questionable, and only recently, has the computational power been available for the development of rigorous numerical models of thruster plumes. Moreover, ground tests are very costly. Historically, much effort in the U.S. has focused on the development of ion thrusters. Hence, the issues of ion thruster contamination have received the most attention. The thruster effluents were characterized, and efforts were made to develop simple models of contaminating fluxes. In contrast, magnetoplasmadynamic (MPD) thrusters, despite years of research, have not reached the same level of maturity as ion thrusters. Consequently, issues of thruster backflow have not been investigated to the same level as with ion thrusters, and relatively little is known of the backflowing thruster effluents of MPD thrusters.

The objective of this thesis is to build upon the experimental evidence and physical insights of the last few decades, and employ modern computational methods to develop a rigorous model of EP thruster plume backflow with engineering predictive capability. In addition, we will investigate the physical processes within the plume and develop a comprehensive understanding of the backflow. Due to their maturity, the relatively large data base with which to compare results, and their planned near-future commercial use, we have focused on ion thrusters. Currently, no other comprehensive model exists that can predict in a self-consistent manner, the charged particle backflow from an ion thruster plume.

This thesis addresses two important issues dealing with ion thruster backflow. One issue associated with ion thrusters is that complete ionization can not be achieved with reasonable levels of power, and hence, neutral gas is emitted at thermal speeds. We are interested in these slow neutrals because they undergo CEX collisions with the fast beam ions producing fast neutrals and slow ions which can be influenced by local electric fields

---

in the plume. Slow ions can also be produced by electron impact ionization if the electron temperature is sufficiently high, but CEX is generally the dominant collisional process. The electric field structure in the plume, as seen in experiments is radial, and hence the slow ions are pushed out of the beam and move back towards the spacecraft. The second issue is that the grids of ion thrusters are bombarded by some of these CEX ions causing erosion. Hence molybdenum, a common grid material, is sputtered into the plume. A fraction of the sputtered grid atoms becomes charged, and eventually flows back towards the spacecraft creating a potentially serious contamination hazard due to the low vapor pressure of these metals. The behavior of the first species is examined in two and three dimensional models, and the second, in a two dimensional model. It is important to understand how these species behave as a function of thruster operating conditions. Current ion thrusters operate at maximum power levels of a few kW. However, as spacecraft power supplies increase capacity in the future, thrusters will be able to operate at higher power levels, and a predictive model for contamination is needed since extrapolation of data from the present ground tests is problematic.

In this introductory chapter, we review the literature on EP thruster effluents and EP thruster spacecraft interactions. To place the field of EP plume contamination in context, we briefly discuss chemical rocket plume modelling and contamination. Even though this thesis concentrates on ion thrusters, we also review the status of the field in regards to other EP thrusters such as Hall thrusters, MPD thrusters, and arcjets. The thruster effluents are described, ground experiments of plume contamination are reviewed, and current inadequacies are highlighted. The few space experiments that have been conducted are also surveyed. Previous backflow prediction models are critically examined, and the shortcomings and needs for a more accurate predictive model are discussed. Lastly, an outline of the research approach taken in this thesis is given.

## **1.1 Electric Propulsion Contamination - A Review**

Spacecraft contamination from plumes consisting primarily of neutral gases produced by chemical rockets has been studied extensively [Roux and McCay, 1984; Dentleff, 1991]. The plumes produced by such thrusters consist of a high velocity jet that expands in the vacuum of space. In addition, viscous effects in the rocket nozzles lead to less energetic gases that expand at large angles to the plume centerline. In many situations, the plume will impinge on spacecraft surfaces and will cause undesirable forces and torques, heat loads, and surface contamination. In addition, unburned or incompletely burned propellant droplets, as well as combustion products, can condense on surfaces. Neutral plume

---

contamination has been studied for many situations including small attitude control thrusters on satellites, booster stage separation, spacecraft rendezvous and docking, and even the plumes from the thrusters on Manned Maneuvering Units (MMU's). Neutral plumes have also been modelled for surface landing interactions, such as the surface impingement and subsequent dust layer erosion by descent rockets in lunar and planetary landings [Dettleff, 1991]. To study neutral plumes and their interactions with spacecraft, models ranging from simple point source models, to analytical solutions of the Boltzmann equation, to numerical fluid codes, to numerical discrete particle methods have been employed.

The simple point source models are generally used for estimates of the plume and zeroth order analysis due to their simplicity. With these models, the neutral density in the plume flow field for distances greater than several thruster diameters away, is expressed in spherical coordinates as,

$$n_n(R, \theta) = \frac{A}{R^2} f(\theta) \quad (1.1)$$

where  $A$  is a constant determined by the mass flow rate, and  $f(\theta)$  is an angular shape function with the properties that  $f(0)=1$  along the plume centerline, and  $f \rightarrow 0$  at some limiting angle. For an inviscid expansion, this limiting angle is related to the Prandtl-Meyer turning angle. On the basis of empirical evidence, various forms of  $f(\theta)$  have been proposed [Albini, 1965; Hill and Draper, 1966; Boynton, 1967; Simons, 1972], but the *Simons* model has received widespread popularity in that it incorporates the effects of the boundary layer flow, and agrees most closely with experimental data. The mathematical accuracy of the *Simons* model, which is based on the assumption that the ratio of the boundary layer thickness to the nozzle radius is small, has been increased by *Zana et al* [1987] and was applied to the plumes of resistojets and compared reasonably well with experiments.

However, these models are only valid within the region bounded by a limiting angle which is defined by the gas dynamic expansion. Moreover, they contain parameters that are usually adjusted to fit data. They are not valid for the transition and free-molecular flow regimes in the backflow regions. The exact calculation of the density of an expanding gas passing from viscous continuum flow to a free molecular flow by means of the Boltzmann equation is quite difficult, but solutions have been developed by *Hamel and Willis* [1966], *Peracchio* [1970], and *Baum* [1973]. *Noller* [1966] developed an approximate solution method by replacing the actually continuous transition from continuum to free molecular flow with a suitably defined discontinuity surface. Molecules that leave the core plume leave this surface with a Maxwellian velocity distribution and continue in ballistic

trajectories. The discontinuity surface is usually taken to be a surface of constant Knudsen number. *Grier* [1969] coupled the backflow model of *Noller* with a plume model similar to that of *Hill and Draper* for estimates of backflow contamination from chemical rocket plumes. Viscous effects, as incorporated in the *Simons* model, were included by *Jenkins et al* [1990] and comparisons with data were within an order of magnitude.

The above analytical models, while relatively simple to use, can not be used for accurate backflow predictions. A government and industry effort in the 1970's produced a numerical model, called CONTAM, that was a single code capable of predicting the production, transport, and deposition of chemical rocket contaminants, and the effects on spacecraft surfaces [*Hoffman et al*, 1972]. However, the numerical plume model was based on the method of characteristics technique, and is not able to model the free molecular flow in the backflow region. Modern numerical plume models now incorporate the Direct Simulation Monte Carlo (DSMC) method developed by *Bird* [1976] that treats the free molecular flowing gas as a collection of discrete computational particles. While computationally much more intensive, the DSMC approach is able to rigorously treat the backflow, and comparisons with experimental data are very good [*Boyd and Stark*, 1988]. It has become the standard approach today for plume expansion modelling with detailed chemical reactions [*Elgin et al*, 1990; *Woronowicz and Rault*, 1994]. Thus, aside from some detailed issues remaining such as a complete understanding of the effect of nozzle lip boundary layers, it is felt that there is a fairly good understanding of chemical plumes and their associated contamination [*Detleff*, 1991].

However, the status of plume modelling and contamination prediction for EP thrusters is still in a state of relative infancy. The issues of contamination have focused most closely on ion thrusters due to their relatively advanced state of development. Hall, or Stationary Plasma Thrusters (SPT), have recently received much attention, and a number of plume studies have been conducted. For MPD thrusters, the megawatt power requirements and still unresolved physical mechanisms of operation have prohibited a high level of maturation. Thus, MPD contamination has hardly been investigated, even though the contamination potential is potentially large due to the erosion of electrode material, and the possible use of alkali metals that have very low vapor pressures. Arcjets also have similar contamination potential due to electrode erosion, although erosion rates are much less than in MPD thrusters.

To understand the scope of the contamination problem, it is important to understand the nature of the plumes emitted. We shall review the plumes of ion, Hall, MPD, and arcjet thrusters, drawing in part, from previous summaries by *Byers* [1979], *Carruth* [1982], *Deiningner* [1985], *Gatsonis et al* [1993], and *Samanta Roy et al* [1994]. EP thrusters have



traditionally been divided into electrostatic, electromagnetic, and electrothermal types. These categories reflect the three possible ways in which a flow can be accelerated, although more than one mechanism may be present depending on the thruster. In the following sections, we present the most common types of electric propulsion devices, and review the effluents and contamination potential. In addition, we review previous EP plume and spacecraft contamination modelling efforts.

### 1.1.1 Ion Thrusters

In ion thrusters, ions are formed in a chamber either by electron bombardment, radio frequency excitation, or surface contact ionization. These ions are then extracted and accelerated as a beam to very high velocities ( $>10$  km/s) by a system of grids. Systems with two and three grids have been developed (screen-accel and screen-accel-decel). Typical acceleration voltages between the screen and accel grids are quite high and can reach several thousand volts. Figure 1.2 shows a schematic of a modern electron bombardment ion thruster. To maintain charge neutrality (and current balance for the spacecraft), electrons are injected into the beam from a neutralizer either by thermionic emission from a hot wire, or from a hollow cathode. The hollow cathode produces a neutral plasma cloud through which electrons can be easily transported, and is the preferred neutralizer in use today.

Since the focus of this thesis is ion thrusters, we will give a brief historical background. The earliest known record of the concept of ion thrusters is attributed to the U.S. rocket pioneer R. H. Goddard in 1906, and he and his students conducted preliminary experiments as early as 1916. In Germany, H. Oberth investigated ion propulsion independently in the 1920's, and published his studies in 1929 in his landmark book, *Wege zur Raumshiffahrt*. During the 1950's the field was investigated seriously on a theoretical level, most notably by E. Stuhlinger, who later wrote the first textbook, *Ion Propulsion for Spaceflight* [Stuhlinger, 1964]. The theoretical efforts rapidly led to experimental investigations. In 1959, the first cesium contact ionization thruster in the U.S. was developed by A. T. Forrester of Rocketdyne, and in 1960, H. Kaufman of NASA successfully operated (on the ground) an electron bombardment ion thruster - the precursor of today's thrusters [Brewer, 1970]. The first test flight of an ion thruster was conducted in 1964 with the NASA Space Electric Rocket Test (SERT) I spacecraft that contained a mercury electron bombardment thruster, and a cesium contact ionization thruster. The suborbital flight lasted for about 30 minutes during which the mercury thruster functioned successfully and demonstrated the operation of an ion thruster in space.

Unfortunately, the cesium thruster was not operated due to a high voltage short circuit [Jahn, 1968]. The prime purpose of the test was to verify the neutralization of the ion beam. In addition, radio interference tests during thruster operation were conducted, and none were found. Little is known of the early Soviet efforts, but in 1958, a paper was published by *Stavisskii et al* [1958] describing measurements of the thrust of a cesium ion thruster in laboratory tests.

Since then, thrusters with diameters ranging from 5 to 150 cm [Nakanishi and Pawlik, 1967] have been built and tested over the last three decades in a number of countries, both on the ground and in a number of space tests. The most notable experiment, SERT II that was launched in 1970, will be discussed later in detail since spacecraft contamination was a main area of investigation. The propellants that previously were used in ion thrusters were mercury and cesium. However, concerns of surface contamination led to their demise, and inert gases such as xenon are currently used, even though performance is somewhat reduced. Currently, more exotic propellants such as C<sub>60</sub> have been under investigation due to the increases in thruster efficiency that result from the use of heavier propellants [Leifer and Saunders, 1991; Torres, 1993; Hruby et al, 1994]. The current status of ion thrusters, including the U.S., Japanese, and European programs, has been recently reviewed by Pollard et al [1993]. Ion thrusters have reached the level of maturity where they have moved out of the research laboratory, and are being incorporated into the designs of commercial geostationary communications satellites.

Numerous experimental and theoretical/numerical studies have been conducted to examine ion thruster plumes. The majority of the studies conducted in the 1960's and 70's in the U.S. have been summarized by Carruth [1982]. The most comprehensive of plume studies were conducted during those years, but unfortunately, they were for thrusters using mercury and cesium. Notable recent studies of plumes and their effects include Monheiser [1991], Beattie and Matossian [1992] and Pollard [1994] in the U.S., Takegahara et al [1993] and Hayakawa et al [1994] in Japan, and Fearn et al [1993] in the U.K. among many others. Due to various test chamber effects and experimental techniques, results are rather diverse and often contradictory, making comparisons between tests and extrapolations to other operating conditions troublesome. For example, for the NASA J-series 30 cm thruster, there exist almost order of magnitude differences between reported electron temperatures [Carruth, 1982]. Nevertheless, it is well agreed upon that ion thruster effluents can be categorized basically into four groups: 1) Primary Beam Ions, 2) Neutral Propellant Efflux due to incomplete ionization in the discharge chamber, 3) Slow Propellant Ions primarily due to CEX collisions between effluents 1 and 2 in the beam, and 4) Non-Propellant Efflux (NPE) which includes sputtered and eroded thruster electrode and

grid material (both charged and neutral). A fifth category for consideration for thruster contamination, is Field Effluxes which include both static and fluctuating electric and magnetic fields, visible and non-visible emissions, and plasma waves. We will use these categories, where applicable, on the other thrusters. Effects of these effluents that will be mentioned in this section on ion thrusters will, in general, be applicable to the other thrusters as well, unless otherwise stated.

### Primary Beam Ions

The primary ion thruster effluent is the directed energetic ions in the beam that are accelerated by the thruster grids. Traditionally, they have been labeled "Group I" ions [Byers, 1979]. In conjunction with these ions, are the electrons emitted from the neutralizer. The electrons that are injected by the neutralizer into the beam have thermal speeds much greater than the directed beam ion velocities. The beam ions follow nearly line-of-sight trajectories since electromagnetic fields are generally too small to perturb their path. The downstream propagation of the beam depends on the coupling to the spacecraft potential as well as the ambient plasma and magnetic field conditions. Experimentally, it is found that most of these ions lie within an expansion cone of half-angle  $15^{\circ}$ - $20^{\circ}$ . Typical values taken 5 cm downstream of a NASA J-series 30-cm beam diameter thruster include electron temperatures of 0.4 eV (although some tests have reported 5 eV for the same thruster), average beam currents of  $3.3 \text{ mA/cm}^2$ , and electron densities of  $1.6 \times 10^{16} \text{ m}^{-3}$  [Deininger, 1985].

The beam ion current density is relatively easy to measure in ground experiments, and analytical plume ion current density models exist based on point source formulations, although they contain parameters that must be fitted with data [Reynolds, 1971; Cuffel, 1975]. In addition to studies of the primary beam ions from single thrusters, multiple thruster arrays have been tested. Masek and Womack [1967] investigated a thruster system comprised of four 20 cm mercury thrusters, although only two thrusters were ever operated simultaneously. Two 30 cm mercury thrusters were also tested together by Lathem [1981]. However, the detailed physics of two ion beams merging together was never studied.

Unless a sensor or spacecraft surface directly intercepts this cone of highly energetic ions, this species does not constitute a direct contamination source. However, the potential structure of the beam, as well as processes within the beam, such as electron thermalization and potential coupling to the neutralizer, exert a large influence on the CEX ions. Therefore, beam properties directly influence the contamination potential via the backflow of the CEX ions. Studies of the effects of directly impinging energetic ions on surfaces of various types of spacecraft materials such as solar cell coverglasses and thermal control

coatings, were carried out by *Hall et al* [1970,1972], but they dealt with mercury and cesium which are no longer of any interest. In other experiments [*Byers*, 1979], a solar array panel for the SERT II satellite was exposed to a total mercury ion flux greater than  $10^{20}$  ions/cm<sup>2</sup> at energies of 3 keV, and surprisingly, no reduction in power output was observed in ground tests. In addition, during actual flight operation, about one-eighth of the solar array on the Advanced Technology Satellite (ATS) - 6 spacecraft was submerged in the cesium thruster ion beam, and no deleterious effects were noted after 92 hours (when the thruster failed).

The major concern due to the beam is interference to communications transmissions passing through the dense portions of the plume. It is likely that missions utilizing electric propulsion will need to communicate through the plasma plume or the plasma cloud. There are several types of wave interactions that must be considered including attenuation, phase shift, reflection and fluctuations. Free electrons in the plume or the plasma cloud are the major source of interaction with radio frequency (RF) transmissions. A recent survey of flight experience of ion thruster systems by *Sovey et al* [1989] showed no major interference, but concluded that further study is needed since all systems flown required less than 1 kW power. However, communications interference was demonstrated during the Russian experiment EPICURE [*Borisov et al*, 1991]. Ion sources similar to SPT's (discussed in Section 1.1.2) of 2 kW power were flown for a total of 100 minutes at an altitude of 900 km. A shadow experiment was conducted where satellite telemetry (VHF 3-300 MHz) and transponder (S-band) signals were transmitted to ground stations during thruster firings. The experiment verified predictions of disruption of communications to ground stations located in the plume-induced radio shadow.

### Neutral Propellant Efflux

Propellant that remains unionized in the discharge chamber flows out through the grids in free-molecular flow at thermal speeds corresponding to the thruster wall temperatures (~500°K). Neutrals that do not succumb to CEX collisions within the grids are emitted in more or less a cosine distribution and follow line-of-sight paths. Also included in this category are neutrals that have beam ion velocities that are formed after CEX collisions. If the neutralizer is a hollow cathode, as opposed to a hot wire filament, a certain amount of the propellant used in the neutralizer also contributes to the neutral efflux. The impact of these neutrals is critically dependent on their condensation properties. Depending on the various properties of the propellant such as vapor pressure, the neutral propellant efflux may or may not be serious. One of the earliest studies on ion thruster neutral contamination effects was a study by *Reynolds and Richley* [1969] that examined mercury deposition

---

with point source relations. Experiments were also conducted that showed that the ratio of solar absorptivity to emissivity of solar cells increased with increased mercury deposition. This has important consequences for the thermal balance since the temperature scales with the fourth root of this ratio. It was noted that the solar array panels in a sense could become self-cleaning since when the temperature rises due to deposition, the surface evaporation rate will increase.

In 1970, NASA launched the SERT II spacecraft with two 15 cm mercury ion thrusters onboard into a 1000 km orbit. The mission objective was the endurance testing of the thrusters for at least six months, and the study of thruster-spacecraft interactions such as surface contamination, radio link interference, and spacecraft potential control. Despite occasional problems, and the loss of one thruster due to a grid short, the other thruster remained operational until 1981 when the propellant supply was exhausted [Kerslake and Ignaczak, 1992]. An experiment onboard to detect surface contamination by the thruster effluents consisted of two sensors that were located adjacent to each thruster downstream from the exit plane. These sensors were small solar cells whose output voltages were monitored to detect surface degradation and resulting deterioration of optical properties. One sensor, maintained at +60°C, was used for detection of sputtered thruster accelerator grid material (molybdenum), and the other at -40°C was used for possible detection of condensation of the neutral mercury as well as molybdenum. The temperatures were chosen to simulate solar array equilibrium temperatures at 1 and 2 A.U. from the sun. The high and low temperature sensors were located at 64° and 62° from the beam axis and 37 cm and 34 cm respectively, from the accel grid centers. For one thruster, after 7.5 hours of operation, the low temperature sensor voltage decayed by 50%, and the high temperature one did so in 6.5 hours. For the other thruster, the sensor voltages decreased by 50% in 12 and 8.8 hours for the low and high temperature sensors respectively [Staskus and Burns, 1970]. While the temperature discrepancy was never resolved, since deposition should occur faster at lower temperatures, no evidence was found suggesting that the mercury propellant condensed. Deposition was only due to the sputtered grid material. No effects on the operational solar arrays providing power to the thrusters were noted.

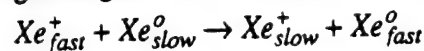
The common propellant in current use, xenon, is unreactive, and poses no concern unless spacecraft surfaces are extremely cold (<170°K). On the other hand, the vapor pressure of C<sub>60</sub> has been recently measured by Tokmakoff *et al* [1991], and it will have a tendency to coat surfaces that are not at sufficiently high temperatures (>500°K). Neutral emission rates vary depending on the thruster's propellant utilization fraction given by  $\eta_p = I_b / (I_b + I_n)$ , where  $I_b$  is the ion beam current, and  $I_n$  is an equivalent neutral current. Depending on the thruster, usual propellant utilization fractions range from 80-90%. It is

---

important to realize that even with high utilization fractions, neutral densities are usually higher than ion densities since the neutral velocities are much lower than that of the ions. For example, a xenon thruster operating at  $I_{sp}=3000$  s with neutrals at  $500^\circ\text{K}$ ,  $\eta_p=0.90$ , and a neutral to ion flow-through area ratio of 0.1, will have a neutral to ion density ratio of over 100.

### CEX Propellant Ions

Charge-exchange ions are formed by CEX reactions between the energetic beam ions and the neutrals that flow through the grid. For example with xenon,



Most of the CEX ions are formed within a couple of thruster radii downstream where both the beam ion and propellant neutral densities are the highest. CEX ions have been characterized by the general location of their creation according to a convention first employed by *Staggs et al* [1968]. A fraction of CEX ions are formed in the grid region and are emitted over a large range of energies and at angles up to  $90^\circ$  ("Group II"). Others are produced downstream and expand out of the beam ("Group IV"), while some are attracted back to impinge upon and sputter the grids ("Group III"). Grid sputtering is a serious concern and limits the lifetime of a thruster. In general, the trajectories of CEX ions are strongly influenced by radially-directed electric fields within the ion beam that are set up to prevent the escape of electrons and leave the beam with radially directed velocities. Thus, there is a component that can flow back towards the spacecraft and can potentially reach surfaces that do not have a direct view of the plume. The CEX ions initially have the energy of the thermal neutrals, and then acquire energy as a result of falling through the radial beam potential drop. The CEX plasma contributes less than one percent to the thrust, and its transport depends on many factors, including initial energies, and the potentials and geometry of nearby spacecraft surfaces. The CEX plasma will fill all space in the vicinity of the spacecraft, but accurate predictions of its propagation are complex and filled with large uncertainties due to the above factors [*Deininger*, 1985].

A qualitative description of the CEX plasma has been shown by *Kaufman* [1975] to follow the "barometric" equation for the electron density,  $n_e$ , as a function of potential  $\phi$ ,

$$n_e = n_{e0} \exp[e(\phi - \phi_0)/kT_e] \quad (1.2)$$

This equation, more commonly known as the Boltzmann relationship, states that the electrons, in relation to a reference condition denoted by subscript  $o$ , are in a equilibrium between electric fields and pressure gradients with some constant temperature  $T_e$ . It is generally valid only in localized regions where the electron temperature is approximately constant. However, it is not valid in the entire downstream region, since the electrons are



expanding and their temperature is decreasing. Except for a few measurements taken inside the beam and in the CEX plasma by *Kaufman*, to date, the electron temperature in the plume has never been thoroughly investigated. It should be noted that the "barometric" equation was actually first used by *Sellen et al* [1965], but was only applied within the beam.

Experimental measurements of CEX plasmas are quite difficult due to vacuum facility effects. A difficult issue is discriminating between CEX ions from thruster neutrals and neutrals from the residual gases in the test chambers [*Komatsu et al*, 1975; *Komatsu and Sellen*, 1976]. A few tests exploiting the end-effect on Langmuir probes by *Carruth and Brady* [1981] have obtained more reliable data. In addition, CEX plasmas are highly thruster specific and hence general properties are hard to infer. Some general approximate CEX plasma characteristics for a J-series 30-cm thruster 0.5 m downstream are a density of  $10^{12}$ - $10^{13}$  m<sup>-3</sup> and an average energy of 1 eV or less. This effluent is the most difficult to characterize and still the least well understood [*Carruth*, 1982].

In addition to grid sputtering, the sputtering of other spacecraft surfaces by CEX ions will critically depend on the potential acquired by the surface. In general, the impact of low-energy Xe<sup>+</sup> is not well documented. Flight data for return fluxes to spacecraft are very limited, and the SERT II flight offered no direct observations of CEX ion fluxes. One reason is that during thruster operation, the spacecraft potential never became highly negative since thruster operation kept the spacecraft potential near zero. The generation of a CEX ion plasma that surrounds the spacecraft may also lead to parasitic current losses to high voltage solar arrays [*Katz et al*, 1981].

However, it should be mentioned, that while the CEX ion plasma poses a potential impact to the spacecraft it may also help alleviate differential charging through the generation of a plasma cloud that acts as a "plasma bridge". The SERT II flight test showed that spacecraft potential could be controlled by biasing the neutralizer [*Jones et al*, 1970]. In 1974, the Applied Technology Satellite (ATS) - 6 carried two cesium ion thrusters into GEO. Thruster operation clearly demonstrated that extremely negative spacecraft potentials encountered could be alleviated [*Olsen*, 1978]. However, it was unfortunate that only after brief periods of operation, both thrusters failed due to faulty propellant valves, terminating any attempts to gather long exposure contamination data [*Worlock et al*, 1975]. Surface contamination was an important issue, since the thrusters were canted only 37° away from the spacecraft body. One thruster operated only for 20 minutes, and the other for 92 hours. After such brief periods of operation, no deleterious contamination effects were observed.



## Non-Propellant Efflux (NPE)

Perhaps the most important efflux for contamination, are non-propellant effluents (NPE). These particles are composed of neutral material sputtered from thruster components, and the primary component is neutral accelerator grid material, although traces of discharge chamber metals have been detected in the plume [Pollard, 1994]. The most commonly used grid material is molybdenum due to its low coefficient of thermal expansion (almost half the value of titanium). However, recent tests with carbon-carbon grids show much promise due to their high sputter resistance (1/3-1/7 the sputter yield of molybdenum) [Messerole and Hedges, 1993; Messerole, 1994]. Sputtering erosion of the grids is the main life limiting factor for ion thruster operation. A portion of these neutrals undergo CEX collisions with the fast beam ions, but the rest move in straight line trajectories. An extremely important characteristic of this effluent is that it will almost certainly stick and remain on any surface upon which it is deposited due to its low vapor pressure. In one test, a 20% reduction in transmittance occurred after about 2 nm of molybdenum was deposited on a solar cell cover [Deiningner, 1985]. In addition, as we saw above, the SERT II flight tests demonstrated that the sputtered molybdenum grid material easily coated solar cell test cells [Staskus and Burns, 1970]. In ground tests where witness plates are placed in the plume, an equilibrium between ion beam erosion and NPE deposition occurs between 45°-60° with respect to the thruster axis. At angles greater than these, the NPE deposition dominates. For angles less than these, ion beam erosion is dominant and will remove any NPE deposition that forms [Weigand and Mirtich, 1975].

## Field Efflux

Potential effects of the field efflux are electromagnetic interference (EMI) and communication interference. Static or fluctuating electromagnetic fields could also affect plasma transport. In a recent survey by Sovey *et al* [1989] of ion thruster propulsion systems, it was found that there was no adverse impact on previous missions. Specifically, the SERT II mercury thruster with a beam current of 0.2 A showed no radio frequency interference (RFI) on the 1.7 and 2.1 GHz sensors or the wide band radio frequencies. The ATS-6 spacecraft with a cesium thruster operating with a current level of 0.1 A also showed no apparent RFI on telemetry, command or communications bands (153 MHz, 2.25 GHz, 6.15 GHz).

### 1.1.2 Hall Thrusters

Hall or Stationary Plasma Thrusters (SPT) are essentially gridless ion thrusters that

make use of the  $\mathbf{j} \times \mathbf{B}$  force similar to MPD thrusters. Propellant is fed between two concentric cylinders in which a gas discharge takes place. Magnetic coils create a nearly radial magnetic field on the order of 150-200 G. An axial electric field is applied, on the order of 100-700 V, which generates an azimuthal Hall current in the  $\mathbf{E} \times \mathbf{B}$  direction. This current interacts with the magnetic field, producing a volumetric  $\mathbf{j} \times \mathbf{B}$  accelerating force on the plasma. Since the magnetic field is sufficiently weak that the ion gyroradius is much larger than the dimensions of the thruster, the ions are accelerated to nearly the full applied potential [Wetch *et al*, 1991]. The absence of grids, and a quasi-neutral plasma means that the current-limited condition of conventional ion thrusters is not experienced. Similar to ion thrusters, the plumes of SPT thrusters contain fast beam ions, neutral propellant, slow CEX ions, and sputtered electrode material. Xenon is the most common propellant. Between 50-100 SPT thrusters have been used onboard Soviet spacecraft over the last twenty years for attitude control [Wetch *et al*, 1991]. However, only recently have detailed studies of their plume structure been undertaken in the U.S. [Absalamov *et al*, 1992; Garner *et al*, 1993; Myers and Manzella, 1993; Manzella, 1993].

### Plume Particle Efflux

One of the features of SPT thrusters, is that their beams have very large divergence angles, and the flow propagates almost in the entire half plane. Most of the current density however, resides within a  $45^\circ$  angle [Absalamov *et al*, 1992]. The current density is sharply peaked at the centerline, but drops off by a factor of three within  $22^\circ$  of the axis [Myers and Manzella, 1993]. For thruster operation at an accelerating voltage of 300 V and mass flow rate of 5.6 mg/s, the electron density was found to decrease from  $10^{17} \text{ m}^{-3}$  at 0.3 m from the exit to  $10^{14} \text{ m}^{-3}$  4 m downstream. At a fixed downstream distance, the density dropped by an order of magnitude at  $45^\circ$  compared to the centerline. Over the same region from 0.3 to 4 m, the electron temperature varied from 3.4 to 1.7 eV, and no variation of temperature with angular position was observed. The ion energy distribution observed at  $15^\circ$  off the axis peaked at 270 V, with a secondary peak at 160 V [Manzella, 1993].

The ionization fraction at the exit is at least 95%, with 10-20% of the ions being doubly ionized [Manzella, 1993]. The main source of neutrals appears to be the neutralizer cathode, through which about 10% of the total propellant flows. Since the most common propellant is xenon, as in ion thrusters, the neutral flow is not a problem, unless for extremely cold surfaces. However, this neutral flow contributes to the production of CEX ions in the "zone of electromagnetic acceleration" inside the thruster, which exit the thruster and the beam at large angles. A recent, although quite shallow, assessment of SPT

spacecraft contamination by *Tribble et al* [1994] concluded that slow ions in the plume did not present a hazard because electrostatic attraction of contaminants is not expected. While it is true that the influence of the spacecraft potentials is not felt by the CEX ions if the spacecraft sheaths are small, as we shall see later in this thesis, the self-consistent electric fields of the expanding plasma can actually force a component of the CEX ions back towards the spacecraft. In addition, the backflow of CEX ions from ion thrusters has been clearly observed.

The source of most of the NPE is the discharge chamber walls. The efflux is composed of molecules and atoms of boron, nitrogen, and oxygen. The flux is less than 1% of the total mass flow ( $\sim 5$  mg/s), and after 3000 hours of operation, decreases to less than 0.1%. It was found after 4000 hours of operation, that about  $20\text{--}25\text{ cm}^3$  of thruster material had been eroded away. The characterization of the NPE from SPT's is very difficult due to the presence of both neutrals and positive and negative ions [*Absalamov et al*, 1991].

### Field Efflux

From extensive past flight experience, SPT thrusters have apparently not exhibited noticeable detrimental field effluxes, although their plumes interfered with radio signals passing through them [*Borisov et al*, 1991]. SPT operation over 600 hours during the Meteor-18 spacecraft interactions experiment did not disrupt communications. However, it was mentioned that "close location of receiving antennas and thruster in some cases brought a slight influence on the propagation of the radio signals" [*Sovey et al*, 1989]. Data from the other Meteor flights with the SPT's are insufficient for any conclusion.

Optical emissions in the plume were measured in the range from  $3000\text{--}9000\text{ \AA}$  [*Manzella*, 1993]. A total of 250 mW of radiated optical emission was measured from the exit plane, the majority of which was in the blue part of the spectrum.

### 1.1.3 MPD Thrusters

Magnetoplasmadynamic (MPD) thrusters accelerate ionized gases with the volumetric  $\mathbf{j} \times \mathbf{B}$  force caused by the interaction of crossed electrical currents driven through the gas and magnetic fields due to either those electrical currents or external fields. Since the first experiments in the early 1960's [*Ducati et al*, 1964], to the best of our knowledge, no MPD plume backflow measurements in the open literature exist.

Currently, alkali metals, particularly lithium, are being considered to improve performance in a number of important aspects [*Polk and Pivrotto*, 1991]. Firstly, the

---

alkali metals are desirable by virtue of their low ionization energies (5.4 eV for lithium compared to 15.8 eV for argon). Among the alkali metals, lithium appears to be the most attractive due to the large difference between its first and second ionization potentials. These attractive features reduce frozen flow losses and increase efficiency. Indeed, thruster efficiencies up to 70% have been reported with lithium as a propellant. Secondly, the immersion of refractory metal cathodes in alkali metal vapors significantly reduces the work function of the cathode surface and results in a lower surface temperature, thereby increasing cathode lifetime. Experiments have shown reductions in cathode temperature by approximately 300°K, and decreases in erosion rates by a factor of twenty [Polk and Pivrotto, 1991]. However, the vapor pressure of lithium and other alkali metals is quite low, and the condensation coefficient on metal surfaces is essentially unity. Thus, the potential for surface contamination is very high.

### **Plume Beam**

The plume flow field of an MPD thruster can be divided into three regions. The central portion is the highly energetic core that is collisional, quasineutral, and dominated by hydromagnetic effects. Surrounding the core, is a collisional quasineutral flow of lower energy that originates from the cooler boundary layer near the anode. Due to the lower temperature, the degree of ionization will be less, and there will be a neutral component to this flow. The partially-ionized flow can turn around the anode lip, and undergo an expansion similar to the boundary layer flow in a chemical thruster. It is from this region that slow ions can be scattered into the third region, which is the collisionless backflow region. Thus, the boundary layer region acts as the main source for the backflow.

General observations indicate a high velocity, highly ionized, central core and an electrothermally heated relatively lower velocity outer region which is slightly ionized. These slower outer species are from the thin boundary layer region near the anodes where wall recombination effects are important. There are also similar effects from the central cathode, but most of these neutrals reionize in the highly luminous region downstream of the cathode tip. More than 99% of the propellant is ionized. The central core ions have velocities on the order of  $10^4$ - $10^5$  m/s, and travel primarily line of sight paths within a cone of about 15°-20° half-angle [Deininger, 1985].

### **Non-Propellant Efflux (NPE)**

Ablation of the cathode and anode even in stable regimes of operation can be quite high and poses limitations on long duration operation. However, it has been recently shown that increasing the purity of the propellant (predominantly argon) can dramatically reduce

---

erosion by factors over twenty. The presence of impurities such as  $O_2$  can increase erosion. Steady-state cathode erosion values as low as 1-2 ng/C or 2  $\mu\text{g/s}$  for a 2 kA thruster operating with 99.998% pure argon have been reported by *Auweter-Kurtz et al* [1990]. In contrast, other devices have been measured with rates as high as 1  $\mu\text{g/C}$  [*Sovey and Mantenicks*, 1988]. In an argon operated thruster, constituents of the gas surrounding the thruster were found to contain  $CO_2$ , C,  $O_2$ ,  $H_2$ , and  $N_2$  from insulating materials, and copper and tungsten from the anodes [*Deininger*, 1985].

An important issue with regards to contamination is the velocity distributions of the sputtered/ablated species which have never been measured. However, remaining propellant neutrals in the central flow regions seem to have good momentum coupling with the ionized core and exit with high velocities (in contrast to ion thrusters). Thus the probability of charge-exchanging and creating the problem of slow ions around the spacecraft is much lower. Even slower outer neutrals may have about 50% of the core velocity [*Brukhty et al*, 1993]. Except for the heavy metal species from the electrodes (if they do not have high velocities and are charged), transport of species is then line of sight. However, it is known that the strong magnetic fields in applied field thrusters extend well outside the thruster, and thus will act as a confinement mechanism and inhibit expansion of charged particles. On the other hand, self-field thrusters do not have such strong magnetic fields extending outside. At any rate, if MPD thrusters are going to be flown, their ablation rates must be sufficiently low for considerations of electrode lifetime. The Soviets have used cesium and potassium MPD thrusters on satellites and have said that contamination is "low" although films on the order of 100 nm were apparently formed in 13 minute long experiments [*Polk and Pivrotto*, 1991]. Very few details are available, such as the location of the films with respect to the thrusters, but 100 nm is quite a thick film, and on solar arrays can lead to heavy decreases in the coverglass transmittance, and hence power produced.

### Field Efflux

The 2 MW pulsed MPD thruster aboard the Shuttle SpaceLab-1 experiment did not exhibit any hazardous EMI. However, during thruster firing, click noises were heard on the UHF communication link. In addition, on the MS-T4 flight experiment of a 240  $\mu\text{N}$  MPD thruster, pulses corresponding to thruster firings were observed on the signals of a 400 MHz antenna system. However, no serious impacts were seen on the telemetry systems. It should be noted that results to date have been for pulsed systems, and that the emissions from steady-state MPD thrusters may be different [*Sovey et al*, 1989].

#### 1.1.4 Arcjets

Arcjets are very simple devices in which the propellant is heated by passing it through an arc discharge. From their initial development in the late 1950's [Giannini, 1957], they have reached commercial viability with the 1993 launch of the geostationary communications satellite, Telstar 4, that uses arcjets for station keeping [Bogorad *et al.*, 1992]. The propellant gas is heated to a very high temperature (up to 4000° K within a central core) and then expanded by means of a standard high expansion ratio nozzle. Many arcjets are radiatively cooled, and thus the thermal loads must be carefully considered during spacecraft integration. As with conventional chemical rockets, light gases are preferred for high exit velocities and hence hydrogen, hydrazine, or ammonia are typically used.

#### Plume Beam Efflux

Electron densities and temperatures have been measured in a number of recent plume studies by Carney [1988], Liebeskind *et al.* [1993], and Ruyten *et al.* [1993]. Measurements upstream of the exit plane [Ruyten *et al.*, 1993] within a 1 kW arcjet operating on simulated ammonia yield a temperature range of 2000-3500°K, and an electron density of  $1.5 \times 10^{20} \text{ m}^{-3}$ . Measurements 30 cm downstream in the plume of a 1 kW arcjet [Carney, 1988] indicate ionization fractions around 1% or less, electron densities of around  $10^{15} \text{ m}^{-3}$  and an electron temperature less than 1 eV. The gas dynamic expansion of the plume dominates electron-ion recombination processes beyond about two nozzle exit diameters downstream and results in reducing the electron density along the thrust axis.

The most problematic aspect of arcjets is electrode erosion, and a typical material, thorium, poses a very similar threat as do molybdenum grids in ion thrusters. In a thirty day test of a 30 kW hydrogen arcjet, the electrode mass loss was about 9 grams [Deininger, 1985]. During a recent 300 hour endurance test of a 1 kW arcjet, electrode mass loss was measured to be 9 mg, although this was thought to be caused by anomalously low flow rates [Cruciani and Deininger, 1993]. However, Telstar 4, the first commercial satellite to use arcjets, has apparently not experienced any contamination problem in orbit [Lichtin, 1995]. Ground tests conducted prior to the launch demonstrated that the arcjet plume discharged highly biased surfaces, and spacecraft surfaces exposed to the plume for a 40 hour period did not show any significant degradation in absorptance, emittance, and resistance [Bogorad *et al.*, 1992].



## Field Efflux

The radiated and conducted electromagnetic emissions from a 1.4 kW hydrazine arcjet system were measured at frequencies from 30 Hz to 10 GHz. Emissions in the commercial command and communications bands were within limits, while broadband noise above MILSPEC limits was observed below 40 MHz. The source of this noise is still under investigation [Zafran, 1990].

The emission spectra from a 1 kW arcjet was obtained in the 80-500 nm range. For hydrogen, nitrogen, and ammonia as propellants, the irradiance was highest in the vacuum ultraviolet range. The total emitted power was less than 1 W [Crofton, 1992].

### 1.1.5 Existing EP Contamination Prediction Models

The field of thruster plume contamination is very broad, and also encompasses much research in the expansion of neutral gas plumes associated with chemical thrusters which we have already discussed. For EP thruster plume and contamination modelling, efforts have ranged from simple analytical point source models analogous to chemical plume models, to particle tracking codes, to fluid models to recent kinetic approaches.

Simple analytical models of EP plumes based on point source formulations have been employed for ion thrusters [Kaufman, 1975; Carruth *et al.*, 1981], MPD thrusters [Bruckhty *et al.*, 1993], and arcjets [Carney, 1988; Bogorad *et al.*, 1992]. We will examine in detail the models of Kaufman and Carruth *et al.* in Chapter 2 that were developed to estimate the backflow of the CEX ions. The MPD plume model of Bruckhty *et al.* is a point source formulation that attempts to represent the far flow field of a supersonic jet of an ideal fully ionized plasma outflowing into a vacuum. This model completely neglects plasma effects, i.e. the role of electric and magnetic fields, and divides the flow field into a core region, and an outer flow region that is due to the slower boundary layer flow. The plasma density in the core region is described by a relation very similar to Eqn. (1.1) and is contained within the limiting angle of a Prandtl-Meyer expansion. In the outer flow which extends into the backflow regions, the density is given by an empirical relationship. The density is taken to be exponentially attenuated as a function of the angle from the edge of the core region and is actually remarkably similar to the Simons model used in chemical plume models. As with the ion thruster models, the Bruckhty *et al.* model can be used for order of magnitude estimates for the plume, and rough agreement with limited data can be obtained. However, due to the complete lack of inclusion of electric and magnetic effects, the physical structure of the backflow can not be captured properly. No complete model of an MPD plume has yet been constructed incorporating the magnetohydrodynamic effects that



are important in the core with the collisionless backflow.

A model similar to the *Hill and Draper* chemical rocket plume model was used by *Carney* to estimate the plasma density in the plume of an arcjet in order to assess plume - electromagnetic wave interactions for communications interference studies. However, the model used shape parameters that were fit to data. Recently, the powerful tool of DSMC was applied to arcjets by *Boyd et al* [1993] to provide accurate descriptions of the expanding neutral flow field. However, only neutral gas flows were modelled, and no plasma components were considered. Even though the ionization fraction is less than 1% in low-power arcjet plumes, the electron density is  $>10^{15} \text{ m}^{-3}$ , and thus is still a substantial element that must be accounted for. A full arcjet plume model remains to be constructed.

In an attempt to understand the transport of the CEX ions in ion thruster plumes, a number of particle tracking models were developed. *Komatsu and Sellen* [1976] developed a model based on experimental measurements of the ion density within the plume. The barometric equation with an assumed electron temperature was used to deduce potential contours and hence electric fields in the plume. The trajectories of individual ions with various initial conditions were tracked through the fixed electric fields, and it was shown that the CEX ions leave radially from the beam. However, the region of the calculations was only in front of the thruster, and it was not shown clearly that the CEX ions are then transported upstream into the backflow region. *Robinson et al* [1982] developed a computer code, called PLASIM, that was designed to track CEX ion trajectories over regions encompassing both the beam and upstream of the thruster exit. The methodology of this code is very obscure and assumes the plasma flow is "laminar"; that is, ion trajectories do not cross. The barometric equation is used to relate the CEX ion density with the potential. Figure 1.3 shows sample calculations of PLASIM compared with experimental data. Note that the beam divergence is not included. While the CEX plasma density is reasonably close at right angles to the beam, there is not very good agreement in the backflow region. In addition, noticeable differences exist in the structure of the density and for unknown reasons, the PLASIM model was not applied all throughout the backflow region.

An axisymmetric fluid model of the electrons emitted from a neutralizer into the ion beam was developed by *Parks et al* [1981]. However, only the beam was modelled; the CEX plasma was not incorporated. The beam was assumed to be quasineutral with the ion density "assumed to be known", and there was no beam divergence. The electron momentum equation was expressed as Ohm's law with electric field, pressure, and collisional terms. An anomalous electron-ion collision frequency on the order of the electron plasma frequency was assumed, although there is no direct evidence for such,

aside from invoking "plasma turbulence". No interactions between the plasma and the neutrals were modelled, and the energy equation was reduced to a balance between ohmic dissipation and conduction, with the thermal conductivity related to the electric conductivity by the classical Weideman-Franz law. The electric potential was obtained from  $\nabla \cdot \mathbf{j} = 0$ . Potentials and electron temperatures were computed and seemed reasonable, but detailed comparisons with experiment were not made. The boundary conditions imposed on the electron fluid velocity appeared quite arbitrary, and results showed that the electron current emitted from the neutralizer (which was a ring in the axisymmetric geometry) returned to the thruster exit. In reality, the negatively biased accel grid repels backstreaming electrons.

A three-dimensional isothermal fluid model of the CEX plasma was developed by *Katz et al* [1981] and integrated with a spacecraft charging model to study the interaction of the CEX plasma with biased solar array panels. The actual dynamics of the CEX plasma creation were not modelled; only the expansion of a plasma of given density was considered. However, the use of a fluid code to model the expansion of a rarefied plasma over meter length scales is questionable. In addition, none of these fluid models present a unified approach to the plume including both the beam and the CEX plasma.

To address the issue of grid sputtering in ion thrusters, *Peng et al* [1991-1993] developed a three-dimensional model of a single grid aperture hole and studied the dynamics of CEX ions created from beam ions and neutrals and their subsequent impingement upon and erosion of the grids. The plasma particle-in-cell (PIC) technique was used to track the CEX ions under the influence of self-consistent electric fields computed from Poisson's equation with the Boltzmann relationship for the electrons. Grid erosion is a function of the residual background gas pressure in ground vacuum facilities, and hence it is important to separate thruster and facility effects on thruster endurance testing. Grid sputtering patterns on the downstream face of the accel grid seen in experiments were very successfully reproduced, and estimates of grid mass loss were made. However, plasma parameters in the model must be adjusted for mass loss predictions to agree with experiment. This is partly due to the fact that their model does not account for sputtered material redepositing on other locations of the grids, and the fact that sputtering yields are a function of surface topology. The focus of these studies was on the length scales of the grid hole diameter (mm), and hence their model can not compute the transport of the sputtered grid material into the backflow regions. However, the approach of using the computationally intensive PIC method not only reflected the growth in modern computational resources, but also the first application of a technique that rigorously treats rarefied plasmas to ion thruster effluents.

Lastly, there have been recent attempts to directly solve numerically the kinetic

Boltzmann equation for the CEX plasma distribution function in SPT plumes [Bishaev *et al.*, 1993]. The ion and neutral components of the plume were described on the basis of kinetic theory, and the Boltzmann relationship relating the electron density to the potential was assumed, as well as quasineutrality. CEX collisions were incorporated via a Krook collision operator. The method of characteristics was used to compute neutral and plasma densities in the plume and backflow regions. In addition, the effect of a plume shield on reducing the backflow was investigated. This appears to be the only model developed thus far for SPT plumes. The only main deficiencies in the model are that the role of biased surfaces on the potential structure is not included, as well as eroded thruster component species.

In summary, while the basics of the underlying physics of ion thruster plume backflow have been identified, namely, the production of CEX ions from the beam ions and unionized neutral propellant, as well as sputtered grid material, no complete model that includes realistic models of all these components, and their subsequent transport over length scales on the order of a spacecraft body, has been developed. This is the goal of this thesis.

## 1.2 Outline of Research Approach

For a full analysis of spacecraft thruster plume contamination, there are three important questions that must be addressed.

- What are the effluents that are emitted by the thruster, and what are their characteristics?
- What are the transport mechanisms for the effluents, and how are they transported from the thruster/plume onto the spacecraft surface? What are the fluxes?
- What are the effects of the effluents on the spacecraft surface?

In this thesis, we concentrate on the first two issues. To do justice to the last issue fully, requires a separate excursion into plasma-surface interactions, which is not considered within the scope of this work. The first question has been addressed as a result of the literature review, and the thruster effluents for ion thrusters have been identified. However, some of the characteristics of the CEX ions and sputtered material remain to be further investigated. The answer to the second question is the main goal of this thesis. To fulfill this goal requires a numerical approach to modelling the expansion of the CEX ion plasma from the plume. We will develop first a two dimensional axisymmetric model to elucidate the physics of the plasma expansion process, and then a three dimensional model

---

to investigate the effects of geometry. The goal is to accurately assess and quantify ion thruster backflow contamination, and to investigate the physical mechanisms and hence the possibility of controlling or alleviating the problem if it poses severe limitations.

Three aspects will be covered in this research:

- *Physics*

A systematic study of ion thruster backflow and its relation to ion thruster parameters will be conducted.

- *Computational*

Developing a three dimensional numerical model will require the use of state-of-the-art computing resources due to the very large computational requirements. The use of massively parallel computers will be *enabling* for this problem, and will involve the development of algorithms for multi-computer environments.

- *Applications*

The numerical models developed will be applied to specific ion thrusters and spacecraft geometries, and will be used to provide predictions of backflow contamination that will be useful to spacecraft designers.

The structure of this thesis is as follows. In Chapter 2, an analytical assessment is conducted of ion thruster plume contamination by employing simple models to yield estimates and bounds on the problem. In Chapter 3, a detailed particle/fluid model of an ion thruster plume is presented that includes all the important species: beam ions, neutral propellant, CEX ions, neutralizing electrons, and sputtered grid material. Chapter 4 discusses a two-dimensional axisymmetric simulation model, and the numerical aspects. Results of this model are presented in Chapter 5 and are compared with experimental data. A fully three-dimensional model is presented in Chapter 6, along with a discussion of the parallel implementation. The three-dimensional model results are presented in Chapter 7, and comparisons with the two-dimensional model are made. Lastly, conclusions and recommendations for future work are offered in Chapter 8.

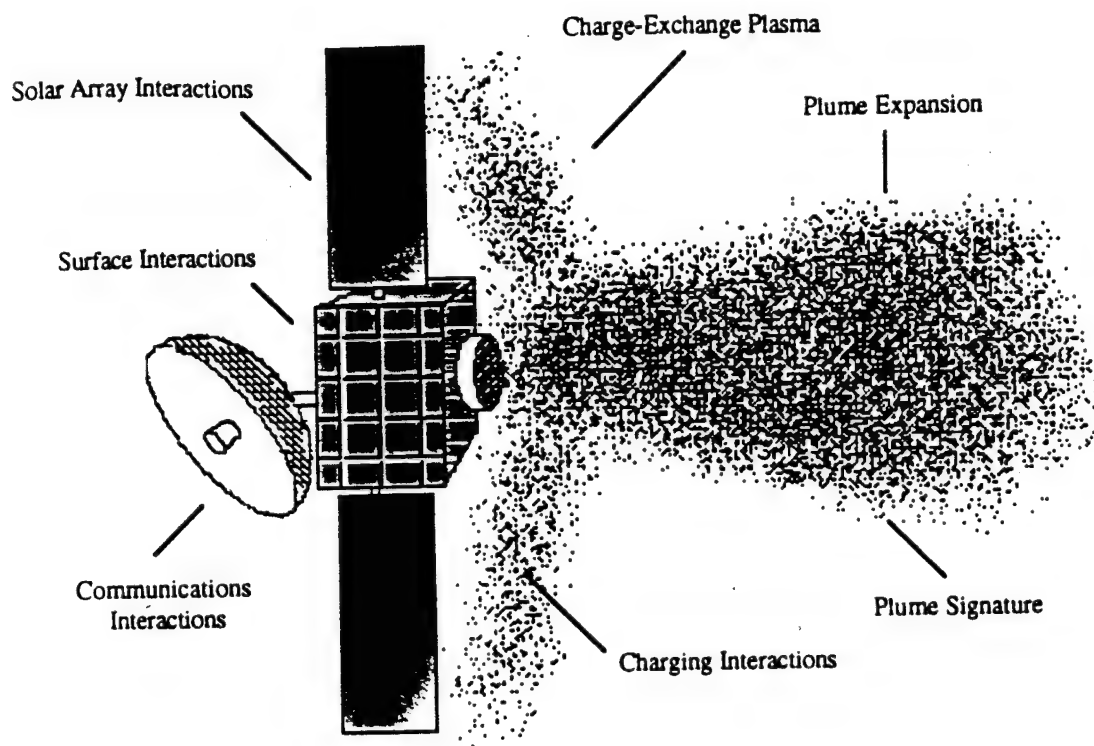


Figure 1. 1 Schematic of EP Thruster-Spacecraft Interactions

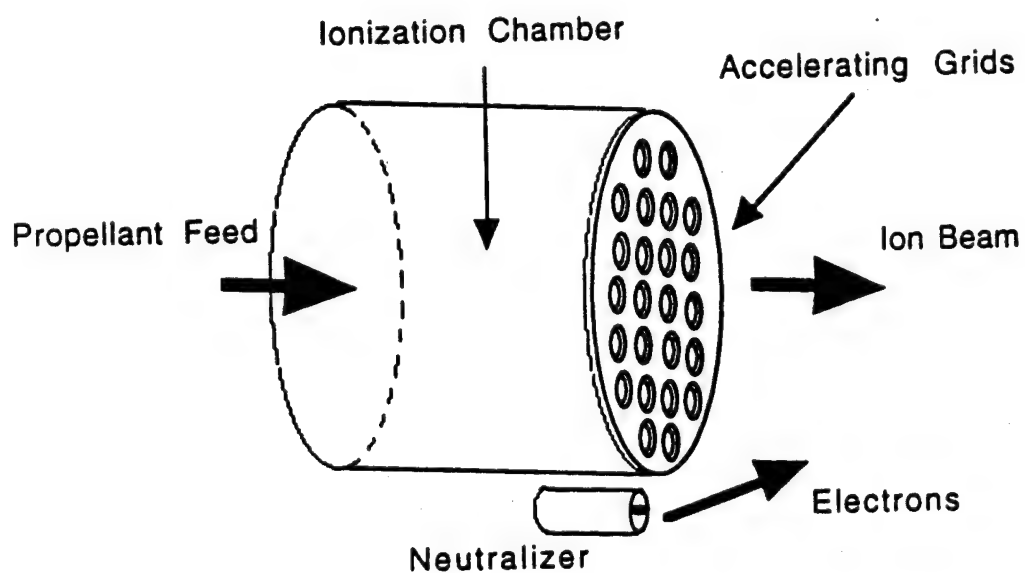


Figure 1. 2 Schematic an electron bombardment ion thruster

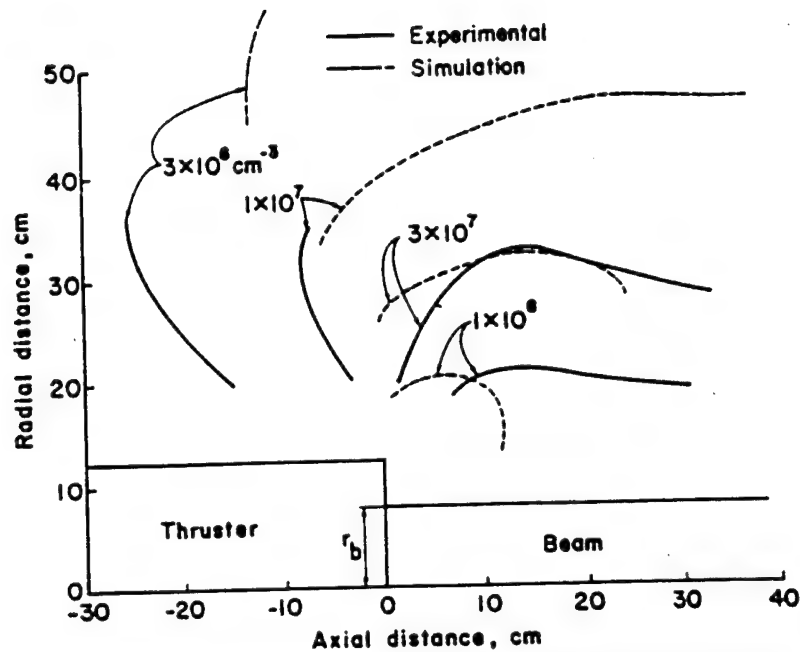


Fig. 7 Map of plasma density for 15 cm thruster with a beam current of 0.63 A and a propellant utilization of 0.85.

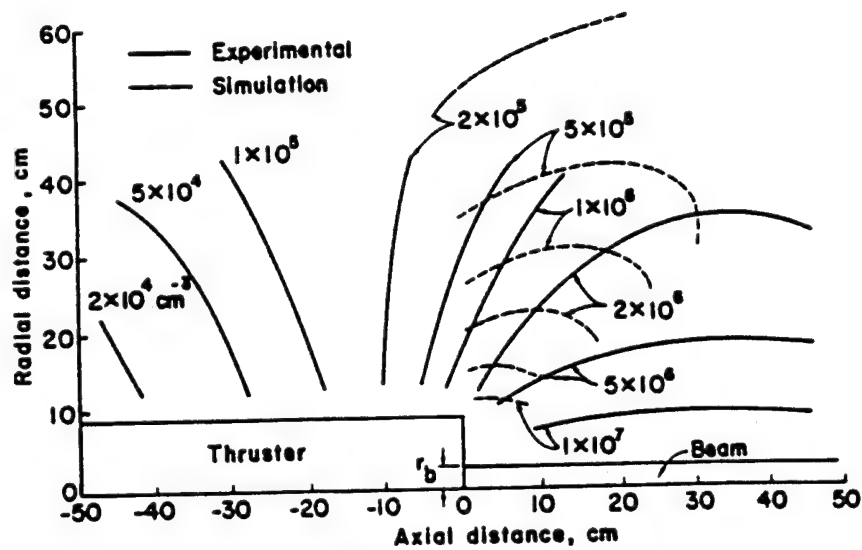


Fig. 8 Map of plasma density for 5 cm thruster with a beam current of 0.05 A and a propellant utilization of 0.71.

Figure 1.3 Computational results of CEX ion density from PLASIM code compared with experimental data (from Robinson *et al* [1982], reprinted with permission from AIAA)

# Chapter 2

## Analytical Study of Ion Thruster Contamination

In Chapter 1, we discussed previous experimental work that identified the main components of ion thruster plumes. Potentially, the most problematic issue for spacecraft contamination is the CEX plasma that is created inside the beam within a few thruster radii downstream of the thruster. This CEX plasma consists of both propellant ions, and most importantly, sputtered grid metal ions and propagates back towards the spacecraft. Since these species are charged, electric fields can influence their trajectories which will not be line of sight. In this section, we perform a simple analysis using existing simple models [Kaufman, 1975; Carruth *et al.*, 1981] to obtain a rough estimate of the CEX plasma parameters. The crudeness of the approximations will be pointed out and will show the need for a numerical model capable of modelling the CEX ion transport. A much more detailed description of the physical components of the plume will be given in Chapter 3.

### 2.1 Simple CEX Ion Production and Backflow Model

As we saw in Chapter 1, the beam ions are collimated and flow within a certain beam divergence angle, usually 15-20°. These beam ions do not present a direct contamination hazard unless a spacecraft surface is placed directly within the beam. However, this is highly unlikely due to the detrimental surface erosion effects that may occur from impingement by keV ions. Neutral propellant that is unionized in the discharge chamber flows out of the thruster in free-molecular flow, with a distribution that can be described with a general function in spherical polar coordinates  $(R, \theta)$ ,

$$n_n(R, \theta) = f(R) \cos(\theta) \quad (2.1)$$

Since the neutral flow is collisionless, the density of neutrals decays to zero for angles greater than 90° from the plume centerline, and neutral contamination is not likely for

---

surfaces located in the backflow regions ( $\theta > 90^\circ$ ). The only mechanisms possible for neutral transport into the backflow regions are scattering collisions, but they are negligible since the neutral mean free path is very large (km's). In Chapter 3, we will discuss the beam ion and neutral distributions in detail. In this simple analysis, we concentrate on the CEX ion production rates and a very simple model of the distribution.

Consider the region in front of an ion thruster of radius  $r_T$  as shown in Figure 2.1. We will deal first with the propellant CEX ions. The volumetric production rate of the propellant CEX ions is proportional to both the beam ion and propellant neutral densities as,

$$\dot{N}_{cep}(\mathbf{x}) = n_n(\mathbf{x})n_{bi}(\mathbf{x})v_{bi}\sigma_{cep}(v_{bi}) \quad (2.2)$$

where  $\sigma_{cep}$  is the propellant CEX cross-section, and the relative collision velocity is taken to be the beam ion velocity since it is much greater than the neutral propellant velocity. Typically, the beam ion velocity is 20,000-40,000 m/s, and the neutral velocity is the mean thermal velocity based on a temperature of 500°K. For xenon, the neutral thermal velocity is only 308 m/s. For this simple analysis, we take both the beam ion and propellant neutral density to be constant in the region on the order of a few thruster radii downstream of the thruster exit, within which the dominant amount of CEX ions are created. In this region, the beam ion density is given by,

$$n_{bi} = \frac{I_b}{e v_{bi} \pi r_T^2} \quad (2.3)$$

The neutral propellant flow leaving the thruster is characterized by a propellant utilization efficiency,  $\eta_p$ , which is defined as the ratio of the flux of propellant leaving as beam ions to the total propellant flow rate. Thus, the neutral flow rate (as an equivalent current) that leaves the thruster is,

$$I_n = I_b \left( \frac{1 - \eta_p}{\eta_p} \right) \quad (2.4)$$

The neutral propellant is flowing in free-molecular flow since the neutral mean free path is much greater than the grid hole dimensions. The temperature of the neutrals is assumed to be that of the thruster walls,  $T_w$ , and the flux leaving the thruster is given by the Knudsen efflux,  $n_{n0}C/4$ , where  $C = (8kT_w/\pi m_i)^{1/2}$  and  $n_{n0}$  is the neutral density in the thruster discharge chamber. The neutral density in the plume at the thruster exit is,

$$n_n = \frac{2 I_b (1 - \eta_p) / \eta_p}{e \bar{C} \beta \pi r_T^2} \quad (2.5)$$

where  $\beta$  is the grid neutral transparency fraction - the fraction of the thruster grid area through which the neutrals flow. It should be pointed out, that this density is actually the



density right at an individual hole in the thruster grid. The actual density downstream a few cm where the fine hole structure of the grid is lost may be slightly different. Thus,  $\beta$  may not necessarily be the exact geometrical open area of the grid, but will be close. To account for the neutral background pressure in ground tank tests, another term can be added to the neutral density:  $p_0 k T_0$ , where  $p_0$  is the tank pressure, and  $T_0$  is the temperature, usually near 300°K. We can now write the CEX ion production rate. If we take the volume in which the CEX ions are produced to be a cylindrical region of radius  $r_T$ , with length some  $a$  times  $r_T$ , the number of CEX propellant ions produced per second is,

$$\dot{N}_{cex p} = \left( \frac{I_b}{e v_{bi} \pi r_T^2} \right) \left( \frac{2 I_b (1-\eta_p)/\eta_p}{e C \beta \pi r_T^2} \right) v_{bi} \sigma_{cex p}(v_{bi}) (\pi r_T^2) (a r_T) \quad (2.6)$$

The constant,  $a$ , is usually on the order 1-3. If  $a=4/3$ , the volume is equivalent to a spherical region of radius  $r_T$ . Upon simplification, Eqn. (2.6) can be reduced to,

$$\dot{N}_{cex p} = \left( \frac{2 a}{e^2 \beta \pi} \right) \left( \frac{I_b^2 (1-\eta_p)/\eta_p}{C r_T} \right) \sigma_{cex p}(v_{bi}) \quad (2.7)$$

In our calculations, we will take  $a=2$ . With this value and  $C = (8kT_w/\pi m_i)^{1/2}$ , we have,

$$\dot{N}_{cex p} = 1.08 \times 10^{37} \left( \frac{I_b^2 (1-\eta_p)/\eta_p \sigma_{cex p}(v_{bi}) \sqrt{\mathcal{M}}}{\beta \sqrt{T_w} r_T} \right) \quad (2.8)$$

where  $\mathcal{M}$  is the molecular weight [kg/mole] of the propellant. This expression gives the production rate of propellant CEX ions per second. For typical values of a modern 30 cm beam diameter ( $r_T=15$  cm) xenon ion thruster,  $I_b=0.72$  A,  $\eta_p=0.75$ ,  $I_{sp}=2929$  s,  $T_w=500^\circ\text{K}$ ,  $\beta=0.24$ , and the xenon CEX cross-section is  $3.33 \times 10^{-19}$  m<sup>2</sup> corresponding to a beam velocity of 40,300 m/s [Rapp and Francis, 1962]. These values give a propellant CEX ion production rate of  $2.8 \times 10^{17}$  s<sup>-1</sup>.

For inert propellants like xenon, surface contamination is not a critical issue, unless the spacecraft surface is very cold (i.e. <170°K). However, the sputtered grid material, typically molybdenum, is a serious concern due to its low vapor pressure. As we saw in Chapter 1, propellant CEX ions are attracted back to the negatively biased accel grid and sputter it, causing erosion. To estimate the amount of molybdenum in the plume, we need to estimate the amount of sputtering of the accel grid - the component of the thruster that is eroded the most. One of the most common, and conservative, means of estimating the accel grid sputtering is to measure the impingement current to the accel grid in ground tests and extrapolate to space operating conditions. Given the ratio of the grid impingement current to the beam ion current,  $F_i$ , and the sputtering yield of molybdenum for the appropriate energy range,  $Y$ , the sputtered neutral flux from the grids is given by,

$$\Gamma_s = \frac{Y F_i I_b}{e A_g} \text{ [#}/\text{m}^2\text{s}] \quad (2.9)$$

where  $A_g$  is the surface area of the grid being eroded. A fraction of the neutral grid metal atoms will become charged via CEX collisions with the beam ions and the CEX ion creation rate is similar to that in Eqn. (2.2). The grid metal CEX creation rate is given by,

$$\dot{N}_{ceg} = \left( \frac{I_b}{e v_{bi} \pi r_T^2} \right) \left( \frac{Y F_i I_b}{e v_g \pi r_T^2} \right) v_{bi} \sigma_{ceg}(v_{bi}) (\pi r_T^2) (a r_T) \quad (2.10)$$

where  $v_g$  is the velocity of the ejected neutral grid atoms. The relative velocity is again taken to be the beam ion velocity, which is a conservative estimate. Hence, we can see that the ratio of propellant to grid CEX ion creation is,

$$\frac{\dot{N}_{ceg}}{\dot{N}_{cep}} = \frac{\beta Y F_i}{2} \left( \frac{\eta_p}{1 - \eta_p} \right) \left( \frac{C}{v_g} \right) \left( \frac{\sigma_{ceg}}{\sigma_{cep}} \right) \quad (2.11)$$

In Chapter 3, we will later see that for typical modern thruster conditions with xenon as the propellant and molybdenum grids,  $F_i$  is generally 0.1-0.2% in space,  $Y=0.5$ ,  $\sigma_{ceg}$  is  $6 \times 10^{-20} \text{ m}^2$ , and  $v_g$  is about 3170 m/s. Thus, the ratio of the CEX ion creation for xenon to molybdenum with all the given parameters, is only about  $4.4 \times 10^{-6}$ , a very small fraction.

Before pursuing the issue of how the CEX ions expand in the plume, it is important to note that the above expressions reveal scaling relationships in terms of how thruster operating parameters affect the CEX ion production. From Eqn. (2.8), we can see for a given thruster and propellant, the propellant CEX ion production rate scales as,

$$\dot{N}_{cep} \sim I_b^2 \left( \frac{1 - \eta_p}{\eta_p} \right) \sigma_{cep}(v_{bi}) \quad (2.12)$$

We will examine this scaling relationship later in Chapter 5.

To model the expansion of the CEX ions - both propellant and those from the sputtered grid metal, we assume they expand spherically from a point source which is a distance  $r_T$  away from the thruster exit on the plume centerline. An important issue is the velocity of the CEX ions as they leave the beam. Previous models [Kaufman, 1975], have taken the expansion velocity to be given by the Bohm velocity,

$$v_B = \sqrt{\frac{kT_e}{m_i}} \quad (2.13)$$

on the basis that this is the minimum velocity of ions for a stable sheath. Physically, the Bohm velocity is the minimum velocity of ions *entering* a sheath, not necessarily leaving a sheath, thus this assumption is questionable.

Another approach, is to view the CEX ions as falling through the radial potential drop of the beam edge which gives the expansion velocity,

$$v_{cex} = \sqrt{\frac{2e\Delta\Phi}{m_i}} \quad (2.14)$$

Comparing Eqns. (2.13) and (2.14), the Bohm velocity is analogous to a potential drop of  $kT_e/2e$ . The beam voltage drop can either be measured from experiment, or can be estimated by assuming that the electrons in the plume plasma are described by a Boltzmann distribution, i.e.,

$$n_e = n_\infty \exp\left[\frac{e\phi}{kT_e}\right] \quad (2.15)$$

so that when the potential decays to zero at "infinity" far from the thruster plume, the plasma density is the background density,  $n_\infty$ . The assumption of a Boltzmann distribution will be discussed at greater length in Chapter 3. Given this assumption, the beam potential drop can be estimated by taking the ratio of the beam ion density to the background density,

$$\Delta\Phi = \frac{kT_e}{e} \ln\left(\frac{n_{bi}}{n_\infty}\right) \quad (2.16)$$

For the above typical thruster values, Eqn. (2.3) yields a beam ion density of  $n_{bi} = 10^{15} \text{ m}^{-3}$ , and we use a typical ambient plasma density in LEO which is around  $n_\infty = 10^{10} \text{ m}^{-3}$ . For an electron temperature of 1-5 eV, the beam voltage drop is 10-60 V. Thus, xenon CEX ion expansion velocities are on the order of 3800-9400 m/s for xenon. In comparison, the Bohm velocity is 850-1900 m/s. Since the Bohm velocity is smaller, it will give a higher estimate of the density in comparison to using the velocity in Eqn. (2.14).

With the assumption of a constant expansion velocity, the current density of the spherically expanding CEX ions can be written as,

$$j_{icex} = e v_{cex} n_{icex} = \frac{e \dot{N}_{cex}}{4\pi R^2} \quad (2.17)$$

for  $R > r_T$  where  $R$  is the distance from the point of expansion as depicted in Figure 2.1. The CEX ion density is readily determined from,

$$n_{icex} = \frac{\dot{N}_{cex}}{4\pi R^2 v_{cex}} \quad (2.18)$$

Thus, we have an expression for the CEX ion distribution around the spacecraft. At  $R=r_T$ , we have the maximum CEX values within the beam.

However, we must ask the question whether the expansion process is truly isotropic, particularly in the backflow region. Examining Figure 2.1, the density would appear to decay as  $\theta \rightarrow 180^\circ$ . A simple model to deal with angular variations in the  $90^\circ$ - $180^\circ$  range was constructed by *Kaufman* [1975] as depicted in Figure 2.2. On no actual physical basis, it was hypothesized that the CEX ions leave the beam radially at the Bohm velocity, while the

backstreaming velocity is due to a hypothetical potential gradient of magnitude  $\Delta\phi$ , i.e.,

$$v_{\text{radial}} = \sqrt{\frac{kT_e}{m_i}} ; v_{\text{upstream}} = \sqrt{\frac{2e\Delta\phi}{m_i}} \quad (2.19a,b)$$

The angle of the velocity of the backflowing CEX ions,  $\theta$ , is related to the upstream and radial velocities by,

$$\cot(\theta) = \frac{v_{\text{upstream}}}{v_{\text{radial}}} \quad (2.20)$$

thus,

$$\cot^2(\theta) = \frac{2e\Delta\phi}{kT_e} \quad (2.21)$$

for  $180^\circ < \theta < 90^\circ$ . For the CEX plasma density, a Boltzmann relationship is assumed to relate the density (at a fixed radial distance from the point source) at  $\theta=90^\circ$  to densities at angles  $>90^\circ$  by,

$$n_{\text{cex}} = n_{\text{cex}90^\circ} \exp\left[-\frac{e\Delta\phi}{kT_e}\right] \quad (2.22)$$

where the  $\Delta\phi$  is actually the difference between the local potential at  $\theta > 90^\circ$ , and the potential at  $90^\circ$ . Thus, when the potential is lower than the value at  $90^\circ$ , the density will be lower than  $n_{\text{cex}90^\circ}$ . Eqns. (2.21) and (2.22) can be combined to yield,

$$\frac{n_{\text{cex}}}{n_{\text{cex}90^\circ}} = \exp\left[-\frac{\cot^2(\theta)}{2}\right] \quad (2.23)$$

valid for  $180^\circ < \theta < 90^\circ$ , which gives an angular distribution for the density with respect to a reference density,  $n_{\text{cex}90^\circ}$ , at  $\theta=90^\circ$ , for a fixed radial position. Thus at  $\theta=90^\circ$ ,  $n_{\text{cex}}=n_{\text{cex}90^\circ}$ , and as  $\theta \rightarrow 180^\circ$ ,  $n_{\text{cex}} \rightarrow 0$ .

## 2.2 Analytical Model Results

We will now apply this model to estimate both the propellant and sputtered grid material CEX ion distributions around a model spacecraft, and will compare the results with experimental measurements. *Kaufman* [1975] investigated the propellant CEX plasma produced by the 15 cm SERT II ion thruster that used mercury as a propellant. We compare the simple model predictions of propellant CEX ion density with measurements for the specific operating conditions of:  $I_b=0.63$  A,  $\eta_p=0.85$ ,  $\beta=0.1$ , and a beam voltage drop of about 40 V. A mercury ion-neutral CEX exchange cross section of  $4.17 \times 10^{-19}$  m<sup>2</sup> [*Rapp and Francis*, 1962] is used, which corresponds to the beam ion velocity of 31,011 m/s.

In Figure 2.3, a contour plot of the mercury CEX ion density is shown along with experimental measurements of the total ion density (including the beam ion density).

Experimental error is assessed to be  $\pm 20\text{-}50\%$  [Kaufman, 1994]. The model spacecraft/thruster body is 30 cm long and has a radius of 12 cm. We can see that the analytical model predicts higher densities in the backflow region behind the thruster exit, even though the role of the background neutrals is not included here (tank pressure was  $p_0 = 5 \times 10^{-6}$  Torr). At  $z=0$ , predicted values are at least an order of magnitude higher than the measured ones. However, for contamination estimates, it is better to be conservative and overestimate rather than underestimate the backflow. Nevertheless, overdesigning a spacecraft is generally undesirable due to the mass penalties incurred, and it is desirable to determine the backflow contamination with a much higher degree of accuracy.

Sputtered molybdenum grid material was not measured in the experiment, but we employ the model to estimate the molybdenum fluxes. We take  $F_i = 0.15\%$ ,  $Y = 0.05$ ,  $v_g = 3170$  m/s, and use a mercury-molybdenum CEX cross-section of  $8 \times 10^{-20}$  m<sup>2</sup> [Rutherford and Vroom, 1981]. It is assumed that the molybdenum distribution is the same as the mercury, aside from the magnitude. This is a very conservative approach since the grid material is sputtered away from the thruster at relatively high velocities in comparison to the propellant CEX ions. However, a molybdenum atom has about half the mass of a mercury atom, and is more easily influenced by the beam edge potential. In Figure 2.4, we show a plot of the molybdenum flux along a radial plane at  $z=0$  which is 30 cm upstream of the thruster exit plane. Note we have used the unit of *monolayer/year*. Depending on the mission, ion thrusters will operate for over 10,000 hours, and the unit of a monolayer relates to surface deposition. The atomic radius of molybdenum is 1.4 Å [Chang, 1988], and hence a monolayer corresponds to roughly  $1.6 \times 10^{19}$  atoms per square meter. Assuming all the atoms stick to the surface, the deposition rate ranges from 0.04 monolayers/year on top of the spacecraft, to 0.85 monolayers/year 26 cm above the thruster top.

In general, the growth rate of a deposited film is given by the relationship,

$$n \frac{dx}{dt} = \epsilon \Gamma - \frac{p}{\sqrt{2\pi m k T}} \quad (2.24)$$

where  $n$  is the atomic density of the film (m<sup>-3</sup>),  $x$  is the film thickness,  $\Gamma$  is the flux of atoms of mass  $m$  to the surface,  $\epsilon$  is the sticking coefficient,  $T$  is the surface temperature, and  $p$  is the vapor pressure. Eqn. (2.24) is a statement balancing the flux to the surface with the desorption rate which is a function of the vapor pressure of the material. In equilibrium, when no accumulation occurs, the arrival flux is balanced by the surface desorption rate. In general, the vapor pressure is a sensitive function of the substrate material deposition is taking place on. However, once a monolayer forms, the vapor pressure becomes less dependent on the surface. For our estimates, we will use the vapor

pressure of molybdenum on molybdenum which is given as a function of surface temperature,  $T$  [Weast, 1990],

$$\log(p \text{ [Pa]}) = 5.006 + A + \frac{B}{T} + C \log T \quad (2.25)$$

where  $A = 11.529$ ,  $B = -34626$ , and  $C = -1.1331$ . Given the above molybdenum fluxes, we can compute what the deposition rates will be. Figure 2.5 shows the vapor pressure desorption term as a function of temperature. The flux in monolayers/year is shown on a log scale, and is practically zero for temperatures below 1200°K. What is important to notice is that the vapor pressure is extremely low for temperatures typical of spacecraft surfaces (<500°K), so that any flux to spacecraft surfaces will completely stick ( $\epsilon=1$ ). As we have seen in Chapter 1, the effect of molybdenum adhering to sensitive spacecraft surfaces, such as solar array panels, is extremely detrimental.

In this chapter, we have used a simple analytical model to estimate the CEX plasma produced by an ion thruster. Comparisons of results for the propellant CEX ion density have shown that the model overpredicts by an order of magnitude the density, and predictions of the sputtered molybdenum flux have shown that up to 0.85 monolayers per year will be deposited on a plane 30 cm behind the thruster exit. However, these calculations were for a thruster that operated with beam current of 0.63 A. Since the CEX plasma scales with the square of the beam current, for higher power thrusters, if the beam current is increased by a factor of 10, the CEX plasma density will increase by factor of 100, and molybdenum flux rates will be correspondingly higher - posing a high contamination risk.

In order to assess the backflowing contamination, greater accuracy must be achieved in the calculations of the CEX plasma. There are many physical aspects that are completely neglected in the analytical model we have used. The simple models above essentially treat the plasma as a neutral gas with a constant velocity expansion. The most important factor that will affect the transport of the CEX ions is the self-consistent electric field in the plume. To treat the expansion of the CEX ions properly, these fields can not be neglected and will strongly influence the propagation of the CEX ions. Moreover, given the critical nature of the molybdenum ions, we can not assume that they will follow the distribution of the propellant CEX plasma simply by a scaled factor. The dynamics of their creation and propagation must be followed in closer detail. In addition, the geometry of the spacecraft will play an important role in the plasma expansion over spacecraft surfaces, and biased surfaces will alter the CEX plasma transport. Thus, in order to model properly the CEX plasma, we must turn to a numerical model that will accurately follow the creation and transport of the CEX plasma. This will be the topic of the rest of this thesis.

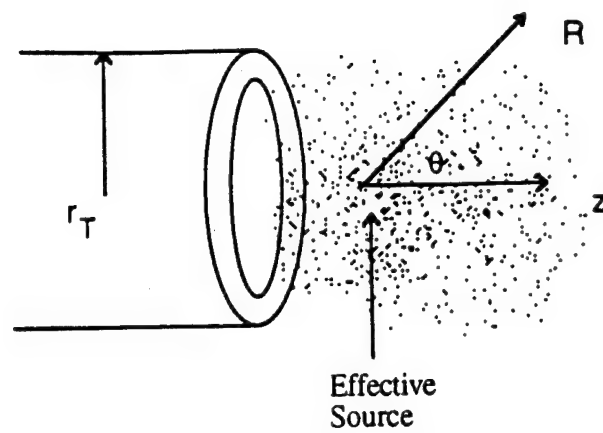


Figure 2.1 Schematic of geometry for simple CEX ion models

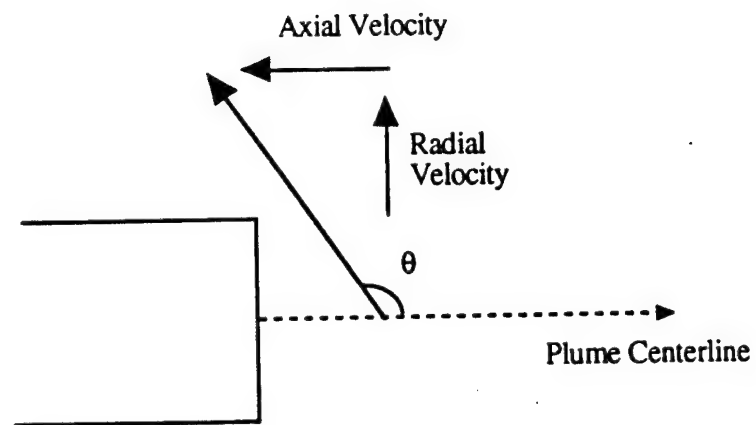


Figure 2.2 Diagram of CEX ion velocity components in backflow region

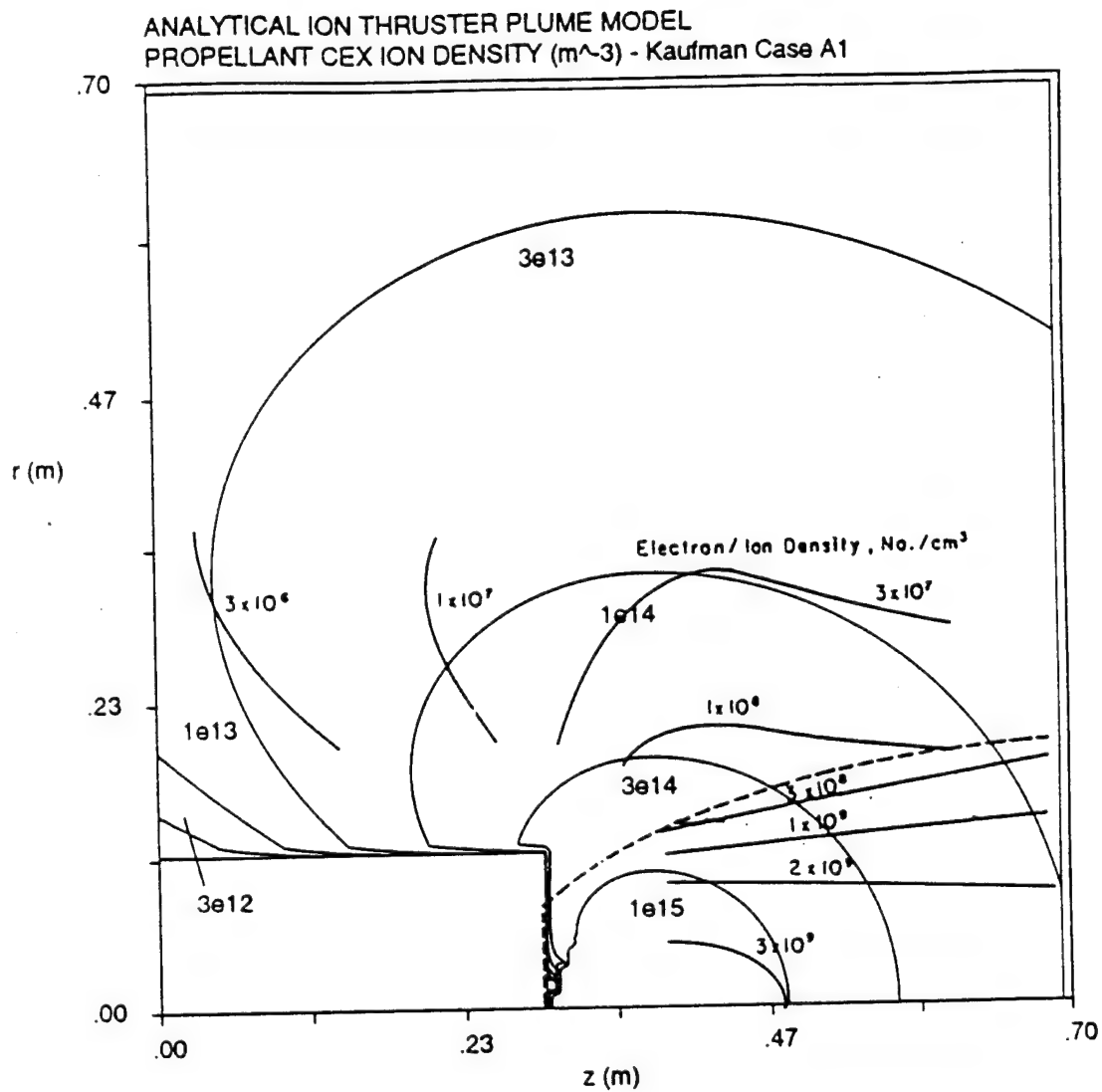


Figure 2.3 Contour plot of mercury CEX ion density predicted by simple analytical model for SERT II thruster compared with experimental measurements from Kaufman [1975]



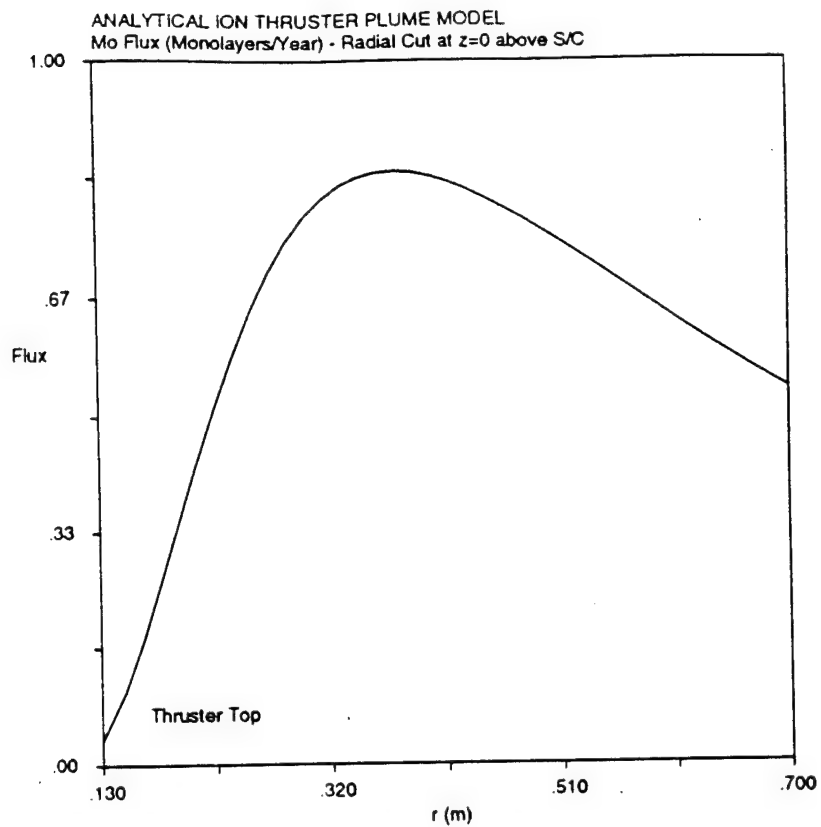


Figure 2.4 Plot of molybdenum flux predicted by simple analytical model along radial plane at  $z=0$  for SERT II thruster

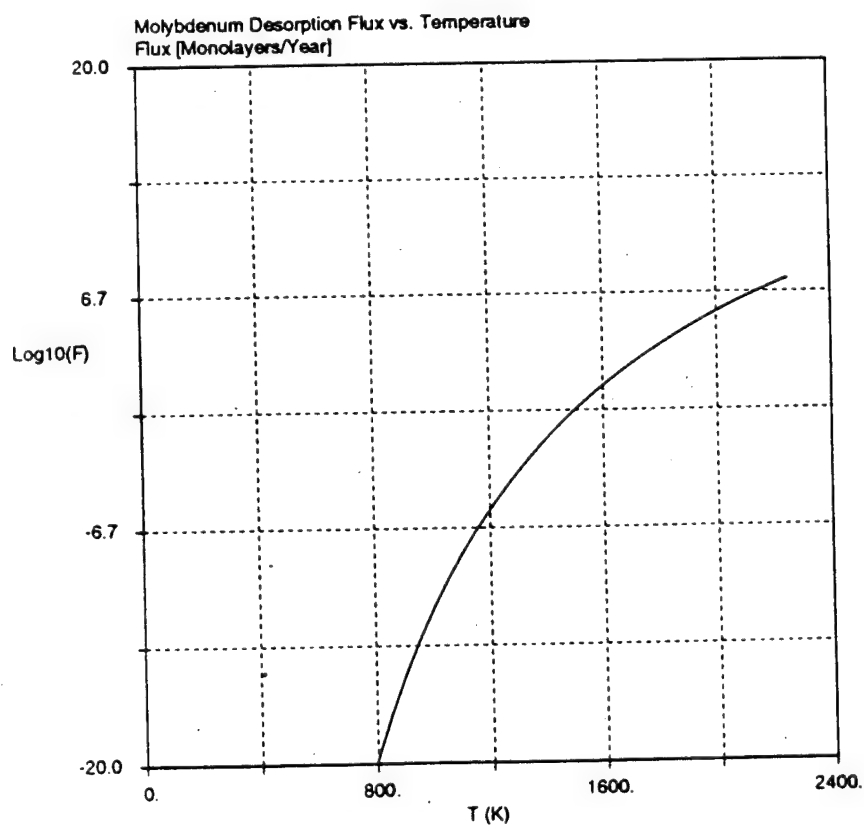


Figure 2.5 Molybdenum desorption flux as a function of temperature

# Chapter 3

## Physical Model of an Ion Thruster Plume

In this chapter, we present a particle and fluid formulation of an ion thruster plume building on the basic elements introduced in Chapter 2. We discuss the general physical processes and develop detailed models of the various elements of the plume.

### 3.1 General Description of an Ion Thruster Plume

As we have seen in our preliminary analysis in Chapter 2, the plumes of ion thrusters contain several major components: 1) fast ( $>10$  km/s) propellant beam ions that provide the thrust, 2) unionized propellant neutrals with thermal energies ( $T_n \approx 500^\circ\text{K}$ ) that flow from both the discharge chamber and neutralizer, 3) slow (initially thermal) propellant ions created by charge-exchange (CEX) collisions between the beam ions and propellant neutrals, 4) non-propellant efflux (NPE), i.e. eroded and sputtered grid and discharge chamber material of which a fraction is ionized, and 5) neutralizing electrons emitted from the neutralizer. We will consider each of these species in detail below.

The focus of our model is the production of ions primarily due to CEX collisions (although electron impact ionization can be important depending on the electron temperature) within the beam, and their transport outward. Since the CEX ion creation rates for both the propellant and NPE ions depend on the beam ion and the respective neutral densities, we must have models for these density fields.

### 3.2 Beam Ion Model

The primary ion thruster effluent is the directed energetic singly-charged ions in the beam that are accelerated by the thruster grids through voltage drops of around 1 kV or

---

more. The beam ions follow nearly line-of-sight trajectories since electromagnetic fields are too weak to perturb their paths due to their high velocities ( $>10$  km/s). Experimentally, it is found that most of these ions lie within an expansion cone of half-angle  $15^\circ$ - $20^\circ$ . The beam divergence is primarily due to the fringe electric fields in the grid holes that defocus the ions, and the curvature of the grids. Thermal effects are very small since the divergence angle due to thermal spreading scales as  $\tan^{-1}(v_{ti}/v_{bi})$  where  $v_{ti}$  is the ion thermal velocity (based on  $T_i=500^\circ\text{K}$ ) and  $v_{bi}$  is the beam velocity ( $>10$  km/s). This angle is typically less than  $1$ - $2^\circ$ .

Early ion thruster grids were planar, but warping problems were encountered due to thermal stresses. Currently, most grids are "dished", and are fabricated as spherical segments with the convex side facing downstream. A number of thrusters have also been operated with the concave side of the grids facing downstream. With this configuration, the resulting beam initially converges, and then diverges, producing a "waist" structure in the plume [Fearn *et al.*, 1993]. For this study, we take the thruster grid to be a spherical segment (convex side downstream), with the velocities of the beam ions normal to the surface. Hence, the ions appear to be leaving a point source located at the radius of curvature of the grids, a distance  $R_c$  behind the thruster exit plane. The radius of curvature is given in terms of the thruster beam radius,  $r_T$ , and beam divergence angle,  $\alpha$ :  $R_c = r_T / [\alpha \cos(\alpha/2)]$ . Figure 3.1 displays the geometry. As an example, the NASA 30 cm (beam diameter) J-series thruster grids have a radius of 16.9 cm, and a depth,  $d$ , of 2.23 cm [Rawlin *et al.*, 1972]. From the geometry in Figure 3.1,  $\alpha = \pi - 2\tan^{-1}(r_T/d)$ , which is about  $15^\circ$ . Experimentally, the beam is observed to have a divergence close to this, although this observation does not necessarily imply that beam divergence is predominantly due to grid curvature.

The mechanism for accelerating the beam ions is the potential drop between the screen and accelerator (commonly referred to as the accel) grids of the thruster. Figure 3.2 shows a schematic of the general behavior of the potential near the grids. The directed beam ion velocities are related to the beam voltage,  $\Phi_b$ , which is the voltage on the screen grid. The accel grid potential is held negative with respect to the beam to repel backstreaming electrons. Note that while the total accelerating voltage is the difference between the screen† and accel grid potentials, the net accelerating voltage for an ion that climbs the downstream potential peak is only the screen voltage. From conservation of energy, the velocity of the singly-charged beam ions of mass  $m_i$  is expressed as,

$$v_{bi} = \sqrt{\frac{2e\Phi_b}{m_i}} \quad (3.1)$$

---

† It is actually the screen plus the discharge voltage, which is generally 20-40 V higher than the screen.

It should be mentioned, that in addition to the more common two grid systems, there are also three grid systems, where the third grid is a decel grid placed downstream of the accel grid with a voltage higher than the accel grid. With the decel grid, the specific impulse can be lowered without reducing thrust. In addition, the ion beam in three-grid systems appears to be more collimated [Meadows and Free, 1975]. The total accelerating voltage is then the difference between the screen and the decel grid, while the net is the same as for the two grid system. Over length scales of interest ( $< 2.5$  m), the beam ion velocities are assumed to be constant throughout the beam. In cylindrical coordinates, ( $r$ - $z$ ), within the beam at a radial position  $r$ , the beam ion velocity components are:  $v_{bi\ z} = v_{bi} \cos \theta$ ,  $v_{bi\ r} = v_{bi} \sin \theta$  where  $\theta = \tan^{-1} [r/(z+R_c)]$ .

The radial current density profile of the collimated beam ions (given in spherical polar coordinates ( $R, \theta$ ) for simplicity) is taken to be approximated by a parabolic axisymmetric profile given by,

$$j_{bi}(R, \theta) = ev_{bi}A \left( \frac{R_c}{R} \right)^2 \left( 1 - \frac{\theta^2}{\alpha^2} \right) \quad (3.2)$$

which is subject to the normalization imposed by continuity at any downstream location in the beam,

$$I_b = \int_0^\alpha j_{bi} 2\pi R^2 \sin \theta d\theta \quad (3.3)$$

where  $I_b$  is the ion beam current being emitted from the thruster. The normalization constant,  $A$ , which is the centerline beam ion density at the thruster exit,  $n_{bio}$ , is given by,

$$A = n_{bio} = \frac{I_b}{2\pi R_c^2 ev_{bi} \delta} \quad (3.4)$$

where  $\delta$  is,

$$\delta = 1 - \frac{2 \cos \alpha}{\alpha^2} - \frac{2 \sin \alpha}{\alpha} + \frac{2}{\alpha^2} \quad (3.5)$$

In the limit  $\alpha \ll 1$ ,  $\delta \rightarrow \alpha^2/4$ , and  $A = 2I_b / [ev_{bi}\pi r_T^2]$ .

It should be noted that the parabolic profile for the beam current density sharply drops to zero at the beam edge. In reality, the transition along the beam edge is more gradual. Previous beam models such as those by Komatsu and Sellen [1976], utilized a "parabolic core" and an "exponential wing". We adopt this approach, and hold Eqn. (3.2) valid for  $\theta \leq \zeta\alpha$ , whereas for  $\theta \geq \zeta\alpha$ , the current density is attenuated by a factor  $\exp(-r/\lambda)$ . Typically,  $\zeta$  is taken to be 0.95, and  $\lambda$  is a decay length scale which is a fraction of the beam radius. Figure 3.3 shows the model beam ion current density along a radial cut through the beam near the exit of a thruster whose operating conditions are given in Table 3.1. The core and wing regions are depicted. Since this smoothing region is small, and the densities are small, we neglect the current density contribution in the calculation of the normalization

constant in Eqn. (3.3). Given the beam ion current density, the beam ion density is then readily determined by,

$$n_{bi}(r,z) = \frac{j_{bi}(r,z)}{e v_{bi}} \quad (3.6)$$

Figure 3.4 shows the beam ion current density predicted by Eqn. (3.2) in the plume of a modern 15 cm (beam diameter) xenon ion thruster with operating conditions given in Table 3.1. The beam divergence, which was not measured, was assumed to be 15°. Experimental measurements taken in the plume of this thruster by *Monheiser* [1991] are overlaid. It was noted in the experiments that the integral of the measured current densities over the thruster exit, which should be the total beam current, was smaller by a factor of 15% due to experimental error. Therefore, we have reduced the results of Eqn. (3.2) by 15% for comparison purposes. As can be seen, the agreement between the model and experimental values is very good. However, it should be noted that due to grid imperfections, the actual beam might not always be perfectly symmetric. For this particular thruster, the current density is slightly skewed towards the top. In Figure 3.5, a radial cut through the experimental beam is shown, highlighting the asymmetry. However, for properly designed thrusters, such effects are not of primary importance, and are not included in our model.

Table 3.1 Modified SERT II 15 cm ion thruster operating conditions [*Monheiser*, 1991]

Propellant:	Xenon
Thrust (mN):	12
Beam current $I_b$ (A):	0.23
Beam voltage $\phi_b$ (V):	1000
Beam ion velocity (m/s):	38,330
Propellant utilization $\eta_p$ :	0.84

Early generation ion thrusters often had much more peaked radial ion density profiles. To model these thrusters, a Gaussian profile fits measured density profiles better than parabolic shapes. For these thrusters, we take the beam ion current density to be given by,

$$j_{bi}(r,z) = \frac{I_b}{\xi^2 \pi r_b^2} \exp \left[ -\left( \frac{r}{\xi r_b} \right)^2 \right] \quad (3.7)$$

where  $r_b = r_T + z \tan \alpha$ , and  $\xi$  is a scaling factor for the Gaussian half-width. Figure 3.6 shows a comparison of a radial parabolic and a Gaussian profile with experimental measurements taken by *Kaufman* [1975] of the ion density in the plume of the original 15 cm mercury SERT II thruster.

While the discharge chambers of ion thrusters are designed to produce singly-charged ions, there is also a fraction of doubly-charged ions that are produced. Due to their increased charge, these ions are unfocused in the grids (which are designed for singly-charged ions) and leave at large angles decreasing the overall thrust efficiency. In ion thruster performance tests, a correction factor due to the doubly-charged ions is usually computed based on singly and doubly-charged ion currents ( $I_b^+, I_b^{++}$ ) measured by a spectrometer probe. The thrust from an ion thruster can be expressed in terms of the beam current and beam voltage as,

$$F = \gamma \sqrt{\frac{2m_i}{q}} I_b \Phi_b^{1/2} \quad (3.8)$$

where  $q$  is the ion charge and  $\gamma$  is a thrust loss correction factor which is the product of a correction factor due to doubly-ionized ions,  $\eta^{++}$ , and a correction factor due to beam divergence effects. The correction factor due to doubly-charged ions is defined as the ratio of the sum of the thrust from both singly and doubly charged ions to the thrust if all ions were singly-charged. This can be expressed as,

$$\eta^{++} = \frac{1 + \frac{1}{\sqrt{2}} (I_b^{++}/I_b^+)}{1 + (I_b^{++}/I_b^+)} \quad (3.9)$$

For a typical modern 30 cm xenon thruster,  $\eta^{++}$  varies between 0.995 at  $I_b = I_b^+ + I_b^{++} = 1.45$  A to 0.956 at  $I_b = 5$  A [Beattie and Matossian, 1992]. The doubly to singly-charged ion density ratios are proportional to the current ratios:  $n_i^{++}/n_i^+ = 1/2^{3/2} (I_b^{++}/I_b^+)$ . Hence, for the above two beam currents,  $n_i^{++}/n_i^+$  is 0.006 and 0.063 respectively. Since their population is small compared to the singly-charged ions, and their charge-exchange probability is also very low, we will neglect the role of any doubly-charged propellant ions in the beam.

### 3.3 Neutral Propellant Model

Not all the propellant is ionized in the discharge chamber of electron bombardment ion thrusters due to discharge chamber inefficiencies and operating constraints. A figure of merit for ion thruster discharge chambers is the beam ion cost. This is the energy required to ionize one beam ion [eV/ion] and is obtained by dividing the discharge power by the ion beam current. For a given thruster, the beam ion cost is commonly shown as a function of the propellant utilization efficiency,  $\eta_p$ , which is defined as the ratio of the beam ion current to the propellant mass flow rate,  $\dot{m}$ ,

$$\eta_p = \frac{I_b (m_i/e)}{\dot{m}} \quad (3.10)$$

Figure 3.7 shows a typical plot of the relationship that is experimentally found between the beam ion cost and the propellant utilization efficiency for constant propellant flow rate [Kaufman, 1974]. To increase the propellant utilization, the discharge current is increased. Typical beam ion costs are around 150-200 V/ion. The physical behavior of this curve was explained by Brophy [1984] with the following expression relating the beam ion cost,  $\epsilon_B$ , to  $\eta_p$ ,

$$\epsilon_B = \frac{\epsilon_p^*}{f_B [1 - \exp(-C_o \dot{m} (1 - \eta_p))]} + C \quad (3.11)$$

where  $\epsilon_p^*$  is the "base-line ion production cost" which is a function of a particular thruster geometry, magnetic field strength, and propellant (i.e. ionization and excitation energy);  $f_B$  is the fraction of ions extracted from the chamber by the grids;  $C_o$  is a parameter dependent on propellant characteristics such as the temperature and ionization cross section; and  $C$  is a function of the discharge chamber operating parameters - mainly the discharge voltage. This expression is actually a statement of conservation of energy in the discharge chamber: the rate of energy supplied into the discharge must be balanced by the energy lost in ionization (of which a fraction,  $f_B$ , of the ions produced is extracted as the beam ion current), excitation, and wall losses. The exponential term arises from the wall loss term: the probability of a primary electron (an electron from the cathode that impact ionizes the propellant) ionizing a neutral before reaching the anode is,  $[1 - \exp(-\sigma_i n_n L_e)]$ , where  $\sigma_i$  is the ionization cross section,  $n_n$  is the neutral density which scales as  $\dot{m} (1 - \eta_p)$ , and  $L_e$  is the primary electron containment length in the discharge chamber. Thus, as  $\eta_p$  increases for a fixed flow rate, the neutral density decreases, and the probability of a primary electron reaching the anode increases, and hence the wall losses increase.

The design goal for thruster operation is to operate at the "knee" of the curve. Any attempt to increase the propellant utilization efficiency beyond this point, leads to excessive discharge power requirements. Thus, there will always be a fraction of neutral propellant in the beam, with a corresponding decrease in the thruster specific impulse, since  $(1 - \eta_p)$  of the propellant expended is not providing thrust.

Typical values of  $\eta_p$  range from as low as 0.70 to as high as 0.95, and is a strong function of the ionization potential of the propellant used. The ideal propellant is one that has a large molecular weight, low ionization potential, and large ionization cross section. As an example, the current NASA 30 cm xenon thruster operates over a propellant utilization efficiency range of 0.71 to 0.91 [Brophy, 1994; Patterson et al, 1993]. However, studies with C<sub>60</sub> have shown that efficiencies on the order of 0.95 can be reached. The ionization potential of C<sub>60</sub> is 7.5 eV, compared to 12.1 eV for Xe, and the molecular weight of C<sub>60</sub> is about 5.5 times greater than Xe [Leifer and Saunders, 1991;

Torres, 1993; Hraby et al, 1994].

The unionized propellant effuses out from the discharge chamber, and exits through the grids in free-molecular flow with a temperature close to that of the thruster discharge chamber walls,  $T_w$ . Typically, this value is around 500°K for thrusters using xenon. If  $C_{60}$  is used, the wall temperatures must be kept at around 800-900°K to prevent condensation on the walls. The thruster grids are actually comprised of thousands of holes with diameters of 1-2 mm. Due to the hole structure, the grids have a "transparency" which, as discussed in Chapter 2, is close to the ratio of the area through which neutrals can leak out to the total geometric area. This value is typically 0.1-0.3. Thus, the flow between the grids and in the immediate vicinity is quite complicated. However, the flow from each individual hole is given by the Knudsen efflux,  $n_{no}\bar{C}/4$ , where  $\bar{C}$  is the mean thermal speed given by,

$$\bar{C} = \sqrt{\frac{8kT_w}{\pi m_i}} \quad (3.12)$$

Far from the grids, the fine structure of the holes decays, and the neutral flow can be regarded as the superposition of a vast array of point sources. The average neutral density right at the thruster grids,  $n_{no}$ , can be determined from the beam ion current and the propellant utilization efficiency by the relation,

$$n_{no} = \frac{4 I_b}{e \bar{C} A_n} \left( \frac{1 - \eta_p}{\eta_p} \right) \quad (3.13)$$

where  $A_n$  is the flow-through area of the neutral propellant through the grids. It is important to realize that even with high utilization fractions, neutral densities are higher than ion densities since the neutral velocity is much lower than that of the ions. For example, let us compute the ion and neutral densities at the exit of a 30 cm ( $r_T=0.15$  m) xenon ion thruster with a beam divergence angle of 20° operating at  $I_{sp}=3477$  s ( $v_{bi}=40,200$  m/s),  $I_b=1.74$  A with neutrals at 500°K,  $\eta_p=0.89$ , and a grid transparency fraction of 0.24. The ion density is given by Eqn. 3.4, and Eqn. 3.13 gives the neutral density. We find that  $n_{bio}=7.5 \times 10^{15} \text{ m}^{-3}$ , and  $n_{no}=1.1 \times 10^{18} \text{ m}^{-3}$ . Thus, there is a substantial neutral component to the plume.

In this work, we model the neutral density field as the flow from a single point source that is located one thruster radius behind the exit plane of the grids. For a gas of density  $n_{no}$  effusing through a hole of radius  $r_o$ , the density downstream along the axis is given by Bird [1976],

$$n_n(z) = \frac{n_{no}}{2} \left[ 1 - \left\{ 1 + \left( \frac{r_o}{z} \right)^2 \right\}^{-1/2} \right] \quad (3.14)$$

For small  $r_o/z$ , i.e. far from the source, this can be expanded as,



$$n_n(z) = \frac{n_{no}}{4} \left( \frac{r_o}{z} \right)^2 \left[ 1 - \frac{3}{4} \left( \frac{r_o}{z} \right)^2 + \frac{5}{8} \left( \frac{r_o}{z} \right)^4 + \dots \right] \quad (3.15)$$

and we can see the dominant  $1/z^2$  behavior. From rarefied gas dynamics theory, the density off the axis decays with a cosine factor. Thus, the well known expression for the density far from a source in spherical polar coordinates  $(R, \theta)$  is,

$$n_n(R, \theta) = \frac{n_{no}}{4} \left( \frac{r_o}{R} \right)^2 \cos \theta \quad (3.16)$$

where the velocity of the expanding gas is a constant. It is interesting to compare the density decay along the axis ( $\theta=0^\circ$ ) between Eqns. (3.14) and (3.16). Figure 3.8 shows this comparison. We can see that the two models become comparable at about five source radii away. Since we are interested not only in the far-field density distribution, but also within distances less than five beam radii, we use the exact expression in Eqn. (3.14) with a cosine angular distribution to specify the neutral density field. In spherical polar coordinates with the source located one beam radius,  $r_T$ , behind the thruster exit, the neutral density is given by,

$$n_n(R, \theta) = a \frac{n_{no}}{2} \left[ 1 - \left\{ 1 + \left( \frac{r_T}{R} \right)^2 \right\}^{-1/2} \right] \cos \theta \quad (3.17)$$

where  $a=[1-1/\sqrt{2}]^{-1}$  is a correction factor to account for the shifting of the point source, and  $R=[r^2+(z+r_T)^2]^{1/2}$ ,  $\theta=\tan^{-1}[r/(z+r_T)]$ . By placing the point source within the thruster, we eliminate any singular behavior.

It is important to note that there is a fraction of the total mass flow rate that flows through the neutralizer. Typically, the neutralizer flow rate is between 5-10% of the discharge chamber flow rate. The effect of these neutrals is incorporated into the neutral density by using the total mass flow rate (discharge + neutralizer) instead of only the discharge mass flow rate. The neutral density flowfield in reality will be affected by the presence of the neutralizer as a point source off the beam axis, and will depend on its location. However, such perturbations on the structure of the neutral flowfield are neglected given the other approximations of the neutral model.

In order to compare our model with experimental data, which unfortunately are ground based, we must be able to take into account some of the effects of ground facilities. The most dominant one is the background facility pressure in the vacuum chambers wherein thruster experiments are conducted. Since the vacuum pumps can not achieve perfect vacuum, there is a finite background neutral density that resides in the tanks. This background density increases when the thruster is operated. Given the background pressure,  $p_o$ , and assuming a temperature for the gas,  $T_o$ , (which may be close to room temperature - or colder for cryopumped tanks), the background neutral density is

$n_0 = p_0 / kT_0$ . The tank pressure is of course a function of the size of the tank, the pumping capacities, and the propellant used. Previous propellants such as mercury condensed easily on the tank walls, decreasing the tank pressure. However, the prevalent propellant now, xenon, is much harder to pump. As we will see in Chapter 5, most test chambers of meter-size class can not achieve a pressure below  $10^{-6}$ - $10^{-5}$  torr ( $10^{-4}$ - $10^{-3}$  Pa). This results in a residual background density of around  $3 \times 10^{16}$ - $3 \times 10^{17} \text{ m}^{-3}$ , which can be comparable to the neutral density in the thruster plume.

Another important ground test effect is the influence of the test chamber walls. Of course, if the tank is large enough compared to the thruster size, the effects will diminish. Depending on the experimental setup, the tank walls are biased in some way and will affect the plasma distributions as well as the potential fields. If the tank walls are biased negatively, ions will be attracted and the tank walls can sputter leading to traces of metallic species. In addition, secondary electrons can be emitted which may be more energetic than the background tank electrons and will elevate the electron temperature. All of these wall effects are complex, and are beyond the scope of this thesis.

However, from the plume modeling perspective, the background gas is a significant factor in estimating thruster backflow contamination and must be included. As we shall see, the background gas substantially increases the CEX ion production rates. In addition, the velocity characteristics of the background neutrals are different from those of the neutrals coming from the thruster. The temperature of the facility neutrals is less, and the velocity distribution is isotropic. In comparison, the thruster neutrals are hotter, and their velocities are oriented downstream (they are flowing away from the thruster). The slow initial velocities of the neutrals once converted to CEX ions, play a role in determining their trajectories under the influence of the electric fields within the plume. The backflow distribution is subsequently affected. This is an important point in that the behavior of the CEX plasma in ground-based tests will be different from that which will be observed in space. To validate our numerical model, we must be able to incorporate the ground-based influences, and show reasonable agreement with experimental ground data. Then, we will be able to remove the ground-based influences and be able to predict space-based performance with a higher degree of confidence.

In Figure 3.9a, we show the neutral density field computed from Eqn. (3.17) for the thruster with operating conditions shown in Table 3.1. Included is also a uniform background density of  $9.7 \times 10^{16} \text{ m}^{-3}$  ( $3 \times 10^{-6}$  torr). Figure 3.9b is the density computed from a detailed numerical model by *Monheiser* [1991] that accounts for the flow from all the holes in the grid. We can see that the simple single point source model is in reasonably good agreement.

Lastly, we should mention the neutrals in the plume that are created from the CEX processes. These neutrals, formerly beam ions, possess the beam ion velocity and leave the vicinity of the spacecraft rapidly. Their density is that of the CEX ion density which we will see is orders of magnitude less than the beam neutral density. Thus, the contribution of this component to the total propellant neutral density can be neglected.

### 3.4 Propellant Charge-Exchange (CEX) Ion Model

Slow propellant ions are created both within the thruster grids and downstream inside the beam due to resonant charge-exchange collisions of the following type between the fast beam ions and the slow thermal neutrals; i.e. for xenon:



The result is a fast neutral that travels in a line of sight manner, and a slow ion that is affected by the strong radial electric fields in the beam. The CEX ions created can be classified according to the regions wherein they were born as denoted in Figure 3.2b, a convention first due to *Staggs et al* [1968] and elaborated upon by *Monheiser* [1991]. Those CEX ions created in Region 1 generally gain enough energy to escape the grid system, although most likely on largely divergent trajectories. In Region 2, CEX ions are created within a potential well and generally can not escape. These ions are attracted to the accelerator grid and sputter erode it. CEX ions created in Region 3, downstream of the axial beam potential peak, are the source of ions that can be expelled from the beam radially. We are most interested in the CEX ions in Region 3 because they are the dominant component of the backflow. The production of CEX ions within the grids (Region 2) has been studied by *Peng et al* [1990-1993], and a schematic of CEX ion trajectories impinging on the accel grid determined from their work is drawn in Figure 3.2a.

An important quantity measured in ground tests, is the impingement current on the accelerator grid. This is comprised of the current from Region 2 ions, highly divergent ions from Region 1, as well as any from Region 3 that flow back. The impingement current is important because it is proportional to the sputtering erosion of the grid, which is the main lifetime limiting factor in ion thruster operation. In three-grid systems, accel grid sputtering still occurs, but the impingement current is decreased, and a fraction of the eroded material accumulates on the decel grid, decreasing the amount of grid material that can escape into the plume [*Zhang et al*, 1993]. We will discuss grid sputtering in greater detail in Section 3.5.

The CEX collision frequency between the beam ions and propellant neutrals is given

by,

$$v_{cex} = n_n v_{bi} \sigma_{cex}(v_{bi}) \quad (3.19)$$

and the spatial volumetric production rate of CEX ions is given by,

$$\dot{N}_{cex}(\mathbf{x}) = n_n(\mathbf{x}) n_{bi}(\mathbf{x}) v_{bi} \sigma_{cex}(v_{bi}) \quad (3.20)$$

where the relative collision velocity is taken to be the beam ion velocity. Since the beam ions can be considered monoenergetic and their energy is much greater than that of the neutrals, there is no need to average over an energy distribution in the above expressions. From the quantum-mechanical theory of collisions, the velocity dependent resonant CEX cross section can be expressed as [Rapp and Francis, 1962],

$$\sigma_{cex}^{1/2} = k_1 \ln v_{bi} + k_2 \quad (3.21)$$

where,

$$k_1 = -\sqrt{\frac{\pi}{2}} \left( \frac{a_o}{f} \right), \quad k_2 = \sqrt{\frac{\pi}{2}} \left( \frac{a_o}{2f} \right) \ln \left[ \frac{72b^3}{f \pi a_o} \left( \frac{E_i^2}{\hbar^2} \right) \left( 1 + \frac{a_o}{b f} \right)^2 \right] \quad (3.22)$$

where  $a_o$  is the Bohr radius,  $E_i$  is the ionization potential,  $f$  is a function of  $E_i$ , and  $b$  is an energy averaged atomic impact parameter. Figure 3.10 displays the CEX cross sections for xenon and mercury as a function of beam ion velocity. For numerical purposes, the cross sections in  $\text{m}^2$  as a function of  $v_{bi}$  in  $\text{m/s}$  are,

$$\sigma_{cex} = (k_1 \ln v_{bi} + k_2)^2 \cdot 10^{-20} \text{ m}^2 \quad (3.23)$$

For xenon,  $k_1 = -0.8821$ ,  $k_2 = 15.1262$ , while for mercury,  $k_1 = -0.9097$ , and  $k_2 = 15.8687$ . These cross section values have been compared with experimental measurements, and are in good agreement with available data [Rapp and Francis, 1962]. Note that the CEX cross section for mercury, an old ion thruster propellant, is slightly larger than that of xenon, the propellant currently in use. Maximum CEX collision frequencies for xenon thruster conditions discussed in Section 3.3 are around  $10^4 \text{ s}^{-1}$ , and CEX volumetric production rates are around  $10^{20} \text{ m}^{-3} \text{ s}^{-1}$ .

Thus far, we have assumed (following the literature) that CEX collisions are the dominant mechanism for the creation of slow ions in the beam. However, we must also examine the possibility of ion creation due to electron impact ionization to see whether it can truly be neglected. In addition, ion-electron recombination must be assessed. To evaluate ionization in the plume, the ionization model of Drawin is used [Mitchner and Kruger, 1973] which is presented in Section 3.7.2. For recombination, there are two types: three-body ( $i + e + e \rightarrow n + e$ ) and radiative ( $i + e \rightarrow n + h\nu$ ) that are discussed in Section 3.7.1. The important parameter in ionization and recombination processes is the electron temperature. In most current ion thrusters, the electron temperature in the beam

near the exit is around 1 eV, although it could be as high as 5 eV in older thrusters. Figure 3.11 shows a comparison of volumetric rates for CEX, ionization (singly), and three-body and radiative recombination as a function of electron temperature for xenon. The beam ion and neutral densities used are the values in Section 3.3. We can see that CEX is the dominant ion creation mechanism for electron temperatures up to 3 eV or so, when ionization, although still less, becomes increasingly important. Beyond 5 eV, ionization is the dominant process since CEX ion creation is independent of electron temperature. Even though an electron temperature of 5 eV is less than the ionization energy of xenon which is 12.1 eV, the energetic tail of the electron distribution is able to ionize. We also can see that recombination is negligible in the beam, with radiative recombination dominant compared to three-body since ion thruster plume plasmas are relatively collisionless. Since most current ion thrusters operate with electron temperatures close to 1-2 eV, we will only include CEX processes in our model and neglecting ionization is justified. However, when we examine older thrusters with electron temperatures near 5 eV, we will see that including only CEX collisions still gives reasonably good agreement with experimental measurements of backflowing ion densities.

There is also the possibility of ion impact ionization, since the beam ions have energies over 1 keV. Unfortunately, data for xenon ion impact ionization cross sections remains to be found, and thus we must draw conclusions from available data on argon. The cross section for 1 keV argon ions ionizing neutral argon is about  $2.2 \times 10^{-20} \text{ m}^2$  [Massey and Burhop, 1952]. In comparison, the resonant CEX cross section for argon at this energy is about  $2.5 \times 10^{-19} \text{ m}^2$  [Rapp and Francis, 1962]. Since ion impact ionization is an order of magnitude less than resonant CEX, this mechanism is not included.

Volumetric CEX production rates using Eqn. (3.20) in the plume of the thruster with operating conditions in Table 3.1 are shown in Figure 3.12. The beam ion and neutral densities used are the computed values shown in Figures 3.4 and 3.9a respectively. Overlaid on the computed values from Eqn. (3.20), are those computed from the measured current density (see overlay on Figure 3.4) and the neutral density shown in Figure 3.9b from a detailed model. The CEX production rates agree well. (Recall though that the measured current densities are 15% too low and this has been adjusted in our model).

It must be pointed out that there is a limit to the validity of this method for computing the CEX ion creation. If the CEX ion production rate is too high, then the beam ion and neutral densities can not be taken to be fixed quantities. If we define a CEX ion current, to be the current produced within a sphere of radius  $r_T$  (using maximum parameters),

$$I_{cex} = \frac{4}{3} \pi r_T^3 e n_{nd} n_{bio} v_{bi} \sigma_{CEX}(v_{bi}) \quad (3.24)$$

then it must be the case that the ratio of  $I_{CEX}$  to the beam current  $I_b = en_{bio}v_{bi}\pi r^2$  is small:

$$\frac{I_{CEX}}{I_b} \sim r_T n_{no} \sigma_{CEX} \ll 1 \quad (3.25)$$

This is indeed the case, and typically this ratio is less than 10%. It is interesting to note that this quantity is the ratio of the thruster radius to the CEX collisional mean free path.

An important consideration for the transport of the slow CEX ions is the ambient and thruster-induced magnetic fields. Table 3.2 shows the gyroradii for thermal and beam xenon ions in various magnetic field strengths corresponding to a range of orbital altitudes. The thermal speed of the CEX ions is the minimum speed, and represents ions that have just been created within the beam and have not been accelerated through the potential drop at the beam edge. For the length scales that we are interested in currently, (<2-5 m), the ions can be considered unmagnetized with respect to the ambient magnetic field.

Table 3.2 Gyroradii for xenon ions

	LEO (B=0.2G)	GEO (B=0.001G)
Thermal CEX ion (T=500°K)	12 m	2 km
Beam ion V>10 km/s	> 680 m	> 136 km

Ion thrusters have magnetic fields surrounding them due to the magnets inside the thruster that serve to confine primary electrons to increase their ionization efficiency. Early thrusters, such as the original SERT II thruster, used bar magnets which gave maximum magnetic field values of 35 G inside the chamber. Outside the thruster, the field is much weaker. For the SERT II thruster, the field decayed to 0.3 G within 0.5 m downstream axially, and seemed to be represented well by a dipole field [Kaufman, 1980]. Modern ion thrusters, use "ring cusp" magnetic fields [Sovey, 1982] which are much more localized within the chamber. Maps of the magnetic field inside the thruster show values of 100 G at the back of the discharge chamber, and a "nearly field-free volume upstream of the ion extraction system" [Sovey, 1982]. No data was found for magnetic field strengths outside modern thrusters, but it is believed that the external fields are much weaker than the earlier thrusters. Thus, the effect of external thruster magnetic fields is not modelled.

### 3.5 Non-Propellant Efflux (NPE) Model

The presence of sputtered grid and discharge chamber metals in the plume presents a



serious contamination hazard due to these species' low vapor pressures. As we have seen in Chapter 1, the main NPE species is sputtered metal which is eroded from impingement of propellant CEX ions that are accelerated back to the negatively biased accel grid. The most common grid metal currently in use is molybdenum, although carbon-carbon composite grids are being tested now and show much promise due to their high sputter resistance [Messerole, 1994]. For this work, we will only consider molybdenum grids. Ground experiments by Rawlin [1988], Patterson and Verhey [1990], and Fearn [1993] and computational modelling by Peng *et al* [1990-1993], have shown that sputtering occurs within the aperture holes, and on both the up and downstream faces of the accel grid due to its negative bias. However, the downstream face is eroded the most. The sputtered molybdenum is ejected as neutral atoms, since the ionization energy, 7.1 eV, is greater than the work function of the metal surface which is 4.58 eV. A fraction of the neutral molybdenum then becomes ionized, either by CEX or electron impact ionization depending on the electron temperature.

In Chapter 2, simple estimates of NPE CEX ion production rates were orders of magnitude less than those of the propellant CEX ions, and thus the perturbative effect of NPE ions on the self-consistent potential structures in the plume will be negligible. Hence, given an NPE production model, one can use the potential fields computed self-consistently from the beam and propellant CEX ions, and then track the NPE ions in this field. This approach will be valid as long as the NPE ion density remains much smaller than the plasma density from which the potentials were calculated.

There are two approaches to computing the flux of neutral sputtered grid material that we consider. One, is to use the grid impingement current that is a measure of the propellant CEX ion current impinging on the accel grid. By knowing the sputtering yield, i.e. how many atoms are knocked off the surface per incident ion, the sputtering rate can be determined. This approach was used in the simple analysis of Chapter 2. However, this approach will overestimate the amount of sputtered material downstream in the plume, since not all of the grid metal sputtered is ejected in the downstream direction, but also redeposits on other areas of the grids. A more accurate approach is to use grid mass loss data, if they are available. This approach will give an average erosion rate, since in reality, the erosion rate varies as a function of time. Typically, erosion rates are higher at initial thruster operation and decay with time.

We now compare estimates of sputtering rates using both approaches for a 30 cm xenon thruster. At an operating condition with a beam current of 3.2 A, the ratio of the grid impingement current to beam ion current in ground tests was measured to be 0.55%. Grid mass loss over a 890 hour operating period was 17.8 g, with an estimated 17.2 g



eroded solely from the downstream face [Patterson and Verhey, 1990]. The accel grid was biased at -331 V. For the same case, computational modelling by Peng *et al* [1993] gave a mass loss of 23.2 g over the same time period, and predicted space operational values of a 0.16% grid impingement to beam current ratio, and a 3.73 g grid mass loss in 890 hours. We will use these predicted values for space operation for our analysis.

Given the grid impingement to beam ion current ratio,  $F_i$ , and sputtering yield,  $Y$ , the sputtered flux from the grids is given by,

$$\Gamma_s = \frac{Y F_i I_b}{e A_g} \text{ [#}/\text{m}^2\text{s}] \quad (3.26)$$

where  $A_g$  is the surface area of the grid being sputtered. The sputtering yield of polycrystalline molybdenum bombarded by xenon has been measured as a function of energy by Weijsenfeld and Hoogendoorn [1961] and Rosenberg and Wehner [1962]. An average of their data is shown in Figure 3.13. Peng *et al* [1993] used the values of Rosenberg and Wehner [1962] which are higher than those of Weijsenfeld and Hoogendoorn [1961], which may have contributed to the overestimated mass losses we saw above. This sputtering yield data is only for normally incident ions, which the ions that hit the face of the accel grid predominantly are. However, a number of the propellant CEX ions hitting the interiors of the aperture holes, may strike with large incident angles. Experimentally, it has been observed that the sputtering yield increases with bombarding incident angle. However, the number of CEX propellant ions that strike the interiors of the holes at large angles is much less than those that strike the downstream face. From Figure 3.13, we can see that the sputtering yield for an incident energy of 330 V, is about 0.5.

Using the measured mass loss from the accel grid, the sputtered flux can also be determined. If an amount  $M$  of mass is lost over a period of time  $\tau$ , then the average flux is,

$$\Gamma_s = \frac{M}{\tau A_g} \frac{\mathcal{N}_A}{\mathcal{M}} \text{ [#}/\text{m}^2\text{s}] \quad (3.27)$$

where  $\mathcal{N}_A$  is Avogadro's number, and  $\mathcal{M}$  is the molecular weight (0.09594 kg/mol for molybdenum). Using the above predicted space-based figures, and taking the grid area,  $A_g$ , to be simply  $\pi r^2$ , we obtain from Eqn. (3.26) a flux of  $2.26 \times 10^{17} \text{ m}^{-2}\text{s}^{-1}$ , and from Eqn. (3.27), a flux of  $1.03 \times 10^{17} \text{ m}^{-2}\text{s}^{-1}$  which are comparable, but show the overestimation using the grid impingement current.

There are two important issues to address concerning the sputtered molybdenum neutrals: their sputtering distribution, and energy distribution. If we know an average velocity of the atoms leaving the surface, then we can compute an average density at the surface, and then knowing the sputtering distribution, we can construct a density map of

the sputtered atoms. Unfortunately, the energy distribution of sputtered molybdenum atoms by xenon ions apparently has not been measured, but data exists for bombardment by krypton, a lighter noble gas, measured by *Stuart et al* [1969]. However, this data is only for bombardment energies of 1200 eV - three to four times as high as the energies of impinging CEX ions in ion thrusters. It would be expected that the sputtered atom energy would increase with increasing incident energy. It was noted, however, that ejection energies decrease with lighter bombarding ions (for a fixed energy level). Since a krypton atom has only 63% of the mass of a xenon atom, it is not clear exactly what the scaling relationship between high energy krypton versus lower energy, but more massive xenon, will be. Thus, we will simply use this data. Our calculations of sputtered molybdenum contamination can only be as accurate as the data of the underlying physical mechanisms.

The energy distribution of the sputtered atoms is found to resemble a Maxwellian speed distribution, although the energetic tail is broader. The most probable ejection energy of molybdenum being bombarded by 1200 eV krypton ions is about 5 eV (3170 m/s), and the average energy is about 21 eV (6500 m/s) [*Stuart et al*, 1969]. We model the energy distribution simply as a Maxwellian speed distribution,

$$F(E) \sim E \exp(-E/E_{mp}) \quad (3.28)$$

where  $E_{mp}$  is the measured most probable ejection energy. While using a simple Maxwellian distribution does not capture the broader energetic tail, its use is more conservative since lower energy ions will be influenced more by the electric potentials in the plume. Using the most probable ejection velocity, we can now compute the neutral molybdenum density near the grids. Dividing the above flux values by 3170 m/s, we obtain densities of  $7.13 \times 10^{13} \text{ m}^{-3}$  and  $3.25 \times 10^{13} \text{ m}^{-3}$  based on the grid impingement current and grid mass loss respectively. The neutral molybdenum density is about four orders of magnitude less than the neutral propellant density.

Sputtering from monocrystalline metal surfaces, usually exhibits preferred directions of ejection due to the crystallographic orientations [*Chakarov et al*, 1989]. However, for a polycrystalline surface, the crystal surfaces are randomly oriented, and the sputtered distribution has generally been modelled as a cosine distribution [*Weigand and Mirtich*, 1975]. Experimental data supports this model [*Wehner and Rosenberg*, 1960; *Wehner and Anderson*, 1970]. We assume that the neutral sputtered molybdenum distribution downstream of the thruster is very similar to the propellant neutral distribution, i.e. a cosine distribution that falls off as  $1/R^2$ . Therefore, we use Eqn. (3.17) to describe the neutral molybdenum density distribution in the plume.

Lastly, we must examine the mechanisms by which the molybdenum becomes ionized. There are two possible mechanisms we consider: CEX with the propellant ions, and

electron impact ionization. Impact ionization by the beam ions is another possibility. Although there are no measurements of the ion impact ionization cross section between xenon and molybdenum, the ratio of non-resonant CEX to ion impact ionization cross sections for protons in helium is at least a factor of five [Massey and Burhop, 1952]. Thus, this mechanism does not appear to be very important and is not considered.

The CEX cross section between xenon and molybdenum for the energy range of interest (0.1-10 keV) is relatively constant, with a value around  $6 \times 10^{-20} \text{ m}^2$  measured by Rutherford and Vroom [1981]. These CEX collisions are non-resonant, i.e. they are between two different species, and are much smaller than the resonant values we saw for xenon and mercury in Section 3.4. Figure 3.14 shows a comparison of volumetric rates of CEX, electron impact ionization (singly), and three-body and radiative recombination as a function of electron temperature for molybdenum. For maximum estimates, the relative collision velocity for the CEX rates is taken to be the beam ion velocity, and the beam ion density in Section 3.3 is used. The molybdenum neutral density used is  $3.25 \times 10^{13} \text{ m}^{-3}$ . We can see that at lower electron temperatures near and below 1 eV, CEX is dominant. However, at temperatures beyond 1.75 to 2 eV, electron impact ionization is the dominant ion production mechanism. This is due to molybdenum's low ionization energy of 7.1 eV.

### 3.6 Electron Fluid Model

Electrons play a vital role in ion thruster operation in neutralizing the ion beam. The role of the neutralizer is to supply an electron current to balance the ion current of the beam. It is beyond the scope of this work to include a detailed model of the physics of an electron emitting hollow cathode, which is still not completely understood today. Recently, preliminary efforts have been made to kinetically model the electrons [Wang *et al.*, 1995]. Essentially, the neutralizer produces a quasi-neutral plasma cloud that acts as a "bridge" for the passage of electrons to the beam. In ion thruster beam plasmas, the thermal velocity of the electrons ( $T_e = 1\text{-}5 \text{ eV} \rightarrow 4 \times 10^5\text{-}9 \times 10^5 \text{ m/s}$ ) is much higher than even the ion beam velocity ( $2\text{-}4 \times 10^4 \text{ m/s}$ ), and thus the electrons can diffuse rapidly to provide neutralization. In this work, we simplify the electron momentum equation to a generalized Boltzmann relationship between the electron pressure and electric field. In addition, the electron energy is included to provide the electron temperature distribution in the plume and backflow region.

Physically, the electrons in our model are those that are emitted from the neutralizer and rapidly spread throughout the plume and backflow regions to provide charge neutralization. Since the densities of the thruster produced plasmas are orders of magnitude

greater than that of the ambient space plasma, the neutralizer electrons play a dominant role compared to the ambient electrons in the vicinity of the spacecraft. However, far away, the ambient plasma becomes very important, but we are not interested in these large length scales. As a rough estimate, if the thruster plasma decays as  $(r_T/r)^2$ , the length scale for a 30 cm thruster plasma of density  $7 \times 10^{15} \text{ m}^{-3}$ , will take almost 125 m to decay to an ambient value of  $10^{10} \text{ m}^{-3}$  in LEO, and over 12.5 km to a value of  $10^6 \text{ m}^{-3}$  in GEO.

### 3.6.1 Electron Momentum Equation

The general momentum balance for the electrons including electric (E) and magnetic fields (B), pressure forces, and collisional drag terms is,

$$\frac{\partial \mathbf{v}_e}{\partial t} + \mathbf{v}_e \cdot \nabla \mathbf{v}_e = -\frac{e}{m_e}(\mathbf{E} + \mathbf{v}_e \times \mathbf{B}) - \frac{\nabla p_e}{m_e n_e} + \mathbf{R}_e \quad (3.29)$$

where  $\mathbf{R}_e$  is the drag term due to ion and neutral collisions,

$$\mathbf{R}_e = -\sum_i \nu_{ei}(\mathbf{v}_e - \mathbf{v}_i) - \sum_n \nu_{en}(\mathbf{v}_e - \mathbf{v}_n) \quad (3.30)$$

where  $\mathbf{v}_e$  is the electron drift velocity,  $\nu_{ei}$  is the collision frequency between electrons and ions of velocity  $\mathbf{v}_i$ , and  $\nu_{en}$  is the collision frequency between electrons and neutrals of velocity  $\mathbf{v}_n$ . The collisional terms are summations over all species involved. In the case of ions, this would include the beam ions, CEX ions - both propellant and NPE, and ambient ions. For the neutrals, there are the propellant and NPE neutrals and ambient species.

A scaling analysis of the momentum equation leads to insight and significant simplification. Taking the drift velocity to be  $V$ ,  $\tau$  to be a characteristic time scale for changes in the drift velocity, and  $L$  to be a characteristic length over which  $V$  changes, each of the accelerations in Eqn. (3.29) have the following scalings:

Unsteady	Inertia	Lorentz	Pressure	Collisional Drag
$\frac{V}{\tau}$	$\frac{V^2}{L}$	$\frac{eE}{m} + \omega_{ce} V$	$\frac{v_{te}^2}{L}$	$\nu V$

where  $\omega_{ce}$  is the electron gyrofrequency, and  $v_{te}$  is the electron thermal velocity. Since we are interested in the motion of the CEX ions, the time scales involved are much larger than the electron time scales. Thus, as a very good approximation, the electron unsteady and inertia terms can be neglected.

Since the electron thermal velocity is much greater than the beam ion velocity there is no reason to believe that the electrons will ever be supersonic. At most, the electrons will drift near the beam ion velocity in the beam as they are convected downstream. Outside of the beam, the CEX plasma is expanding as a result of being accelerated by the radial beam potentials. Typical radial beam potential drops are on the order of 10-60 V, and hence the

CEX ions attain velocities on the order of  $4\text{--}9 \times 10^3$  m/s (for Xe). Electrons with drift velocities of this magnitude will be highly subsonic in the regions exterior to the beam. This behavior of the electrons also shows that the inertia term, which scales as the square of the electron Mach number, is much smaller than the pressure term.

The ratio of the electric to magnetic components in the Lorentz acceleration term is  $\Delta\phi/VBL$ . The characteristic length scale,  $L$ , is the length scale of density and potential gradients in the plume which is on the order of the beam radius in the radial direction. The average magnetic field strength is  $2 \times 10^{-5}$  T in LEO, and  $1 \times 10^{-7}$  T in GEO. Numerically, this ratio is at least  $10^2$  taking  $V$  to be on the order of the beam ion velocity. Thus, magnetic field effects are negligible compared to electric field forces. Thus, in this work, we neglect the magnetic field in the electron momentum equation. However, it is noted that the plasma "beta" (the ratio of the plasma pressure,  $n_e k T_e$ , to the magnetic pressure,  $B^2/2\mu_0$ ) is only slightly greater than unity at the thruster exit, and becomes less than one within a meter.

Lastly, we examine the importance of the collisional drag terms compared to the remaining electric field and pressure gradient terms. In Figure 3.15, we show the ratio of the electron-ion collision frequency to the electron-neutral collision frequency in the beam of a typical xenon thruster as a function of the electron temperature. In Section 3.7, we give full details on the collision frequency models. As can be seen, electron-neutral collisions are dominant for electron temperatures above 2 eV due to the Coulomb cross section decaying with temperature. The total electron collision frequency ( $\nu_e = \nu_{ei} + \nu_{en}$ ) is on the order of  $10^5$  s $^{-1}$  in the beam over the temperature range of 1 to 5 eV. With collision frequencies of this order, and our estimates of the electron drift velocity, the collisional drag terms are several orders of magnitude less than both the electric field and pressure gradient terms. It should be mentioned that if both the magnetic field and collision terms were to be included, the magnetic field term is dominant in LEO since the Hall parameter,  $\beta = \omega_{ce}/(\nu_{ei} + \nu_{en})$  is greater than one in the plume. However, in GEO, the Hall parameter is much less than one, and the magnetic field can be neglected.

As a result of our scaling analysis and the identification of dominant terms, we find that the electron momentum equation, Eqn. (3.29), reduces to a balance between the pressure and electric potential gradients,

$$e\nabla\phi = \frac{k\nabla n_e T_e}{n_e} \quad (3.31)$$

If the electron temperature is constant, Eqn. (3.31) can be readily integrated to yield the well known isothermal Boltzmann relation which gives the electron density as a function of potential. However, as seen in experiments, the electron temperature decreases radially and

axially due to cooling as the plume expands. The variation of the electron temperature, however, is much less than that of the plasma density due to the high electron thermal conductivity [Kaufman, 1975]. Thus, the electron temperature is "slowly-varying" in comparison to the density variation, i.e.  $(1/L)\Delta T_e/T_e \ll (1/L)\Delta n_e/n_e$ . A multiple-scales argument can be invoked (although a mathematical " $\epsilon$ " is not present in the momentum equation) that the temperature varies on a "slow" scale, while the density varies on a "fast" scale. A first order solution to Eqn. (3.31) yields a Boltzmann relationship with a spatially varying temperature,

$$n_e(\mathbf{x}) = n_{e\infty} \exp\left(\frac{e \phi(\mathbf{x})}{k T_e(\mathbf{x})}\right) \quad (3.32)$$

This modified form of the Boltzmann distribution is a statement that, since the electron thermal velocity is much greater than ion drift velocities, the electrons are in a local equilibrium between the electric field and pressure forces. It should be pointed out that Eqn. (3.32) is actually an exact solution to the steady Boltzmann equation with arbitrary  $\mathbf{E}$  and  $\mathbf{B}$  fields, if  $T_e$  is a constant and provided that the net electron drift velocity is much smaller than the thermal velocity, which is the case in ion thruster plumes.

It is important to stress that the multiple scales argument is based on experimental observations. It is checked *a posteriori* that indeed, temperature gradients are less than density gradients, as well as potential gradients, which are large - particularly at the beam edge. Note that with this model, the electron density is a specified background density, denoted by subscript  $\infty$ , when the potential far from the beam falls to zero.

### 3.6.2 Electron Temperature Equation

The electron temperature is given by the general electron energy equation,

$$\frac{3}{2}n_e \left( \frac{\partial}{\partial t} + \mathbf{v}_e \cdot \nabla \right) k T_e + p_e \nabla \cdot \mathbf{v}_e = -\nabla \cdot \mathbf{q}_e + Q_e \quad (3.33)$$

where  $\mathbf{q}_e = -\kappa_e \nabla T_e$  is the conductive heat flux. For the electron heating/cooling term,  $Q_e$ , we consider collisional transfer and ohmic heating,

$$Q_e = -3 \frac{m_e}{m_i} v_e n_e k (T_e - T_H) + \mathbf{j}_e \cdot \mathbf{E} \quad (3.34)$$

where the heavy species temperature,  $T_H$ , of the ions and neutrals is taken to be a constant corresponding to the temperature of the thruster chamber walls. The electron velocity,  $\mathbf{v}_e$ , is taken to be the beam ion velocity in the beam, and zero outside.

The electron thermal conductivity is given by *Mitchner and Kruger* [1973],



$$\kappa_e = \frac{2.4}{1 + \nu_{ei}/\sqrt{2}} \frac{k^2 n_e T_e}{m_e \nu_e} \quad (3.35)$$

Figure 3.16 shows the variation of the electron thermal conductivity as a function of the electron temperature. Typical values of the plasma and neutral densities in the beam are used as in Figure 3.15 where the electron collision frequency behavior was shown. We can see that the electron thermal conductivity at 5 eV is on the order of 0.5 W/m<sup>2</sup>K, whereas at 1 eV, it is about 0.1 W/m<sup>2</sup>K.

It is useful to also conduct a scaling analysis of Eqn. (3.33). We take the electron pressure to be given by,  $p_e = n_e k T_e$ , and neglect the unsteady term since we are interested in the steady-state behavior:

Convection	Conduction	Collisional Transfer	Ohmic
$\frac{V p_e}{L}$	$\frac{\nu_{te}^2 p_e}{\nu L^2}$	$\frac{m_e}{m_i} \nu p_e$	$e n_e V \frac{\Delta \phi}{L}$

Within the beam, the convection and ohmic terms play a role (with convection being comparable to the ohmic term), but they are weak compared to the conduction term which is dominant throughout the plume (due to the  $\nu_{te}^2$  scaling). Collisional transfer is also weak compared to conduction due to the electron-ion mass ratio factor. Thus, the electron temperature equation basically represents a conductive heat transfer problem with weak sink terms. However, since the convective terms pose no computational difficulties, we include them for completeness. In addition, it should be noted that the heavy species temperature will actually rise due to collisional heating with the electrons. However, since the collisional transfer term is weak, the assumption of isothermal ions and neutrals has little effect. Lastly, although we are not considering ionization in our ion model, the effect of an ionization energy sink term in Eqn. (3.34) can be assessed. The rate of energy loss from the electrons scales as  $\dot{n}_e E_i$  where  $\dot{n}_e$  is the ionization rate and  $E_i$  is the ionization energy. For ionization of xenon at 1 eV, this inelastic loss term is greater than the elastic collision term by an order of magnitude, but is still six orders of magnitude less than the conductive term. However, for electron temperatures above 5 eV, the ionization rate is about four orders of magnitude greater, and would create an energy sink that would have to be accounted for.

### Thermal Boundary Conditions

Since the steady-state energy equation is conduction dominated, the boundary conditions imposed on the electron temperature play an important role in determining the solution. The electron temperature close to the thruster exit where neutralization takes place

is a function of neutralizer operation and the beam-neutralizer coupling potential. This value, denoted by  $T_{eo}$ , is specified as an input set by thruster operating conditions.

### Radial

For the far-field temperature behavior in the radial direction, the high temperature region near the thruster will behave as a thermal point source. Since thermal conduction is the dominant term, the electron energy equation, Eqn. (3.33), written in spherical coordinates, reduces to,

$$\frac{1}{r^2} \frac{d}{dr} \left( r^2 \kappa_e \frac{dT_e}{dr} \right) = 0 \quad (3.36)$$

We take the thermal conductivity to depend on the temperature via an exponent:  $\kappa_e = AT_e^n$ . For electron temperatures below roughly 2 eV, electron-ion collisions are dominant, and  $n=5/2$  since  $\kappa_e \sim T_e/\nu_{ei}$  and  $\nu_{ei} \sim T_e^{-3/2}$ . For electron temperatures above 2 eV, electron-neutral collisions are dominant, and  $n=1/2$  since  $\kappa_e \sim T_e/\nu_{en}$  and  $\nu_{en} \sim T_e^{1/2}$ . (We will see how the collision frequencies scale with the electron temperature in Section 3.7) Eqn. (3.36) can be readily solved, subject to the boundary conditions  $T_e = T_{eo}$  at  $r = r_o$ , and  $T_e \rightarrow T_{e\infty}$  as  $r \rightarrow \infty$ . The result is,

$$\frac{T_e^{n+1} - T_{e\infty}^{n+1}}{T_{eo}^{n+1} - T_{e\infty}^{n+1}} = \frac{r_o}{r} \quad (3.37)$$

This model can be used to fix the far-field temperature at the far radial boundaries of the computational domain. A cylindrical coordinate model was also investigated for the far field temperature behavior. However, in such geometry, the temperature logarithmically diverges at infinity, and therefore was not further considered.

### Axial

In the axial direction within the beam, it is useful to estimate the heat flux that is conducted and convected downstream. A simple model can be used to impose axial boundary conditions on the temperature or heat flux, or at least to gain insight into the far-field behavior. We consider a quasi-one-dimensional model as shown in Figure 3.17. We investigate the heat transfer in a beam of divergence angle  $\alpha$ , with axial flow  $V$ , and radial heat loss. Since this is a quasi-one-dimensional analysis, it is valid only for small divergence angles. Considering an element in the beam, we include the axial convective heat flux ( $5/2nVkT$ ), axial conductive heat flux ( $-\kappa dT/dz$ ), and a radial loss term  $\kappa(T - T_\infty)/\Delta L$ , where  $\Delta L$  is a gradient length scale for radial heat transfer. We denote the cross sectional area of the beam at axial position  $z$  as  $A_b(z) = \pi b(z)^2$ , and the cross sectional area at  $z + \Delta z$  as  $A_b(z) + 2\pi b(z) \tan \alpha \Delta z$ . With  $q = -\kappa dT/dz$ , the heat flow into the cylindrical element is,



$$\left[ q + (nV)\left(\frac{5}{2} kT\right) \right] \pi r_b^2(z) \quad (3.38)$$

and the heat flow out is,

$$\begin{aligned} & \left\{ \left[ q + \frac{dq}{dz} \Delta z \right] + \left[ nV \frac{5}{2} kT + \frac{d}{dz} \left( nV \frac{5}{2} kT \right) \Delta z \right] \right\} (\pi r_b^2(z) + 2\pi r_b(z) \tan \alpha \Delta z) \\ & + 2\pi r_b(z) \Delta z \kappa \frac{(T - T_\infty)}{\Delta L} \end{aligned} \quad (3.39)$$

Equating the net heat flow (OUT-IN) with a heat creation - loss term,  $S(T)$ , we have a second order differential equation for the axial temperature profile,

$$\frac{d}{dz} \left[ nV \frac{5}{2} kT - \kappa \frac{dT}{dz} \right] \frac{(r_T + z \tan \alpha)}{2} + \left[ nV \frac{5}{2} kT - \kappa \frac{dT}{dz} \right] \tan \alpha + \kappa \frac{(T - T_\infty)}{\Delta L} = S(T) \quad (3.40)$$

Let us examine the solution to a reduced form of this equation where  $S$  is negligibly small,  $\kappa$  is constant, and  $\alpha=0$ , hence  $(nV)$  is constant. Eqn. (3.40) then becomes,

$$\kappa \frac{d^2 T}{dz^2} - nV \frac{5}{2} k \frac{dT}{dz} - \frac{2\kappa}{r_T \Delta L} (T - T_\infty) = 0 \quad (3.41)$$

with the solution given by a decaying exponential,

$$\frac{T - T_\infty}{T_o - T_\infty} = \exp \left[ \frac{1}{2} \left( \frac{5knV}{2\kappa} - \sqrt{\left( \frac{5knV}{2\kappa} \right)^2 + \frac{8}{r_T \Delta L}} \right) z \right] \quad (3.42)$$

subject to the boundary conditions that  $T=T_o$  at  $z=0$ , and  $T \rightarrow T_\infty$  as  $z \rightarrow \infty$ . Note the appearance of two terms: a convective term  $5knV/2\kappa$ , and the conductive heat loss term  $8/r_T \Delta L$ . If radial heat loss is negligible, we expect the beam to be isothermal, which is indeed the case. On the other hand, if there is no convection,  $(r_T \Delta L/2)^{1/2}$  is a length scale for axial temperature decay.

From numerical solutions of Eqn. (3.33), which we will see later in Chapter 5, we compute the heat flux at the beam edge which can be related to  $\Delta L$ . We find that the radial heat loss is typically on the order of 100-200 W/m<sup>2</sup>. Thus,  $\Delta L$  is on the order of 280-560 m with  $T_\infty=0.1$  eV, a typical value in LEO. With  $\Delta L$  and previous values for electron density and beam velocity, the convective term is  $O(10^{-3})$ , while the conductive term is  $O(10^{-1})$ . However, the significance of a large  $\Delta L$  is that the axial temperature decay is weak. We can use this result to justify imposing a zero gradient condition on the temperature downstream in the plume.

### 3.7 Collision Models

We have already discussed the role of both electron-ion and electron-neutral collisions in relation to the electron momentum and energy equations. In this section, detailed

discussions of the collision models are presented. We follow *Banks* [1966] in the general development of the average momentum transfer collision frequency, and examine electron-ion, electron-neutral, and ion-neutral interactions. In addition, ionization and recombination models are discussed.

Consider a particle of species 1 and a particle of species 2 colliding. The relative velocity is  $g$ , and the center of mass scattering angle is denoted by  $\theta$ . The velocity dependent momentum transfer cross section,  $Q(g)$ , is defined as,

$$Q(g) = 2\pi \int \sigma(g, \theta) (1 - \cos \theta) \sin \theta d\theta \quad (3.43)$$

where  $\sigma(g, \theta)$  is the differential scattering cross section for the particular collisional process. The average momentum transfer collision frequency between particles of species 1 with species 2 of number density  $n_2$  is,

$$\nu_{1-2} = \frac{4}{3} n_2 \left( \frac{8}{\pi} \right)^{1/2} \left[ \frac{kT_1}{m_1} + \frac{kT_2}{m_2} \right]^{1/2} \langle Q \rangle \quad (3.44)$$

where  $\langle Q \rangle$  is the momentum transfer cross section averaged over a suitable distribution function. In the case of a Maxwellian distribution,

$$\langle Q \rangle = \frac{1}{c^3} \int_0^\infty g^5 Q(g) \exp(-g^2/c^2) dg \quad (3.45)$$

where,

$$c = \left[ \frac{2kT_1}{m_1} + \frac{2kT_2}{m_2} \right]^{1/2} \quad (3.46)$$

The form of  $Q(g)$  is dependent upon the type of collisional process as we shall see in the next sections.

### 3.7.1 Charged Particle Interactions

#### Coulomb Collisions

For interactions between particles of charge  $Z_1e$  and  $Z_2e$ , the interaction force varies as  $1/r^2$  as given by Coulomb's law. The differential cross section, due to Rutherford, is,

$$\sigma(g, \theta) = \left( \frac{Z_1 Z_2 e^2}{8\pi\epsilon \mu g^2} \right)^2 \sin^{-4} \left( \frac{\theta}{2} \right) \quad (3.47)$$

where  $\mu$  is the reduced mass of the two particles. The averaged cross section is then found to be,

$$\langle Q \rangle = \frac{\pi}{2} \left( \frac{Z_1 Z_2 e^2}{4\pi\epsilon_0 \mu} \right)^2 \frac{\ln \Lambda}{(kT_1/m_1 + kT_2/m_2)^2} \quad (3.48)$$

where  $\ln \Lambda$  is the Coulombic logarithm that takes into account Debye shielding between the

two particles and is given by,

$$\Lambda = \frac{12\pi\epsilon_0(kT_1 + kT_2)}{Z_1 Z_2 e^2} \lambda_D \quad (3.49)$$

For electron-ion collisions, usually  $T_e/m_e \gg T_i/m_i$ , and numerically,

$$\Lambda = 1.24 \times 10^7 \left( \frac{T_e^3}{n} \right)^{1/2} \quad (3.50)$$

where  $T_e$  is in  $^{\circ}\text{K}$  and  $n_e$  in  $\text{m}^{-3}$ . Over a wide range of plasma conditions,  $\ln \Lambda$  varies between 10 and 20, and is usually around 15.

Lastly, the collision frequency of charged particles is given by,

$$\nu_{1-2} = \frac{4}{3} \sqrt{\frac{8}{\pi}} \frac{\pi}{2} \left( \frac{Z_1 Z_2 e^2}{4\pi\epsilon_0} \right)^2 \frac{1}{k^{3/2} \mu^2} \frac{n_2 \ln \Lambda}{(T_1/m_1 + T_2/m_2)^{3/2}} \quad (3.51)$$

or numerically, again for electron-ion collisions, we have,

$$\nu_{ei} = 3.63 \times 10^{-6} \frac{n_i \ln \Lambda}{T_e^{3/2}} \quad (3.52)$$

For a typical ion thruster beam plasma density of  $n_e = n_i = 7 \times 10^{15} \text{ m}^{-3}$ ,  $\nu_{ei} = 247,000 \text{ s}^{-1}$  for  $T_e = 1 \text{ eV}$  ( $11,600^{\circ}\text{K}$ ), and  $\nu_{ei} = 26,000 \text{ s}^{-1}$  for  $T_e = 5 \text{ eV}$  ( $58,000^{\circ}\text{K}$ ).

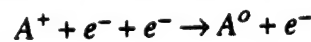
It is interesting to examine both electron-electron and ion-ion collisions, and determine their scaling compared to the electron-ion collision frequency. Using Eqn. (3.51), we find that,

$$\frac{\nu_{ee}}{\nu_{ei}} = \sqrt{2} \quad , \quad \frac{\nu_{ii}}{\nu_{ei}} = \sqrt{\frac{2m_e}{m_i}} \left( \frac{T_e}{T_i} \right)^{3/2} \quad (3.53a,b)$$

Thus, we see that electron self collisions are on the order of the electron-ion collisions. Ion self collisions can also be on the order of electron-ion collisions if  $T_e \gg T_i$ , which usually is the case.

## Recombination

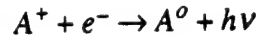
In addition to scattering collisions, electrons and ions within the plume can recombine in a number of ways. One mechanism is via three body recombination,



where the third body is usually another electron that gains energy during the encounter. The Hinov and Hirschberg model [Mitchner and Kruger, 1973] is generally used for three body recombination. The recombination rate factor [ $\text{m}^3/\text{s}$ ] is given by,

$$\alpha_{\text{recomb}} = 1.09 \times 10^{-20} \frac{n_e}{T_e^{9/2}} \quad (3.54)$$

with  $n_e$  in  $\text{m}^{-3}$  and  $T_e$  in  $^{\circ}\text{K}$ . The volumetric recombination rate is given by  $\alpha_{\text{recomb}} n_e n_i$  which at its maximum value in a typical plume is around  $10^9 \text{ m}^{-3}\text{s}^{-1}$ . Compared to volumetric CEX rates which are on the order of  $10^{20} \text{ m}^{-3}\text{s}^{-1}$ , three body recombination is insignificant due to the relatively low collisionality in ion thruster plumes. Another recombination mechanism is radiative recombination,



where a photon is released in the encounter. The radiative recombination rate of xenon apparently has not been measured, but an upper bound can be estimated using the values for hydrogen which are over two orders of magnitude larger than cesium [Mitchner and Kruger, 1973]. Over the electron temperature range of interest of 1-5 eV, the radiative recombination cross section of hydrogen is about  $1 \times 10^{-25} \text{ m}^2$ . Despite the use of such an upper bound, we saw in Figures 3.11 and 3.14 that radiative recombination, although being orders of magnitude larger than three body recombination, is still orders of magnitude less than the ion production mechanisms.

### Plasma Turbulence

Lastly, we mention that it is possible that instabilities and plasma turbulence may result in anomalous electron-ion collision frequencies. A probable instability is the hot electron beam plasma instability that can occur since  $v_{te} > v_{bi} > v_{ti}$ . The frequency of this instability,  $\nu_{ei}^*$ , scales as  $(v_{bi}/v_{te})\omega_{pe}$  [Book, 1987], which then makes  $\nu_{ei}^*/\nu_{ei} \approx O(10^3)$  even at 1 eV. Thus, turbulence can greatly enhance the electron-ion collision frequency and hence transport coefficients like the thermal conductivity will be reduced. However, it remains for experiments to verify the presence and role of turbulence in ion thruster plumes. Tests to determine the electromagnetic noise spectrum of ion thrusters for spacecraft compatibility have mainly concentrated on noise produced in the discharge chamber and in the power conditioning equipment [Macie and Whittlesey, 1973; Sovey et al, 1989; Fearn et al, 1993].

### 3.7.2 Electron-Neutral Collisions

#### Elastic Scattering Collisions

Eqn. (3.44) can also be applied to the elastic scattering electron-neutral collision frequency, with a relevant averaged cross section  $\langle Q_{en} \rangle$ . Since  $T_e/m_e \gg T_n/m_n$ , we have,

$$\nu_{en} = \frac{4}{3} n_n \sqrt{\frac{8kT_e}{\pi m}} \langle Q_{en} \rangle \quad (3.55)$$

Figures 3.18a,b shows curve fits of the measured electron-neutral elastic cross sections for

xenon [Mitchner and Kruger, 1973] and mercury [Massey and Burhop, 1952] as functions of electron energy. For xenon, from Figure 3.18a, we find that  $\langle Q_{en} \rangle$  is  $2 \times 10^{-20} \text{ m}^2$  for  $T_e = 1 \text{ eV}$ , and  $3.5 \times 10^{-19} \text{ m}^2$  for  $T_e = 5 \text{ eV}$ . With a typical beam neutral density of  $n_n = 5 \times 10^{17} \text{ m}^{-3}$ , the respective electron-neutral collision frequencies are  $\nu_{en} = 9,000 \text{ s}^{-1}$  and  $350,000 \text{ s}^{-1}$ .

### Ionization

Depending on the electron temperature, ionization in the plume may be important. To assess the degree of ionization, we use the model of Drawin [Mitchner and Kruger, 1973]. According to Drawin's model, the ionization cross section as a function of the ratio of the electron energy to the ionization energy,  $u = E/E_i$ , is,

$$Q_i(u) = Q_i^* g(u) \quad (3.56)$$

where,

$$Q_i^* = 2.66 \pi a_o^2 \xi_k \left( \frac{E_i^H}{E_i} \right)^2 \quad (3.57)$$

and,

$$g(u) = \left( \frac{u-1}{u^2} \right) \ln(1.25 u) \quad (3.58)$$

In Eqn. (3.57),  $a_o$  is the Bohr radius,  $0.529 \times 10^{-10} \text{ m}$ ,  $E_i^H$  is the ionization energy of hydrogen, 13.6 eV, and  $\xi_k$  is the number of electrons in the outer shell of the atom being ionized. Table 3.3 shows values of  $Q_i^*$  for xenon, mercury, and molybdenum.

Table 3.3 Ionization Values for Xe, Hg, and Mo

	Xe	Hg	Mo
$E_i$ (eV)	12.13	10.44	7.10
$\xi_k$	6	10	5
$Q_i^*$ (m <sup>2</sup> )	$1.77 \times 10^{-19}$	$3.97 \times 10^{-19}$	$4.29 \times 10^{-19}$
$Q$ (m <sup>3</sup> /s)	$4.13 \times 10^{-13}$	$8.58 \times 10^{-13}$	$7.66 \times 10^{-13}$

To compute the volumetric ionization rate, Eqn. (3.56) must be integrated over the distribution function of the electrons,

$$\dot{n}_e = \int_{c_{\min}}^{\infty} n_e n_n c Q(u) 4\pi c^2 dc \quad (3.59)$$

where  $c$  is the speed of the electrons, and the lower limit of the integral is the minimum speed that corresponds to the ionization energy,  $(2E_i/m_e)^{1/2}$ . We assume a Maxwellian distribution, and with the following change of variables,

$$c = \sqrt{\frac{2E}{m_e}} \quad u = \frac{E}{E_i} \quad \theta = \frac{kT_e}{E_i} \quad (3.60)$$

the ionization rate is,

$$\dot{n}_e = Q n_e n_n \frac{I(\theta)}{\theta^{3/2}} \quad (3.61)$$

where  $I(\theta)$  is a function that is evaluated numerically,

$$I(\theta) = \int_1^\infty \frac{u-1}{u} \ln(1.25u) e^{-u/\theta} du \quad (3.62)$$

and  $Q = 4Q_i^*(E_i/2\pi m_e)^{1/2}$ . Values of  $Q$  are also shown in Table 3.3.

### 3.7.3 Ion-Neutral Collisions

The dominant ion-neutral collision we have dealt with is the resonant CEX collision process which we saw in Section 3.4. However, there are also non-resonant ion-neutral scattering collisions that should be assessed. The ion-neutral elastic scattering cross section at low energies is due to the polarization attraction of the neutral by the ion, as well as quantum-mechanical repulsion. The velocity dependent cross section [cm<sup>2</sup>] is given by Banks [1966],

$$Q_{in}(g) = 2.21\pi \left( \frac{\psi e^2}{\mu g^2} \right)^{1/2} \quad (3.63)$$

where  $\psi$  is the polarizability of the atom. The averaged cross section then is,

$$\langle Q_{in} \rangle = \frac{3\sqrt{2}}{16} \pi^{3/2} \left( \frac{4.88 \psi e^2}{\mu} \right)^{1/2} \left[ \frac{kT_i}{m_i} + \frac{kT_n}{m} \right]^{-1/2} \quad (3.64)$$

which results in a collision frequency of,

$$\nu_{in} = 2.6 \times 10^{-15} \left( \frac{\psi_o}{\mu_A} \right)^{1/2} n_n \quad (3.65)$$

where  $\psi_o$  is the polarizability in units of 10<sup>-24</sup> cm<sup>3</sup>,  $n_n$  is the neutral density in m<sup>-3</sup>, and  $\mu_A$  is the ion-neutral reduced mass in atomic mass units (amu). The polarizabilities of xenon, mercury, and molybdenum are shown in Table 3.4 [Weast, 1990].

Table 3.4 Polarizabilities of Xe, Hg, and Mo

Xe	Hg	Mo
4.044	5.4	12.8

For xenon, the ion-neutral scattering collision frequency with a typical thruster exit neutral density of 5 × 10<sup>17</sup> m<sup>-3</sup> is about 800 s<sup>-1</sup>, which is much less than the CEX collision

frequency ( $\sim 10^4 \text{ s}^{-1}$ ). For the sputtered molybdenum, since the densities are so low ( $10^{13} \text{ m}^{-3}$ ), this scattering frequency is less than unity.

At higher energies, scattering collisions between ions and neutrals are closer to hard sphere encounters. For xenon, the atomic radius is about  $1.3 \text{ \AA}$  [Chang, 1988], and hence the scattering collision frequency with the same neutral density as above, is about  $10^3 \text{ s}^{-1}$ , still less than CEX collision rates. In addition, most of these scattering collisions will be in the forward direction, i.e. away from the thruster and spacecraft.

### 3.8 Electric Potential Field

The electromagnetic fields that govern the transport of the plasma in the plume of an ion thruster are given by Maxwell's equations which in full form are,

$$\text{Gauss' Law } \nabla \cdot \mathbf{E} = \frac{\rho}{\epsilon_0} \quad (3.66a)$$

$$\nabla \cdot \mathbf{B} = 0 \quad (3.66b)$$

$$\text{Faraday's Law } \nabla \times \mathbf{E} = -\frac{\partial \mathbf{B}}{\partial t} \quad (3.66c)$$

$$\text{Ampere's Law } \nabla \times \mathbf{B} = \mu_0 \left[ \mathbf{j} + \epsilon_0 \frac{\partial \mathbf{E}}{\partial t} \right] \quad (3.66d)$$

Since we not considering magnetic fields, neither time varying behavior, Faraday's law reduces to  $\nabla \times \mathbf{E} = 0$ , which implies that the electric field can be expressed as the gradient of a potential,  $\phi$ . Thus in this electrostatic limit,  $\mathbf{E} = -\nabla \phi$ , which when coupled with Gauss' Law, yields Poisson's equation,

$$\nabla^2 \phi = -\frac{\rho}{\epsilon_0} = \frac{e(n_e - n_i)}{\epsilon_0} \quad (3.67)$$

where the electron density is given by Eqn. (3.32), and the ion density is the sum of the beam ion density, the CEX ion density, and a uniform background ion density.

Within most regions of the plume, the plasma is quasi-neutral with the electron and ion densities being approximately the same. Hence, it can be argued that it is not necessary to solve Poisson's equation, but use a quasineutral approximation. However, at the beam edge, and in the sheaths around biased spacecraft surfaces, there can be significant departures from quasi-neutrality. Rather than dealing with the difficult issues of how to patch together various solutions in the different regions of the plume, we solve Poisson's equation throughout the entire computational domain with suitable boundary conditions. We discuss boundary conditions in the next chapter.

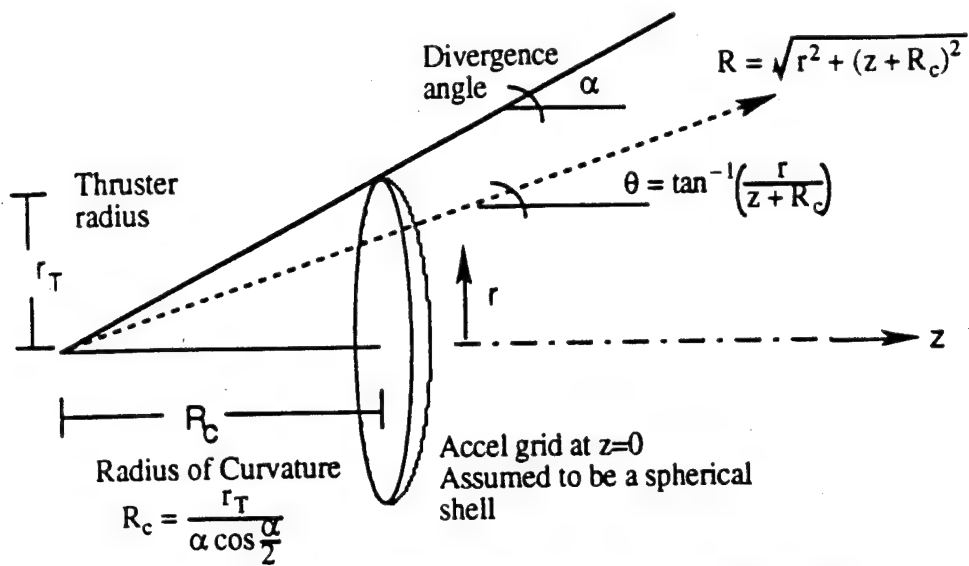


Figure 3.1 Geometry for beam plasma and neutral density models

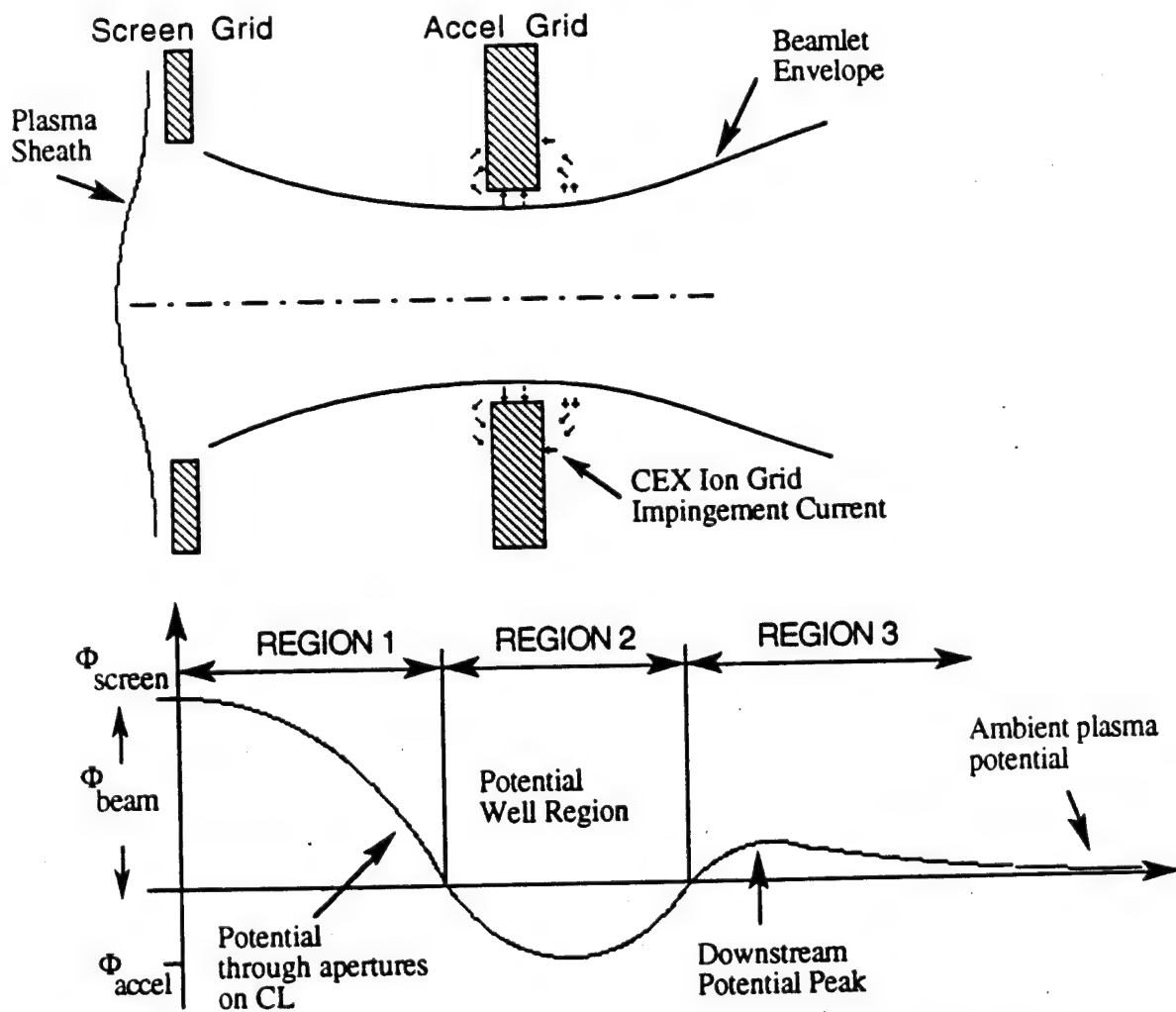


Figure 3.2a (Upper) Geometry of grid aperture and CEX ion impingement patterns  
Figure 3.2b (Lower) Schematic of potential along aperture centerline through grids  
(adapted from Monheiser [1991])



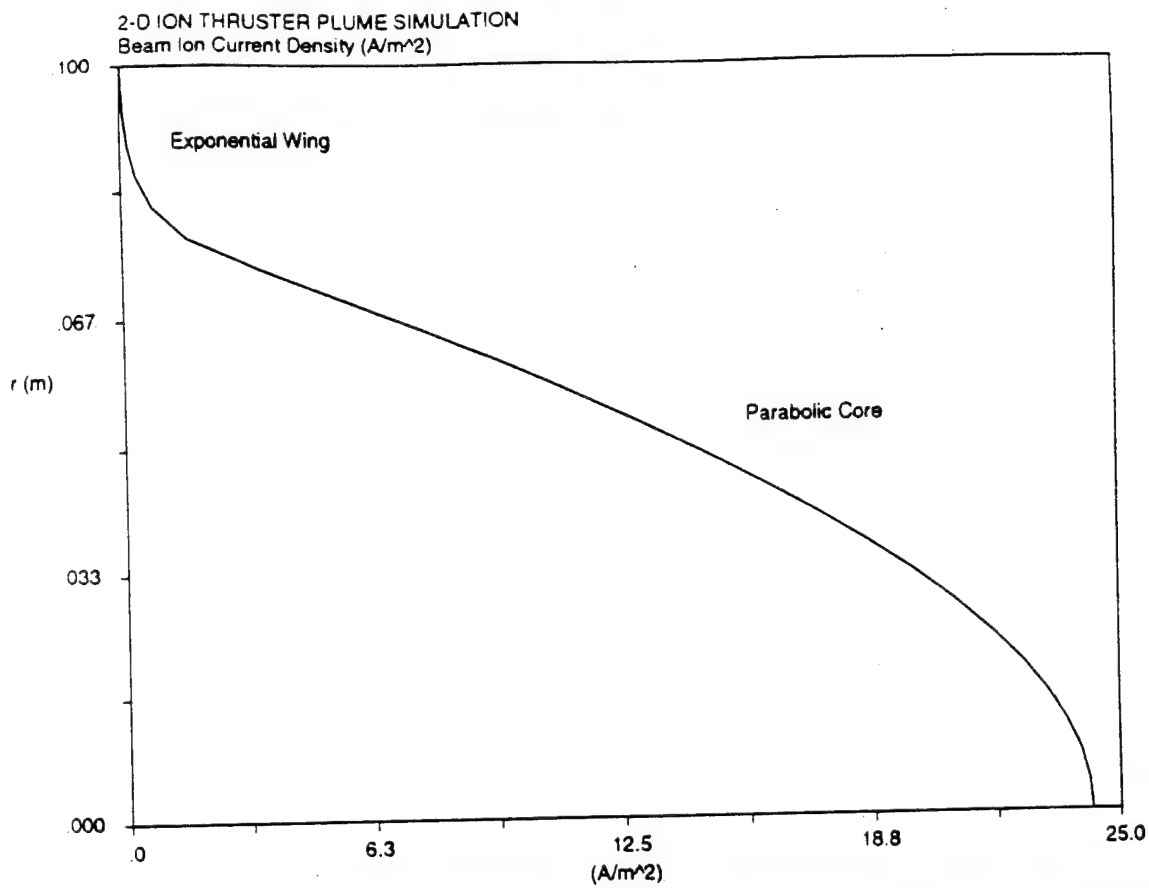


Figure 3.3 Radial cut of model beam ion current density profile showing parabolic core and exponential wing regions

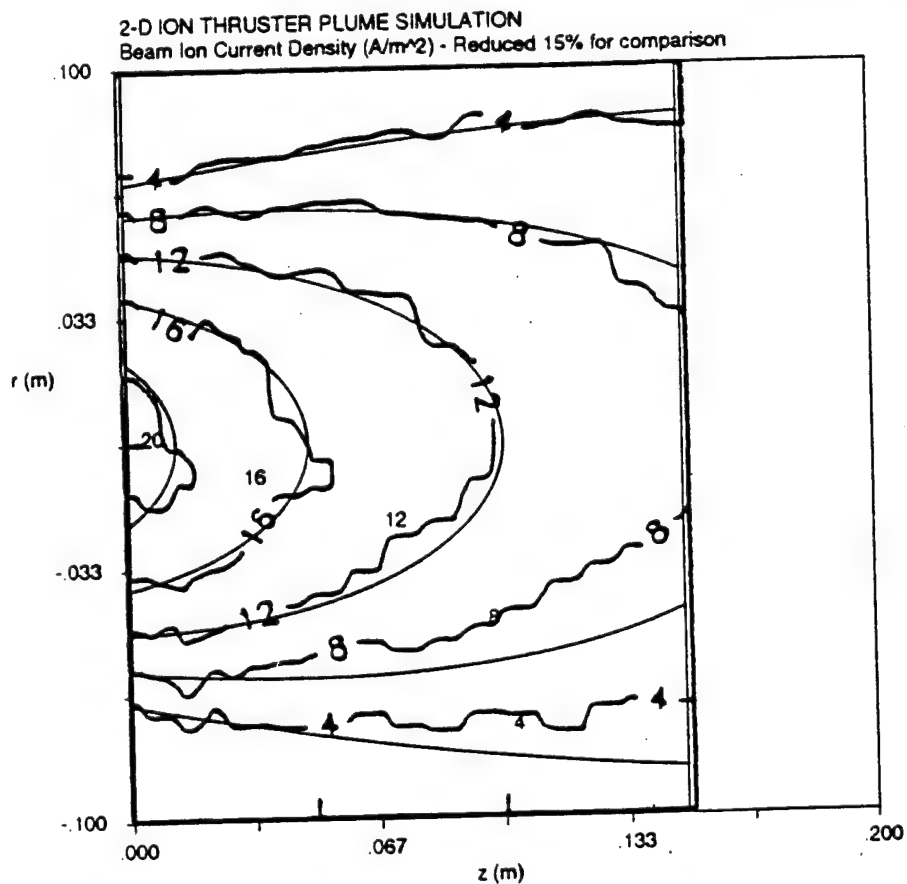


Figure 3.4 Beam ion current density model contours compared to experimental measurements by Monheiser [1991]

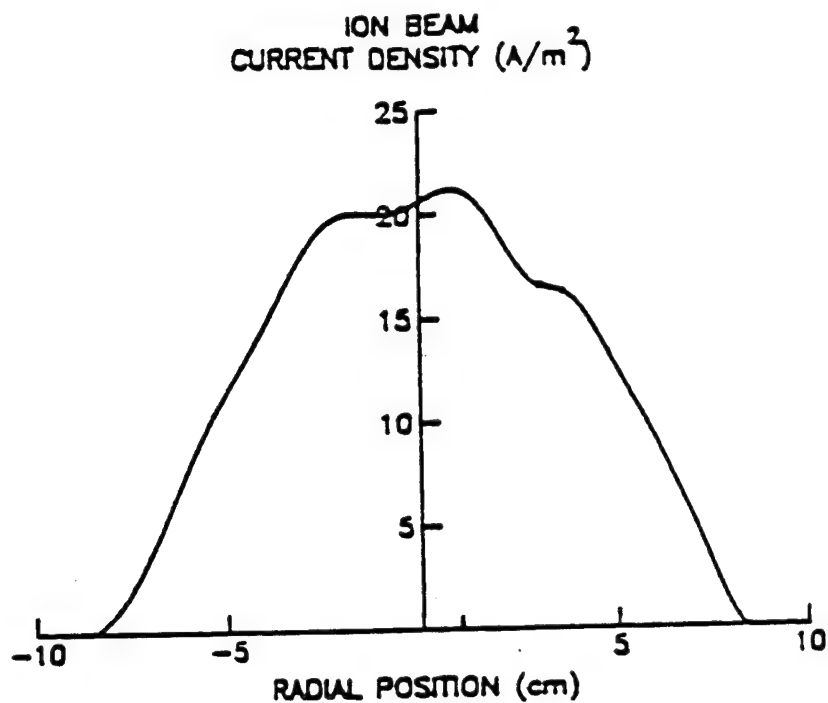


Figure 3.5 Radial cut of experimental beam ion current density from *Monheiser* [1991] showing non-uniformities

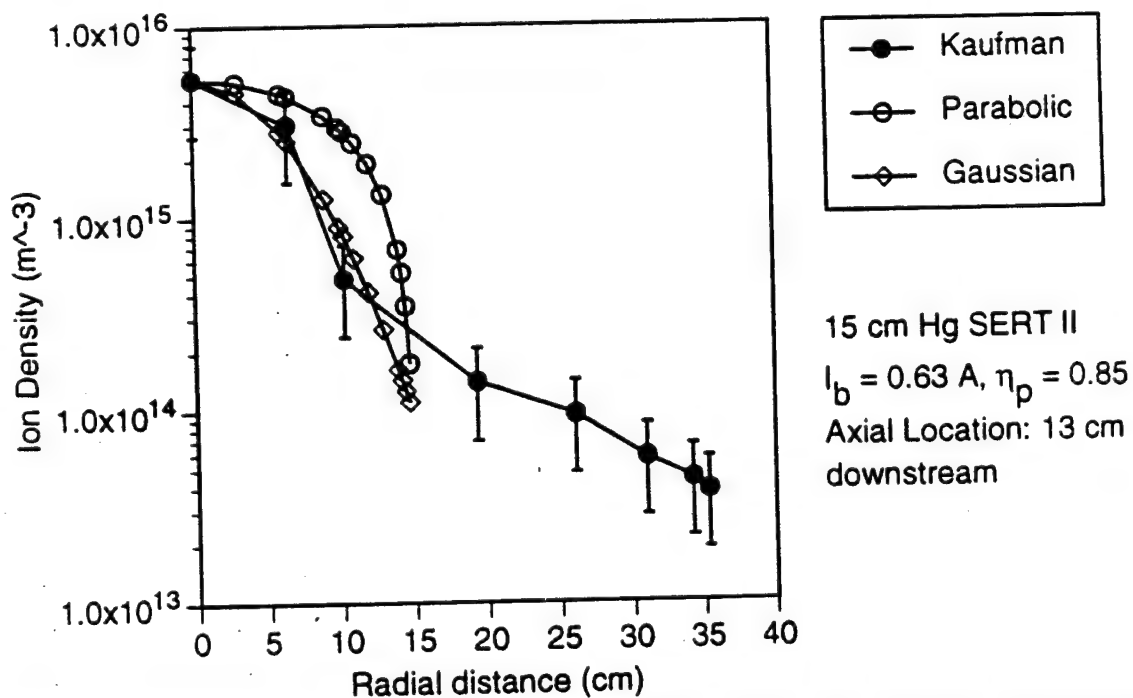


Figure 3.6 Comparison of experimental radial ion density profile with parabolic and Gaussian beam ion models; data from *Kaufman* [1975]

Figure 3.7 Typical relationship between beam ion cost and propellant utilization efficiency for constant discharge voltage and propellant flow rate for electron bombardment ion thrusters (adapted from Kaufman [1974])

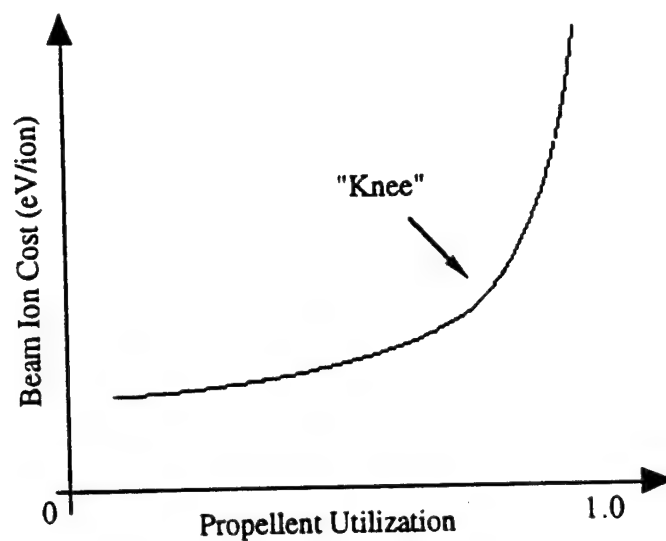
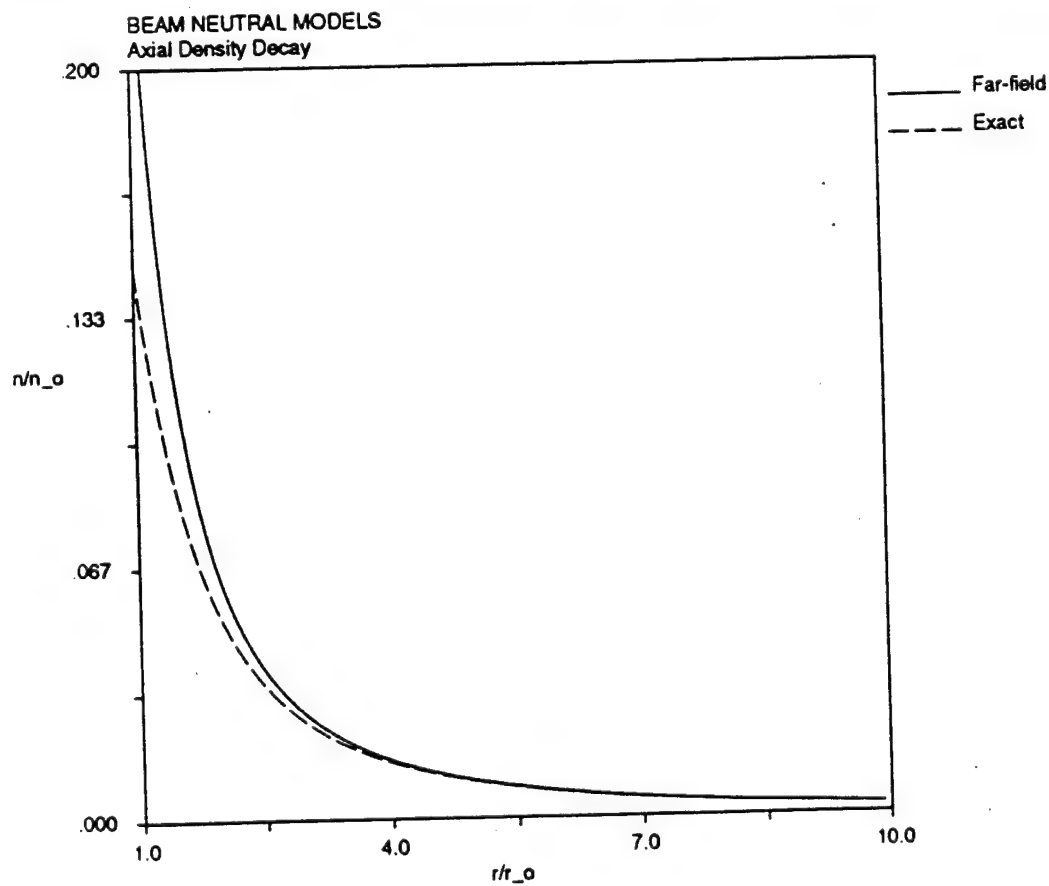


Figure 3.8 Comparison of exact and far-field neutral density profiles along centerline



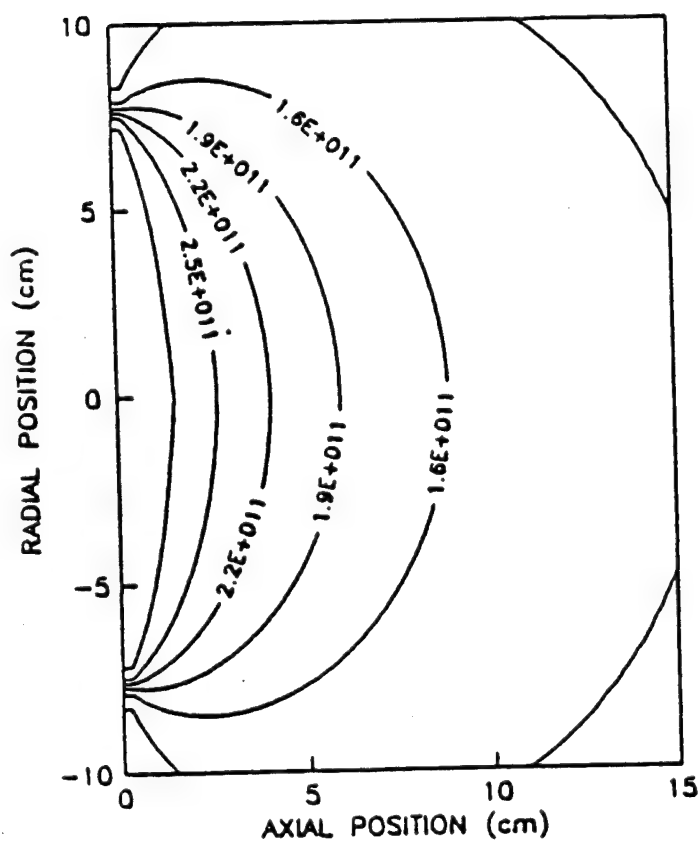
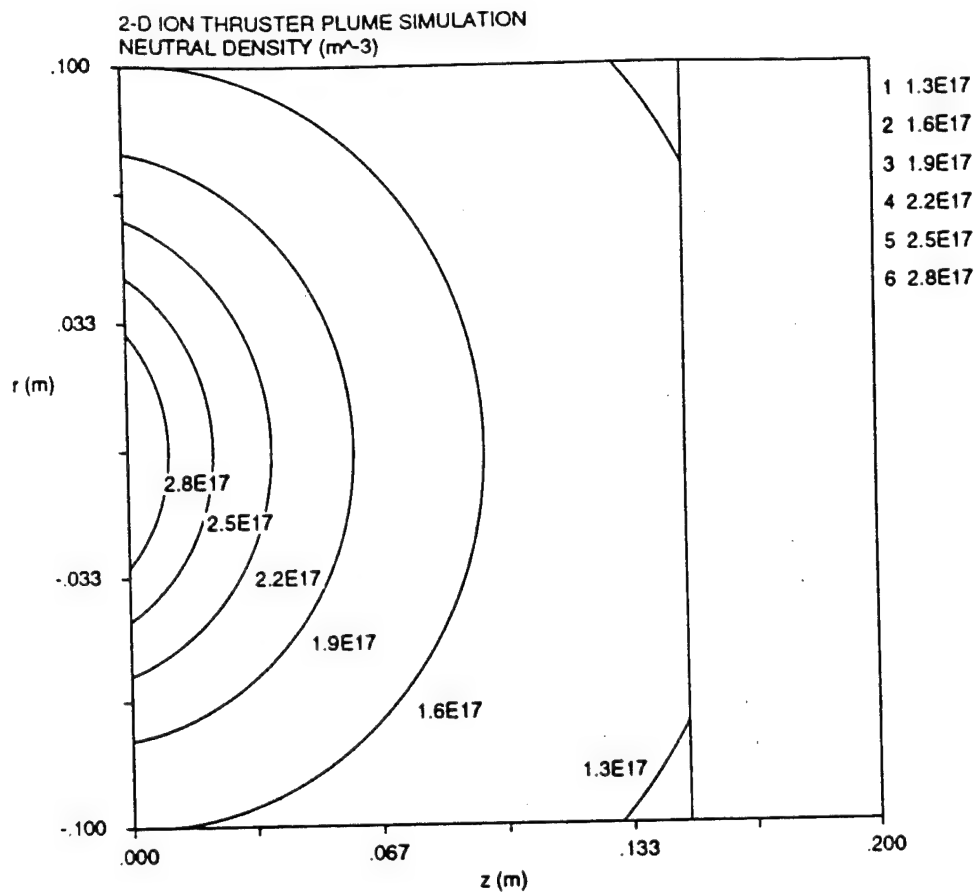


Figure 3.9 a) Computed neutral propellant density contours in plume - simple point source; b) Neutral propellant density contours from detailed numerical model by Monheiser [1991]

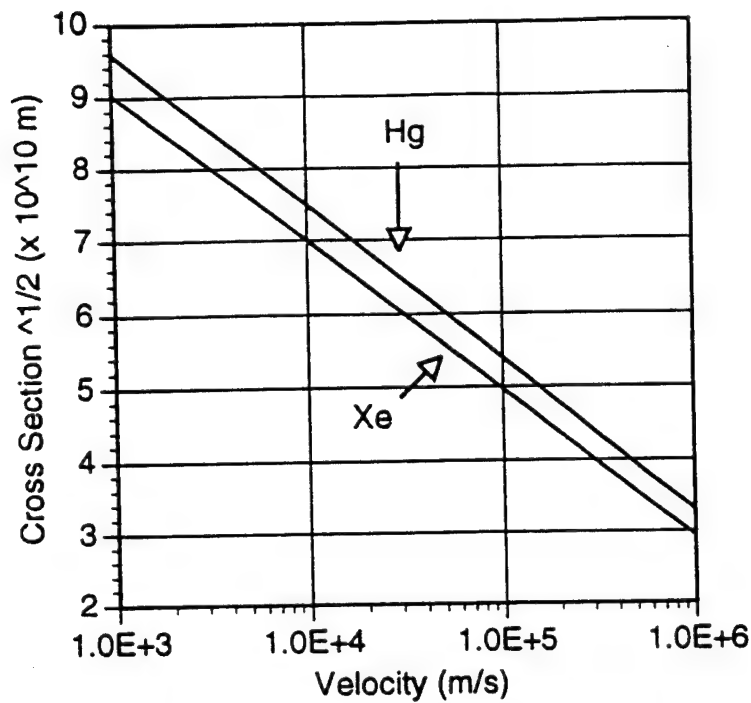


Figure 3.10 CEX cross sections for xenon and mercury from *Rapp and Francis* [1962]

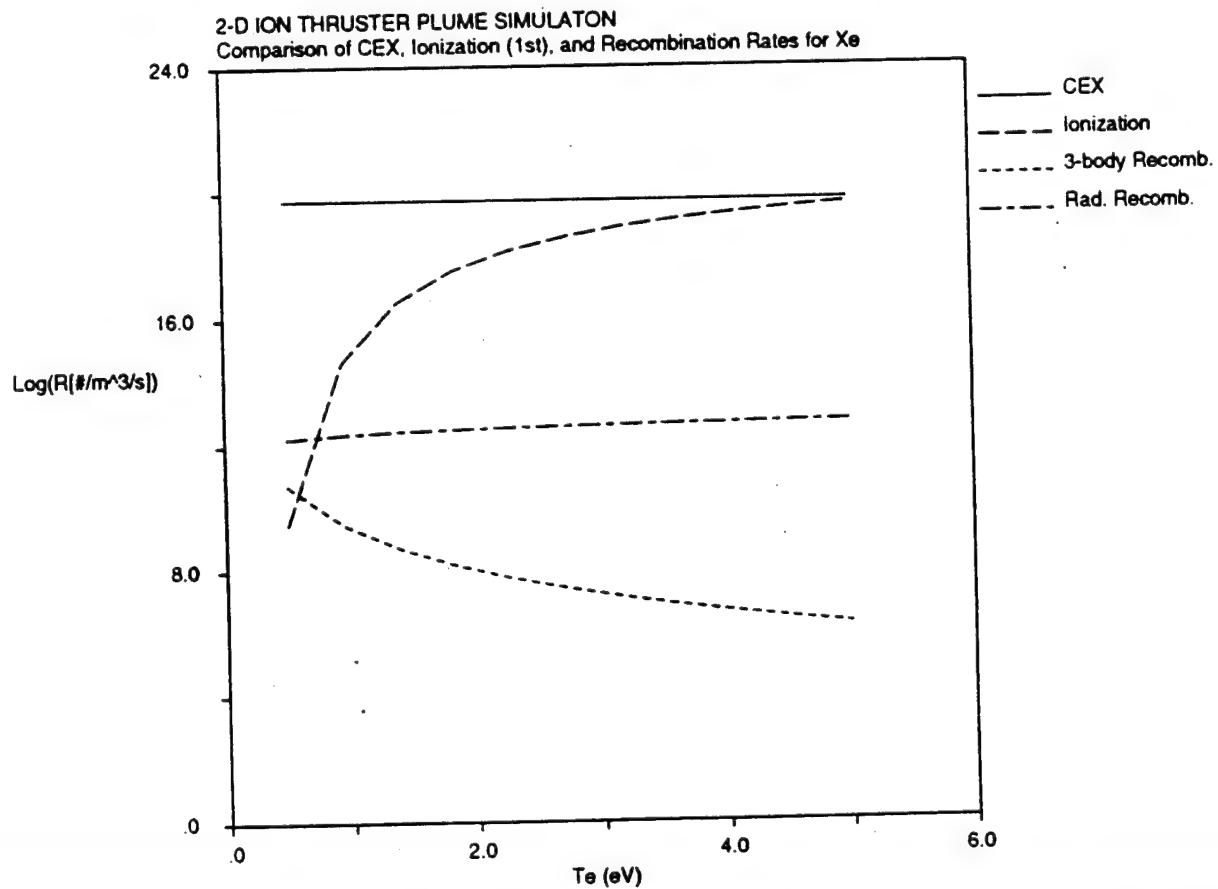


Figure 3.11 CEX, ionization, and three-body and radiative recombination rates for xenon as a function of electron temperature for densities at thruster exit

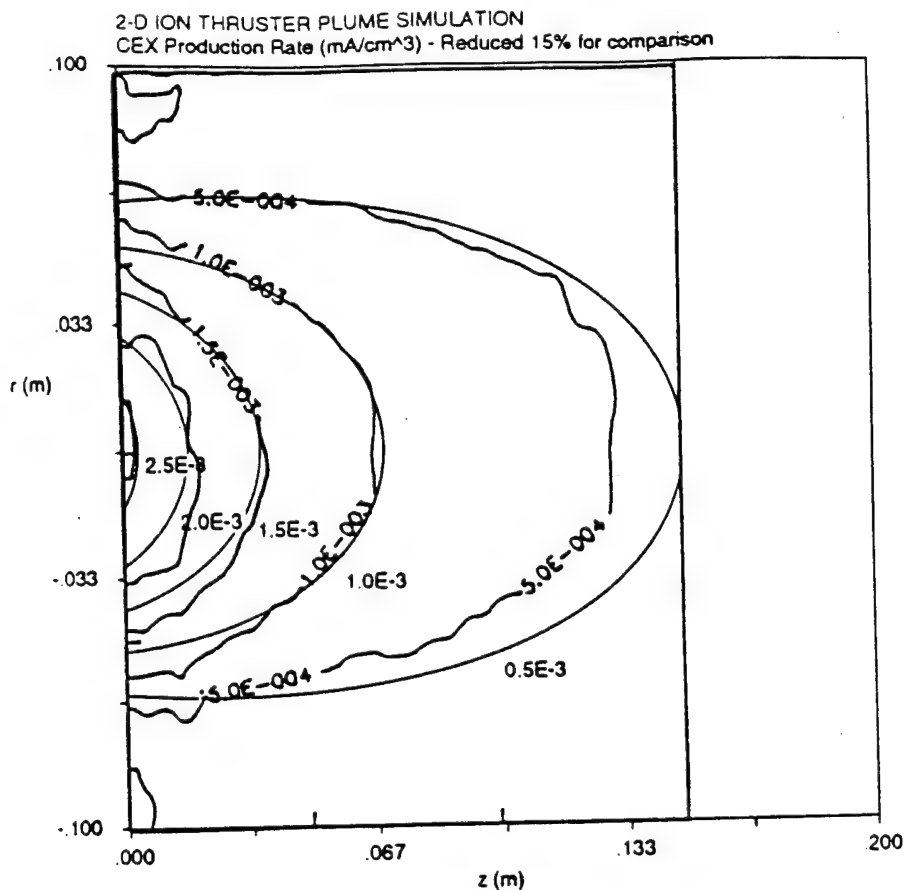


Figure 3.12 Computed CEX ion production contours in plume compared with those of *Monheiser* [1991]

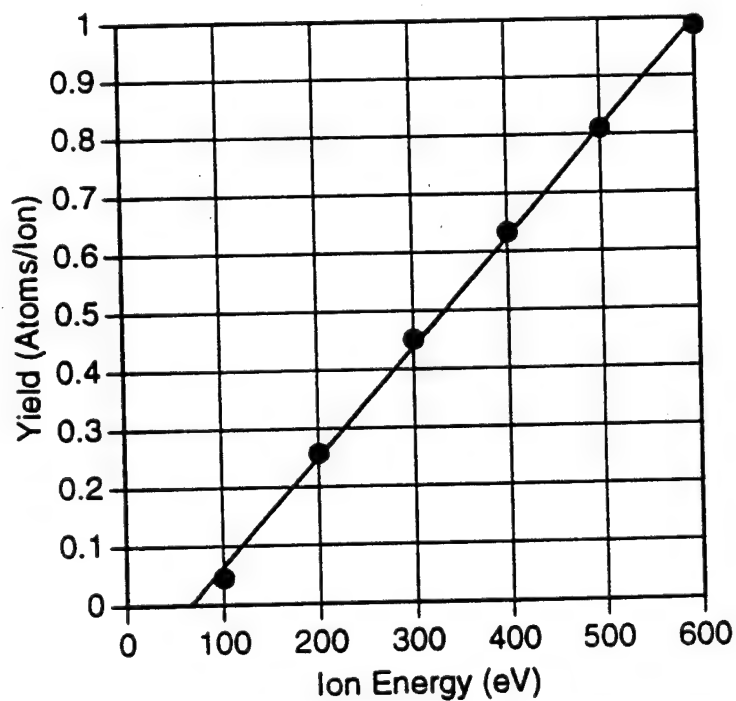


Figure 3.13 Sputtering yield of Mo by Xe; averaged data from *Weijsenfeld and Hoogendoorn* [1961] and *Rosenberg and Wehner* [1962]

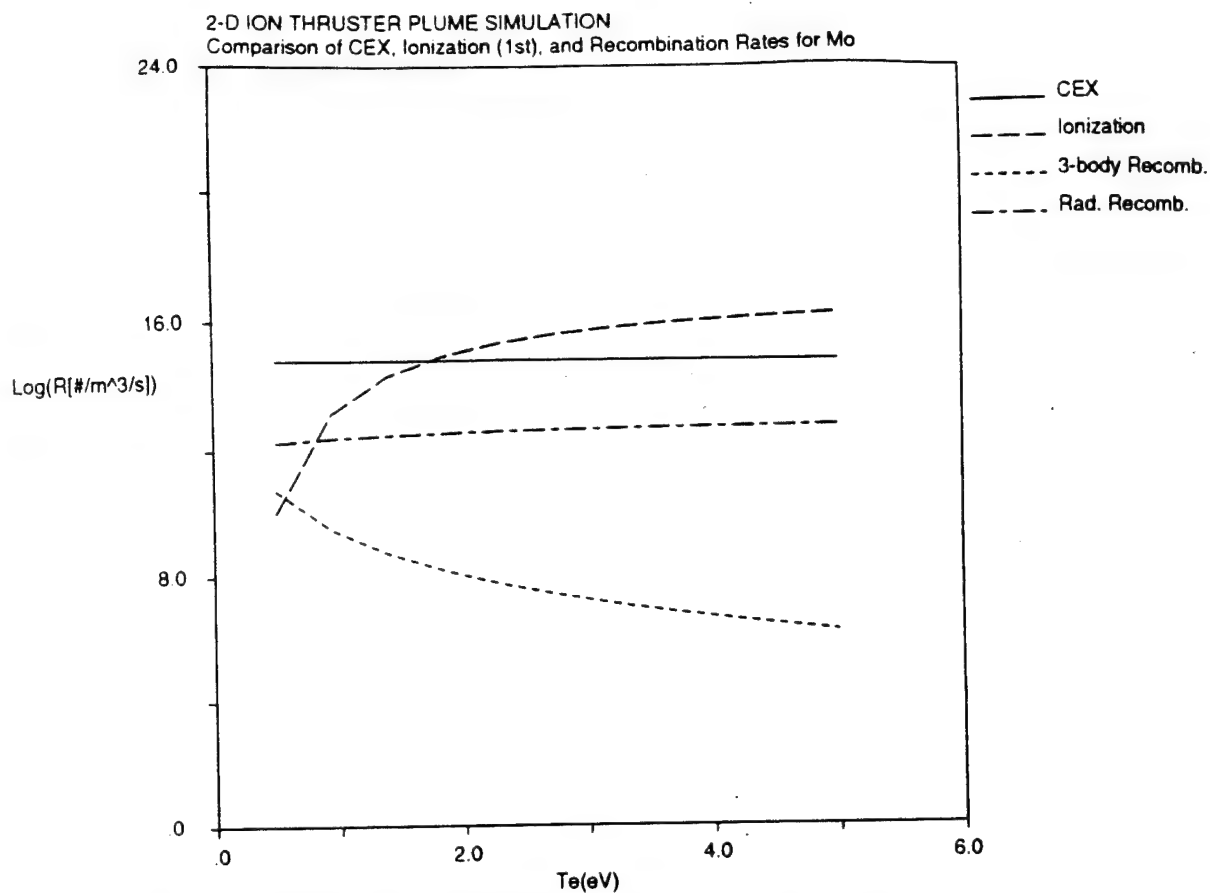


Figure 3.14 CEX, ionization, and three-body and radiative recombination rates for molybdenum as a function of electron temperature for densities at thruster exit

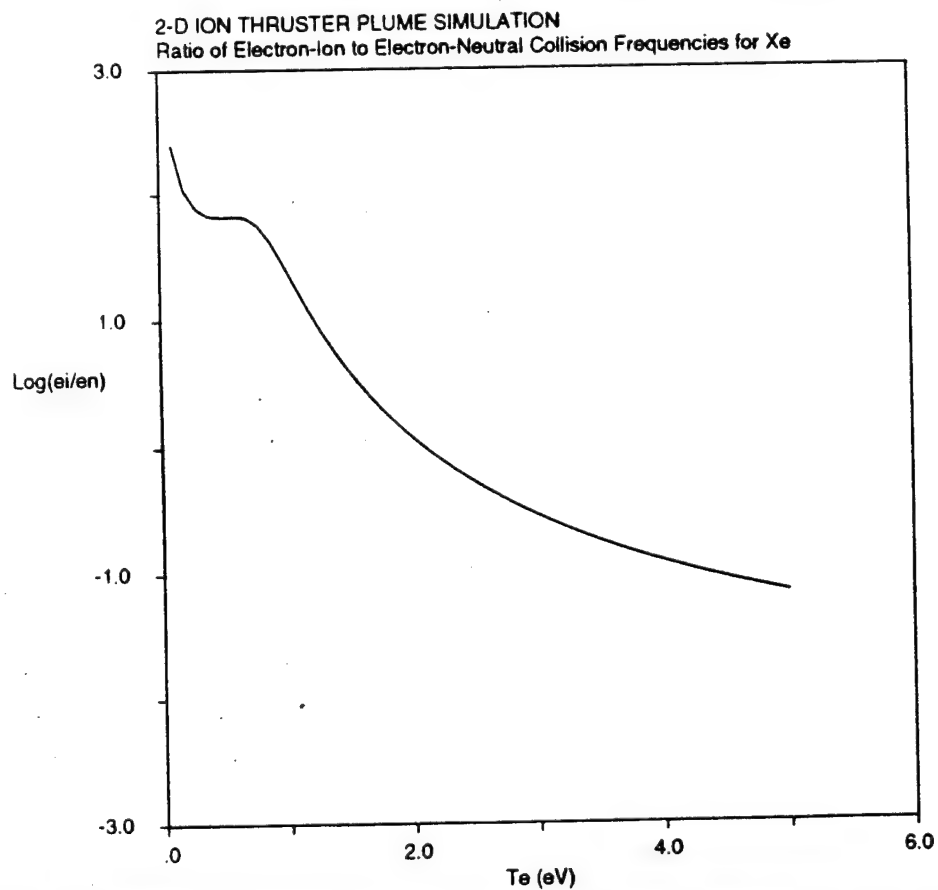


Figure 3.15 Ratio of the electron-ion to electron-neutral collision frequencies for xenon as a function of electron temperature with maximum plume densities

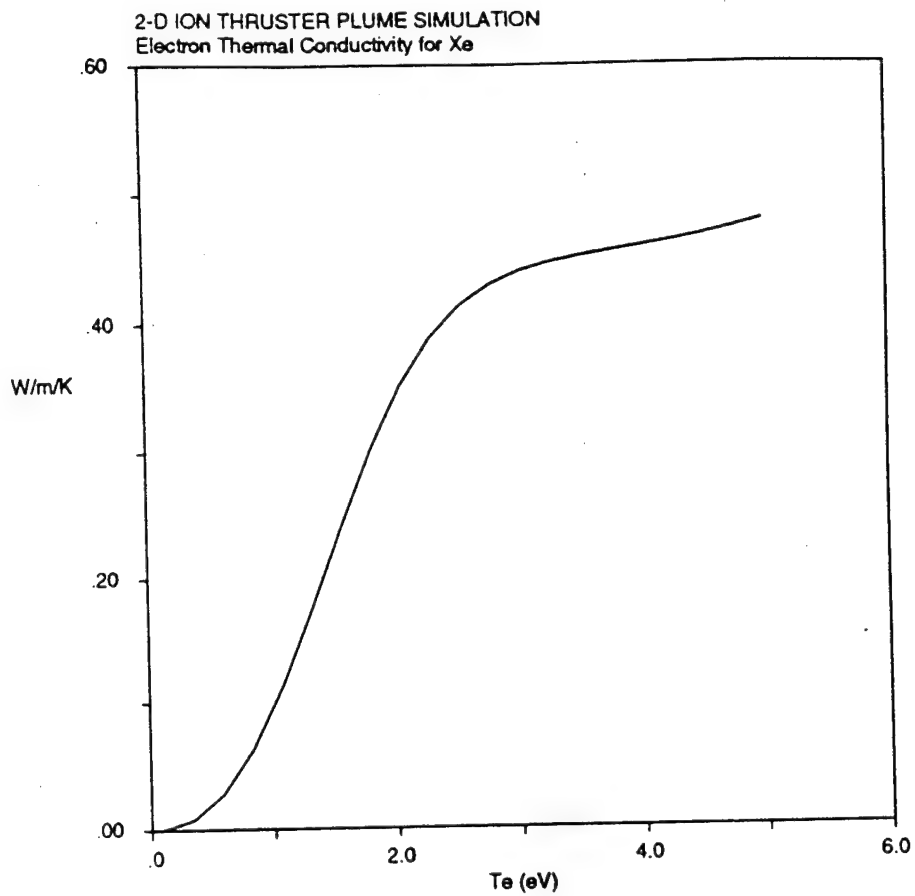


Figure 3.16 Electron thermal conductivity of xenon as a function of electron temperature with maximum plume densities

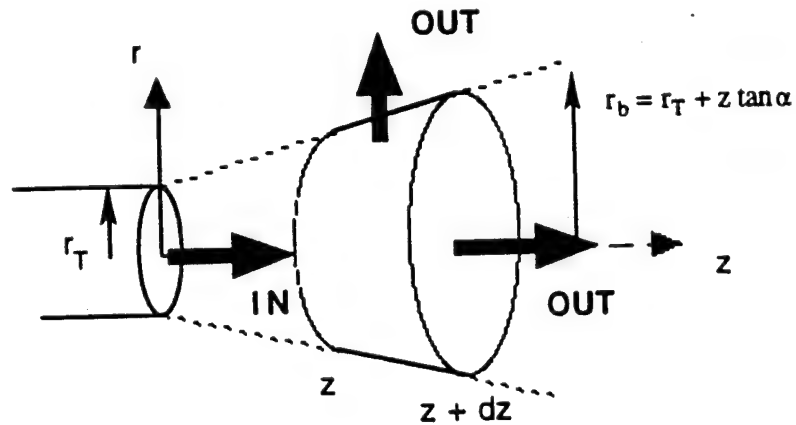


Figure 3.17 Axial heat conduction model geometry



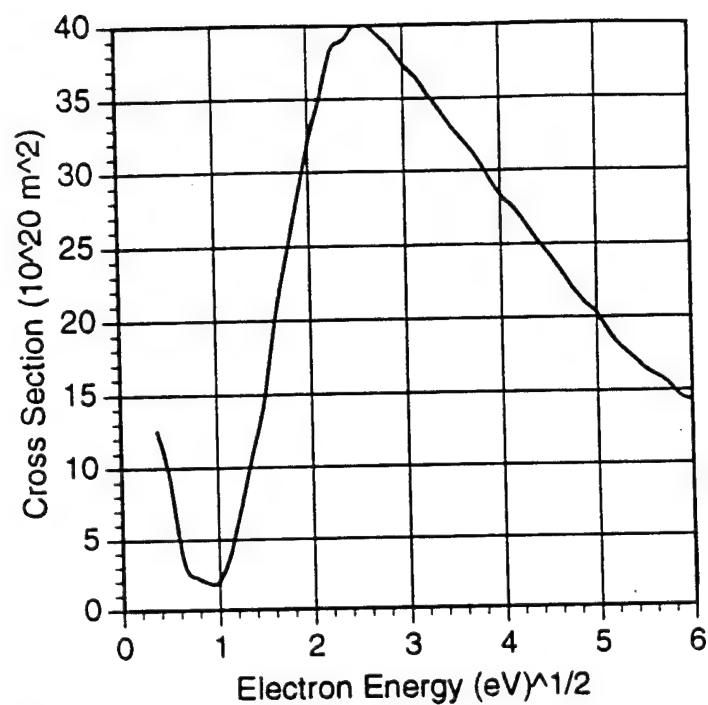


Figure 3.18a Elastic electron-neutral collision cross section for xenon  
(from *Mitchner and Kruger* [1973])

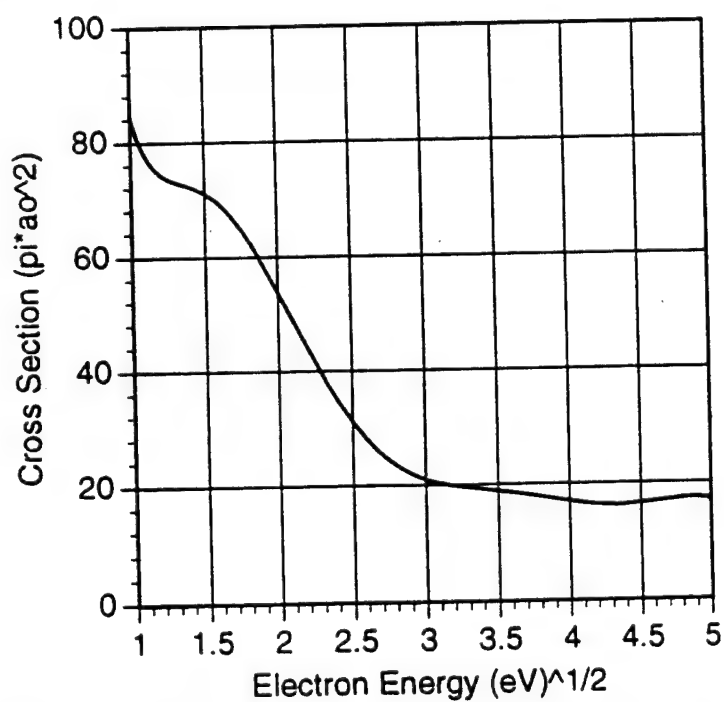


Figure 3.18b Elastic electron-neutral collision cross section for mercury  
(from *Massey and Burhop* [1952])

# Chapter 4

## Numerical Plume Model and Methods (Axisymmetric)

In Chapter 3, we formulated a physical model of an ion thruster plume. In this chapter, we present an axisymmetric numerical model incorporating this physical model, and discuss the numerical techniques that are employed to simulate the backflow of CEX ions. The general simulation model is first presented, then related details are discussed.

### 4.1 General Backflow Simulation Model

Our approach to understanding and predicting ion thruster contamination will be to begin with a two-dimensional model to understand the basic physics in terms of the phenomena and scaling relationships. The two-dimensional numerical model is axisymmetric ( $r$ - $z$ ) which is naturally suited for the cylindrical ion thruster plume. We assume no variation in the azimuthal direction. It must be noted that there are two main factors that would destroy this axisymmetry. One, is the geomagnetic field that, in general, will have a component perpendicular to the plume axis. However, in Chapter 3, estimates of the effects of the geomagnetic field indicated that we could neglect its effect on the CEX ions. The second factor is the effect of the geometry of the spacecraft on the plume backflow. Spacecraft structures are generally not axisymmetric, and biased surfaces will influence electric fields and consequently, the structure of the CEX plasma surrounding the spacecraft. In addition, the neutralizer, which is located to the side of the thruster exit, destroys axisymmetry. In order to investigate the effects of the geometry of an arbitrarily shaped spacecraft on the backflow, we will have to develop a fully three-dimensional numerical model. In Chapter 6, we present this model.

Figure 4.1 shows a schematic of the general computational domain which includes a

---

model spacecraft with optional solar array panels. Typical domain sizes are 1-3 meters. All surfaces of the spacecraft are biased - either at fixed potentials, or they are allowed to float as a single isolated conductor. An optional plume shield can be included to investigate its effect on reducing the backflow from the thruster which is located on the front face of the spacecraft. The beam ion and neutral propellant models developed in the previous chapter give the beam properties in the region of the plume, and the volumetric CEX propellant ion production model is used to determine the number of propellant CEX ions that are created per unit time per unit volume within the plume. To model the expansion of the CEX ions, a hybrid electrostatic plasma particle-in-cell (PIC) technique is employed. The PIC method follows the propellant CEX ions under the influence of self-consistent electric fields as they are transported out of the beam and form a plasma cloud that surrounds the spacecraft. The NPE ions, are also created volumetrically - either by CEX or ionization at higher electron temperatures. However, since the NPE ion density is much smaller than the propellant plasma densities, the effect on the potential is negligible. Hence, the NPE plasma propagation is determined solely by ion tracking in the potential determined from the propellant CEX expansion.

The simulation is run until steady-state is achieved when the number of particles within the domain becomes constant, i.e. the loss of particles at the boundaries and spacecraft surfaces balances the production rate within the plume. At steady-state, the current backflowing to biased spacecraft surfaces due to propellant CEX and NPE ions can be computed, and assessments of surface deposition can be made. In this work, the surfaces are assumed to be absorbing. The elliptic potential and temperature equations are solved throughout the computational domain. The far right, top, and far left upper boundaries are left open to space, although potentials can be fixed to simulate a ground testing chamber. The lower boundary of the domain in front of the spacecraft is the plume centerline; particles that reach this boundary are reflected. A uniform background plasma density is assumed. Since the thruster produced plasma environment is orders of magnitude larger than the ambient, we ignore the dynamics of the background plasma over the length scales of interest.

## 4.2 Plasma Particle-in-Cell (PIC) Technique

The plasma PIC technique is an established numerical method for the simulation of plasmas [*Birdsall and Langdon*, 1991; *Hockney and Eastwood*, 1988; *Tajima*, 1989]. With the PIC method, ions and electrons in the plasma are treated as macro-particles, where each macro-particle represents many physical particles, i.e.  $O(10^6)$  or more. Depending on

the physics of the problem, either the full, or a reduced set of Maxwell's equations are solved, and the particles' equations of motion are integrated under the influence of the computed self-consistent electromagnetic fields. For our problem concerning the propagation of the CEX ions, only the electrostatic electric potential is considered since self-induced magnetic fields due to currents are completely negligible. The charge of the simulation particles is deposited onto a computational grid and a charge density is computed. From this density, Poisson's equation for the electrostatic potential is solved on the grid, and the resulting self-consistent electric fields are extrapolated to the particles whose equations of motion are then integrated.

A major shortcoming of explicit fully kinetic PIC methods where electrons are treated as particles, is the very small time step (on the scale of the electron plasma frequency) that is required to resolve the electron motion. Since we are interested in the CEX ion motion, we adopt the *hybrid* approach where the ions are treated as particles, but the electrons are treated as a fluid. In this manner, the time step is now on the ion time scale, which for xenon ions, is about 490 times larger than the electron time scale. Thus, long time scale (ion time scale) phenomena can be simulated without excessive computational times.

#### 4.2.1 Non-dimensionalization of Governing Equations:

The PIC method is applied to both species of CEX ions that are encountered in thruster plumes - propellant and sputtered NPE ions. As mentioned earlier, the propagation of the NPE ions can be uncoupled from the propellant CEX ions due to their small densities. Thus, in our PIC algorithm, there is only one species that needs to be treated during one simulation. We non-dimensionalize the governing equations by reference characteristic time and length scales which are an ion plasma frequency,  $\omega_{pio}$ , and Debye length,  $\lambda_{Do}$ , respectively. Thus we have,

$$\tilde{t} = \omega_{pio} t \quad , \quad \tilde{\mathbf{x}} = \frac{\mathbf{x}}{\lambda_{Do}} \quad (4.1a,b)$$

where the reference ion plasma frequency and Debye length are,

$$\omega_{pio} = \sqrt{\frac{e^2 n_o}{\epsilon_o m_{io}}} \quad , \quad \lambda_{Do} = \sqrt{\frac{\epsilon_o k T_{eo}}{e^2 n_o}} \quad (4.2a,b)$$

The reference quantities, denoted by subscript "o", are based on propellant CEX plasma properties in the plume at the thruster exit. Thus,  $m_{io}$  is the mass of the propellant ions,  $n_o$  is the maximum CEX ion density which is less than the maximum beam ion density, and  $T_{eo}$  is the electron temperature at the thruster exit that is specified by neutralizer operation. The CEX ion velocities are non-dimensionalized by the reference ion acoustic speed

$$\lambda_{Do}\omega_{pio} = C_{so}.$$

The equation of motion without the presence of a magnetic field for a computational particle ion of species  $k$  is,

$$\frac{d\mathbf{v}_k}{dt} = \left(\frac{q_k}{m_k}\right) \mathbf{E} \quad (4.3)$$

where  $q_k$  is the charge  $W_p Z_k e$  and  $W_p m_k$  is the mass.  $W_p$  is the computational particle weighting, i.e. the number of real particles each macro-particle represents, and is the same for every computational particle in the simulations. Applying the above non-dimensionalizations to the time and ion velocity, we find that the electric field is non-dimensionalized as,

$$\tilde{\mathbf{E}} = \frac{e\mathbf{E}}{m_{io}\lambda_{Do}\omega_{pio}^2} \quad (4.4)$$

Thus, the non-dimensionalized equation of motion becomes,

$$\frac{d\tilde{\mathbf{v}}_k}{d\tilde{t}} = \left(\frac{Z_k m_{io}}{m_k}\right) \tilde{\mathbf{E}} \quad (4.5)$$

Since the CEX ions in ion thruster plumes are singly-charged,  $Z_k=1$ . Note that for the propellant CEX ions,  $m_k=m_{io}$ . It is also interesting to note that the macro-particle weighting,  $W_p$ , does not play a role in the equation because it is the charge to mass ratio that is important. Once the velocity of the particle is determined, its position can be updated. The non-dimensionalized kinematic expression for particle position is simply,

$$\frac{d\tilde{\mathbf{x}}_k}{d\tilde{t}} = \tilde{\mathbf{v}}_k \quad (4.6)$$

Poisson's equation for the electrostatic potential, Eqn. (3.67), in non-dimensionalized form is,

$$\nabla^2 \tilde{\phi} = \tilde{n}_{e\infty} \exp[\tilde{\phi} / \tilde{T}_e] - \tilde{n}_i \quad (4.7)$$

where,

$$\tilde{\phi} = \frac{e\phi}{kT_{eo}}, \quad \tilde{T}_e = \frac{T_e}{T_{eo}}, \quad \tilde{n}_{i,e\infty} = \frac{n_{i,e\infty}}{n_o} \quad (4.8a,b,c)$$

The electric field is then readily computed from the potential,

$$\tilde{\mathbf{E}} = -\nabla \tilde{\phi} \quad (4.9)$$

#### 4.2.2 Various Numerical Aspects of the PIC Technique

Macro-particles representing the propellant CEX or NPE ions are created each time step in each grid cell based on the local volumetric production rate. For the propellant CEX

ions, this is given by Eqn. (3.20). For the NPE ions, the production rate is given by a similar expression if CEX is dominant, or by the local ionization rate at higher electron temperatures. In each grid cell  $i$  of volume  $\mathcal{V}$ , the number of computational particles to create in time  $\Delta t$  is computed by,

$$N_{p\ cell\ i} = \text{INT} \left[ \frac{\dot{N}_i \mathcal{V}_{cell\ i} \Delta t}{W_p} \right] \quad (4.10)$$

where  $\dot{N}_i$  is the local ion production rate ( $\text{m}^{-3}\text{s}^{-1}$ ), and INT is the integer function which rounds down. Due to the large particle weighting which may be  $10^7$  or larger, there may be cells where the ratio in Eqn. (4.10) may be less than one. Instead of never loading any particles in these cells, and to handle fractional cases close to the larger integer value, we compare the fractional part,  $\mathcal{F}$ , of the above ratio to a random number  $\mathcal{R}(0,1)$ . If  $\mathcal{R} \leq \mathcal{F}$ , we add an additional particle.

When creating the propellant CEX ions with a large neutral background density as in ground tests, it is important to decide whether the CEX ion was born from a background neutral, or a thruster propellant neutral since the velocity distributions are different. To decide which type of CEX ion is to be created, we examine the ratio of the background neutral density to the total neutral density, and compare it to a random number  $\mathcal{R}(0,1)$ . If the random number is less than or equal to this ratio, we create the CEX ion with the background neutral properties, or else the CEX ion is created as a thruster propellant neutral. The velocities of the particles are drawn from Maxwellian distributions with the appropriate temperatures. The angles of the velocity vectors are random; however, for the propellant CEX ions, only positive axial velocities are allowed since those neutrals are drifting away from the thruster. A simple technique that is used to generate the Maxwellian velocity for a particle is to take  $N$  random numbers  $\mathcal{R}(0,1)$ , and compute [Birdsall and Langdon, 1991],

$$v_M = v_t \left[ \sum_{i=1}^N \mathcal{R}_i - \frac{N}{2} \right] \left( \frac{N}{12} \right)^{-1/2} \quad (4.11)$$

where  $v_t$  is the mean thermal velocity of the Maxwellian distribution. Taking  $N$  to be six yields a reasonable representation of a Maxwellian distribution. Figure 4.2 shows a comparison of the distribution using this approximation for 10,000 particles (i.e. Eqn. (4.11) was computed 10,000 times with  $N=6$ ) compared to the exact Maxwellian distribution.

For the NPE ions, the energy of the particles is taken from the sputtered energy distribution, Eqn. (3.28). The angle of the velocity vector is chosen randomly from the view factor angle of the grid face from a given particle's position.

To compute the charge density of the ions, the charge of the particles is weighted onto the grid, (to be discussed in the next section), with an axisymmetric area weighting scheme developed by *Ruyten* [1993]. Given a grid cell arrangement as shown in Figure 4.3, the radial weighting factors (in  $r$ ) are,

$$S_j = \frac{(r_{j+1} - r_p)(2r_{j+1} + 3r_j - r_p)}{2(r_{j+1}^2 - r_j^2)} \quad (4.12a)$$

$$S_{j+1} = \frac{(r_p - r_j)(3r_{j+1} + 2r_j - r_p)}{2(r_{j+1}^2 - r_j^2)} \quad (4.12b)$$

The axial weighting factors (in  $z$ ) are more straightforward, and are the same as for a Cartesian ( $x, y$ ) grid,

$$S_i = \frac{z_{i+1} - z_p}{z_{i+1} - z_i} \quad (4.13a)$$

$$S_{i+1} = \frac{z_p - z_i}{z_{i+1} - z_i} \quad (4.13b)$$

The fraction of charge assigned to each corner of a grid cell is depicted in Figure 4.3. The charge density is then the charge divided by the volume of the cell, which at grid point  $i, j$ , is,  $\pi(r_{j+1/2}^2 - r_{j-1/2}^2)(z_{i+1/2} - z_{i-1/2})$ . It should be noted that charge is conserved with these weightings, i.e. for a particle, the sum of its charge contributions to the four corners of a cell is unity. These same weighting factors are used to extrapolate the electric field computed on the grid to the particles within a cell, and to weight particles' velocities for computing the current density.

Aside from the CEX collisions, the PIC method implemented ignores all other particle interactions. In terms of ion-ion and electron-ion collisions, the plasma is considered "collisionless". For this approximation to be valid, we must examine the ratio of the electron-ion collision frequency to the ion plasma frequency,

$$\frac{\nu_{ei}}{\omega_{pi}} \sim \frac{n \ln \Lambda}{\sqrt{n}} \quad (4.14)$$

where  $n$  is the plasma density and  $\Lambda$  is the Coulomb factor that scales as  $1/n^{1/2}$ . The number of ions and electrons within a sphere with a radius the size of the local Debye length is referred to as the plasma parameter,  $N_D \sim n\lambda_D^3 \sim 1/n^{1/2}$ . Hence, the collisionality parameter, Eqn. (4.14), scales as  $\ln N_D / N_D$ . In ion thruster plumes,  $N_D \sim 10^4$ . Thus, since the plasma parameter is large, collisional effects can be neglected. It is for this reason, as well as for an adequate statistical representation of the plasma, that a minimum of around ten particles per cell (which scales as a Debye volume) is usually used.

The particle mover is a force time centered leap-frog scheme, as shown in Figure 4.4.

Applied to a simple harmonic oscillator of frequency  $\omega_0$ , the amplitude error is zero for  $\omega_0 \Delta t \leq 2$ , and the phase error scales as,  $\omega_0 \Delta t + (1/24)(\omega_0 \Delta t)^3$ . For stability reasons,  $\omega_{pi} \Delta t \leq 0.2$  is generally used. This timestep is smaller than the transit time for a CEX particle to cross a grid cell which has dimensions on the order of the local Debye length. One of the manifestations of error in the leap frog scheme is energy non-conservation of the particles. The sum of the kinetic and electrostatic potential energies of all the particles in the simulation must be constant, within a reasonable tolerance ( $\sim 5\%$ ), once steady state is achieved. This quantity is a fundamental check on the PIC method's validity, and must be monitored throughout the simulation to verify that a small enough time step is chosen.

### 4.3 Computational Grid

The fundamental length scale in a plasma is the Debye length which is a characteristic distance over which electric fields can be supported by the plasma. Near biased surfaces, the electric fields are confined within a narrow region - a sheath - which is on the order of a few Debye lengths. In order to resolve these length scales, at least near biased surfaces, the computational grid must be on the order of the local Debye length. However, the Debye length within the densest region of the plume is a fraction of a millimeter. A uniform grid with this resolution throughout a meter-size domain would require large computational resources. Moreover, the grid will be inefficient since the high resolution will be unnecessary in regions where the plasma density decreases from the thruster exit. In addition, we are not attempting to capture the sub-millimeter-level details in front of the thruster grid. This would only be important for studying the details of sputtering at the grid aperture level, as was done by *Peng et al* [1993].

The computational grid is non-uniform based on the simple approximation that the plasma density,  $n$ , from the thruster decays as  $1/R^2$ . Since the Debye length, varies as  $1/n^{1/2}$ , we see that the Debye length increases linearly away from the thruster exit. To simplify implementation, we linearly stretch each of the grid axes ( $r$  and  $z$ ), so that for grid index  $i$  in the axial direction and  $j$  in the radial direction,

$$z_{i+1} = z_i + \Delta z(z_i) \quad ; \quad r_{j+1} = r_j + \Delta r(r_j) \quad (4.15)$$

where  $\Delta z(z_i)$  and  $\Delta r(r_j)$  are the linearly increasing grid cell lengths.

Since we are applying the PIC method to the CEX ions whose maximum density is less than the maximum beam plasma density, we base our reference Debye length on the CEX plasma density at the thruster exit. The smallest grid cell is the one in front of the thruster exit on the centerline where the plasma density is the highest. The dimensions of this cell are  $Z_c$  by  $R_c$  where  $Z_c$  and  $R_c$  are proportional to the reference Debye length. It



should be noted that grid cell size and the total number of particles in the domain are tied together since increasing grid resolution also increases the number of particles required to maintain approximately ten particles per cell.

The computational domain, of length  $L$  and width  $W$ , is partitioned into four regions as seen in a representative grid in Figure 4.5. Since the geometry is axisymmetric, the domain represents a half-plane of the plume. The model spacecraft is  $z_{front}$  long and has a radius of  $r_{top}$ . The thruster front is located at  $z=z_{front}$ . The  $z$  axis is partitioned into a section behind the thruster exit, and a region in front of the thruster exit. At the far left domain boundary, the grid cell size in  $z$  is stretched by an amount  $\zeta_z^0 = (z_{front}/r_T)$ , and at the far right, by  $\zeta_z^L = (L-z_{front})/r_T$ . In the radial direction, the grid is partitioned into a region from the plume centerline ( $r=0$ ) to the top of the spacecraft,  $r_{top}$ , and from  $r_{top}$  to the upper boundary,  $W$ , where the grid cell is stretched in  $r$  by an amount  $\zeta_r^W = (W/r_T)$ . These stretching factors are derived from the approximation that the plasma density decreases as  $(r_T/R)^2$ .

The grid cell increments,  $\Delta z(z_i)$  and  $\Delta r(r_j)$  from Eqn. (4.15), are taken to have linear variations in the various regions, except for the radial direction in the plume where it is a constant. For the axial direction,

$$\Delta z(z_i) = \frac{Z_c}{z_{front}} (1 - \zeta_z^0) z_i + \zeta_z^0 Z_c, \quad 0 \leq z_i \leq z_{front} \quad (4.16a,b)$$

$$\Delta z(z_i) = Z_c \left( \zeta_z^L - 1 \right) \frac{(z_i - z_{front})}{(L - z_{front})} + Z_c, \quad z_{front} \leq z_i \leq L$$

Note that for  $z_i=0$ ,  $\Delta z = \zeta_z^0 Z_c$ , for  $z_i=z_{front}$ ,  $\Delta z = Z_c$ , and for  $z_i=L$ ,  $\Delta z = \zeta_z^L Z_c$ . For the radial direction,

$$\Delta r(r_j) = R_c, \quad 0 \leq r_j \leq r_{top} \quad (4.17a,b)$$

$$\Delta r(r_j) = R_c \left( \zeta_r^W - 1 \right) \frac{(r_j - r_{top})}{(W - r_{top})} + R_c, \quad r_{top} \leq r_j \leq W$$

where for  $r_j=W$ ,  $\Delta r = \zeta_r^W R_c$ .

Since the grid is orthogonal, a disadvantage of this scheme is apparent in Figure 4.5. We can see that since the axial grid points are clustered near the front of the thruster, they are also clustered throughout the domain in the radial direction which leads to unnecessary resolution and skewed grid cells. However, they are not too troublesome. In this work, we are interested in capturing the physics of the problem; numerical refinements such as multi-blocking and imbedded mesh schemes are reserved for future work.

#### 4.4 Poisson's Potential Equation Solution

Poisson's equation, Eqn. (4.7), in axisymmetrical coordinates is,

$$\frac{1}{\tilde{r}} \frac{\partial}{\partial \tilde{r}} \left( \tilde{r} \frac{\partial \tilde{\phi}}{\partial \tilde{r}} \right) + \frac{\partial^2 \tilde{\phi}}{\partial \tilde{z}^2} = \tilde{n}_e \exp[\tilde{\phi}/\tilde{T}_e] - \tilde{n}_i \quad (4.18)$$

The finite difference form of this equation can be derived using Gauss' law in order to avoid difficulties as  $r \rightarrow 0$  [Birdsall and Langdon, 1991]. Consider a number of grid cells as in Figure 4.6. Applying Gauss' Law at grid point  $(i,j)$ , we have (assuming all quantities are already non-dimensionalized),

$$Q_{i,j} = 2\pi r_{j+\frac{1}{2}}(z_{i+\frac{1}{2}} - z_{i-\frac{1}{2}})E_{r,i,j+\frac{1}{2}} - 2\pi r_{j-\frac{1}{2}}(z_{i+\frac{1}{2}} - z_{i-\frac{1}{2}})E_{r,i,j-\frac{1}{2}} + \pi(r_{j+\frac{1}{2}}^2 - r_{j-\frac{1}{2}}^2)(E_{z,i+\frac{1}{2},j} - E_{z,i-\frac{1}{2},j}) \quad (4.19)$$

The electric field terms are determined from differencing the potential,

$$E_{r,i,j+\frac{1}{2}} = -\frac{\phi_{i,j+1} - \phi_{i,j}}{r_{j+1} - r_j}, \quad E_{r,i,j-\frac{1}{2}} = -\frac{\phi_{i,j} - \phi_{i,j-1}}{r_j - r_{j-1}} \\ E_{z,i+\frac{1}{2},j} = -\frac{\phi_{i+1,j} - \phi_{i,j}}{z_{i+1} - z_i}, \quad E_{z,i-\frac{1}{2},j} = -\frac{\phi_{i,j} - \phi_{i-1,j}}{z_i - z_{i-1}} \quad (4.20)$$

and the charge enclosed is related to the charge density by,

$$Q_{i,j} = \rho_{i,j} \pi (r_{j+\frac{1}{2}}^2 - r_{j-\frac{1}{2}}^2) (z_{i+\frac{1}{2}} - z_{i-\frac{1}{2}}) \quad (4.21)$$

Substituting these into Eqn. (4.19), we obtain,

$$\frac{2r_{j+\frac{1}{2}}}{(r_{j+\frac{1}{2}}^2 - r_{j-\frac{1}{2}}^2)(r_{j+1} - r_j)} (\phi_{i,j+1} - \phi_{i,j}) - \frac{2r_{j-\frac{1}{2}}}{(r_{j+\frac{1}{2}}^2 - r_{j-\frac{1}{2}}^2)(r_j - r_{j-1})} (\phi_{i,j} - \phi_{i,j-1}) \\ + \frac{1}{(z_{i+\frac{1}{2}} - z_{i-\frac{1}{2}})} \left[ \frac{\phi_{i+1,j}}{z_{i+1} - z_i} + \frac{\phi_{i-1,j}}{z_i - z_{i-1}} - \phi_{i,j} \left( \frac{1}{z_{i+1} - z_i} + \frac{1}{z_i - z_{i-1}} \right) \right] = -\rho_{i,j} \quad (4.22)$$

The left hand side of this equation is the Laplacian operator.

Since the right hand side contains a non-linear potential term due to the Boltzmann expression for the electrons, we apply the Newton-Raphson scheme for the solution. The Newton-Raphson scheme applied to a function  $N(\phi)=0$ , is [Hockney and Eastwood, 1989],

$$\left( \frac{\partial N}{\partial \phi} \right)^t \phi^{t+1} = -N^t + \left( \frac{\partial N}{\partial \phi} \right)^t \phi^t \quad (4.23)$$

In our case,  $N$  is of the form,  $N = \nabla^2 \phi - c_1 \exp(\phi/T) + c_2 = 0$ . Since  $\partial N / \partial \phi = \nabla^2 - (c_1/T) \exp(\phi/T)$ , we must solve the following for the potential at iteration  $t+1$ ,

$$\left(\nabla^2 - \frac{\bar{n}_{\infty} \exp(\bar{\phi}^t/\bar{T}_e)}{\bar{T}_e}\right) \bar{\phi}^{t+1} = \bar{n}_{\infty} \left(1 - \frac{\bar{\phi}^t}{\bar{T}_e}\right) \exp\left(\frac{\bar{\phi}^t}{\bar{T}_e}\right) - \bar{n}_i \quad (4.24)$$

where the Laplacian is given by the left hand side of Eqn. (4.22).

An Alternate Direction Implicit (ADI) scheme is used to solve Eqn. (4.24) [Press *et al*, 1989; Anderson *et al*, 1984]. Unlike point iterative schemes such as Gauss-Seidel, or Successive-Over-Relaxation (SOR), ADI schemes sweep in alternating directions across the computational domain and update an entire row or column simultaneously by solving tridiagonal systems of equations. The ADI scheme is computationally more intensive than point iterative schemes, but its convergence rates are much faster. Thus, ADI is in general, superior to point iterative schemes.

To apply the ADI scheme, consider Eqn. (4.24) written in finite difference form with a template as shown in Figure 4.7. We have,

$$A_{i,j}^W \phi_{i+1,j}^{t+1} + A_{i,j}^E \phi_{i-1,j}^{t+1} + A_{i,j}^U \phi_{i,j+1}^{t+1} + A_{i,j}^L \phi_{i,j-1}^{t+1} + A_{i,j}^C \phi_{i,j}^{t+1} - \frac{\bar{n}_{\infty} \exp(\phi_{i,j}^t/T_{i,j})}{T_{i,j}} \phi_{i,j}^{t+1} = \bar{n}_{\infty} \exp(\phi_{i,j}^t/T_{i,j}) \left(1 - \frac{\phi_{i,j}^t}{T_{i,j}}\right) - \bar{n}_i \quad (4.25)$$

where the coefficients  $A$  are functions of the grid discretization. This equation can be recast into "delta" formulation where,  $\Delta\phi_{i,j} = \phi_{i,j}^{t+1} - \phi_{i,j}^t$ . In addition, let,

$$A_{i,j}^{C*} = A_{i,j}^C - \frac{\bar{n}_{\infty} \exp(\phi_{i,j}^t/T_{i,j})}{T_{i,j}} \quad (4.26)$$

Thus we have,

$$\begin{aligned} & A_{i,j}^W \Delta\phi_{i+1,j} + A_{i,j}^E \Delta\phi_{i-1,j} + A_{i,j}^U \Delta\phi_{i,j+1} + A_{i,j}^L \Delta\phi_{i,j-1} + A_{i,j}^{C*} \Delta\phi_{i,j} \\ & = \omega \left[ -A_{i,j}^W \phi_{i+1,j}^t - A_{i,j}^E \phi_{i-1,j}^t - A_{i,j}^U \phi_{i,j+1}^t - A_{i,j}^L \phi_{i,j-1}^t - A_{i,j}^C \phi_{i,j}^t + \bar{n}_{\infty} \exp(\phi_{i,j}^t/T_{i,j}) - \bar{n}_i \right] \end{aligned} \quad (4.27)$$

where  $\omega$  is an over-relaxation parameter. The ADI scheme decomposes the left hand side of this equation into two operators corresponding to the two directions (three if in three-dimensions). Consider a computational grid of dimension  $N_z \times N_r$  where  $N_z$  and  $N_r$  are the number of grid points in the  $z$  and  $r$  directions respectively. First we sweep in the  $r$  direction from  $j=2$  to  $N_{r-1}$ , and at every  $j$ , solve the tridiagonal system for  $i=2$  to  $N_{z-1}$ ,

$$A_{i,j}^E \Delta\phi_{i-1,j} + A_{i,j}^{C*} \Delta\phi_{i,j} + A_{i,j}^W \Delta\phi_{i+1,j} = \text{RHS of (4.27)} \quad (4.28a)$$

Then we sweep in the  $z$  direction from  $i=2$  to  $N_{z-1}$ , and at every  $i$ , solve the tridiagonal system for  $j=2$  to  $N_{r-1}$ .

$$A_{i,j}^L \Delta \phi_{i,j-1} + A_{i,j}^{C*} \Delta \phi_{i,j} + A_{i,j}^U \Delta \phi_{i,j+1} = \text{RHS of (4.27)} \quad (4.28b)$$

The tridiagonal systems are solved with the standard Thomas algorithm for  $\Delta \phi_{i,j}$  [Anderson *et al.*, 1984]. The potential at each iteration is then updated by,  $\phi_{i,j}^{t+1} = \Delta \phi_{i,j} + \phi_{i,j}^t$ . To speed convergence, the non-linear Boltzmann term is updated after each directional sweep. Depending on the grid size, the over-relaxation parameter,  $\omega$ , is determined numerically to give optimal convergence for values between 1.5 and 2.0. To handle the spacecraft region which is within the computational domain, all coefficients are set to zero, except for  $A_{i,j}^{C*}$  which is set to one. Thus, effectively, the equation for the spacecraft interior is  $\Delta \phi = 0$ .

### Potential Boundary Conditions

The boundary conditions on the potential that are enforced are of two types: Dirichlet (potential specified) and Neumann (electric field specified). Figure 4.5 shows a schematic of the potential boundary conditions imposed on the boundaries of the computational domain. On all spacecraft surfaces, Dirichlet boundary conditions apply. The calculation of the floating spacecraft ground potential,  $\phi_{SC}$ , is discussed in Section 4.6. The thruster front is set to the accelerator grid voltage which is usually 100 to 300 V negative with respect to the spacecraft ground, and the solar array panels are taken to have a linear voltage distribution. Generally, solar arrays are negatively grounded on U.S. spacecraft so that the potential along the solar array is given by,

$$\phi_{SA}(r) = \phi_{SC} + \Delta \phi_{SA} \left( \frac{r - r_{top}}{L_{SA}} \right) \quad (4.29)$$

where  $L_{SA}$  is the length of the solar panel,  $r_{top}$  is the top of the spacecraft, and  $\Delta \phi_{SA}$  is the voltage drop across the array. On current satellites, voltage drops of 28 V are common, but voltages up to 150 V or more are planned for future arrays.

On the plume centerline, the normal slope of the potential is held at zero due to the axisymmetry. On all other boundaries, the normal derivative of the potential is also held at zero. With elliptic equations, the boundary conditions have a strong influence on the solution. However, due to Debye shielding, the influence of these far field boundary conditions is negligible. In Figure 4.8, we show a radial cut through the potential in the plume comparing a Neumann condition (with zero slope) at the boundary  $r=W$ , with a Dirichlet condition with potential set by the Boltzmann relation and quasi-neutrality,  $\phi = (kT_e/e) \ln(n_i/n_{e\infty})$ . Note that the effect of the two boundary conditions on the internal solutions is negligible. First order Neumann conditions are used on all the exterior boundaries for simplicity and robustness, i.e. at  $z=L$ ,  $\phi_i = \phi_{i-1}$  where  $i$  represents the grid index of the boundary. The delta formulation used to solve Poisson's equation is ideal for

the implementation of Dirichlet conditions, because  $\Delta\phi$  is zero on spacecraft surfaces.

As a test case for the Poisson solver, the potential in the sheath at a biased wall of potential  $\phi_w$  is computed. The analytical solution to the one-dimensional Poisson equation with Boltzman electrons and a fixed uniform background ion density is,

$$\phi = \phi_w \exp(-x/\lambda_D) \quad (4.30)$$

under the assumption that  $e\phi/kT_e \ll 1$ . In Figure 4.9, we compare computational and analytical results for various background ion densities. Here, the wall potential is 1 volt, and  $T_e=5$  eV. The ion density is varied from  $10^{10} \text{ m}^{-3}$  to  $10^{12} \text{ m}^{-3}$  to show how the sheath varies since the sheath thickness is proportional to the Debye length (1.7 cm to 17 cm). We can see that the numerical and analytical solution are almost identical for the smaller Debye length cases. However, for a density of  $10^{10} \text{ m}^{-3}$ , the Debye length is larger, and the potential is affected by the boundary condition at the right boundary (zero slope is enforced). Thus the numerical and analytical solutions are slightly different, but the overall agreement is still good. In actual plume simulations, the plasma densities are sufficiently high that the outer boundary conditions exert little influence as was seen in Figure 4.8. Nevertheless, care must always be taken that the outer boundaries are at an adequate distance.

#### 4.5 Electron Temperature Equation Solution

The electron temperature equation is a convection-conduction equation that is conduction dominated. Thus, it is strongly elliptic, even with the presence of the convective terms. It is also non-linear due to the temperature dependence of the thermal conductivity. Initial solution attempts with the ADI scheme above gave poor performance in terms of convergence rates and overall accuracy, and it was decided to turn to a more sophisticated scheme. The scheme employed was a Generalized Minimal Residual Method (GEMRES) coupled with an Incomplete Cholesky Preconditioner, which was implemented in numerical routines, called NSPCG (for Nonsymmetric Preconditioned Conjugate Gradient) which is part of the ITPACK software [Oppe *et al*, 1988] that is in the public domain. This solution technique was used successfully to solve the potential field in ionospheric plasma cloud simulations [Gatsonis, 1991], and is very stable and robust.

We begin by non-dimensionalizing the electron temperature equation,

$$\frac{3}{2}n_e \mathbf{v}_e \cdot \nabla kT_e + p_e \nabla \cdot \mathbf{v}_e = \nabla \cdot (\kappa_e \nabla T_e) - 3 \frac{m_e}{m_i} v_e n_e k(T_e - T_H) + \mathbf{j}_e \cdot \mathbf{E} \quad (4.31)$$

consistent with other non-dimensionalizations. Lengths are non-dimensionalized with respect to the reference Debye length, the electron collision frequency is non-

dimensionalized with the electron plasma frequency, the electric field as in Eqn. (4.4) and,

$$\tilde{T}_{e,H} = \frac{T_{e,H}}{T_{eo}}, \tilde{v}_e = \frac{v_e}{\sqrt{\frac{kT_{eo}}{m_e}}}, \tilde{n}_e = \frac{n_e}{n_o} \quad (4.32)$$

Since we are using cylindrical coordinates  $(r, z)$ , we multiply the temperature equation by  $r$  to remove any singularity at the origin. After dividing by  $\kappa_e$  for simplification, the resulting equation is,

$$\begin{aligned} \tilde{r} \left[ \frac{\partial^2 \tilde{T}_e}{\partial \tilde{r}^2} + \frac{\partial^2 \tilde{T}_e}{\partial \tilde{z}^2} \right] + \left( 1 + \tilde{r} \frac{\partial \ln \tilde{\kappa}_e}{\partial \tilde{r}} \right) \frac{\partial \tilde{T}_e}{\partial \tilde{r}} + \tilde{r} \left( \frac{\partial \ln \tilde{\kappa}_e}{\partial \tilde{z}} \right) \frac{\partial \tilde{T}_e}{\partial \tilde{z}} = \frac{3}{2} \frac{\tilde{r} \tilde{n}_e}{\tilde{\kappa}_e} \left[ \tilde{v}_{ez} \frac{\partial \tilde{T}_e}{\partial \tilde{z}} + \tilde{v}_{er} \frac{\partial \tilde{T}_e}{\partial \tilde{r}} \right] \\ + \frac{\tilde{n}_e \tilde{T}_e}{\tilde{\kappa}_e} \left[ \frac{\partial}{\partial \tilde{r}} (\tilde{r} \tilde{v}_{er}) + \tilde{r} \frac{\partial \tilde{v}_{ez}}{\partial \tilde{z}} \right] + 3 \left( \frac{m_e}{m_i} \right) \frac{\tilde{r}}{\tilde{\kappa}_e} \nabla_e \tilde{n}_e (\tilde{T}_e - \tilde{T}_H) + \frac{\tilde{r} \tilde{n}_e}{\tilde{\kappa}_e} [\tilde{v}_{er} \tilde{E}_r + \tilde{v}_{ez} \tilde{E}_z] \end{aligned} \quad (4.33)$$

The Laplacian terms are finite-differenced as (assuming all non-dimensionalized values),

$$\frac{\left( \frac{T_{i+1,j} - T_{i,j}}{z_{i+1} - z_i} \right) - \left( \frac{T_{i,j} - T_{i-1,j}}{z_i - z_{i-1}} \right)}{(z_{i+1} - z_{i-1})/2} + \frac{\left( \frac{T_{i,j+1} - T_{i,j}}{r_{j+1} - r_j} \right) - \left( \frac{T_{i,j} - T_{i,j-1}}{r_j - r_{j-1}} \right)}{(r_{j+1} - r_{j-1})/2} \quad (4.34)$$

and the convective terms are central differenced. Since the convective terms are weak compared to the conduction terms, there was no difference in the solution whether they were upwinded or central differenced. The resulting finite-difference equation for each grid point  $i, j$  can be written as,

$$A_{i,j}^W T_{i+1,j} + A_{i,j}^E T_{i-1,j} + A_{i,j}^U T_{i,j+1} + A_{i,j}^L T_{i,j-1} + A_{i,j}^C T_{i,j} = S_{i,j} \quad (4.35)$$

where  $S_{i,j}$  is the source/sink energy term.

In order to utilize standard numerical matrix solution packages, we must represent this system of equations in matrix form as  $Ax=b$ . If the computational grid is  $N_z \times N_r$  where  $N_z$  and  $N_r$  are the number of grid points in the  $z$  and  $r$  directions respectively, we see that the matrix  $A$  will be  $(N \times N)$  where  $N = (N_z - 2)(N_r - 2)$  is the number of interior grid points. In full matrix form, we have,

$$\begin{bmatrix} A_{1,1} & \cdots & A_{1,N} \\ \vdots & \ddots & \vdots \\ A_{N,1} & \cdots & A_{N,N} \end{bmatrix} \begin{bmatrix} T_{2,2} \\ \vdots \\ T_{N_z-1, N_r-1} \end{bmatrix} = \begin{bmatrix} S_{2,2} \\ \vdots \\ S_{N_z-1, N_r-1} \end{bmatrix} \quad (4.36)$$

where each row of  $A$  has only five non-zero elements. The solution vector  $\mathbf{x}$ ,  $(T_{i,j})$ , is mapped into a one-dimensional vector with the following order:  $L = (i-1) + (j-2)(N_z-2)$ . Thus  $T_{i,j}$  is mapped into  $T_L$ , with  $T_{2,2}$  mapping to  $T_1$  and  $T_{N_z-1,N_z-1}$  mapping to  $T_N$ . For efficient storage of the coefficient matrix  $A$ , the non-zero elements can be compressed into an  $(N \times 5)$  matrix as,

$$\begin{bmatrix} A_{1,1} & \cdots & A_{1,5} \\ \vdots & \vdots & \vdots \\ A_{irow,1} & \cdots & A_{irow,5} \\ \vdots & \vdots & \vdots \\ A_{N,1} & \cdots & A_{N,5} \end{bmatrix} \quad (4.37)$$

where for every grid point  $(i,j)$ , we have,

$$\begin{aligned} irow &= L(i,j) \\ A_{irow,1} &= A_{i,j}^C \\ A_{irow,2} &= A_{i,j}^W \\ A_{irow,3} &= A_{i,j}^U \\ A_{irow,4} &= A_{i,j}^E \\ A_{irow,5} &= A_{i,j}^L \end{aligned} \quad (4.38)$$

Lastly, a pointer scheme that will relate the column index of the reduced coefficient array to the full  $N \times N$  array, is given by,

$$\begin{aligned} P_{irow,1} &= L(i,j) \\ P_{irow,2} &= L(i+1,j) \\ P_{irow,3} &= L(i,j+1) \\ P_{irow,4} &= L(i-1,j) \\ P_{irow,5} &= L(i,j-1) \end{aligned} \quad (4.39)$$

Since our computational domain has a spacecraft within which no values are computed, for the points inside the spacecraft, all matrix elements are zero, except for  $A_{ij}^C=1$ .

A full flowchart of the overall numerical simulation is provided in Appendix A. However, at this point, it should be mentioned that the solution of the temperature equation requires iteration with Poisson's equation since the electron density is related to both the potential and the temperature.

### Temperature Boundary Conditions

To implement boundary conditions in this matrix scheme, we must incorporate them into the coefficient matrix,  $A$ . Figure 4.5 displays temperature boundary conditions on the

computational domain. We first consider Dirichlet conditions, and then Neumann. Let us consider the situation at boundary  $r=W$  where  $T=T_o$ ; extensions to all other boundaries are straightforward. The finite difference equation, Eqn. (4.35), becomes,

$$A_{i,j}^W T_{i+1,j} + A_{i,j}^E T_{i-1,j} + A_{i,j}^L T_{i,j-1} + A_{i,j}^C T_{i,j} = S_{i,j} - A_{i,j}^U T_o \quad (4.40)$$

where the right hand incorporates the boundary condition. On other boundaries, the same procedure is followed.

For Neumann conditions, if the slope at  $r=W$  is given by  $\chi$ , i.e.,

$$\frac{\partial T}{\partial r} = \chi \quad (4.41)$$

then the first order accurate finite difference form is,  $T_{i,Nr} = T_{i,Nr-1} + \chi \Delta r$ . Eqn. (4.35) accordingly becomes,

$$A_{i,j}^W T_{i+1,j} + A_{i,j}^E T_{i-1,j} + A_{i,j}^L T_{i,j-1} + (A_{i,j}^C + A_{i,j}^U) T_{i,j} = S_{i,j} - A_{i,j}^U \chi \Delta r \quad (4.42)$$

## 4.6 Spacecraft Floating Potential

Submerged in the ambient space plasma environment, a spacecraft will float to a potential such that the electron and ion currents will balance, i.e., from charge conservation,  $I_e(\phi) + I_i(\phi) = 0$ . The operation of an ion thruster will significantly modify the surrounding plasma environment, and the currents from this plasma must be taken into account when computing the spacecraft's floating potential. In reality, many complex phenomena such as secondary-electron emission, and photo-electron emission from the spacecraft surfaces must also be taken into account for the overall current balance depending whether the spacecraft is in sunlight or darkness, and sophisticated models such as NASCAP [Katz *et al*, 1977] and POLAR [Katz *et al*, 1989] exist for such purposes. Our goal here is to qualitatively demonstrate a major impact ion thruster operation will have on the spacecraft floating potential; namely, the collapse of the sheath around the spacecraft, and the alleviation of severe negative biasing due to highly energetic ambient electrons. Below, we present the rudiments of spacecraft charging theory that are used for this calculation.

Consider a spacecraft of current collecting surface area  $A_{SC}$  in a plasma of electron temperature  $T_{e\infty}$ , and density  $n_{\infty}$ . The ion current collected is the sum of the ambient thermal current and a ram component which is important in LEO,

$$I_{i\infty} = \frac{en_{\infty}}{4} \sqrt{\frac{8kT_{e\infty}}{\pi m_i}} A_{SC} + en_{\infty} V_{SC} A_{ram} \quad (4.43)$$

where  $A_{ram}$  is the ram current collecting area and  $V_{SC}$  is the relative spacecraft velocity



through the plasma. Notice that the electron temperature is used for the ion velocity, because the ions falling through the sheath around the spacecraft are accelerated by a pre-sheath to the ion acoustic velocity which is based on the electron temperature. Neglecting photo-electron and secondary electron effects in this simple analysis, the electron flux from the ambient plasma to the spacecraft is composed entirely of a thermal component since the electron thermal velocity is much higher than the spacecraft velocity,

$$I_{e\infty} = \frac{-en_{\infty}}{4} \sqrt{\frac{8kT_{e\infty}}{\pi m_e}} \exp\left(\frac{e\phi_{SC}}{kT}\right) A_{SC} \quad (4.44)$$

where  $\phi_{SC}$  is the floating spacecraft potential which will be negative to repel enough of the highly mobile electrons so that the electron current balances the ion current. Equating the electron and ion current yields this spacecraft floating potential,

$$\phi_{SC} = \frac{kT_{e\infty}}{e} \ln \left( \sqrt{\frac{m_e}{m_i}} + \frac{4 V_{SC}}{\sqrt{\frac{8kT_{e\infty}}{\pi m}}} \frac{A_{ram}}{A_{SC}} \right) \quad (4.45)$$

In LEO conditions,  $T_{e\infty}=0.1$  eV,  $V_{SC}=8000$  m/s, and the ions are predominantly monoatomic oxygen. Taking the simple case of a sphere,  $A_{ram}/A_{SC} = 1/4$ , the floating potential is about -0.3 V. For GEO conditions, the spacecraft is stationary with respect to the ambient plasma which is highly energetic, especially during geomagnetic storms, due to high energy particles from space and is mostly composed of hydrogen [Jursa, 1985]. With  $V_{SC}=0$ , and  $T_e=1$  keV, the floating potential will be about -3750 V. It should be mentioned that the GEO plasma actually consists of multiple species, each with a separate electron temperature, so that this potential is a simple estimate.

This is the potential that a passive spacecraft will float to. However, the operation of an ion thruster will significantly modify the plasma environment surrounding the spacecraft. The ion and electron fluxes from the thruster-produced CEX plasma must now be considered. The total ion current to the spacecraft now becomes,

$$I_i = I_{i\infty} + \int_{SC} \mathbf{j}_{i\text{ cex}}(\phi) \cdot d\mathbf{A} - I_b \quad (4.46)$$

which includes the ambient ion flux, the ion current from the CEX plasma surrounding the spacecraft which must be computed numerically from the CEX ion particles, and the thruster beam current. Similarly, the total electron current to the spacecraft becomes,

$$I_e = I_{e\infty} + \int_{SC} \frac{en_p \bar{C}_e}{4} \exp\left(\frac{e(\phi_{SC}-\phi_p)}{kT_{ep}}\right) \hat{n} \cdot d\mathbf{A} - I_{neut} \quad (4.47)$$

which includes the ambient electron flux, the electron current from the CEX plasma, and

the neutralizer electron current emitted,  $I_{neut}$ . The electron current from the CEX plasma must be computed numerically by evaluating plasma properties at the edge of the sheath ( $n_p, \phi_p, T_{ep}$ ) around the spacecraft. The sheath potential drop is  $\phi_{sc} - \phi_p$ , where the spacecraft potential is computed again from equating electron and ion currents. The resulting equation is solved with a bisection technique.

The effect of the CEX plasma surrounding the spacecraft will be seen to be most dramatic in GEO where a passive spacecraft charges to very negative voltages due to the highly energetic ambient electrons. Not only can the entire spacecraft float to such potentials, but dielectric surfaces can differentially charge, and arcing can occur causing damage to the spacecraft. When the ion thruster is operating, there are two mechanisms that are available to raise the spacecraft potential from negative kilovolt potentials to values close to zero. One, is the presence of the CEX plasma that presents a large source of ions to neutralize the electron current. In addition, the CEX plasma, due to its enhanced electrical conductivity, acts as a conduit to channel electrons emitted by the neutralizer away from the spacecraft. What is important for the spacecraft floating potential is the global current balance. It may very well be, that the beam ion and electron neutralizer currents are not exactly the same, but that the neutralizer emission current is slightly higher to offset the ambient electron currents to the spacecraft. It appears that the neutralizer emission current is set "automatically" (i.e. the plasma potentials adjust) by the coupling potentials to the beam. Indeed, during the SERT II flight in a highly polar orbit, it was observed at times that neutralizer emission currents were higher than the beam ion currents [Jones *et al*, 1970]. Spacecraft potential control in GEO was successfully demonstrated when the reduction of kilovolt spacecraft potentials was observed during the operation of the cesium ion thrusters on the ATS-6 satellite that flew in 1974 [Olsen, 1978]. (After the thrusters failed, potential control was still achieved with only neutralizer operation.) In addition to global spacecraft charging, differential charging of surfaces can be alleviated due to the presence of a dense plasma that can discharge the surfaces.

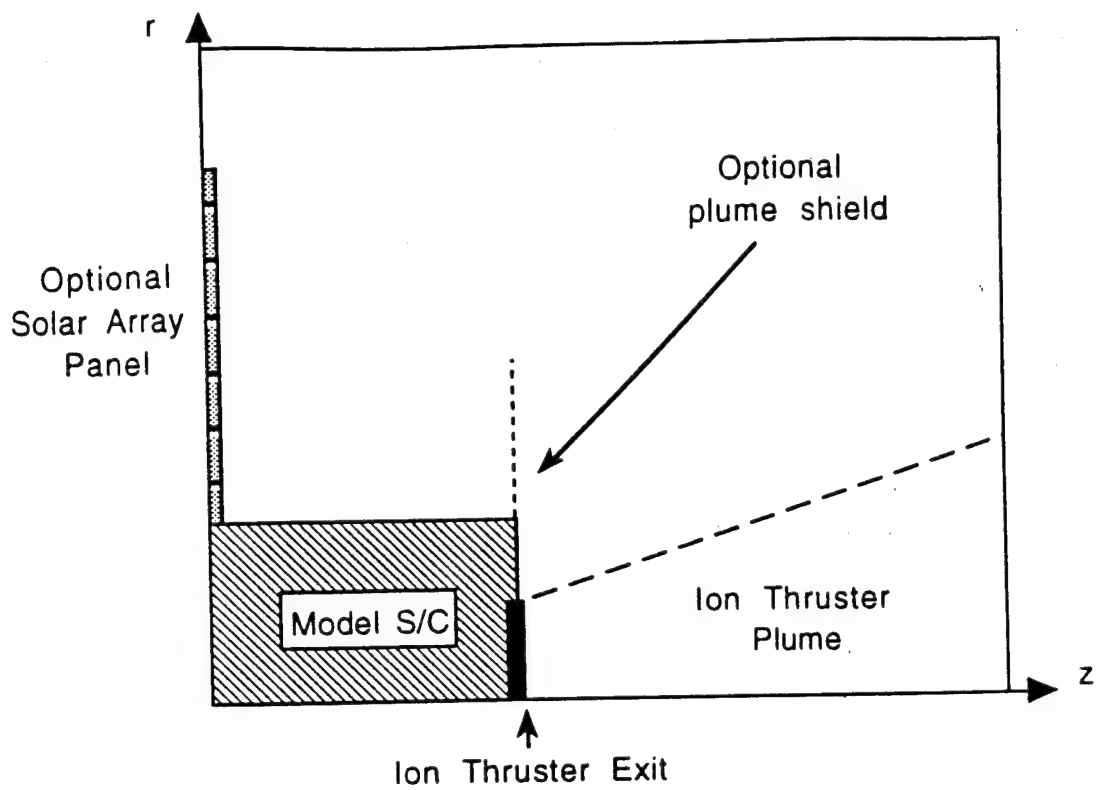


Figure 4.1 Schematic of computational domain

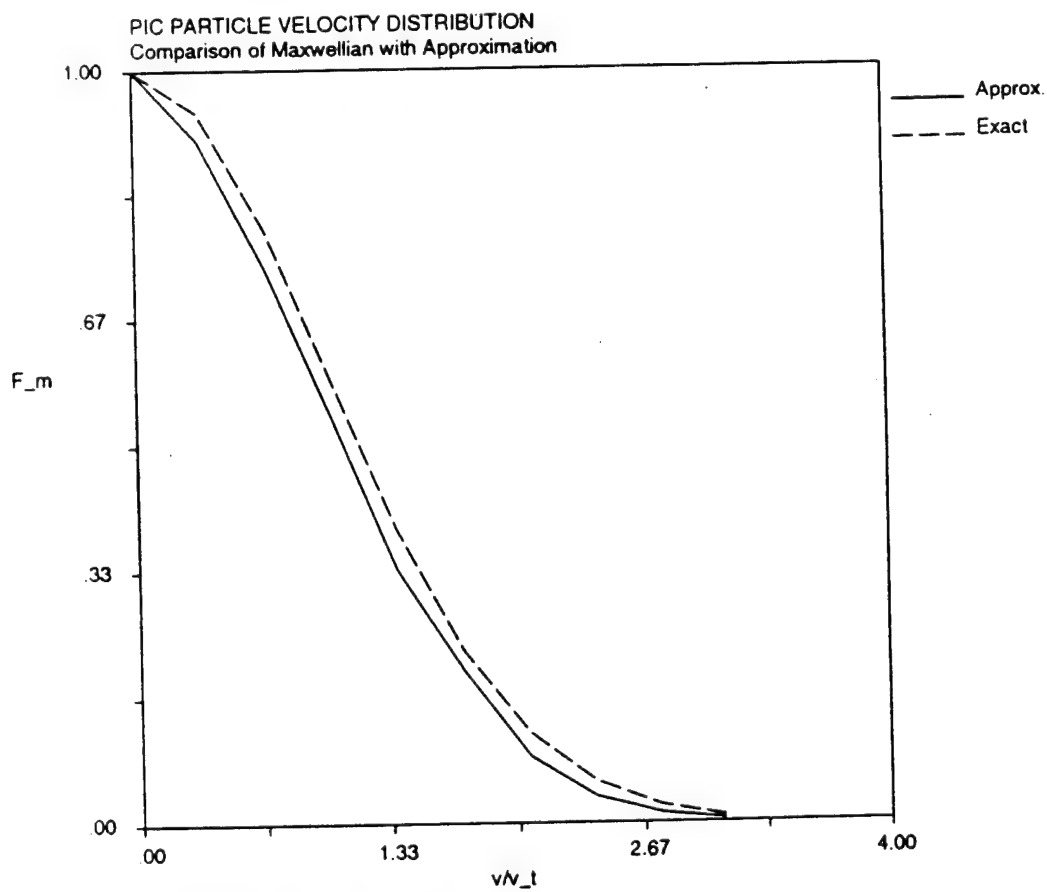


Figure 4.2 Comparison of Maxwellian velocity distribution with approximation used for particles

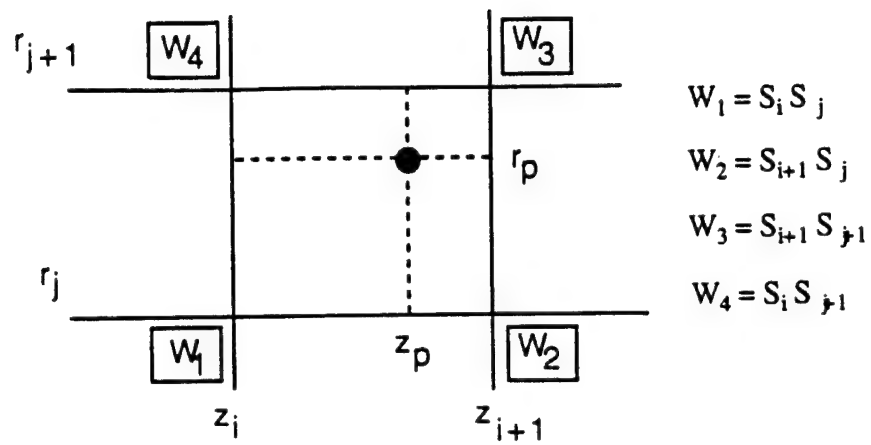


Figure 4.3 Grid cell particle weighting geometry

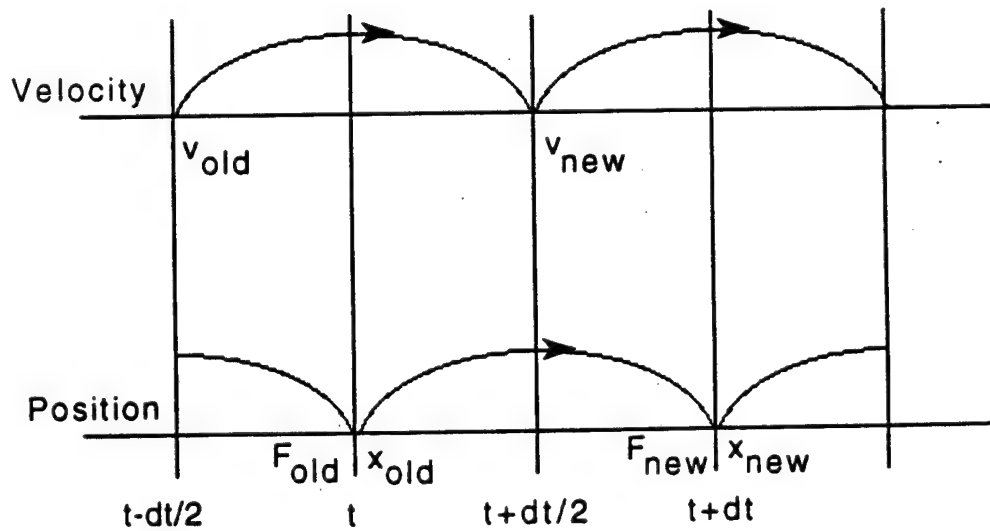


Figure 4.4 Schematic of leapfrog integration scheme

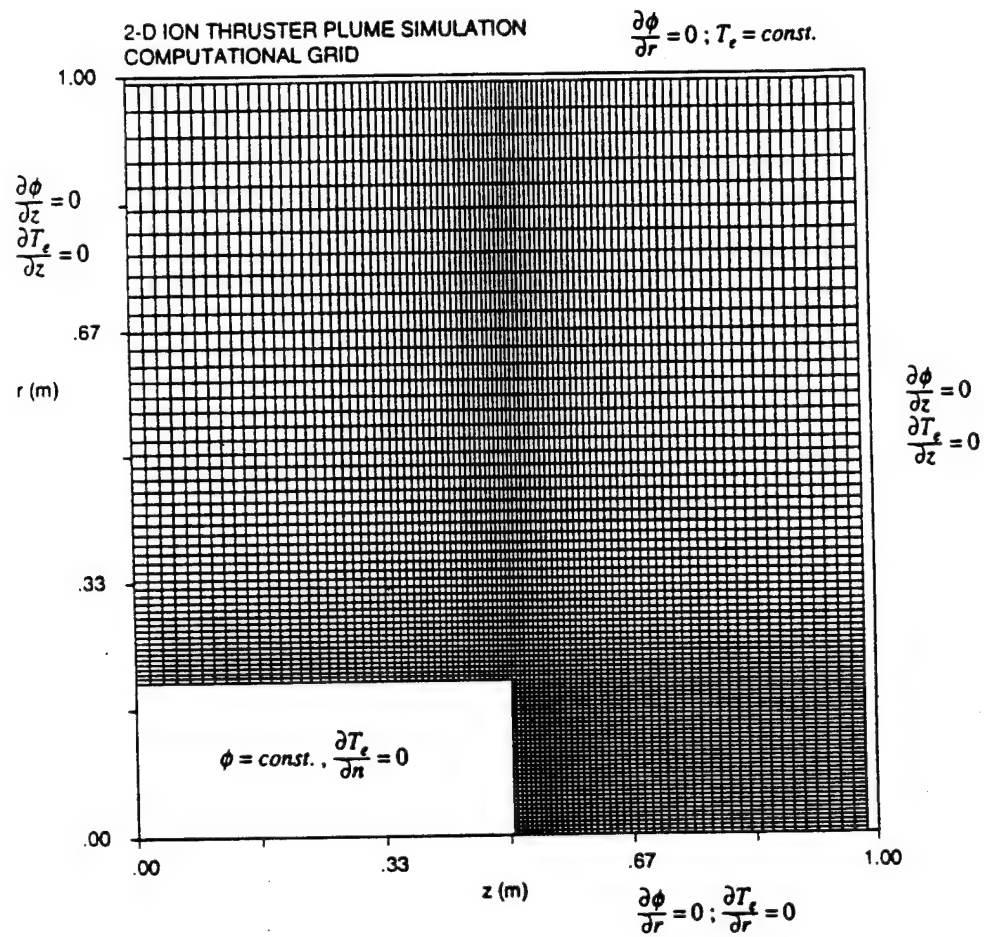


Figure 4.5 Computational grid

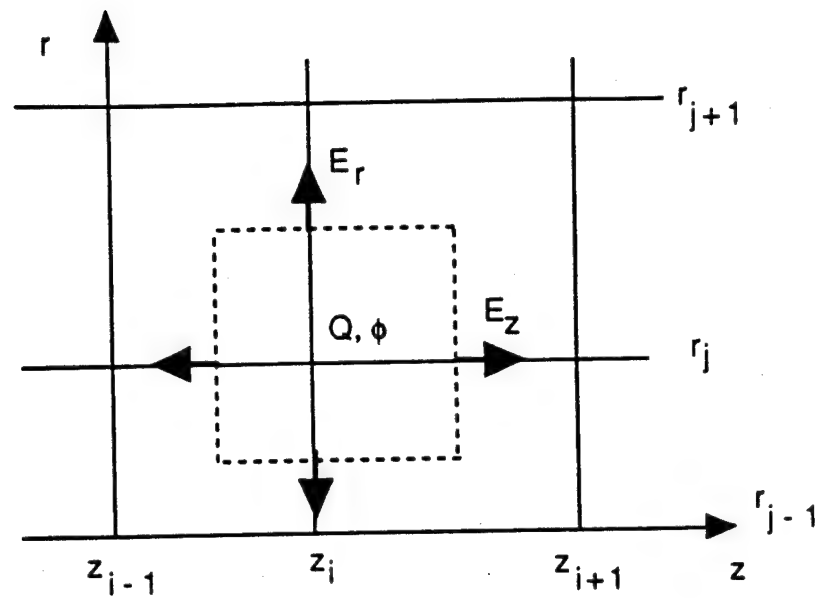


Figure 4.6 Gauss' law in cylindrical coordinates

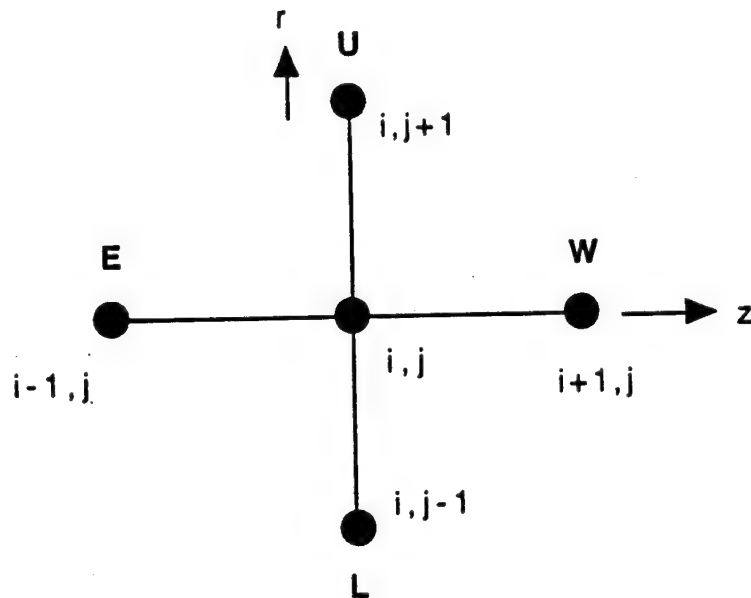


Figure 4.7 Template for Poisson's equation

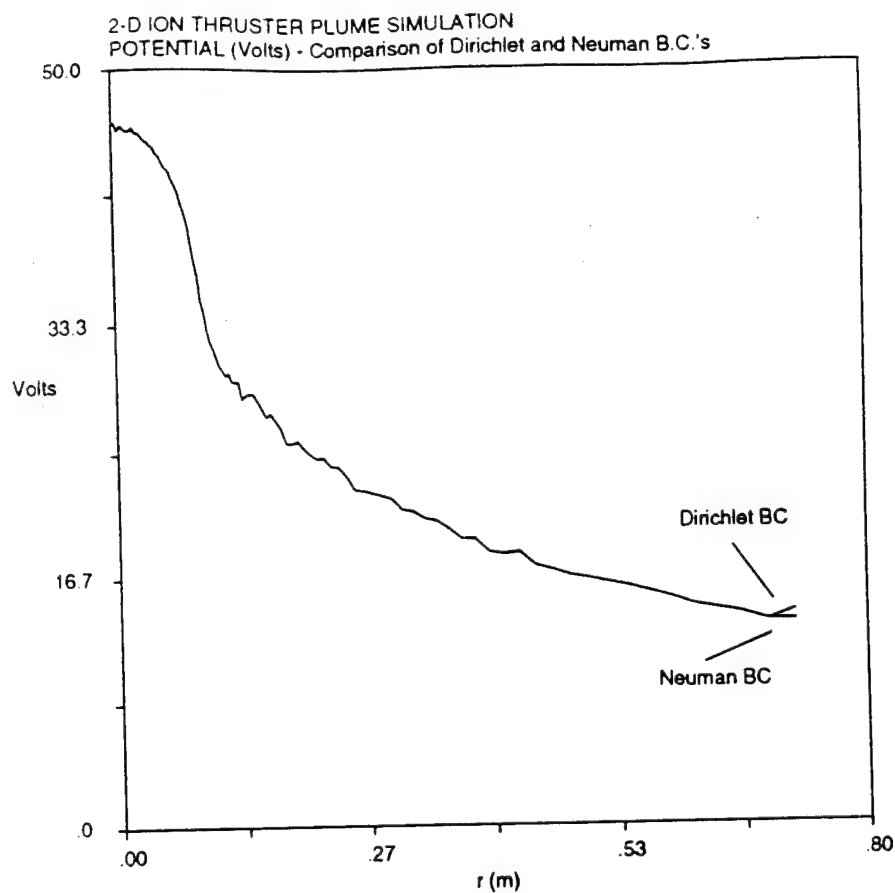


Figure 4.8 Comparison of far-field Neumann and Dirichlet boundary conditions on Poisson equation solution

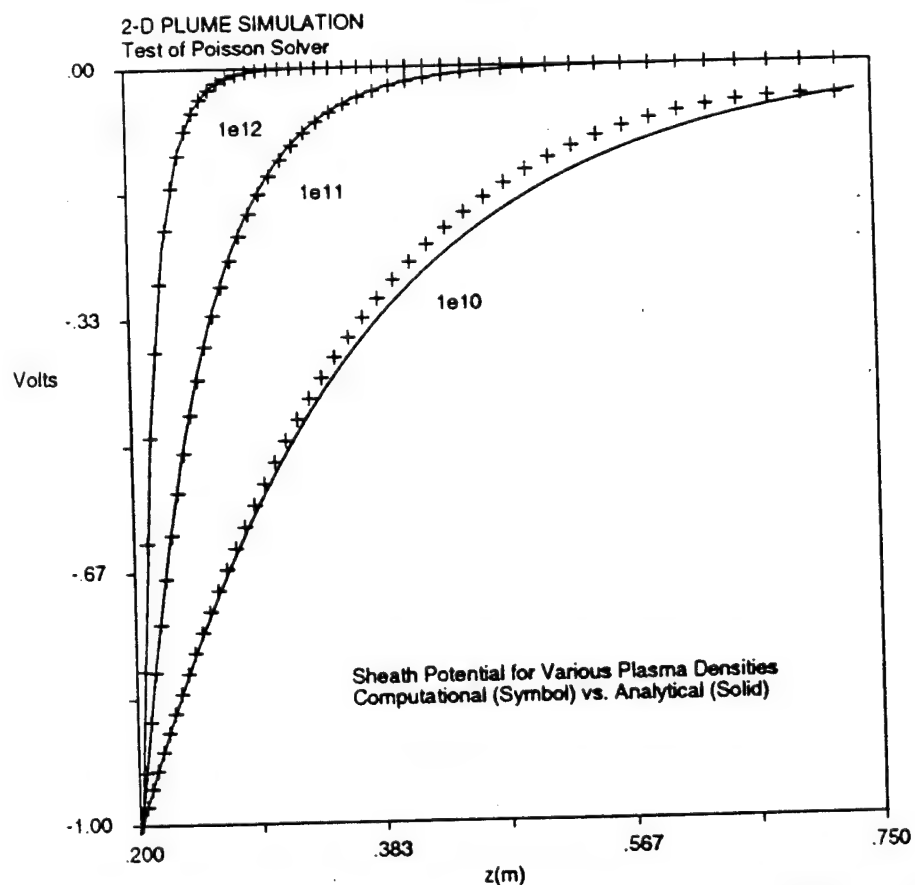


Figure 4.9 Comparison of one-dimensional analytical solution with two-dimensional numerical solution (along a wall) of Poisson's equation at biased wall for various background plasma densities

# Chapter 5

## Two-Dimensional Simulation Results

In this chapter, we present and discuss the two-dimensional results of the simulation model. We first compare results with experimental data to show the validity of the model, and investigate the effect of the background tank pressure in ground experiments, and the accelerator grid impingement current. The backflow contamination from NASA's current 30 cm xenon ion thruster is then investigated over the entire operating envelope of the thruster, and predictions for space operation are made. This thruster is currently being proposed for use on a number of planned space missions, and backflow contamination calculations are needed by spacecraft designers. Issues regarding the electron temperature are explored, as well as the effect of the spacecraft geometry on the backflow structure. The contamination from the sputtered molybdenum grid material is also examined. In addition, we demonstrate the effect of thruster operation on the spacecraft floating potential, and simulate the use of a plume shield to show the reduction in plume backflow unto a spacecraft. Lastly, comparisons are made between the numerical model results, and the simple analytical models that were presented in Chapter 2.

### 5.1 Preliminary Numerical Comments

The numerical model is run until steady state is reached when the number of particles in the simulation reaches a constant value which is determined when the production rate of particles in the plume balances the loss rate at the exterior domain boundaries. Particles are also lost to the spacecraft/thruster body in the form of the backflowing current and the grid impingement current. Figure 5.1 shows a time history of the number of particles in a typical simulation. The particle population linearly grows as the CEX plasma spreads from the thruster beam throughout the domain, and then asymptotically reaches a constant value -



in this case about a third of a million in about 4000 timesteps. Depending on the size of the domain and the CEX production rate, the maximum number of particles used is generally between 200,000 to 500,000. The time step is a fraction of the CEX ion plasma frequency, which generally is around  $10^6$  rad/s. Thus, each time step represents about 0.1  $\mu$ s of time.

An important quantity that we will use to quantify the backflowing CEX plasma, is the *backflow current*, which we define to be the integral of the CEX ion current density over some specified plane. In steady state, this quantity must be constant. Figure 5.2 shows a time history of the backflow current over a plane at  $z=0$  - in this case 30 cm behind the thruster exit plane. The values are negative, indicating current in the negative axial direction (backflowing current). The backflow current for a given thruster is determined by taking an average over 1000 or so timesteps at steady state to eliminate the effect of noise due to the particles' motion.

A very important quantity in PIC simulations, is the average total energy of the particles, where the kinetic and electrostatic potential energy of each particle is summed over the number of particles in the simulation,  $N_p$ ,

$$\langle E \rangle = \frac{\sum_{i=1}^{N_p} \frac{1}{2} m_i |\mathbf{v}_i|^2 + e \phi_i}{N_p} \quad (5.1)$$

Energy conservation must be monitored, analogously to mass conservation in fluid codes. Once steady state is achieved, this quantity must be constant, as shown in Figure 5.3 which is a time history. In addition, aside from the inherent fluctuations of the particles, the solution should not depend upon the number of particles used in the simulation. Of course, if too few are used, the solution will be extremely noisy. Figure 5.4 shows the backflow current over a plane above the thruster exit for a case that was run with various numbers of particles ranging from 175,000 to 340,000 (hence the macroparticle weighting was varied). The backflow current does not show significant dependence on the number of computational particles, which it must not. The variation is less than 1%.

Lastly, we mention that due to the noisy nature of particle simulations, it is useful to smooth the fluctuations due to this noise in plots of various quantities such as density. Some of the results such as ion density benefit aesthetically from smoothing. We apply a simple smoothing routine where for each grid point  $(i,j)$  we perform the following average,

$$\langle n \rangle_{i,j} = \frac{n_{i,j} + n_{i+1,j} + n_{i-1,j} + n_{i,j+1} + n_{i,j-1}}{5} \quad (5.2)$$

which can be applied recursively to increase the smoothing. This smoothing is only a post-processing operation, and is not used during the computation. Figure 5.5 compares the

effect of the smoothing that has been applied five times to the ion density from a typical simulation. The smoothing operation only eliminates the fluctuations; the average value is not changed. The particle noise of course can be reduced to a degree by increasing the number of particles in the simulation. However, computational resources place a limit on the total number of particles. In this example, about 300,000 particles have been used.

## 5.2 Comparison of Model to Experiments of Kaufman

*Kaufman* [1975] investigated the propellant CEX plasma produced by a 15 cm SERT II thruster operating with mercury as the propellant and dished grids that permitted higher beam currents than the original flat grids that were used in the 1970 space flight. The screen and accelerator potentials were maintained at +1000 and -500 volts<sup>†</sup> respectively throughout the investigation, yielding an ion beam velocity of 31,011 m/s. The thruster was operated at two operating conditions, summarized in Table 5.1. The ground tests were conducted in a vacuum facility that was 1.2 m in diameter and 4.6 m long. However, the thruster exit was apparently only 30 cm from the back tank wall. This is an important point in that the proximity of the chamber wall may have influenced plasma properties in the backflow region. A neutral background pressure around  $5 \times 10^{-6}$  Torr was maintained during thruster operation. This was achieved by diffusion pumps, and a liquid-nitrogen cooled liner that condensed residual mercury vapor in the tank. In addition, mercury has a low vapor pressure which aids considerably in maintaining low tank pressures. The CEX plasma produced by the thruster was surveyed with Langmuir probes for the plasma density and potential, and the electron temperature of the plasma was deduced from density - potential probe traces. Experimental error of measurements was assessed to be  $\pm 20$ -50% [*Kaufman*, 1994].

Table 5.1 *Kaufman* SERT II Hg 15 cm ion thruster operating conditions

	Case A	Case B
Beam Current $I_b$ (A):	0.63	0.38
Propellant Utilization $\eta_p$ :	0.85	0.51

An examination of radial density profiles through the beam of this particular SERT II thruster showed that the beam ion density was better described by a Gaussian radial profile, rather than a parabolic profile, as was seen in Figure 3.6. Thus, Eqn. (3.7) was used to model the beam ion density. Based on measurements of the beam ion density, a  $15^\circ$  beam

<sup>†</sup> Potentials were referenced to a target in the beam that was +60 V with respect to the tank walls

divergence angle was used, although it was never directly measured in the experiment.

The simulation domain was chosen so as to be able to capture the experimental data that was taken. Kaufman mapped the potentials and densities 40 cm downstream of the thruster, and 30 cm upstream, as well as 40 cm in the radial direction from the thruster plume centerline. The thruster body was 30 cm long and had a radius of 12 cm. Thus, the simulation domain was chosen to be 75 cm by 75 cm, with the thruster exit at  $z=30$  cm. The width of the domain was extended to 75 cm to ensure that the potential and temperature boundary conditions did not affect the solution in the radial direction.

As was noted in Chapter 3, an important input in the electron temperature model is the electron temperature in the beam at the thruster exit. Based on Kaufman's measurements, the electron temperature, independent of beam current, was about 5 eV. Thus, this value was used as the beam electron temperature at the thruster exit. For lack of any data, or estimates, we set the far field electron temperature ( $T_{e\infty}$  in Eqn. (3.37)) to be 0.1 eV, the value in LEO. The radial electron temperature boundary condition model then yields a value of 1.86 eV at the upper simulation boundary (0.75 m from the centerline). In addition, due to lack of knowledge of what potential the thruster body was held at or whether it was floating, the potential was fixed to be -1 V with respect to the background plasma which is assumed to be at 0 V. The background neutral mercury density was set to  $1.61 \times 10^{17} \text{ m}^{-3}$ , corresponding to a tank pressure of  $5 \times 10^{-6}$  Torr and a temperature of 300°K.

### 5.2.1 Plasma Density Comparisons

A contour map of the smoothed total ion density for the high current Case A is shown in Figure 5.6. Overlaid are variable temperature results (gray-scale), constant temperature ( $T_e=5$  eV) results (thin contours), and experimental data (bold contours in CGS units). Qualitatively, the agreement is quite good. Note that noticeable deviations between model and data take place in the beam; the plasma density measured within the beam is higher. This is due to the fact that ionization is important with mercury at electron temperatures above 4 eV. Figure 5.7 shows a comparison of CEX and ionization rates of mercury as a function of electron temperature using maximum beam densities. We can see that at 5 eV, ionization rates are slightly higher than CEX rates, effectively doubling the thermal ion production rate. However, we are interested in the plasma densities outside of the beam, and we can see that agreement is reasonably good, with constant temperature results yielding larger densities in the backflow region. It must be kept in mind that these experimental contours have up to a 50% error associated with them. We will discuss the

differences between the variable and constant temperature models in greater detail later in Section 5.2.4. Even though calculations with a constant temperature do not accurately reflect all the physical processes in the plume, if the backflow density is close to, or gives an upper bound to values obtained with the full temperature model, the reduced computational burden allows the constant temperature model to be more efficient for parametric studies.

In Figure 5.6, we can see that the total ion density (beam and CEX) falls from values of  $3\text{-}5 \times 10^{15} \text{ m}^{-3}$  in the beam to around  $3 \times 10^{12} \text{ m}^{-3}$  30 cm behind the thruster exit plane - a three order of magnitude decrease. In the beam, the beam ion plasma dominates, however, the CEX plasma still is on the order of  $10^{15} \text{ m}^{-3}$ , while outside the plume, the beam ion density is zero, and the CEX plasma is the sole component. In these simulations, we have set the background plasma density to  $10^{12} \text{ m}^{-3}$ , a value inferred from the Boltzmann relationship and experimental measurements of the beam potential. In Figure 5.8, we show the ratio of the CEX plasma density to the beam ion density. Note how the CEX plasma density is always less than the beam ion density, but is comparable in the beam close to the thruster. Most of the CEX ions are created within 2-3 beam radii downstream of the thruster. To show that these results are independent of the computational domain, Figure 5.9 shows contours of the ion density in a  $1.5 \text{ m} \times 1.5 \text{ m}$  domain in contrast to those shown in the  $0.75 \text{ m} \times 0.75 \text{ m}$  domain above. We can see that there is no difference in the solutions, and that the "bulge" in the CEX ion density protruding from the beam is not an artifact of the boundaries.

A contour map of the total ion density for the low current Case B is shown in Figure 5.10 similar to Figure 5.6. For Case B, the beam current is less by a factor of 0.6 compared to Case A, and therefore the beam ion density is smaller by the same factor since the beam ion velocity is the same for both cases. The propellant utilization efficiency is also less by the same factor. However, since the neutral density scales as  $I_b(1-\eta_p)/\eta_p$ , (Eqn.(3.13)), the neutral density is greater by a factor of 3.3. Since the CEX ion production rate is proportional to the product of the beam ion and neutral densities, the CEX production rate for Case B is higher by about a factor of two, and we expect the CEX ion densities to be higher, which is what we see both in the model results and in experimental data. In this case, the differences between constant and variable temperature models are more noticeable, with the constant temperature model giving higher densities than the variable temperature model. However, qualitatively, we see that the agreement is reasonably good in the backflow region. For example, the  $3 \times 10^{12} \text{ m}^{-3}$  experimental contour 20 cm behind the thruster exit plane falls directly between the variable and constant temperature model results.

It is interesting to look at the backflow currents, comparing Case A and B. We integrate the CEX ion current density over two planes. Plane 1 is at  $z=30$  cm, i.e. right at the thruster exit plane, extending from the thruster top to the upper boundary (a distance of 0.63 m), while plane 2 is at  $z=0$  cm, extending over the same radial distance. Table 5.2 shows the backflow current normalized by the beam current both for the variable and constant temperature models. An important observation is that for every 10,000 ions that are emitted from the thruster providing thrust, 1-10 ions will cross a plane 30 cm *behind* the exit of the thruster.

Table 5.2 Ratio of backflow current to beam current (variable / constant temperature)

	Case A	Case B
Plane 1 ( $z=30$ cm)	$1.3 \times 10^{-3} / 2.0 \times 10^{-3}$	$2.4 \times 10^{-3} / 5.3 \times 10^{-3}$
Plane 2 ( $z=0$ cm)	$3.0 \times 10^{-4} / 6.3 \times 10^{-4}$	$5.9 \times 10^{-4} / 1.8 \times 10^{-3}$

We now examine in closer detail the radial and angular distributions of the backflow plasma. Figure 5.11 shows a radial cut of the unsmoothed total ion density through the plume at an axial location 13 cm downstream from the thruster operating with conditions of Case A. Both constant and variable temperature simulation results are shown, and they are very similar, with the constant temperature giving slightly higher densities farther from the plume centerline. The total ion density falls from about  $5 \times 10^{15} \text{ m}^{-3}$  at the beam centerline, to below  $10^{13} \text{ m}^{-3}$  70 cm away. These densities are compared with experimental data in Figure 5.12. With  $\pm 50\%$  error bars on the data, we see that the numerical results are in good agreement.

Figures 5.13 and 5.14 show similar radial cuts, but closer to the thruster - at 7.5 cm downstream. Case A is shown in Figure 5.13, and Case B in Figure 5.14. Kaufman measured the total ion density at three radial points outside of the beam at 25, 30, and 35 cm, and they are shown for comparison. The variable temperature results are in moderately good agreement, falling within the error bars. However, in this region, the constant temperature model overestimates the CEX ion density by a factor of approximately two.

Kaufman also presented polar plots of total ion density. The total ion density along an arc at a distance of 34 cm away from a point 7.5 cm downstream of the thruster was measured. In Figure 5.15, we show the smoothed total ion density along this arc for both the variable and constant temperature models for Case A. For angles below  $30^\circ$ , the beam ion density is dominant, while for angles greater, the CEX plasma is the sole component. The CEX density becomes zero at about  $160^\circ$  where the radial line intersects the top of the thruster body. The increase in density as the angle increases around  $60^\circ$  is due to the

"ballooning" structure seen in the contour plots. In Figure 5.16, we show a comparison of this data with the experimental data. We see that agreement is moderately good within experimental error. Similar results for Case B are shown in Figures 5.17 and 5.18, and again, agreement with experimental data is moderately good. For both cases, we see that the constant temperature results yield higher densities at large angles from the plume. A general trend observed is that model results are higher than experimental results for angles less than 90-100°, while experimental results are higher in the backflow region. In addition, the experimental data indicates a slower decay in plasma density as a function of angle. However, it should be noted that the points in Figures 5.16 and 5.18 at 120° are only about 20 cm from the back tank wall. It is very possible that enhanced plasma density in the backflow region may be due to tank wall effects.

### 5.2.2 Plasma Potential Comparisons

Plasma potentials were also measured in Kaufman's experiments. To prevent CEX ions from being repelled from the vacuum tank walls, the chamber walls were biased negative with respect to the plasma to absorb them. The negative facility bias was established by operating a "target", which was a cooled plate that the beam impinged on at the far downstream end of tank, at +60 volts relative to the facility walls. It was assumed that due to the good electrical conductivity of the plasma, the plasma potential would be close to the target potential, and all plasma potentials were measured relative to the target potential. In the numerical simulations, we do not model the tank walls, nor a target. The plasma potential is assumed to be zero at "infinity" where the plasma density is a specified background. Based on the Boltzmann electron distribution, Eqn. (3.32), the potentials scale as,

$$\phi = \frac{kT_e}{e} \ln\left(\frac{n_e}{n_{\infty}}\right) \quad (5.3)$$

Figures 5.19a and b show the contour maps of the potential structure for the variable and constant temperature models respectively for Case A. Overlapped on each are the experimental data points. Within the beam close to the thruster, the potential is on the order of 40 V, and the largest potential gradients (hence electric fields), are at the radial edge of the beam. It is interesting to note that the potentials decay from the thruster exit more rapidly within the beam in the variable temperature case in comparison to the constant temperature case. This is because the electron temperature decreases as the plume expands in the variable temperature model, and the plasma potential scales with the electron temperature variations as well as density variations. In contrast, the potential only scales with density variations in the constant temperature case. We will discuss the differences



between the variable and constant temperature models in greater detail shortly. Similar results for Case B are shown in Figures 5.20a and b.

It is quite apparent that the numerical potential structure differs noticeably from experimental data, although the isothermal model gives better agreement. This is suggestive that in ground experiments, the presence of the facility walls may play an important role in the potential distribution, and perhaps to a certain degree, the electron temperature. Due to the negative bias on the walls, the electrons from the thruster are repelled, and it is quite likely that secondary electron emission from the tank walls occurs which may alter the temperature near the walls. No direct electron temperature maps were measured; however, the electron temperature in various regions of the plume was inferred from potential-density characteristics, which we shall examine shortly.

In addition, the bending structure in the measured potential structure (20 V contour in Case A and 15 V contour in Case B) is indicative of some wall interaction effect, since there is no physical mechanism that would suggest that the potential should bend as such. Indeed, for a purely isothermal situation, contours of constant potential are lines of constant plasma density, and such an effect is not present in the measured density maps. Due to the presence of such effects, the computed potential contours do not agree as well as the density contours. However, the experimental error of  $\pm 20$ -50% must be kept in mind. A measured value of 10 V can be either 5 V or 15 V, which causes considerable spread in the experimental data. However, since the electric field is the physical mechanism that forces the CEX plasma into the backflow region, what matters for CEX propagation is the potential difference, and not the absolute value of the potential. Unfortunately, Kaufman never measured the potential with enough resolution to compute electric fields in the plume. Detailed measurements of electric fields and electron temperatures in the plume are extremely desirable, because they will enable closer comparison, and perhaps will shed light on the role of test chamber walls. It must be kept in mind that the electron temperatures computed in this work are based on simple boundary condition models, and the effects of walls are not included. In Section 5.3.2, we will compare numerical results with other experimental data that were taken in a tank that had twice the diameter (hence wall effects are expected to be weaker), and better agreement with plasma densities is found.

### 5.2.3 Electron Temperature Comparisons

We now examine the electron temperature which plays an important role in determining the potential in the plume. We begin by showing the electron temperature

maps computed in the simulation in Figures 5.21a and b for Case A and B respectively. The electron temperature has been set to 5 eV at the thruster front, and the far radial boundary is fixed at nearly 2 eV. We see that the electron temperature drops as the plume expands in both the axial and radial directions. The predominant temperature drop, however, is in the radial direction since heat is conducted well axially within the beam. What is noteworthy are the differences in temperature decay between Case A and B. Since the neutral to ion density ratio for Case B is over three times that of Case A, the electron thermal conductivity is affected. Figures 5.22a and b show the electron thermal conductivity for Case A and B respectively. The thermal conductivity for Case A is higher due to the higher plasma density, and hence heat can conduct better throughout the plume elevating the electron temperature.

Kaufman did not present similar spatial electron temperature measurements. However, based on probe potential-density measurements, the electron temperature can be inferred. In Figure 5.23a, we show both the computed and measured density versus potential characteristic for Case A. Error bars corresponding to  $\pm 20\%$  in potential and  $\pm 50\%$  in density have been added to the experimental data which has considerable scatter. We display both the isothermal and variable temperature results. For higher potentials corresponding to the beam ion density, the numerical results fall within the error bars of the experimental data, with the isothermal model yielding lower density values for a given potential. However, at lower densities corresponding to the CEX plasma, numerical values of the corresponding potentials are much lower as was seen in the contour plots.

The purpose of Figure 5.23a is to show the raw data. However, if the natural log of the density is plotted versus the potential, the slope of a line drawn through points on such a plot will yield the electron temperature for an isothermal plasma by virtue of Eqn. (3.32). Such a plot for Case A is shown in Figure 5.23b. Here, we have constructed a least-squares fit line to Kaufman's data which were measured for the CEX plasma, and deduce an electron temperature of 3 eV. Kaufman, in presenting his data, graphically drew a line with a slope of 2.5 eV. If we construct a least-squares fit line through all of the numerical points for the variable temperature case, we deduce a temperature of 4 eV. However, we can see that there are two distinct components of the computational result. There is a high density, high potential component that corresponds to the beam ions, and a lower density, lower potential component that corresponds to the CEX plasma. If we construct a line through the denser population, we have a temperature of 5 eV which corresponds to our electron temperature map in Figure 5.21a. For the lower density population, a least squares fit line gives a temperature of 2.6 eV which is in close agreement to Kaufman's 3 eV (or 2.5 in his plot). We also construct a line through the isothermal ( $T_e = 5$  eV) results,



and deduce a temperature of 4.9 eV (which is a check on this computation). Thus, we see that qualitatively, the electron temperatures in the CEX plasma are close to what were measured, although the actual points on the plots are quite different due to the different points of corresponding potential.

Similar results are shown for Case B in Figures 5.24a and b. A bulk of the numerical results fall within the experimental data which have a large amount of scatter. We also can identify two different energy components in the lower current case. A least squares fit line through all the variable temperature model points yields an average temperature of 3.1 eV. A similar line through the widely scattered experimental data gives a temperature of 4.0 eV, (although the correlation coefficient is only 0.55), whereas the line that Kaufman displayed through his data had a slope of 2.5 eV. The temperature of the lower density component is found to be 2.3 eV, and the higher density one is 3.8 eV. The temperature for the higher density component is lower than 5 eV since the temperature falls off more rapidly for Case B as was seen in Figure 5.21b. Lastly, we note that the slope of the line through the isothermal model results ( $T_e=5$  eV) is 5 eV which it must be.

#### 5.2.4 Discussion of Variable and Isothermal Temperature Models

As was mentioned earlier, we consider the isothermal model since the reduced physics decreases the computational time for a solution, thus allowing the model to be used more effectively for parametric studies. Typically, factors of at least three in execution speedup are achieved since the electron temperature equation does not have to be solved and iterated with Poisson's equation.

To understand differences between the isothermal and variable temperature models, it is necessary to examine phase space to see the velocity distributions of the CEX ions. These plots will also show distinctly how the CEX ions are accelerated into the backflow region. Intuitively, since the potential scales with the temperature, and the velocity of the CEX ions scales with the square root of the potential, there will be some effect on the ion velocities depending on the temperature model. In Figure 5.25a, we show a phase plot of velocity space comprising the radial and axial velocity components for the variable temperature model with Case A conditions. Along the horizontal axis, we plot the axial velocity, and along the vertical axis, the radial velocity. From this plot, we can distinguish two different populations. There is a low energy population that are the CEX ions created within the beam with a thermal velocity distribution, and there is a high energy population which are the CEX ions that have gained energy from being accelerated through the radial beam potential drop. We can see in the potential contour map in Figure 5.19a, that the

potential drop right at the beam edge is about 20 volts. This translates to an ion velocity of about 4400 m/s which is very close to what we see. The backflow propagation can be seen in the tail of the energetic distribution that has negative axial velocities. These are the CEX ions that are flowing backwards.

If we compare this figure with the isothermal results for Case A in Figure 5.25b, we see that the energy distribution is less diffuse. Now the electron temperature is constant, and the potential variations are only following density variations. In contrast, in the variable temperature model, the potential variations follow both density and temperature variations. Moreover, the backflowing species are more energetic in the isothermal model. The reason for this can be seen in Figure 5.26 which compares the radial electric field in the radial direction for both constant and variable temperature models. We can see at the beam edge that the electric field is larger for the isothermal case, thus giving the CEX ions a greater acceleration. Outside of the plume, the electric fields are quite comparable.

In Figures 5.27a and b, we show a phase plot displaying radial velocity versus radial distance from the plume centerline for Case A again. Figure 5.27a is for the variable temperature case, and Figure 5.27b is for the isothermal case. These figures clearly show the acceleration of the CEX ions by the radial potential gradient. Ions at the origin have a thermal velocity distribution, but as they travel outwards, falling down the beam potential drop, their radial velocity increases. We see that the average velocity of the ions in the variable temperature model is less than those in the isothermal model. In addition, we also see the more diffuse nature in the velocity distributions of the variable temperature model.

We can also examine axial velocity versus axial position of the CEX ions. Figures 5.28a and b show this aspect of phase space for the variable and isothermal models respectively for Case A. Recall that  $z=30$  cm is the front of the thruster exit. We see the CEX ions that are being propagated forward, although the average velocity is around 600 m/s, and also the backflow component that is reaching velocities up to 5000 m/s in the negative axial direction. Again, we see the more diffuse velocity spread of the variable temperature model.

Differences between the isothermal and variable temperature models are also highlighted if we examine the CEX ion current density,  $j_{cex}=en_{cex}v_{cex}$ , which incorporates both the density and the velocity of the CEX ions. In Figures 5.29a and b, we plot the magnitude of the CEX ion current density for variable and isothermal models for Case A. We can see that the CEX ion current density is higher for the isothermal model, notably in the backflow region. It is interesting to note how the CEX flow in the beam appears to be from a spherical point source centered about a thruster radius downstream of the thruster. However, this spherical distribution is affected by the potential structure outside of the

beam.

Lastly, we examine the backflowing CEX ion current density over the radial plane at  $z=0$ , to compare the differences between the variable and isothermal models for Case A. Figure 5.30 displays the results for the variable and isothermal models. We can see that the CEX ion current density for the isothermal case is about twice the level as for the variable temperature model, as we saw in Table 5.2. Thus, in comparison, the isothermal model gives a conservative estimate on the CEX plasma backflow with the benefit of considerable numerical savings since the electron temperature equation does not have to be solved.

### 5.2.5 Effect of Tank Background Pressure

As discussed in Chapter 3, the presence of a finite background pressure in test chambers has an effect on the plume backflow. When conducting ground tests, it is important to know how much of the actual current density, or density of the plasma is due to plasma that has been created by CEX reactions with the background neutral gas. In Figure 5.31, we compare the CEX ion current density contours for a case with a background neutral pressure of  $5 \times 10^{-6}$  Torr (Kaufman's test conditions), and a case with zero background pressure, i.e. space conditions. The isothermal model with the conditions of Case A are used. Grayscale contours are for results with background pressure, and black contours are for results without. We can see a noticeable reduction in the CEX current density without the presence of the neutral background. If we examine the CEX current density over the radial plane  $z=0$ , the ratio of the integrated CEX backflow current along this plane to the beam current is  $6.3 \times 10^{-4}$  with background pressure, compared to  $5.2 \times 10^{-4}$  without, which is about 20% greater. Thus, experimental measurements in ground tests would have to be adjusted accordingly in order to predict values during actual thruster operation in space, although a factor of 20% is most probably less than experimental accuracy.

### 5.2.6 Conclusions from Comparisons with Kaufman's Experiments

From our comparisons with Kaufman's experimental data, we have shown the validity of our numerical model in estimating the backflowing CEX ion plasma density. We have obtained reasonably good agreement with experimental density measurements, both in the structure and magnitudes. Differences that are observed are that experimental measurements of ion density in the beam are higher than in the model, most likely due to ionization. In the backflow region, at angles greater than  $110^\circ$  to the centerline, experimental densities are also higher, which may be due to the proximity of the testing

chamber walls. However, there are regions where the model results are higher than the experimental densities. These regions are 25-35 cm outside of the beam 7.5 cm downstream of the thruster exit, and are not in the backflow region. Overall, computational results and experiment do not deviate more than by a factor of two.

Comparisons with potential measurements are more difficult most likely due to the effects of facility walls. However, experimental values of the electron temperature of the CEX plasma agree well with the model. It must be noted that our numerical model is more suited for the space environment, since we do not include the effect of the test facility walls. Comparisons between the variable temperature model, and isothermal calculations show that the backflow CEX ion density and current density in the far backflow regions differ by about a factor of two, with the isothermal model giving the higher result. Thus, the isothermal model gives conservative estimates for backflow contamination.

Lastly, our comparisons included the effect of a background neutral density. We have demonstrated what ground tests can not do - remove this effect. Our comparisons, for this particular case, show that ground measurements will give about 20% higher values for the CEX plasma density due to CEX collisions between beam ions and facility neutrals.

### 5.3 Comparison of Model to Experiments of Carruth et al

Carruth, with others, investigated the propellant CEX flowfield of a 30 cm beam diameter 900-series Hughes mercury ion thruster using SHAG (small hole accelerator grid) optics in two different experiments. The first we will refer to as (C-B) [Carruth and Brady, 1981], and the second as (C-G-K) [Carruth et al, 1982]. The main objective of these experiments was to use the "end-effect" of a Langmuir probe to determine the flow angle of the CEX plasma. The "end-effect" is the term used to describe the phenomenon where the current collected by a Langmuir probe that is aligned with a flowing plasma is greater than if the probe is oriented at some other angle to the flow direction. Thus, at a given position in the CEX plasma flowfield, the flow direction of the plasma can be determined by sweeping the probe through various angles, and finding the angle where the current collected is maximum. The "end-effect" phenomenon was first reported by *Bettinger and Chen* [1968] to explain anomalous increases in the ion current collected when a cylindrical Langmuir probe on the Explorer 17 satellite was aligned with the satellite's direction of motion, and the associated probe theory was subsequently developed by *Hester and Sonin* [1970] and *Sanmartin* [1972].

The 30 cm mercury thruster was operated over a range of beam currents ranging from 1 A to 1.8 A in the first experiment, and it was found that the CEX plasma flow angle was

insensitive to the beam current. In the second experiment, the thruster was run at a fixed operating point of 1 A with a propellant utilization efficiency of 0.95. The screen potential of the thruster was fixed at 1100 V, yielding a beam ion velocity of 32,525 m/s. Both experiments were conducted within a vacuum chamber 2.1 m in diameter and 4.6 m long. The tank was cryopumped by a liquid nitrogen cooled liner, and the background pressure ranged from  $1\text{--}6 \times 10^{-6}$  Torr. In our simulations, a background pressure of  $3.5 \times 10^{-6}$  Torr with a temperature of 300°K is used.

No beam ion density profiles were measured in the experiments to suggest what type of beam ion density profile to use, i.e. parabolic, Gaussian, or other. However, the modern 30 cm Hughes thruster has a beam flatness parameter near 0.5 [Beattie and Matossian, 1992]. The beam flatness parameter is defined as the ratio of the average density over the maximum density for a given radial profile. For a parabolic profile, it can be easily shown that the flatness parameter is 0.67, while for a Gaussian with half width of beam radius, it is  $\sqrt{\pi/2} \text{Erfi}(1) = 0.75$ . Since the 30 cm Hughes thruster used in the Carruth experiments is a predecessor of the modern 30 cm Hughes thruster, we assume a parabolic radial profile for the beam ion density since the flatness parameter of 0.67 is closer to 0.5.

The CEX plasma flow angle was experimentally measured up to 51 cm both in the up and downstream directions of the thruster front at radial distances up to 66 cm from the plume centerline. Thus, the computational domain was chosen to be 1 m long and 75 cm wide. The thruster body was 50 cm long, and was 20 cm wide (half width). From other measurements by Gabriel and Kaufman [1982], the electron temperature in the beam ranged from 0.2 to 1 eV. The electron temperature at the thruster exit is taken to be 1 eV, and the same temperature and potential boundary conditions as with the Kaufman comparisons are used.

### 5.3.1 Flow Angle Comparisons

Based on the CEX ion velocities, CEX plasma flow direction vectors can be mapped out. In Figure 5.32, we show the CEX ion current density vector flowfield, with the vectors normalized so that only direction is indicated, and not magnitude. CEX ions that are created in the beam near the centerline do not see a strong radial electric field, and hence they are carried downstream by the axial potential gradient in the beam. However, as they move farther out radially in the beam, the radial potential gradient starts to turn the CEX ions towards the beam edge, and we can see that by the time the CEX ions reach the beam edge, they leave completely radially. Outside of the beam, at and behind the thruster exit plane, the electric fields turn the CEX ions towards the backflow direction. We can see that

CEX ions that are close to the top edge of the thruster body are turned back the most, and some are even pulled down toward the thruster body top. We also see directly at the thruster exit, the CEX ions are directly attracted back to the negatively biased accelerator grid, which constitutes the grid impingement current that will be examined more closely in Section 5.4.

In Figure 5.33, we show a vector plot of the electric field, normalized so that only direction is indicated. A comparison of Figures 5.32 and 5.33 clearly shows how the CEX ions are influenced by the electric field. Note how the electric field is almost completely radial at the beam edge even though the beam is divergent, and the almost completely axial electric field in the backflow direction  $90^\circ$  above the thruster exit. In addition, it is interesting to see the electric fields in the sheaths surrounding the thruster body that serve to accelerate CEX ions to the surfaces. Above the thruster body for  $z < 30$  cm, the electric field is noisy due to differencing the potential which is noisy since the CEX ion density is very low in that region. Radial cuts through the plume 10 cm downstream of the thruster, show the beam potential in Figure 5.34a, and the radial electric field in Figure 5.34b. We can clearly see the steep variation in the potential that gives rise to the large electric fields at the beam edge.

In the C-B experiments, the CEX plasma flow angles were measured at distances of 48 and 66 cm from the plume centerline. Measurements up to 51 cm in both the up and downstream directions were taken. In the C-G-K experiments, measurements only at 48 cm from the plume centerline were taken at locations from 30 cm upstream to 40 cm downstream. Experimental error on measurements was assessed to be  $\pm 2-5^\circ$  [Carruth, 1994]. We have done simulations with both variable and isothermal models, and the computed flow angles are shown in Figures 5.35a and b for radial distances of 47 and 65 cm respectively. The simulation results shown are displaced one cm with respect to the experimental data due to the computational grid structure. Measured values from the C-B and C-G-K experiments are superimposed on the computational results.

In the region behind the thruster exit, which is of most concern for contamination, we see that we have excellent agreement with experiment, with very slight difference between variable temperature and isothermal results. Differences can be attributed to the fact that with the isothermal model, the CEX ions are turned back more due to stronger electric fields. This is indeed the case; flow angles with the isothermal model are slightly higher ( $\sim 1-3^\circ$ ). However, for the downstream direction, we see that we do not have that good agreement with the C-G-K measurements, although there is good agreement with the C-B measurements. The cause for the discrepancy between the C-B and C-G-K measurements is not clear. We note that the closer the radial distance to the plume, the greater the turning



angle. At 50 cm behind the thruster front, the flow has turned up to  $155\text{-}160^\circ$  at  $r=47$  cm, whereas the flow has turned only to  $140\text{-}145^\circ$  at  $r=65$  cm. The flow leaves at  $90^\circ$  to the plume axis at about 10-20 cm downstream of the thruster, which gives the appearance of a point source located about one thruster radii downstream. However, the flow that enters the backflow region leaves from the beam much closer to the thruster. These backflowing ions leave radially, and are then turned back by the electric fields - giving the appearance that they originated from a point further downstream in the beam.

### 5.3.2 Plasma Density Comparisons

In the C-G-K experiments, the plasma density at a radial distance of 48 cm was measured from 30 cm in front of the thruster to about 40 cm behind the thruster. In Figure 5.36, we show the data points, along with model calculations at  $r=47$  cm for both variable and constant temperature models. We can see that there is very good agreement between model and experiment, with the constant temperature model giving slightly higher values again. Based on the experimental measurements, a uniform plasma background of  $10^{13} \text{ m}^{-3}$  was imposed in the simulations.

### 5.3.3 Effect of Tank Background Pressure

Lastly, we examine the effect of the tank background pressure on the CEX flow angle. Without the background neutrals, we expect the flow angles to be slightly less since the velocity distribution of the neutrals solely from the thruster is not completely isotropic, but is oriented predominantly downstream. This is indeed the case, as shown in Figure 5.37, where we compare the flow angles with and without the tank neutral background pressure. These results are at a distance of 65 cm from the plume centerline. The difference is not too significant, being less than  $5^\circ$ .

### 5.3.4 Conclusions from Comparison with Carruth et al Experiments

From our comparisons with Carruth's measurements of the CEX plasma flow angles, we have shown the validity of our numerical model in computing the flow angles of the CEX plasma. The model correctly captures the expansion of the CEX plasma. In addition, we also showed very good agreement again with comparisons of CEX plasma density measurements, with the computational results and experimental data showing the same trend. It must be noted that the Carruth experiments were held in a tank about twice the diameter as the Kaufman experiments, and hence one expects the effects of the test chamber

to be less. The differences between the variable and constant temperature model results of flow angle are very slight, with the isothermal model predicting 1-3° greater flow angles in the negative axial direction. The presence of the tank neutral background pressure is again seen to have an effect, but differences in the CEX plasma flow angle are not as significant as in the CEX current density.

## 5.4 Investigation of Accelerator Grid Impingement Current

As mentioned in Chapter 3, and as seen in Figure 5.32, CEX ions created immediately downstream of the thruster front can be attracted back to the negatively biased accelerator grid. These ions constitute what is measured in experiments as the accelerator grid impingement current. In addition to these CEX ions, there are other, but smaller, components to this current as well. There are highly divergent beam ions that might hit the grid, although with proper grid design, the number that do should be very small. There are also CEX ions created directly within the grids that impinge the grids. The problem of the accelerator grid impingement current has received much attention because the ions that strike the grid are falling under potential drops up to several hundred volts, and thus have enough energy to sputter the grid material. The presence of the sputtered grid material, typically molybdenum, presents a serious contamination hazard due to the metal's low vapor pressure and a sticking coefficient of order unity.

Detailed simulations of the CEX ion dynamics on the length scale of the grid separation distances have been performed by *Peng et al* [1990-1993]. In our simulations, we can not resolve such small length scales, nor do we model the complex grid aperture geometry. However, we can compute the accelerator grid impingement current on a plane representing the thruster accel grid due to the CEX ions that are created downstream of the thruster grids. We will run a case to compare our results with those of *Peng et al* for both ground and space based operation to see whether our model will yield reasonable values for the impingement current. In addition, among numerous ground measurements of grid impingement current over the years of ion thruster development, we will examine two recent experimental efforts and compare our computational results. In all these results, the tank background neutral gas temperature is assumed to be 300°K.

### 5.4.1 Comparison of Model to Computations of Peng et al

*Peng et al* [1993] computed the grid impingement current for the current NASA 30 cm ion thruster for both ground and space based operation. One of the thruster conditions studied corresponded to experimental conditions in a thruster life test at NASA/Jet



Propulsion Laboratory (JPL) [Brophy *et al.*, 1993] where krypton was used as the propellant. The thruster was operated with a beam current of 2.8 A and a beam voltage of 1050 V producing a beam ion velocity of 47,163 m/s. (Peng *et al.* use a screen voltage of 1517 V which seems to be the sum of the published screen voltage, 1050 V, and the accel voltage, -500 V). The propellant utilization efficiency based on the total mass flow rate is 82%. Based only on the discharge chamber flow rate (without the neutralizer), it is 93%. The accel grid was biased to -500 V, and a constant electron temperature of 1.5 eV was assumed by Peng *et al.* (it apparently was not measured).

The accel grid impingement current measured in the ground tests with an average tank pressure of  $2.85 \times 10^{-5}$  Torr, was 35 mA. In order to agree with this experimental value, Peng *et al.* had to adjust the beam ion density in their model to a value of  $1.3 \times 10^{15} \text{ m}^{-3}$ . They used a propellant utilization efficiency of 81%. Using this same beam ion density and propellant utilization, they computed an impingement current of 4.69 mA for space based operation. With our model, the beam ion density is computed to be  $4.2 \times 10^{15} \text{ m}^{-3}$  based on the beam current of 2.8 A and beam voltage of 1050 V. However, in order to achieve an impingement current close to the observed value, we must use a propellant utilization efficiency of 93% - the discharge chamber value. With this value, we compute the impingement current to be 39.8 mA which is within 14%. It is reasonable to use the higher propellant utilization efficiency since in this thruster, the neutralizer is placed outside of the beam slightly downstream and facing in the downstream direction. Thus, the neutral density from the neutralizer (with a cosine distribution), does not contribute significantly to the neutral density directly in front of the accel grid. Hence, the neutral density for CEX creation directly in front of the accel grid, is mainly due to the neutrals leaking from the discharge chamber. This is in contrast to some other thrusters where the neutralizer can be aimed directly into the beam, increasing the neutral density in the beam. If we do use a propellant utilization efficiency of 82%, we compute the impingement current in space to be 15.2 mA which is too high. Using the 93% propellant utilization value, we compute a space based impingement current of 4.42 mA which is in close agreement with the value of Peng *et al.* These results seem to imply that CEX production within the holes is a minor effect. In the work of Peng *et al.* [1992], it was found that about 98% of the grid impingement current was due to CEX ions created downstream of the accel grid.

#### 5.4.2 Comparison of Model to Experiments of Monheiser

Monheiser [1991] studied the grid impingement current of the 15 cm modified SERT II xenon thruster whose operating characteristics were listed in Table 3.1. The accelerator

grid was biased to -500 V. The grid impingement current was measured as a function of the tank background pressure which was varied from  $9 \times 10^{-6}$  to  $3.3 \times 10^{-6}$  Torr. Figure 5.38 shows the measured impingement current in mA for the various tank pressures. On the same plot, we show the computed results from the numerical model. The electron temperature was assumed constant at 5 eV.

Since this thruster was a research model, the neutralizer was attached to a flexible tube that could be positioned anywhere from inside the beam to 30 cm away from the thruster centerline, and it was directed in the plane perpendicular to the thrust axis. In addition, the mass flow rate to the neutralizer was very high compared to flight models. The mass flow rate was 50% of the main flow rate to the discharge chamber - normally it is usually around 5%. Thus, the neutral density from the neutralizer must be taken into account. In Table 3.1, the propellant utilization listed was based on the discharge chamber flow rate - 84%. Including the neutralizer flow rate decreases the propellant utilization to 64%. Calculations with both values are shown in Figure 5.38.

We can see that the computed impingement current is about 4-5 times less than the measured value, without the neutralizer neutrals, but only about 3 times less with the neutralizer neutrals included. One reason for the lower computational value is that our neutral model does not give a uniform density over the grids (see Figure 3.9a). In reality, the neutral density is relatively constant over the face of the thruster and would give a higher CEX ion production rate. Also, there possibly can be focusing effects in the potential due to the apertures of the grids. In addition, the tank density is based on a temperature of 300°K. In a cryogenically cooled tank, with lower temperatures, the density will be higher for a given pressure. However, it is observed that if we extrapolate both experimental and numerical values (with the neutralizer neutrals) to zero pressure (assuming linear variation for the experimental results), we arrive at about the same value. This may just be a fortuitous result.

Monheiser also computed the CEX ion grid impingement current based on the measured beam ion current density, and a detailed numerical model of the neutral density only from the discharge chamber. The values obtained, were about an order of magnitude less than the observed value. He did not account for the neutralizer neutrals. In addition, the integral of the measured beam ion current density over the thruster exit was 15% less than the beam ion current.

#### 5.4.3 Comparison of Model to Experiments of Beattie and Matossian

*Beattie and Matossian* [1992] studied the grid impingement current for the modern 30

cm xenon Hughes thruster. The thruster was operated with a current of 3.22 A, and the beam ion velocity was 41,395 m/s. The discharge chamber propellant utilization was 0.93, and the total utilization was 0.88. There was no mention of the potential of the accelerator, and it was assumed to be -500 V as above. Although this value is higher than most operational values, it will give an upper bound on the grid impingement current. The grid impingement current was measured as a function of tank background pressure over a range from  $2.8 \times 10^{-5}$  Torr to  $1.5 \times 10^{-5}$  Torr.

Figure 5.39 shows the experimental data of the grid impingement current with the simulation results. We have computed values for cases with and without the neutralizer neutrals, although the difference in propellant utilization between the two cases is not as large as with the Monheiser case. Over the small range of pressures, the experimental results are linear with pressure. The computational results are also linear down to  $10^{-5}$  Torr. Below this value, the background neutral density becomes comparable to the beam neutral density and the slope decreases. This non-linear effect is probably due to the effect of the CEX ion density (which scales with the neutral density) on the potential sheath in front of the grid. As the density decreases, the Debye length decreases, and the accel grid potential sheath does not extend as far into the CEX plasma.

It should be noted that the tank pressures in the Beattie and Matossian experiments are an order of magnitude greater than in the Monheiser experiments, and the impingement currents are also an order of magnitude greater. The tank background gas is the dominant source of the impinging ions. We can see that agreement between the computational results and experimental data are closer than in the Monheiser case. In Figure 5.39, we can see again that by extrapolating experimental results to zero tank pressure (assuming linear variation), we have close agreement with the numerical results (without neutralizer neutrals) for zero tank pressure. However, there is no basis to assume that the experimental data is linear over such a large pressure range, and thus the computational results at least provide a lower bound on the impingement current for space based operation.

#### **5.4.4 Conclusions from Comparisons of Grid Impingement Current**

From our comparisons both with experimental data and other computations, we see that our model can be used to estimate the grid impingement current for space based thruster operation. Even though we do not model the details of the grid apertures, nor was the model intended to focus on the impingement current, we find our model gives reasonable results. This is because the CEX ions created directly downstream of the thruster are responsible for the bulk of the accel grid current. We have also found that the

neutralizer neutrals appear to play an important role in determining the impingement current. Unless the neutralizer has a high flow rate and is aimed into the beam, it does not substantially increase the CEX ion impingement current. (However, the neutralizer neutral density is important for the production of CEX ions that are created farther downstream and produce the CEX plasma that surrounds the spacecraft.) More importantly, although our model was not designed explicitly to measure the accel grid impingement current, our results are close to results from computational models strictly designed for such a purpose. In addition, we have shown results computed directly from experimental parameters, and did not "fit" parameters like the beam ion density in the work of *Peng et al.*

## 5.5 NASA 30 cm Xe Ion Thruster Contamination Predictions

Having gained confidence in the validity of our numerical model from comparing with various experiments in the previous sections, we will now conduct contamination assessment predictions for the current NASA 30 cm thruster. We will study how the CEX backflow scales with ion thruster operating conditions and compare numerical results to the scaling relationships in Chapter 2. The 30 cm ion thruster using xenon as a propellant has been developed by NASA as an element in the NASA Solar Electric Propulsion Technology Applications Readiness (NSTAR) program that was established to validate ion propulsion for space flight applications. It was also developed for the USAF/TRW Space Surveillance, Tracking, and Autonomous Repositioning (SSTAR) platform. The thruster incorporates innovations in design, materials, and fabrication techniques compared to those employed in previous ion thrusters. Specific development efforts included thruster design optimizations, component life testing and validation, vibration testing, and performance characterizations. However, thus far, no detailed plume measurements for backflow contamination have been conducted [*Patterson et al.*, 1993,1994].

The operating envelope for the thruster is shown in Figure 5.40. Beam current is displayed on the horizontal axis, and ranges from 0.5 to 3 A, and beam voltage is displayed on the vertical axis and ranges from 550 to almost 1400 V. The input power envelope ranges from 0.5 to 4.9 kW. The black circle points are operating conditions used in NASA/Jet Propulsion Laboratory (JPL) tests [*Brophy*, 1994], and the white box points are those mapped out by NASA Lewis Research Center (LeRC) [*Patterson et al.*, 1993]. Note that the dark line drawn at the bottom of the envelope is the thruster perveance limit (space-charge limit of the grids). For a fixed voltage, the current can not be increased above the space-charge limited flow value.

In this thesis, we study all six of the JPL operating points and a subset of the LeRC

operating points. We choose points from the LeRC envelope that will enable us to study scalings. Thus, we examine points of constant voltage of 1090 V, points of constant current of 1.1 A, and the extreme limits of the operating envelope. The specifics of the JPL operating points are given in Table 5.3, and those of the NASA LeRC points in Table 5.4.

To compute the performance characteristics of the thrusters such as thrust, and specific impulse, the following equations are used. The thrust is computed from experimentally measured values of beam current,  $I_b$ , and beam voltage,  $\Phi_b$ ,

$$F = \gamma \sqrt{\frac{2m_i}{e}} I_b \Phi_b^{1/2} \quad (5.4)$$

where  $\gamma$  is a thruster loss correction factor taking into account the doubly-ionized ions and beam divergence effects. This factor is generally around 0.95-0.97. The specific impulse is computed from,

$$I_{sp} = \frac{\gamma \eta_p}{g} \sqrt{\frac{2e\Phi_b}{m_i}} \quad (5.5)$$

### 5.5.1 JPL Operating Points

The rationale for the JPL power throttling operating points shown in Table 5.3 is that the maximum power point is set to be the minimum power necessary to provide significant benefit for small-body rendezvous missions. The other points are selected to maximize thruster efficiency under the constraints of the propellant feed system design [Brophy, 1994].

Table 5.3 NASA 30 cm xenon thruster - JPL operating points

Point No.	Power (kW)	$I_b$ (A)	$\Phi_b$ (V)	$v_{bi}$ (m/s)	$\eta_p$	$\dot{m}$ (mg/s)	Thrust (mN)	$I_{sp}$ (s)
J1	0.497	0.5	676	31,500	0.71	0.96	20	2177
J2	0.996	0.72	1107	40,300	0.75	1.31	38	2929
J3	1.132	0.81	1119	40,500	0.81	1.36	43	3194
J4	1.521	1.15	1075	39,700	0.84	1.87	59	3238
J5	1.652	1.23	1100	40,200	0.88	1.9	64	3450
J6	2.304	1.74	1100	40,200	0.89	2.67	91	3477

We have applied the numerical simulation model to these six points for both variable and constant temperature cases. Ambient conditions appropriate to the LEO environment were used. Thus, the background plasma density was taken to be  $10^{10} \text{ m}^{-3}$ , the ambient

electron temperature was 0.1 eV, and there was no neutral background pressure. The computational domain was 1 m by 1 m, and the thruster body was taken to be 50 cm long and 20 cm wide (half-width). The beam divergence angle is taken to be 20°, and the neutral propellant grid transparency ratio is 0.24. The spacecraft/thruster body was assumed to have a floating potential of -1 V, and the beam electron temperature was set to 5 eV, although only CEX collisions were included. This higher electron temperature will give a more conservative estimate of the backflow.

The backflow current was computed on two planes extending from the top of the thruster body. One is located at the thruster exit plane (plane 1), and another at  $z=0$  (plane 2). The planes are separated by 50 cm, and the radial height of the planes is 80 cm. In Figure 5.41, we show the ratio of the computed backflow current on the two planes to the beam current as a function of the thruster operating power (points J1 to J6). Results for both the variable and constant temperature models are shown.

As can be seen in Table 5.3, there is a wide range of thruster operating conditions, (i.e.  $I_b$ ,  $\eta_p$ , and  $\Phi_b$ ), that are covered as the power is throttled from 0.5 kW to 2.3 kW. To understand the scaling of the backflow current as a function of thruster operating conditions, we must recall from Chapter 2 (Eqn. (2.12)) that the CEX ion production scales (for a given thruster and propellant) as,

$$\dot{N}_{cex} \sim I_b^2 \left( \frac{1 - \eta_p}{\eta_p} \right) \sigma_{cex}(v_{bi}) = \chi \quad (5.6)$$

We can see whether this relationship is valid or not by applying this scaling factor to the numerical results. In order to do so, given  $\chi$  and the backflow current for the first point, we can compute the backflow current for any other point  $i$ ,  $I_{bf i}$ , by multiplying the backflow current of the first point by  $\chi_i/\chi_1$ ,

$$I_{bf i} = I_{bf 1} \left( \frac{\chi_i}{\chi_1} \right) \quad (5.7)$$

This procedure has been applied, and the results are overlayed on Figure 5.41, where the "x" symbols indicate the scaled predictions of the backflow current that have been normalized by the beam current. As an example, with the variable temperature model, the backflow current over plane 1 for point J1 is  $4.13 \times 10^{-4}$  A, and  $\chi_1 = 0.3995$ . For point J3,  $\chi_3 = 0.5459$  and we predict the backflow current to be  $(0.5459/0.3995)(4.13 \times 10^{-4}) = 5.6 \times 10^{-4}$  A. The numerical result, with the variable temperature model, is  $5.3 \times 10^{-4}$  A, which is very close. From Figure 5.41, we can see that this scaling relationship is in good agreement with the trends predicted by the numerical model. At first glance, it appears that the ratio of the backflow current to the beam current is almost constant as a function of power. However, it must be kept in mind that the propellant utilization efficiency is also



changing.

As we have seen in the previous comparisons with experimental data, the isothermal model gives a higher value for the backflow current than the variable temperature model. For plane 1, the isothermal model gives values around twice those of the variable model, and for plane 2, about three times or more as great. The distributions are different between the two temperature models also. The variable temperature model gives a faster decay in the current as can be seen by comparing the current crossing planes 1 and 2. The current crossing plane 2 is about 8-9 times less than plane 1 for the variable temperature model, but about 4-5 times less for the isothermal model. It should be noted that the scaling relationship, Eqn. (5.6), is independent of the electron temperature, but still follows the numerical results for both constant and variable temperature models well.

Thus far, we have examined scalings on a global quantity - the backflow current on various planes. We would expect these currents to scale with the rate of CEX ion production, in essence, a statement of continuity. However, we must also examine the structure of the backflow field and see how it varies, if at all, as the thruster is throttled through various operating conditions. In Figures 5.42a and b, we show two views of the CEX plasma density distributions computed with the variable temperature model for all six operating points. In Figure 5.42a we show a radial cut through the domain along a ray  $100^\circ$  from the plume centerline from a point 10 cm downstream of the thruster face. We have normalized the density for each case, so that we just see the distribution. Within numerical noise levels of the PIC method, all six cases spanning a power range of a factor of almost five appear to follow the same shape. In Figure 5.42b, we show the density distribution along an arc of radius 0.35 m from the same point 10 cm downstream of the thruster. The density has been normalized with the value of the density at the plume centerline ( $\theta=0^\circ$ ). The CEX density falls to zero at about  $\theta=145^\circ$  where the top of the thruster body is intercepted. In this figure, we can also see that within a certain amount of scatter, the distributions over an entire sweep of  $145^\circ$  are very similar.

In addition to the CEX ion density, it is important to look at the CEX ion current density distributions. Figures 5.43a and b show these distributions computed with the variable temperature model in the same format as in Figures 5.42a and b. Again we see that the distributions are essentially the same, given the fluctuations that are present since the current density is a weighting of both the particles' charge and velocities. Results with the isothermal model for both CEX density and current density yield the same conclusion: the distributions are very similar for all six operating points. However, there are differences between the temperature models as to be expected, with the isothermal distributions being higher in the regions outside of the beam.

The very important point to deduce from these figures, is that the distribution of the CEX plasma is relatively independent of the thruster operating conditions, only the magnitude is dependent upon the beam current, propellant utilization efficiency, and other parameters as shown in the scaling parameter  $\chi$ . It should be noted that slight variations with the variable temperature model may be caused by the influence of the temperature field on the potential. Over the operating envelope, the ion to neutral density ratio changes, which affects the thermal conductivity as we saw in the comparisons with Kaufman's experiments, and this influences the electron temperature, and hence the potential. However, these effects are not very significant. Of course, these conclusions are for a given geometry, i.e. thruster/spacecraft size. One can not use the scaling factor, Eqn. (5.6), to predict the backflow current if say, the thruster body width is doubled. We will examine the effect of thruster/spacecraft body geometry on the backflow structure in Section 5.7. In addition, the role of the electron temperature in the plume will be examined more closely in Section 5.6, and contour maps of the CEX ion density and current density will be shown.

Lastly, for the JPL operating points, we compute the accel grid impingement current for space-based operation. The propellant utilization efficiencies used in Table 5.3 include the neutralizer flow rate, which is only about 7% of the total, but will yield higher estimates. Figure 5.44 shows the ratio of the accel grid impingement current to the beam current for the six operating points. The impingement current fraction varies from 0.2 to 0.5%, with the isothermal model results giving higher values. Based on these impingement currents, we can compute the grid mass loss for sputtered molybdenum estimates. However, for our calculations of molybdenum deposition in Section 5.8, we will use experimentally correlated data.

### 5.5.2 NASA LeRC Operating Points

The NASA LeRC points shown in Table 5.4 have been categorized by alphabetical prefixes: I, V, and L. The four points with I are points of constant voltage, and the current is varied. The six points with V are points of constant current, and the voltage is varied. The four points with L are the four vertices of the thruster operating envelope. Some of the points have multiple labels since they overlap in the envelope. For these parametric studies, only the isothermal model was used. All other variables from the JPL runs, aside from the operating conditions listed in the table, were used in the LeRC runs.



Table 5.4 NASA 30 cm xenon thruster - LeRC operating points

Point No.	Power (kW)	$I_b$ (A)	$\Phi_b$ (V)	$v_{bi}$ (m/s)	$\eta_p$	$\dot{m}$ (mg/s)	Thrust (mN)	$I_{sp}$ (s)
L1	0.7	0.7	552	28,459	0.78	1.23	28	2290
V1	1.12	1.1	730	32,728	0.85	1.76	46	2680
V2	1.26	1.1	843	35,170	0.85	1.76	50	2920
V3	1.4	1.1	963	37,590	0.85	1.76	54	3150
V4,I1	1.56	1.1	1093	40,047	0.85	1.76	59	3400
V5	1.73	1.1	1227	42,431	0.85	1.76	62	3630
V6,L2	1.9	1.1	1372	44,868	0.85	1.76	67	3860
I2	2.43	1.8	1094	40,065	0.85	2.88	95	3370
I3	3.05	2.3	1091	40,010	0.82	3.83	122	3250
I4,L3	3.88	3.0	1090	39,992	0.91	4.5	154	3470
L4	4.88	3.0	1371	44,851	0.91	4.5	178	4030

The backflow currents for variations in beam current for constant beam voltage were computed over the same two planes as in the JPL calculations. In Figure 5.45, we show the ratio of the backflow current to the beam current as a function of the beam current with the beam voltage constant at 1090 ( $\pm 4$ ) V. The scaling factor, Eqn. (5.6), has been used to predict the backflow currents based on the point I1, and these values are marked with the "x" symbol. We can see that there is very good agreement with this scaling relationship. The variations are not only due to changes in the beam current, but also due to changes in the propellant utilization efficiency.

In addition, the backflow current for constant beam current and mass flow rate (hence propellant utilization efficiency) was computed. In this case, only the beam voltage is being varied which only changes the CEX cross section as seen in Eqn. (5.6). In Figure 5.46 we see the ratio of the backflow current to the beam current (1.1 A), which only shows slight decrease because the CEX cross section is weakly decreasing with increasing beam ion velocity (Eqn. (3.21)). The scaling relationship, Eqn. (5.6), again gives good agreement.

Lastly, we present the backflow currents for the limits of the operating envelope to show bounds on the backflow. Two limit points, L2 and L3, have been computed already as points V6 and I4 respectively. The other two points represent the upper and lower bounds on the power of the thruster. The backflow current values are shown in Table 5.5 for L1, the point with the lowest voltage and current, and L4, the point with the highest

voltage and current.

Table 5.5 Lower and Upper limits to backflow contamination for LeRC points

	$I_{bk 1}/I_b$	$I_{bk 2}/I_b$
L1 (Lower) $I_b=0.7$ A	$1.45 \times 10^{-3}$	$3.20 \times 10^{-4}$
L4 (Upper) $I_b=3.0$ A	$1.77 \times 10^{-3}$	$4.05 \times 10^{-4}$

While the ratio of the backflow currents to the beam currents are almost the same, the scaling factor for L4 is about 5.56 times larger than that of L1. Hence, the actual backflow current increases by a factor of 5.56 from the lowest to the highest power settings (a range of 7) for the current 30 cm thruster. The accel grid impingement ratio at the lowest power level is 0.41%, compared to 0.56% at the highest level.

## 5.6 Effects of Electron Temperature

In this section, we study the effect of the electron temperature on the plume backflow structure. The variable temperature model is applied to the JPL operating point J2 with two temperatures: 1 and 5 eV. LEO space conditions are used in the simulation, and the thruster/spacecraft body is given a potential of -1 V. We begin by showing contours of the CEX ion density in Figures 5.47a and b for  $T_{eo}=1$  and 5 eV respectively. The density falls from values around  $2 \times 10^{15} \text{ m}^{-3}$  in the beam to below  $10^{11} \text{ m}^{-3}$  50 cm behind the thruster exit plane. There is very little difference in the CEX ion density in the backflow region; however, near the beam, the density is higher for the higher electron temperature case.

More important for contamination estimates, are maps of the CEX ion current density which directly show the flux of the ions. In Figures 5.48a and b, the magnitude of the CEX ion current density is shown. Now, we can see a noticeable difference in the backflow region, with the  $T_{eo}=5$  eV case yielding higher current densities. The integrated current flowing across a plane at the thruster exit for the 1 eV case is  $2.3 \times 10^{-4}$  A, and across a plane at  $z=0$  is  $2.6 \times 10^{-5}$  A. In contrast, for the 5 eV case, the corresponding currents are  $5.6 \times 10^{-4}$  and  $6.5 \times 10^{-5}$  A. The reason for the enhanced currents can be seen by looking at the potentials in the plume and recalling that the potential scales with the electron temperature.

Figures 5.49a and b compare the potential structures in the plume. Since the electron temperature is five times higher in Figure 5.49b, we can see that in a broad sense, the potentials scale accordingly. For instance, the 1 and 5 V contours in Figure 5.49a closely correspond to the 5 and 10 V contours in Figure 5.49b. However, as we approach the

beam, the exact correspondence is lost, but within the beam, the 11 V contour in Figure 5.49a is close to the 55 V contour in Figure 5.49b. The impact of these potential structures is that the CEX ions are accelerated to a much higher velocity in the 5 eV case, and hence the CEX ion current density is higher in the backflow region. In our comparisons of the backflow currents above, it is noted that the currents for the 5 eV case are roughly  $\sqrt{5}=2.24$  times larger than the 1 eV case. This is because the velocity scales as the square root of the potential difference. However, near the beam edge, the radial potential drop is slightly more than a factor of five. This can be seen by comparing phase space plots for the two cases. In Figures 5.50a and b, the radial velocities as a function of radial distance are shown. For the 1 eV case, the maximum radial velocity is about 2500 m/s, corresponding to a voltage drop of 4.25 V. For the 5 eV case, the maximum radial velocity is about 7000 m/s, corresponding to a voltage drop of 33.35 V, a factor of almost eight higher. Thus, decreasing the electron temperature in the beam is beneficial in lowering the backflowing current. The electron temperature in the beam is predominantly driven by the neutralizer coupling voltage. When the coupling voltage is low, the neutralizer is operating properly and high voltages are not necessary to draw electrons into the beam, and the electron temperature is low. Current thrusters operate at the 1-2 eV level. However, if some malfunction develops, the higher electron temperature resulting would have a detrimental impact on the backflowing current.

It is interesting to also look at the temperature structure to see the differences between the two cases. Recall in Figure 3.16, that the thermal conductivity varied as a function of the electron temperature. The variations are not only due to the explicit appearance of the electron temperature in the expression for the thermal conductivity, Eqn. (3.35), but also due to the dependence in the electron collision frequency. In Figures 5.51a and b, maps of the electron temperature in the plume are shown for the two temperature cases. We can see that the structures are quite different. For the 1 eV case, the electron temperature smoothly varies from 1 eV at the thruster exit to 0.5 eV at the upper boundary 1 m away. In the 5 eV case, the temperature falls from 5 eV at the thruster exit to about 2.3 eV at the upper boundary. However, in the 5 eV case, a distinct boundary is seen slightly behind the thruster exit plane. As we shall see shortly, at electron temperatures of 5 eV, electron-ion collisions are subdominant to electron-neutral collisions, and hence the neutral density plays a strong role in the thermal conductivity. This "boundary" is where the propellant neutral density falls to zero, and electron-neutral collisions are zero. In contrast, at temperatures of 1 eV, electron-ion collisions are dominant, and the structure of the neutral gas is not seen.

In Figures 5.52a and b, radial cuts of the electron temperature are shown for the two

cases. Since the electron thermal conductivity is influenced by the neutral density for the 5 eV case, and the neutral density has a much broader distribution (cosine), in comparison to the narrower (parabolic) profile of the beam ion density, the electron temperature across the beam is more constant for the higher temperature case. In addition, the electron thermal conductivity is higher, which allows better heat diffusion, and hence the temperature is higher. Maps of the thermal conductivity are shown in Figures 5.53a and b. For the 5 eV case, we see that the electron thermal conductivity is about an order of magnitude greater within the beam.

The electron thermal conductivity is affected by the electron collision frequency. In Figures 5.54a and b, we show maps of the total electron collision frequency, and in Figures 5.55a and b, we show the ratio of electron-neutral to electron-ion collision frequency. Within the beam, the total electron collision frequency is on the order of  $10^5 \text{ s}^{-1}$ , falling to 1-10 in the backflow region. Note the sharp fall for the 5 eV case across the boundary where the neutral propellant density goes to zero. In Figures 5.55a and b, we can clearly see how electron-neutral collisions are dominant in the 5 eV case, with the ratio of  $v_{en}/v_{ei}$  being more than  $10^3$  higher within the beam than in the 1 eV case. Thus, the electron temperature at the thruster exit plays a very important role in determining the electron thermal conductivity within the plume.

## 5.7 Effects of Geometry

The geometry of the spacecraft/thruster body plays an important role in the expansion of the CEX backflow. The scaling factor, Eqn. (5.6), discussed in Section 5.5, can only be used for a given geometry. In our simulations, CEX ions striking the body surface are absorbed, thus acting as a sink to the CEX plasma. It is not possible to develop a general scaling relationship for any arbitrary geometry. However, our goal is to demonstrate the effect of the spacecraft body geometry on the CEX plasma. We simulate three cases using an ion thruster with the Kaufman Case A operating conditions and the isothermal electron model. To incorporate large spacecraft bodies, the computational domain is 1.5 m square. In Figures 5.56a,b, and c, maps of the CEX ion current density are shown surrounding a spacecraft 75 cm long by 12, 24, and 36 cm wide respectively. If we track the  $5 \times 10^{-5} \text{ A/m}^2$  contour above the top of the spacecraft, we see that as the spacecraft becomes wider, this contour moves farther away from the upper spacecraft surface showing the decrease in plasma density on that surface.

Thus, the geometry of the spacecraft must be carefully considered when assessing the backflowing CEX plasma. It is not the purpose of this thesis to conduct studies for various

geometries. However, we have developed a numerical model that is capable of being applied to many geometries for applications purposes, and have shown that the geometry is an important factor when assessing backflow contamination for spacecraft/thruster integration.

## 5.8 Sputtered Grid Material

In this section, we examine the transport of sputtered grid material from the NASA 30 cm xenon ion thruster. *Patterson et al* [1993] estimated the in-space accel grid mass loss rate for a number of operating conditions, and these values are shown in Table 5.6. The first point corresponds to point I1 (or V4) in Table 5.4, the second to point I2, and the third point is close to I3. Based on these mass loss rates, the neutral molybdenum density can be computed using Eqn. (3.27), and these values are also shown.

Table 5.6 Anticipated accel grid erosion rates in space for NASA 30 cm xenon thruster  
(Patterson et al [1993])

Power (kW) and Label from Table 5.4	Mass Loss (g/khr)	Mo Neutrals ( $\text{m}^{-3}$ )
1.1 (I1, V4)	1.41	$1.10 \times 10^{13}$
2.40 (I2)	2.89	$2.25 \times 10^{13}$
3.41 (Close to I3)	4.18	$3.250 \times 10^{13}$

As we saw in Figure 3.14, electron-impact ionization of the neutral molybdenum sputtered off the grids is important for electron temperatures as low as 2 eV. In our calculations, for each operating point, we run two cases for the creation of charged molybdenum. The *high* rate case includes ionization with an electron temperature of 5 eV, and the *low* rate case only considers CEX collisions with the xenon ions (valid for electron temperatures near 1 eV or less). These two limits will give a bound on the creation of molybdenum ions. The molybdenum ions created are tracked in the corresponding potential fields computed in the simulations of Section 5.5.2. These potential fields were computed assuming a constant electron temperature of 5 eV.

In Figure 5.57, the ratio of the molybdenum to xenon CEX ion current density for the I3 point with high ion creation rate is shown. Within the beam, the ratio is about  $10^{-4}$ , however, in the backflow region, it is below  $10^{-5}$ . The important point is that the molybdenum ion distribution is considerably different spatially than the xenon CEX ion distribution. Recall in the analytical models of Chapter 2, that the spatial distribution of the species was assumed to be the same, only differing in magnitude. In the backflow region,

the molybdenum density is noticeably less. The reason for this is due to the higher energy of the molybdenum ions, and hence they are turned back less towards the spacecraft. Recall in Chapter 3, the most probable energy of the sputtered molybdenum is about 5 eV, with the average being 15-20 eV. In contrast, the thermal neutrals only have an energy around 0.02 eV (500°K). In Figure 5.58, we show the trajectories of a xenon and a molybdenum ion released radially outward from the same point at the beam edge with energies of 0.02 and 5 eV respectively. Potential contours are superimposed. We can see that the less energetic xenon ion is turned back more than the molybdenum ion. Hence the density of the molybdenum in the backflow area will be less. In addition, the values in Figure 5.57 show that neglecting the molybdenum ion density in Poisson's equation is a good approximation, since the density is negligible compared to the propellant ion density.

For contamination assessment of the molybdenum, the most important quantity of interest is the deposition rate. As seen in Chapter 2, the most useful unit is monolayers/year assuming all the molybdenum sticks. In Figure 5.59, a contour map of the deposition rate of the molybdenum ions is shown for the I3 case with high ion creation rate. These values, assuming normal impingement, are the ion current density multiplied by the conversion factor from A/m<sup>2</sup> to monolayers/year computed in Chapter 2. Within the plume, the deposition rates do not take into account the neutral deposition, nor the fact that the deposition on a surface will be much lower due to sputtering by the energetic beam ions. However, in the backflow region, the deposition rate is solely due to the charged molybdenum, and is about 0.1 monolayers/year. Figure 5.60 shows the deposition rate along a ray 135° from a point near the top corner of the thruster body ( $z=0.48\text{m}$ ,  $r=0.22\text{m}$ ). As the thruster power is decreased, the grid mass loss decreases, and hence the molybdenum backflow. Figure 5.61 shows the deposition rates for the I1 case with only CEX as the ion production mechanism. Here we see that the molybdenum deposition is only around  $5 \times 10^{-4}$  monolayers/year in the backflow region. (For the I1 case with electron-impact ionization, the value is around  $2 \times 10^{-2}$  monolayers/year).

It should be pointed out that the neutral molybdenum density in Table 5.6 varies only by a factor of three over a power range of two. Since the molybdenum is sputtered due to the propellant CEX ions impinging on the grid, we would expect the molybdenum density to scale with the scaling factor for the propellant CEX ions in Eqn. (5.6) which predicts a factor of about 5.4. The reason for this discrepancy is that the accel grid voltage is changing which plays a role in the grid sputtering since the sputtering yield changes with ion impingement energy. The estimates in Table 5.6 by *Patterson et al* [1993] are based on experimental correlations of the grid voltage and the grid impingement current. Moreover, while the propellant CEX impingement current may increase by a factor of 5.4, the actual



grid mass loss may not scale as such since not all material sputtered away is ejected completely from the grid, but may redeposit elsewhere.

However, we are interested in how the molybdenum ion density in the backflow region changes given the sputtering characteristics of a given grid on a thruster with given operating conditions. The issue is: given the molybdenum sputtering characteristics for two different operating conditions, can the backflowing molybdenum densities be scaled? The answer is yes, since we know the molybdenum ions are created, i.e. either via CEX or electron-impact ionization.

The creation rate of the molybdenum ions scales with the neutral molybdenum density, the beam ion density, and a function for the particular collision process. For CEX collisions, this function is the product of the beam ion velocity and the cross section. For electron-impact ionization, this function is solely dependent upon the electron temperature. The neutral density scales with the sputtering rate (which is given), and the beam ion density scales with the ratio of the beam ion current to the beam ion velocity (the beam voltage). Thus, we can write the creation of molybdenum ions due to CEX as,

$$\dot{N}_{cex Mo} \sim \dot{m}_{Mo} \left( \frac{I_b}{v_{bi}} \right) v_{bi} \sigma(v_{bi}) \quad (5.8)$$

and the creation rate due to electron-impact ionization is,

$$\dot{N}_{ion Mo} \sim \dot{m}_{Mo} \left( \frac{I_b}{v_{bi}} \right) f(T_e) \quad (5.9)$$

With these scaling factors, we can see how the molybdenum ion density varies in the backflow region for the three operating points above. Notice that for these three points,  $T_e$  is a constant, and the beam ion velocity is relatively constant. Therefore, the molybdenum deposition will scale as the product of the sputtering loss rate and the beam current. In Figure 5.62, the integral of the molybdenum current density over the two planes as in the previous figures in this chapter is shown. Plane 1 is at the thruster exit, and Plane 2 is located 0.5 m behind at  $z=0$ . Both planes reach from the thruster top at  $r=0.2$  m, to the upper domain boundary at  $r=1$  m. The backflow has been expressed in terms of monolayers/year. This was done by integrating the current density to obtain the current, dividing by the area of the annulus over which the integration occurred ( $\pi(1^2-0.2^2)\text{m}^2$ ), and then multiplying by the conversion factor to monolayers/year. Thus, this value is an average deposition, and is shown as a function of the thruster power for the three operating points and the high/low ion creation rates. Superimposed on the computational values, are the scaled values based on the point I1. These points are marked with the "x" symbol. Therefore, even though the grid mass loss increases only by a factor of three from point I1 to I3, the beam current has increased by a factor of two, and hence, the molybdenum

deposition increases by a factor of six. The difference in deposition rates between the two ion creation bounds is very large, with electron-impact ionization yielding deposition rates 20-30 times larger than CEX ion creation. This observation again demonstrates the importance of the electron temperature in the plume.

Having computed the deposition rates of the molybdenum, we give an example of the seriousness of its effect upon the properties of sensitive surfaces. *Kemp et al* [1972] computed the transmittance of molybdenum films on solar array coverglasses as a function of film thickness. Their results, which agreed well with ground experiments and the SERT II flight tests, are shown in Figure 5.63. Given deposition rates of 0.1 monolayers/year over a 15 year lifetime, a film thickness of 1.5 monolayers or 4.2 Å would result in a transmittance loss of about 10%. Such a decrease in corresponding power is very important in designing the solar arrays since usually 18-25% is lost within 7 years mainly due to radiation damage [Agrawal, 1986]. Equally important are the effects of film deposition on thermal control surfaces. As can be seen in Figure 5.63, the absorptance of the surface is also altered, which will have a direct impact on the temperature control of the surface. We have used the 15 year lifetime figure as representative of modern communications satellites. However, current ion thruster lifetime thus far has been demonstrated only up to a maximum of two years (constant operation). Over this time period, molybdenum film thicknesses of only 0.2 monolayers, or 0.56 Å, would form, which would have significantly less impact. However, the behavior of such thin films has not been thoroughly characterized.

The values shown in Figure 5.63 are typical values on glass. However, for other specific surfaces, the values will change and experimental values are needed. In addition, the values shown do not account for the fact that the molybdenum is charged. The deposition is actually quite complicated for films less than 100Å, and film growth is not always uniform and continuous. In the initial stages of film growth, the atoms cluster in nuclei. The geometrical formations of these nuclei depend upon the various parameters of the deposition such as the rate, angle of incidence, kinetic energy of the impinging atoms, and the conditions of the surface such as roughness and temperature [*Kemp et al*, 1972].

## 5.9 Effect of Thruster Operation on Spacecraft Floating Potential

As discussed in Chapter 3, the CEX plasma cloud produced by the ion thruster can alleviate the extreme negative floating potentials that spacecraft reach in geostationary orbits. As mentioned earlier, the goal of this work is to demonstrate the principle of the CEX plasma cloud "bridging" the spacecraft to the ambient plasma, and hence raising the



potential close to zero. We are not developing a detailed spacecraft charging model, much of which depends heavily on the spacecraft surface properties (i.e. secondary electron emission yields), and on accurate modelling of the ambient plasma species (i.e. multiple species with different electron temperatures).

To demonstrate the control of spacecraft charging, we examine a simple case of a spacecraft in GEO. We assume a very simple model of the GEO plasma, and take the ambient plasma density to be  $10^6 \text{ m}^{-3}$ , and the ambient electron energy to be 0.1 keV. Under these conditions, a passive spacecraft will float to -418 V negative with respect to the ambient plasma which is taken to be at 0 V. In such a rarefied plasma, the Debye length is very large ( $\sim 70 \text{ m}$ ), and hence the effect of the spacecraft's potential is felt over very long distances. The potential profile in the radial direction away from the spacecraft (the top is at  $r=25 \text{ cm}$ ), is shown in the bottom of Figure 5.64. A thruster operating with conditions of JPL point J3 was simulated. The isothermal model was used with a beam electron temperature of 2 eV. The floating spacecraft potential was computed and at steady state, reached a value of 16 V positive to the background. However, the potential of the surrounding CEX plasma was about 25 V. Thus, the spacecraft was still 9 V negative with respect to the surrounding plasma. A radial profile of the potential above the spacecraft is shown in the top of Figure 5.64. Thus, we see that the CEX plasma is indeed able to alleviate large negative spacecraft potentials. Moreover, the extent over which the spacecraft potential reaches is greatly reduced since the Debye length collapses from 70 m to less than a cm. This calculation was done assuming that the beam ion and neutralizer electron currents were equal. In general, this may not be the case as was discussed in Chapter 4. However, to examine this issue more closely, the ambient species and a model of electron emission from the neutralizer would have to be included.

### 5.10 Effect of a Plume Shield to Reduce Backflow

A possible way to reduce the backflow of ions from an ion thruster, is to use a plume shield. In this section, we demonstrate the effect of a simple plume shield that is placed at the thruster exit, perpendicular to the plume axis as shown in Figure 4.1. We attach a plume shield 30 cm high of infinitesimal thickness above the thruster body at the thruster exit, and perform a simulation with thruster conditions from Kaufman's Case A ground experiments. The constant electron temperature model was used, and the shield is biased to +5 V and is assumed to be completely absorbing.

Figure 5.65 shows the total propellant ion density computed with the same contour levels as in Figure 5.6 (no plume shield). We can see that in the backflow region behind

the shield, the propellant CEX plasma is completely eliminated (and hence the molybdenum ions as well). Recall that in this ground test, the density of the background plasma was  $10^{12} \text{ m}^{-3}$ . We show a contour of value  $10^{12} \text{ m}^{-3}$  which is the edge of the CEX expansion. The plume shield is very effective in reducing any backflow contamination from the region behind the shield. However, the plume shield represents additional mass to the spacecraft structure. In any actual spacecraft/thruster integration process, the ratio of the mass of the shield to the effective area protected would have to be minimized. In addition, other shield shapes, such as a conical geometry, may be more effective.

### 5.11 Comparison of Numerical Results to Simple Analytical Models

In Chapter 2, we used a simple analytical model to predict the propellant CEX plasma density distribution produced by the SERT II mercury thruster. The model results were compared with Kaufman's experimental data, and it was found that the model overpredicted the density in the backflow regions by at least an order of magnitude. On the other hand, the numerical model developed in this thesis matched the experimental data well, within a factor of two. The more important differences lie in the structure of the CEX plasma backflow. The analytical model assumes a simple point source distribution, but in actuality, the geometry of the thruster/spacecraft and electric fields play important roles in the backflow expansion as we have seen. The simple model can not take into account the spacecraft geometry, nor the presence of structures like plume shields. Thus, a simple point source model is a vast oversimplification of the expansion process, and is not very useful within a meter or so of the plume. However, the main question is whether the CEX plasma can be described with  $1/r^2$  behavior far from the plume. In the next chapter when we perform 3-D calculations on large domains we will see that the CEX plasma does indeed decay as  $1/r^2$  in the far field.

The predictions of the simple model of Chapter 2 for the sputtered grid material distribution are predicated on the assumption that the grid and propellant ions have the same distribution, only their magnitudes are different. However, we have seen that this is not the case. Due to the energetic nature of the sputtered metal ions, the ratio of the grid to propellant ions in the beam and the backflow region are quite different. The grid material ions are not as easily influenced by the electric fields due to their higher energies and hence are not turned back as much as the propellant ions. Thus, the simple model of Chapter 2 leads to a greater estimate of the grid metal ion flux in the backflow region. As an example, in Figure 5.57, we saw that the ratio of molybdenum to xenon in the backflow region was at least 25 times less than in the plume in front of the thruster. The simple model assumes

the same molybdenum to xenon ratio everywhere based on the ratio of the respective CEX production rates. While overestimation to a certain degree is beneficial, excessive overdesign can be extremely costly.

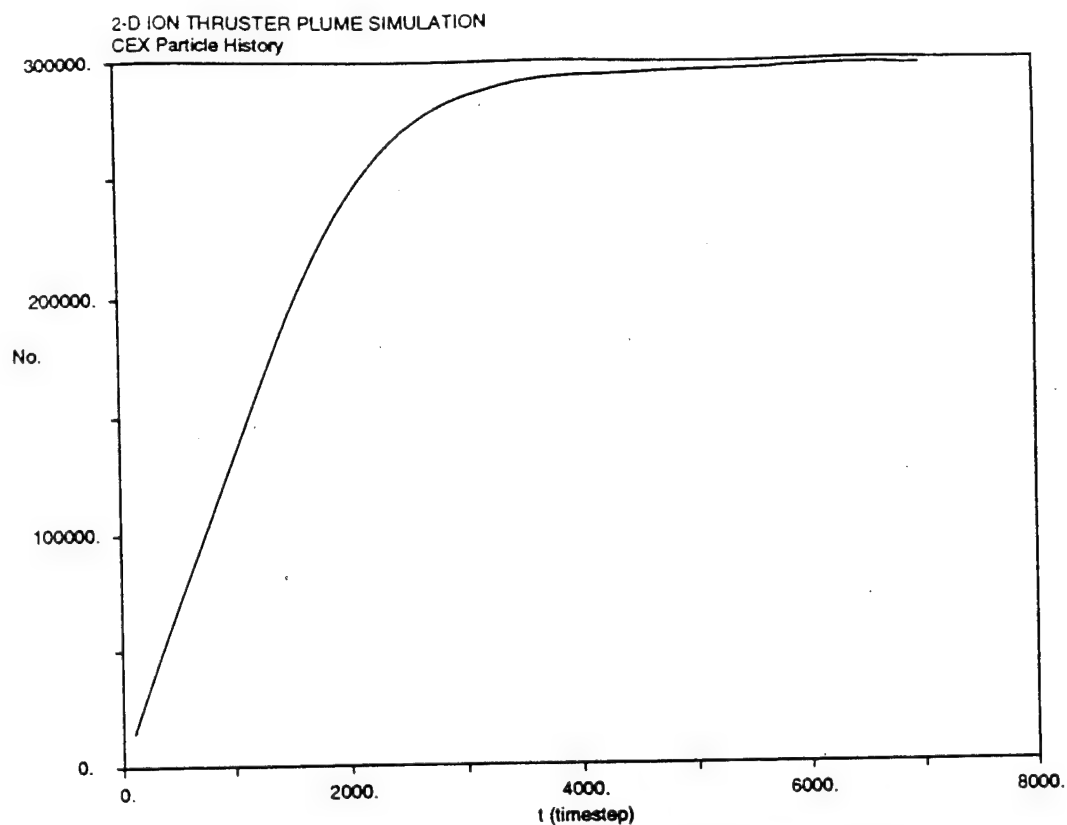


Figure 5.1 Time history of number of particles in a simulation

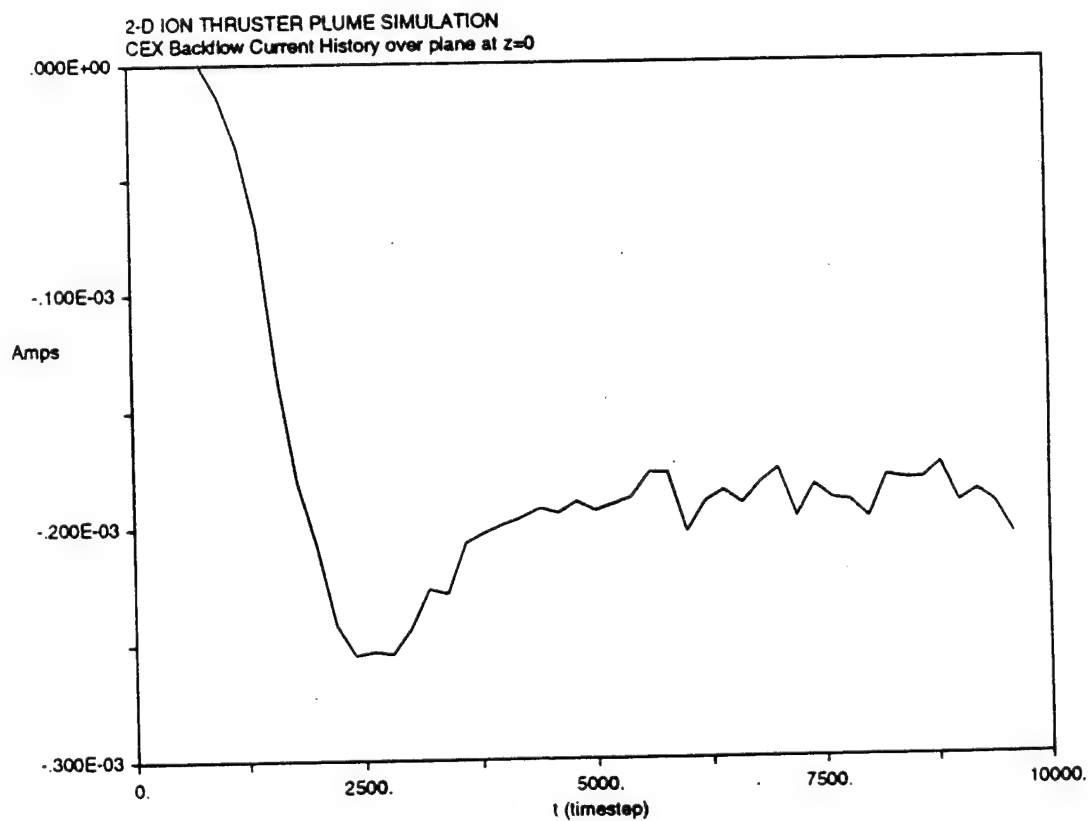


Figure 5.2 Time history of backflow current over plane  $z=0$

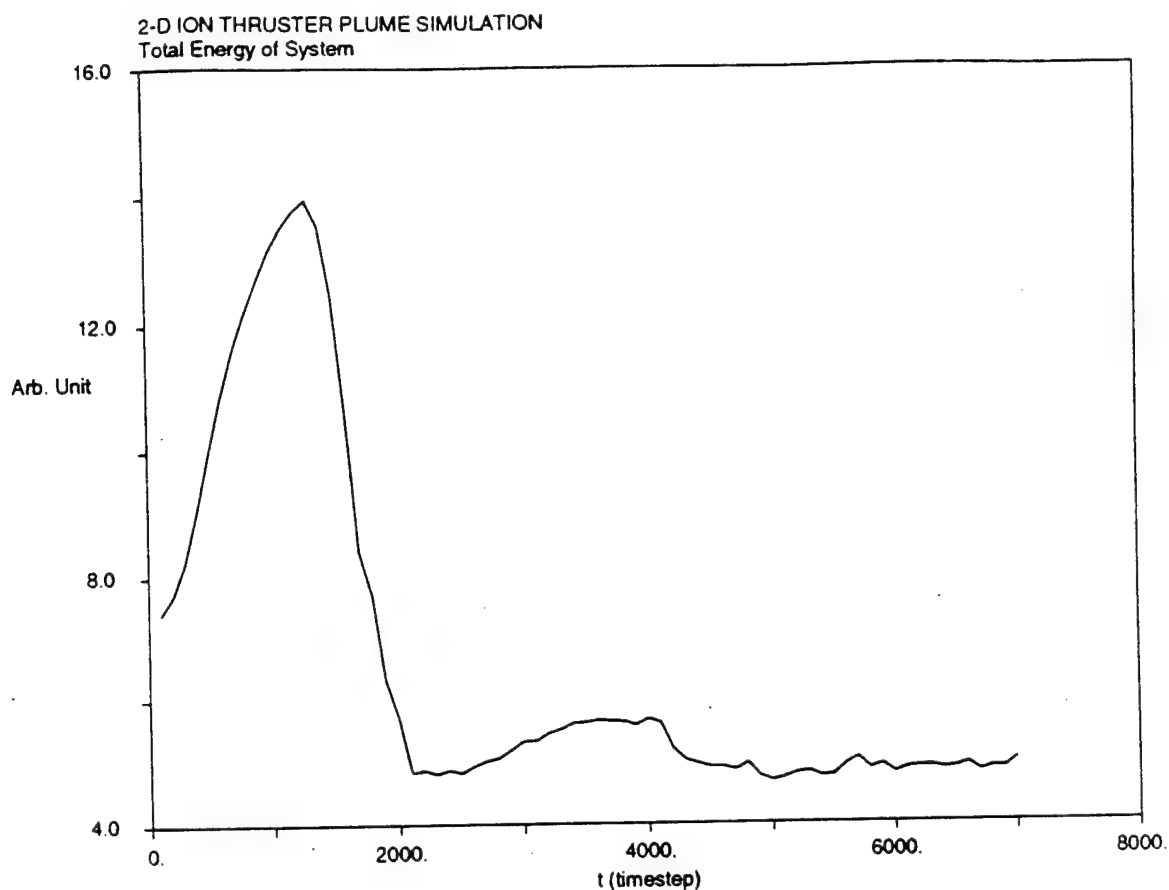


Figure 5.3 Time history of average total energy of particles in simulation

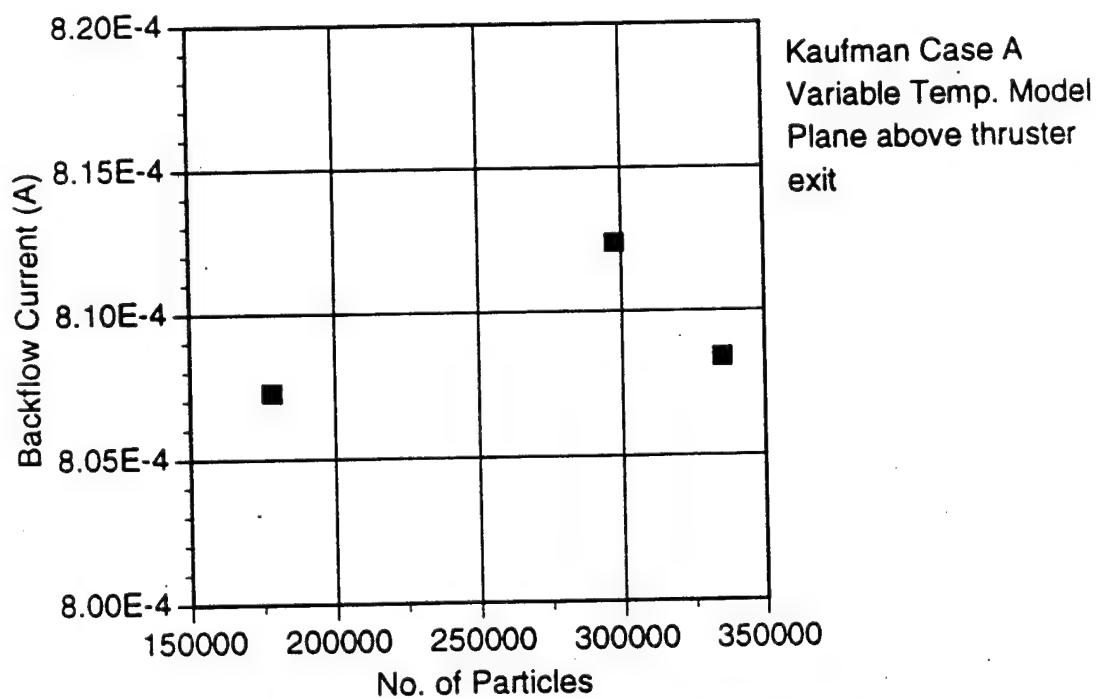


Figure 5.4 Dependence of Backflow Current Results on  
Total Number of Particles in Simulation

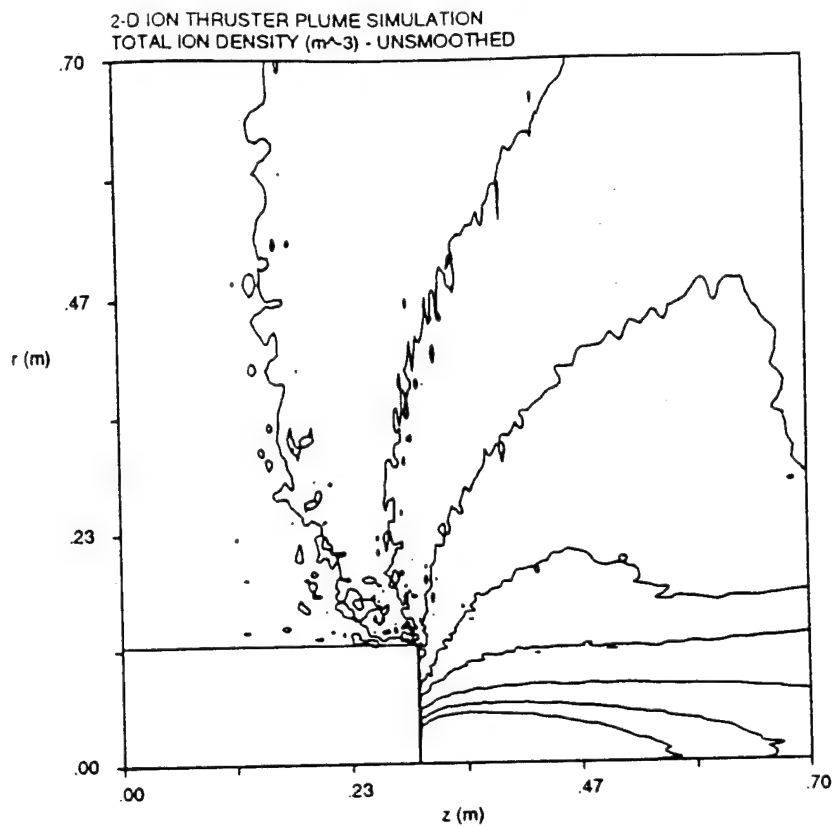
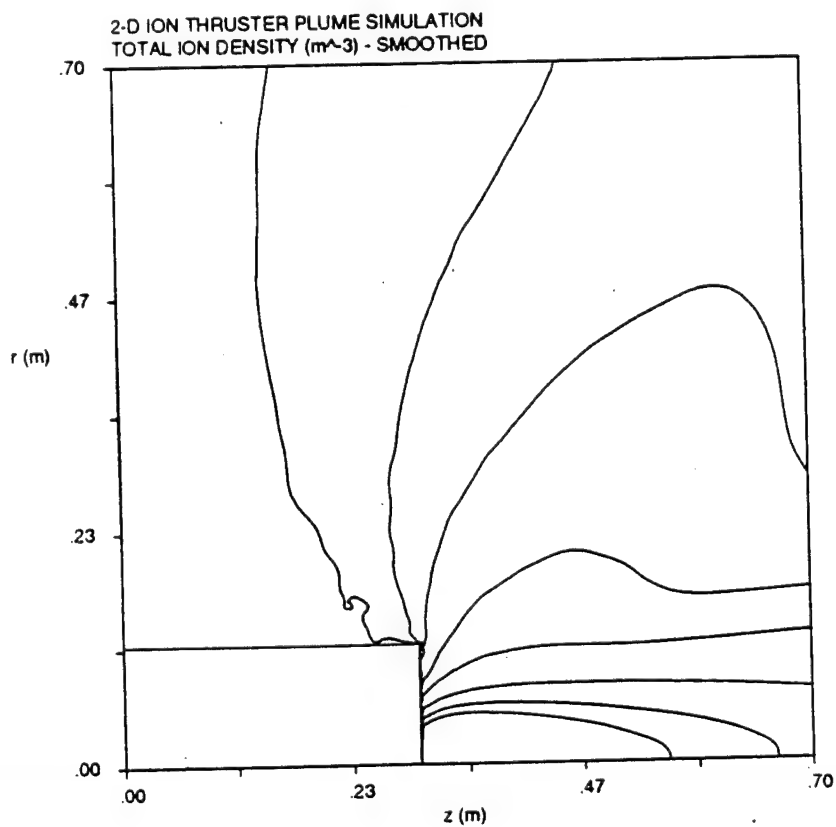


Figure 5.5 Comparisons between a) unsmoothed and b) smoothed ion density in a typical simulation



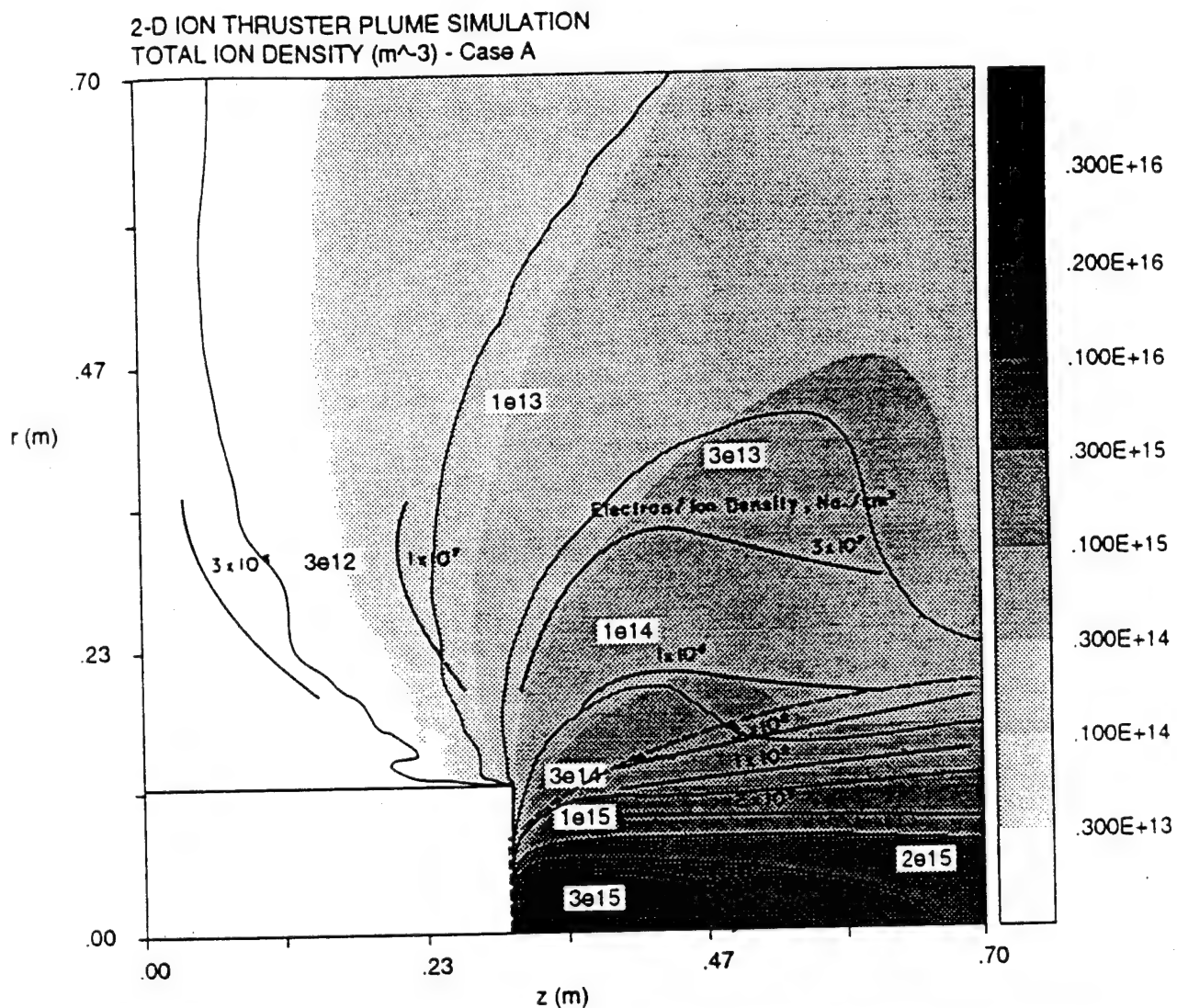


Figure 5.6 Contour plot of smoothed total ion density for *Kaufman* Case A conditions showing variable temperature (gray-scale), isothermal (thin line), and experimental measurements (bold line)

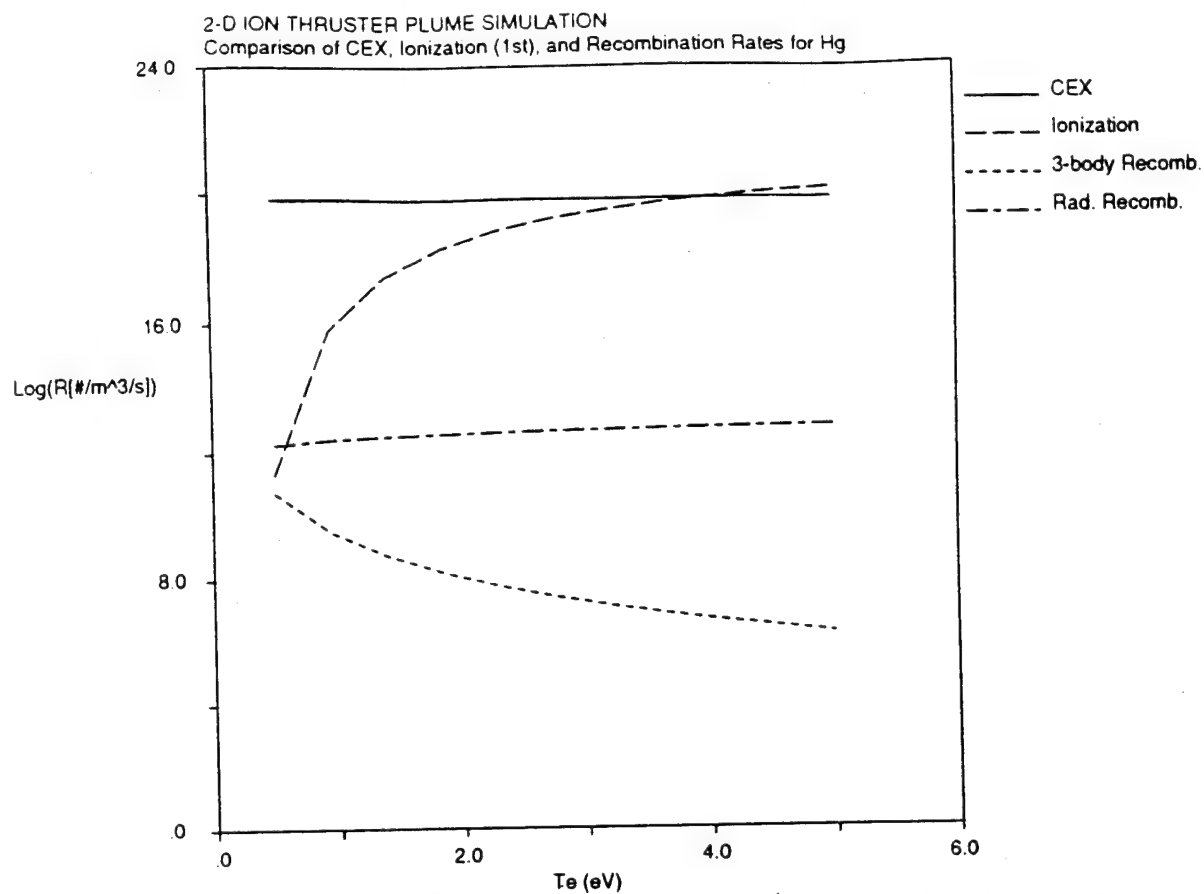


Figure 5.7 Comparison of CEX, ionization, and recombination rates for mercury as a function of electron temperature using densities at thruster exit

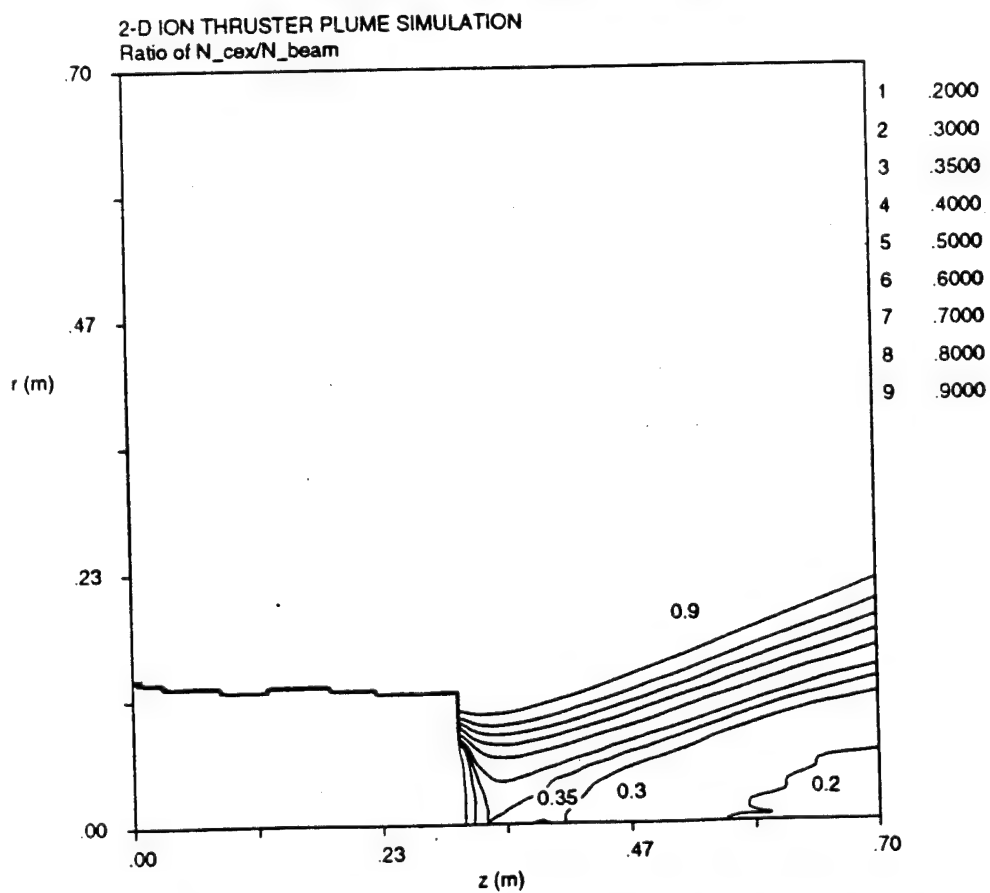


Figure 5.8 Ratio of CEX ion density to beam ion density for Kaufman Case A



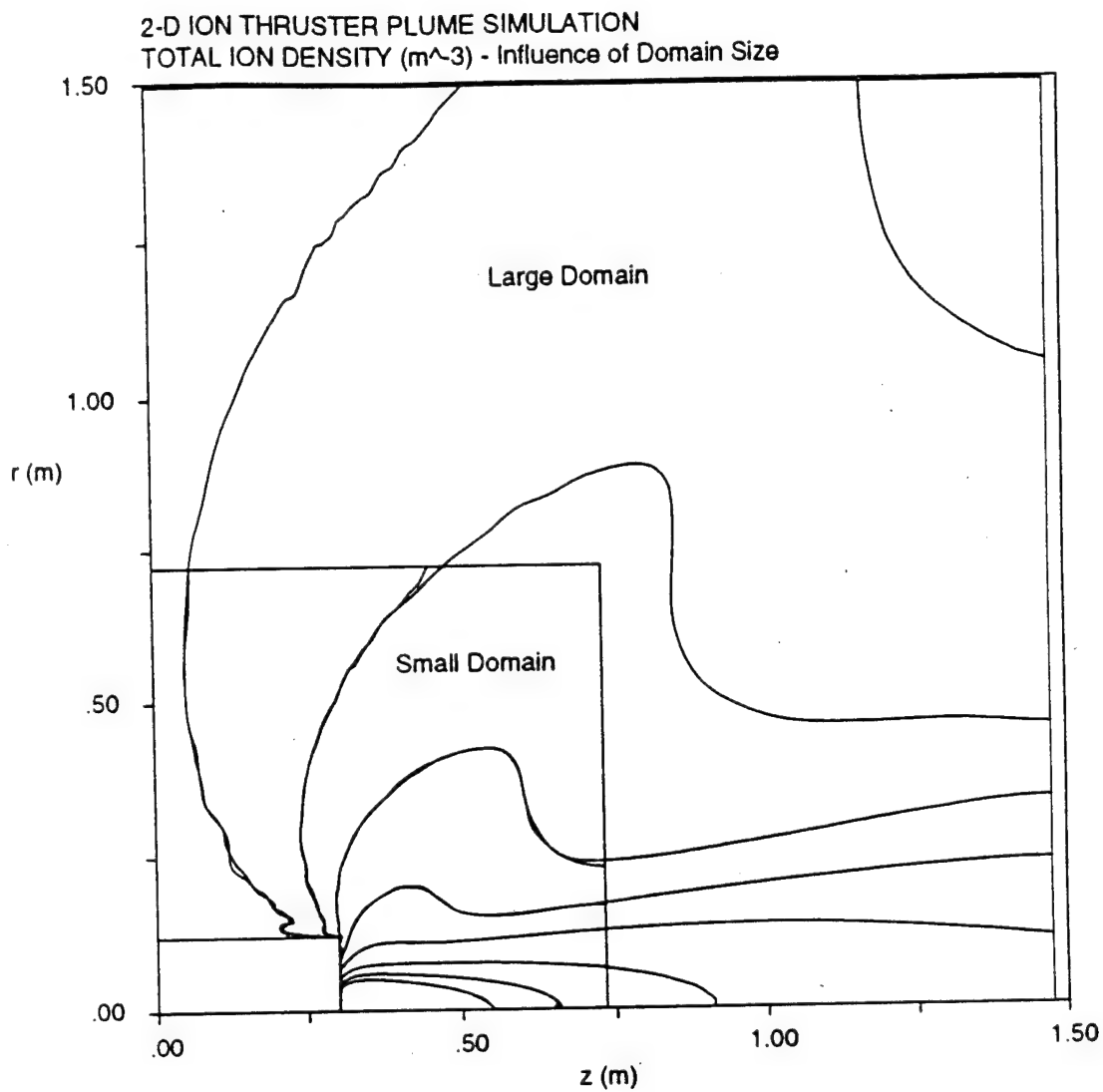


Figure 5.9 Independence of results on computational domain size. Comparison of the smoothed total ion density in a 0.75 m square domain with a 1.5 m square domain for *Kaufman Case A*

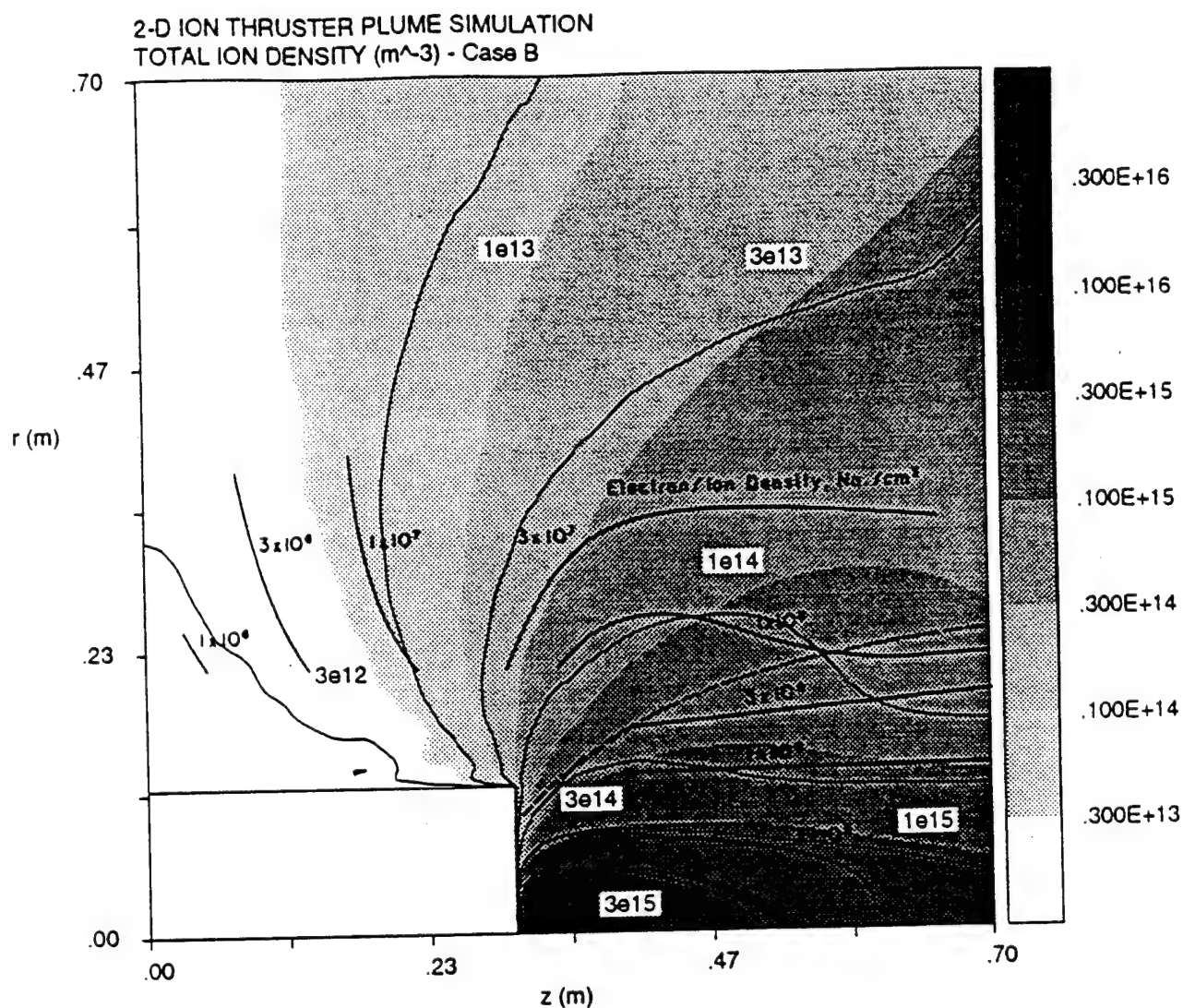


Figure 5.10 Contour plot of smoothed total ion density for *Kaufman* Case B conditions showing variable temperature (gray-scale), isothermal (thin line), and experimental measurements (bold line)

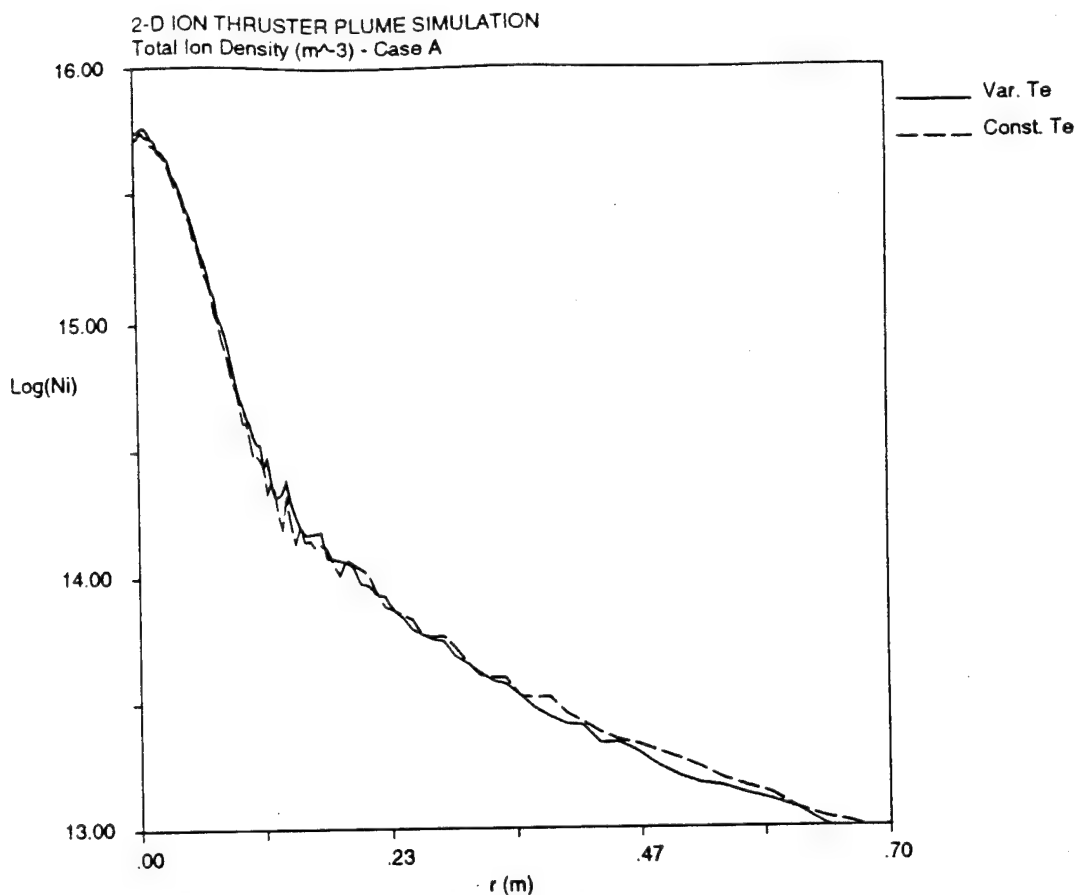


Figure 5.11 Radial cut 13 cm downstream of unsmoothed total ion density from variable and constant temperature models for *Kaufman* Case A

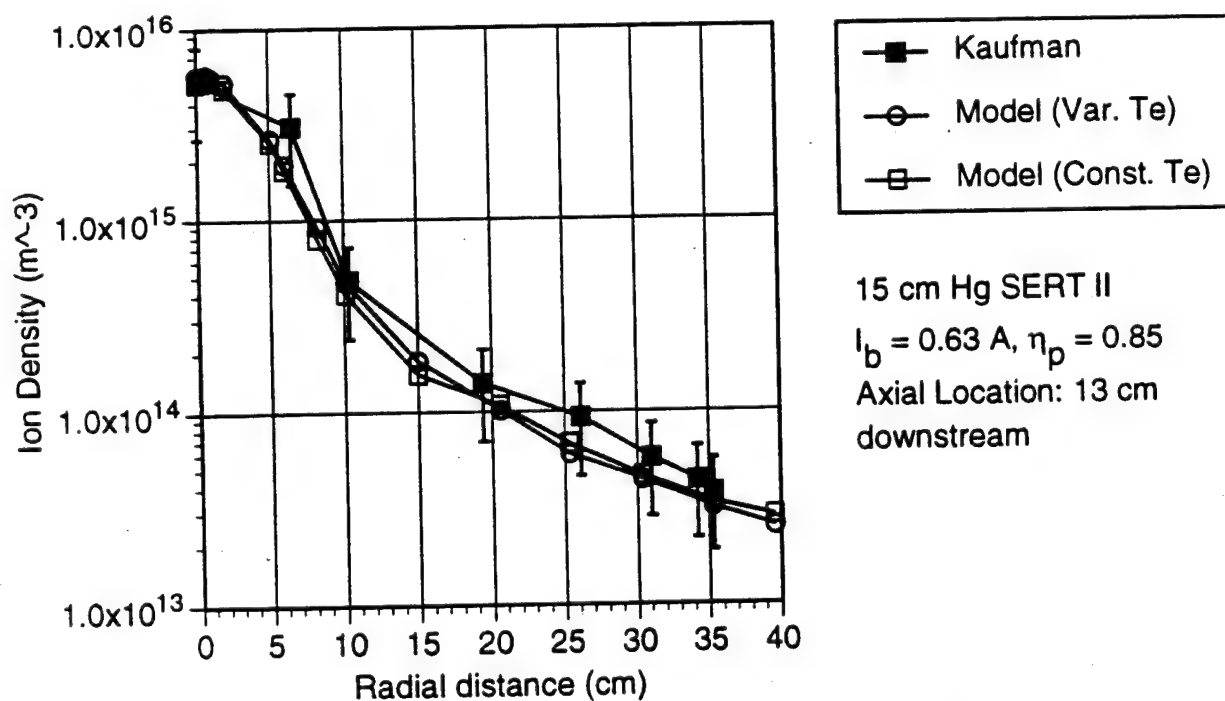


Figure 5.12 Radial ion density profile: comparison of model (Figure 5.11) with data

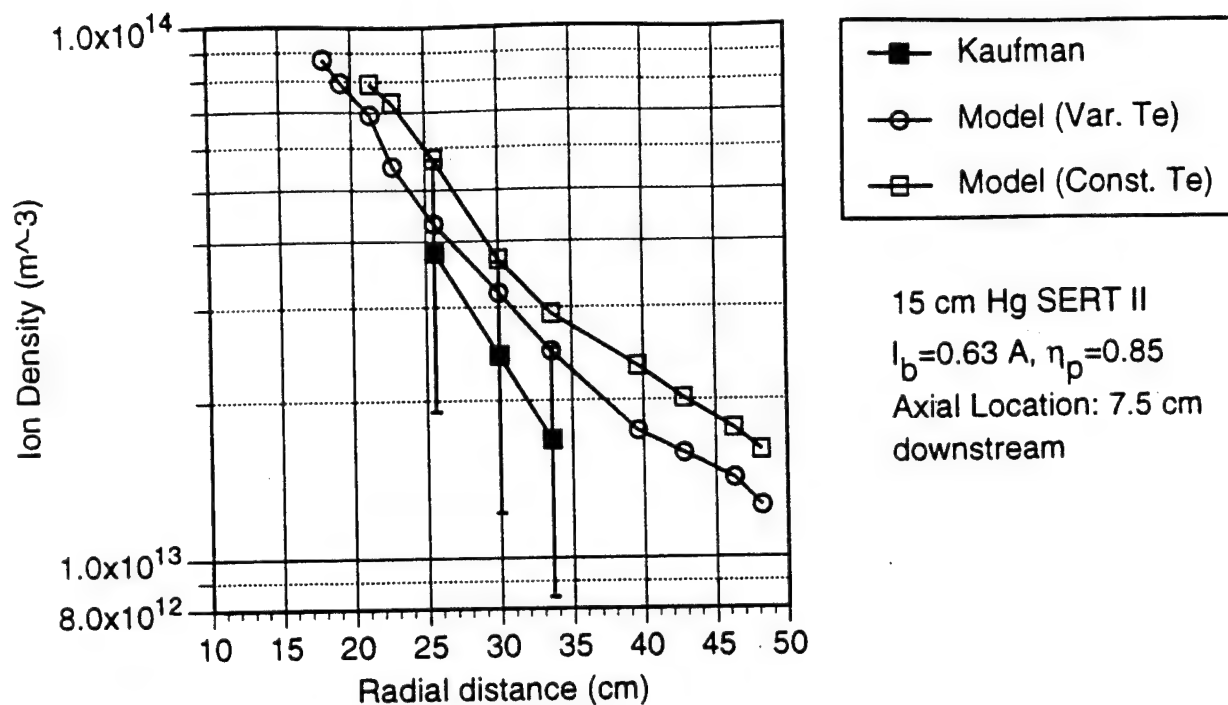


Figure 5.13 Radial ion density values: *Kaufman* Case A data vs. model (variable and constant Te) 7.5 cm downstream

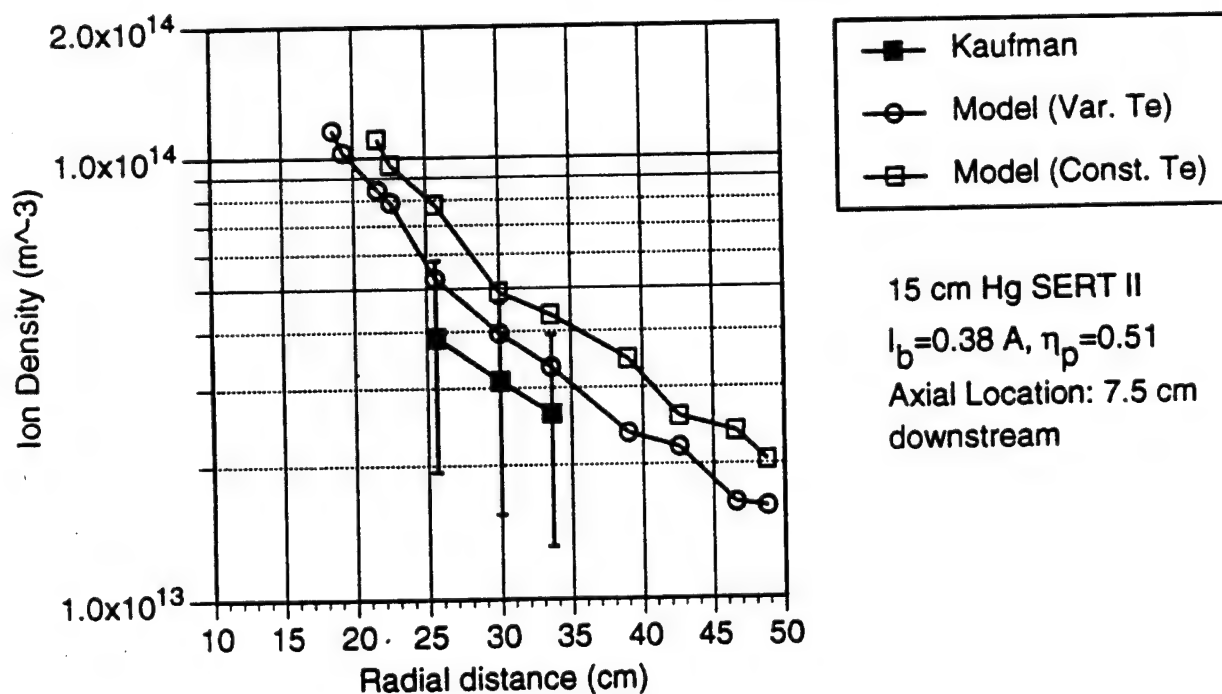


Figure 5.14 Radial ion density values: *Kaufman* Case B data vs. model (variable and constant Te) 7.5 cm downstream

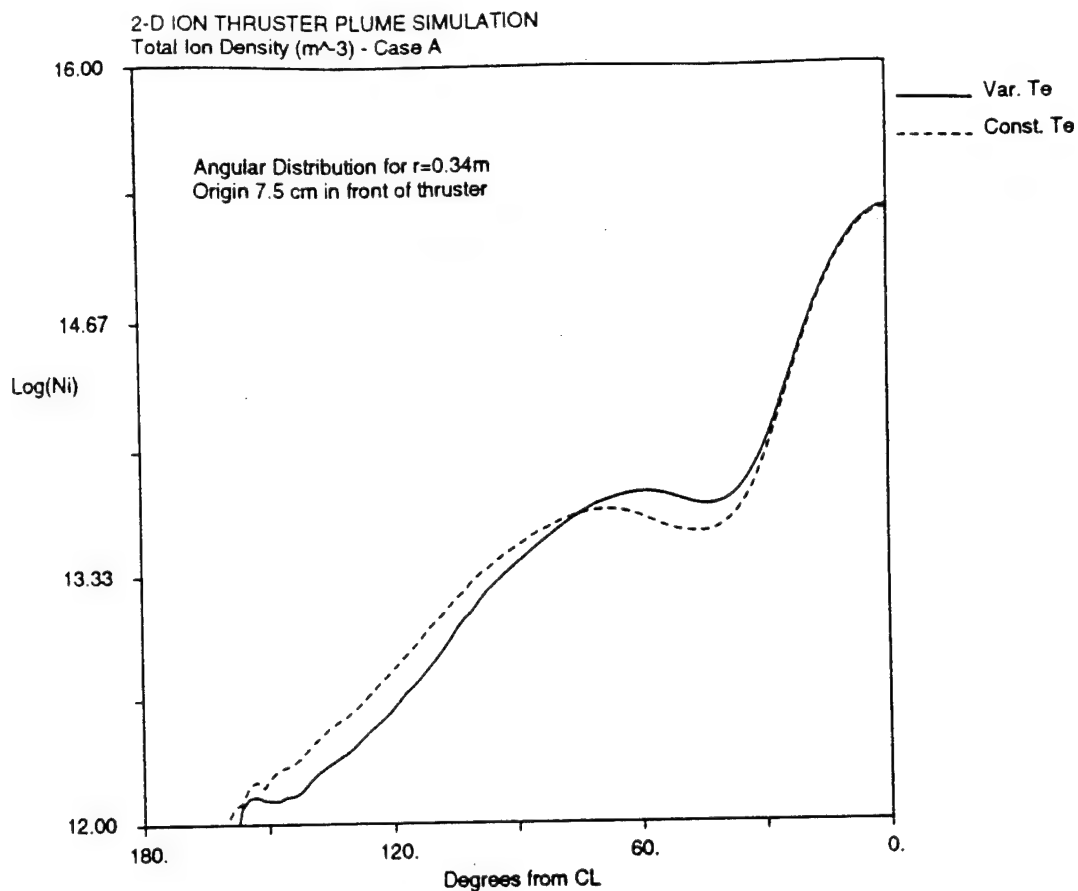


Figure 5.15 Smoothed ion density along an arc a distance 34 cm from a point 7.5 cm downstream; model results for both variable and constant temperature for *Kaufman* Case A conditions

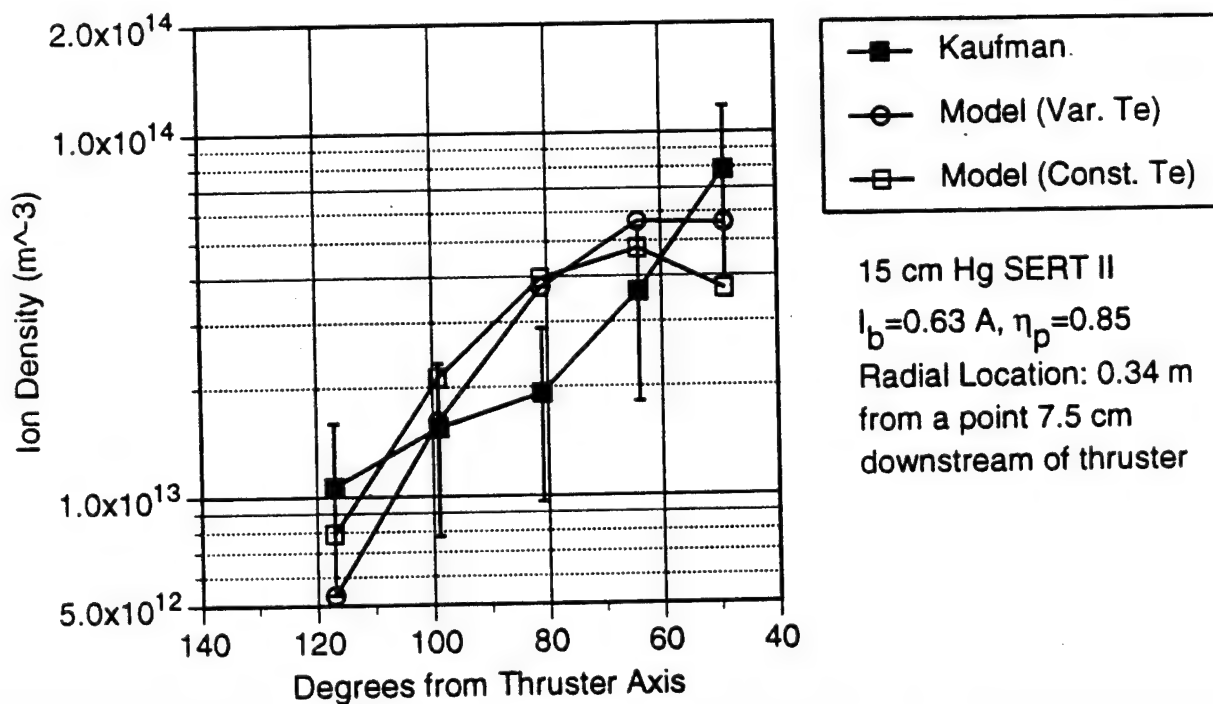


Figure 5.16 Comparison of model results (Figure 5.15) with data

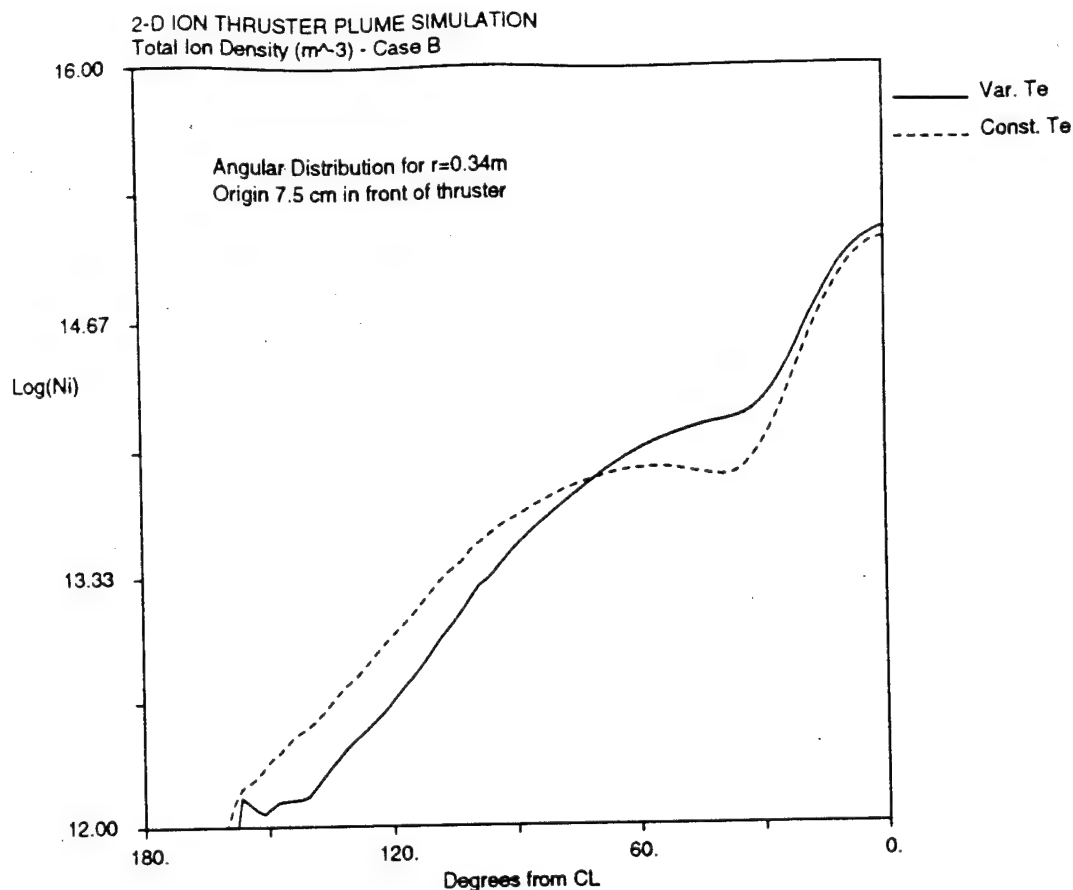


Figure 5.17 Smoothed ion density along an arc a distance 34 cm from a point 7.5 cm downstream; model results for both variable and constant temperature for *Kaufman* Case B conditions

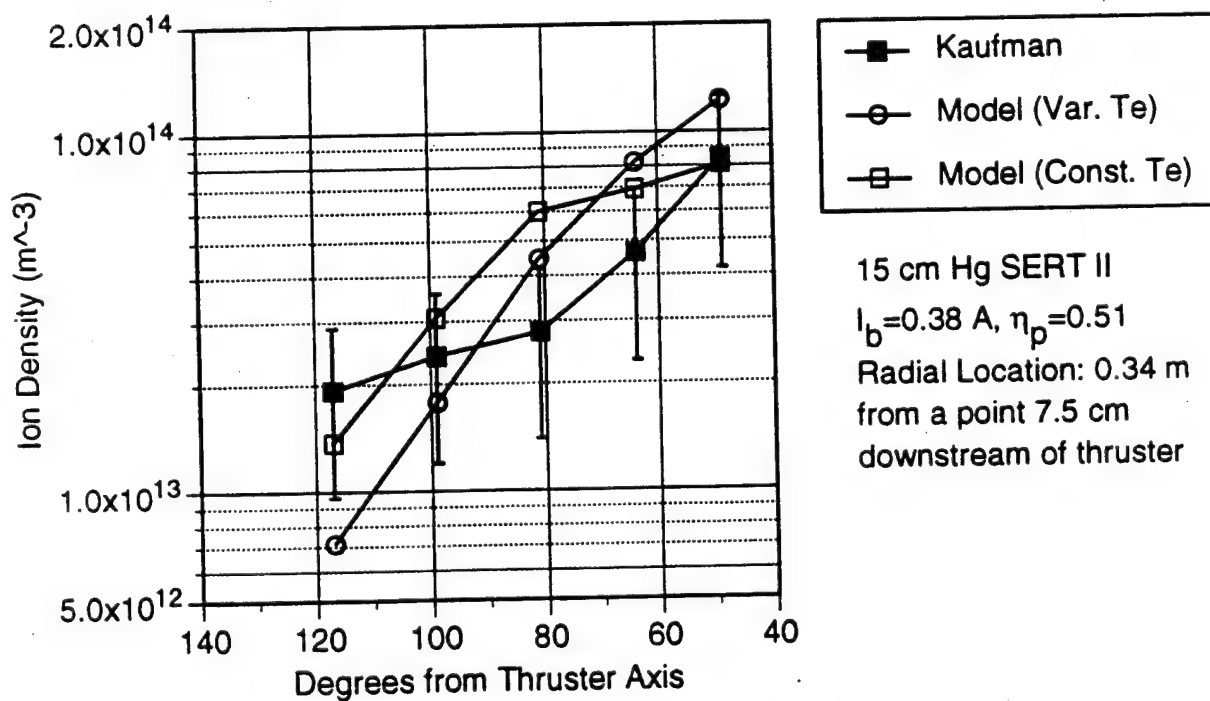


Figure 5.18 Comparison of model results (Figure 5.17) with data

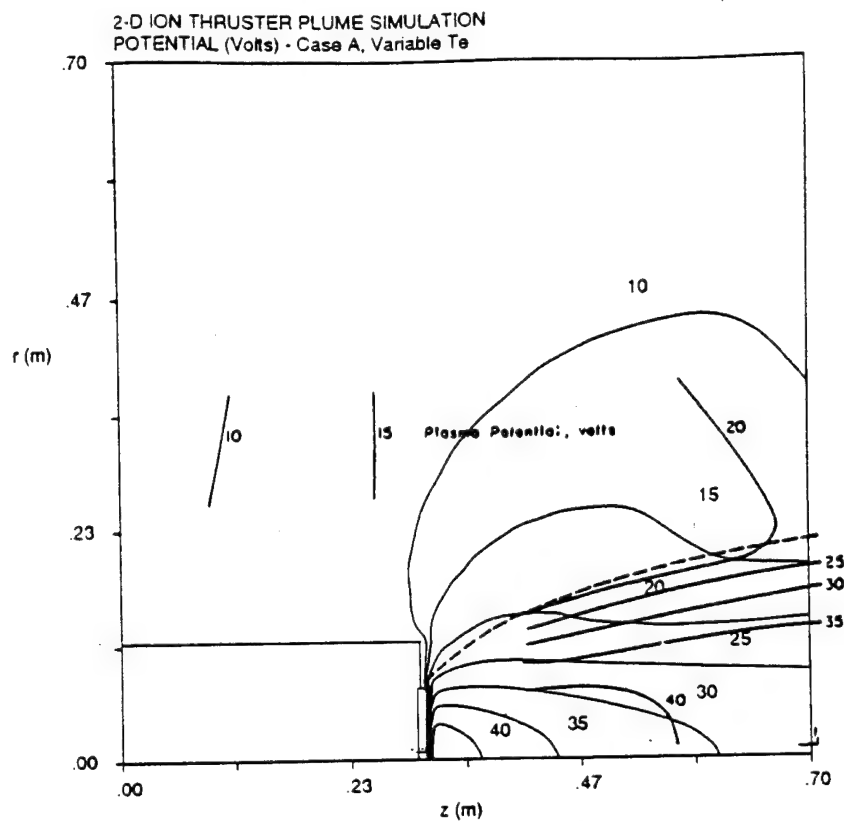
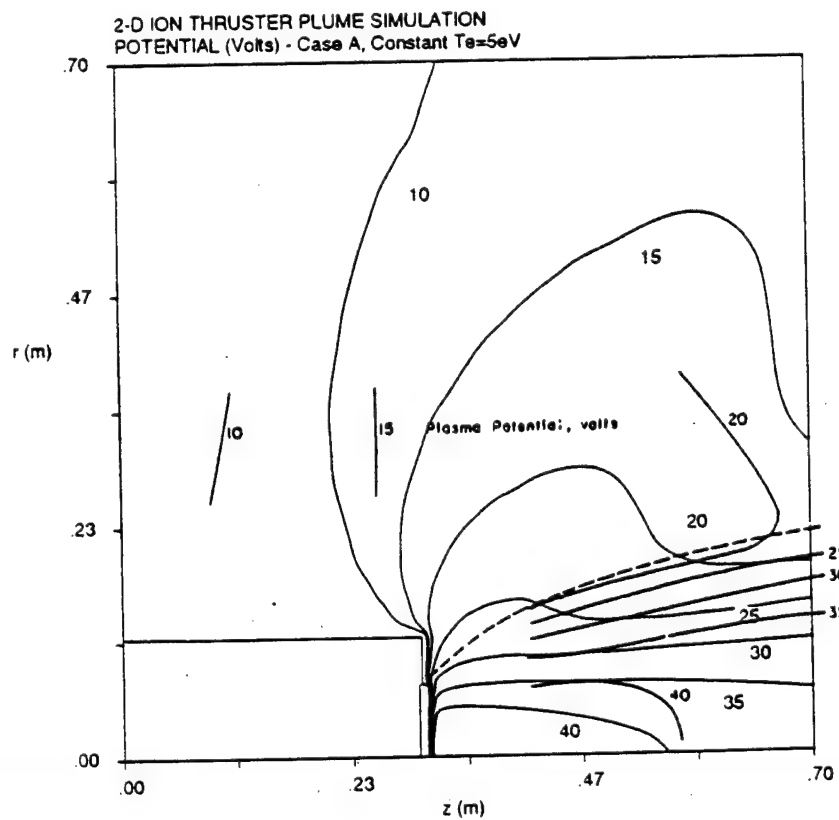


Figure 5.19 Potential contours for a) variable and b) constant temperature models for *Kaufman* Case A, overlaid with experimental measurements



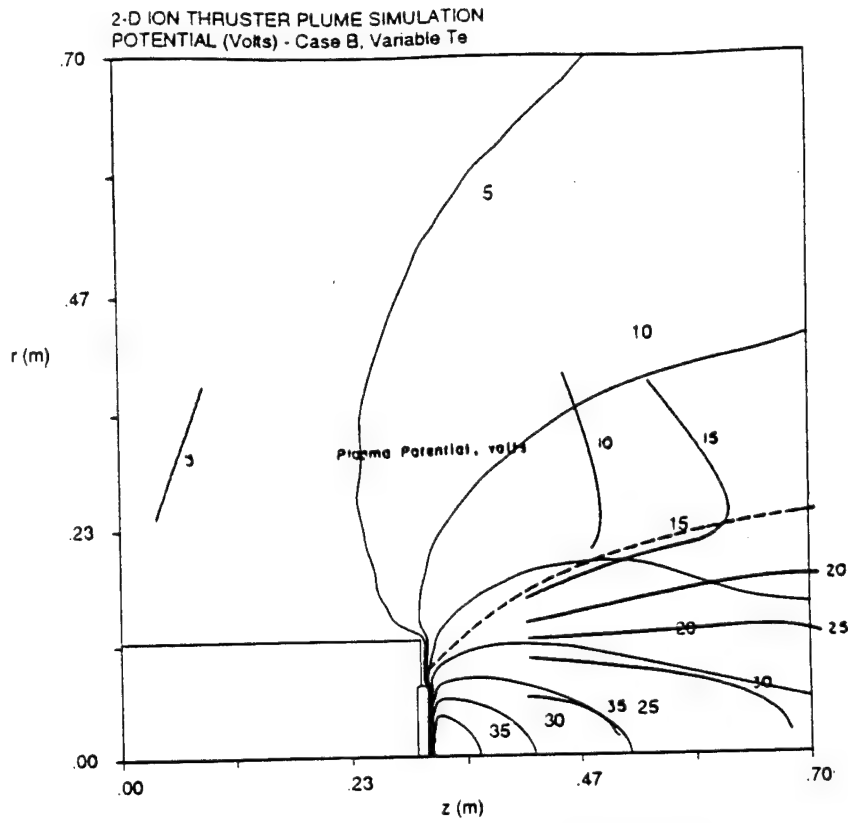
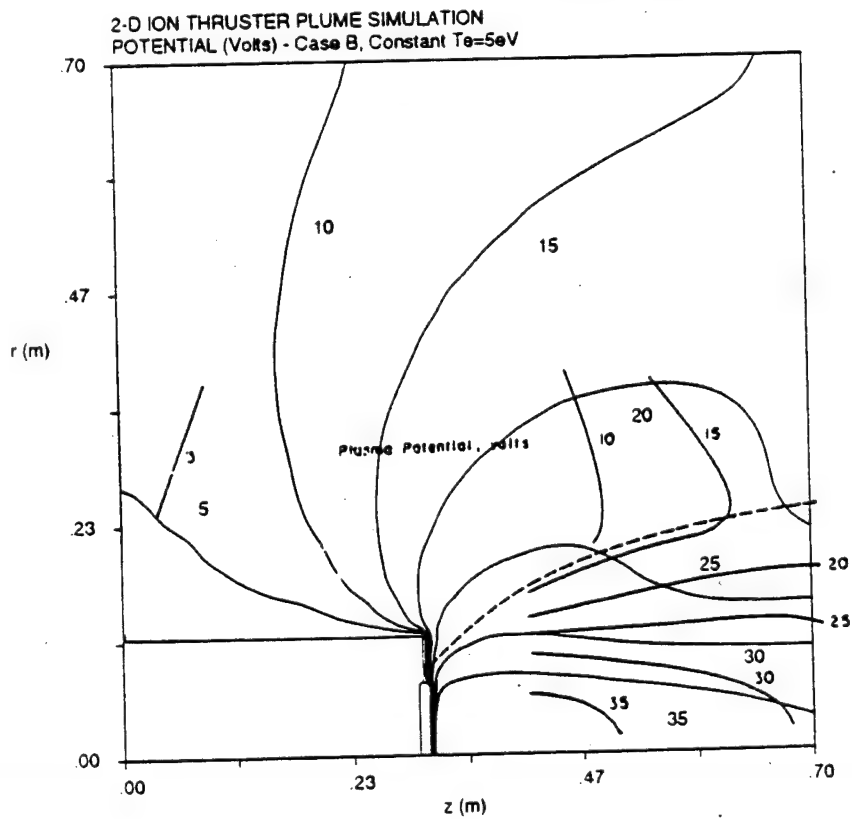


Figure 5.20 Potential contours for a) variable and b) constant temperature models for *Kaufman* Case B, overlaid with experimental measurements





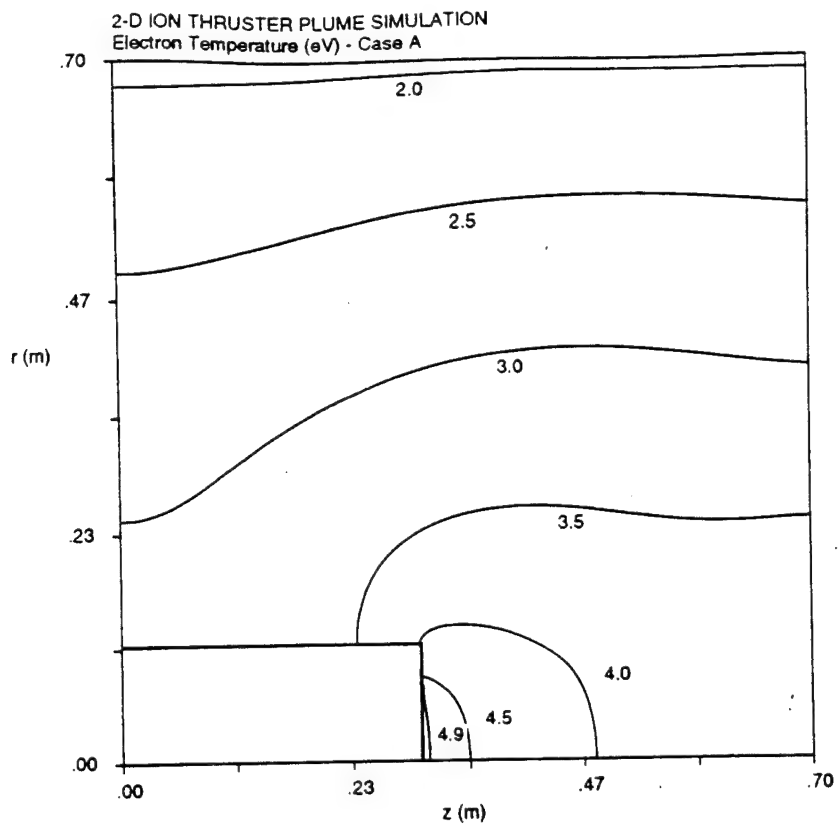
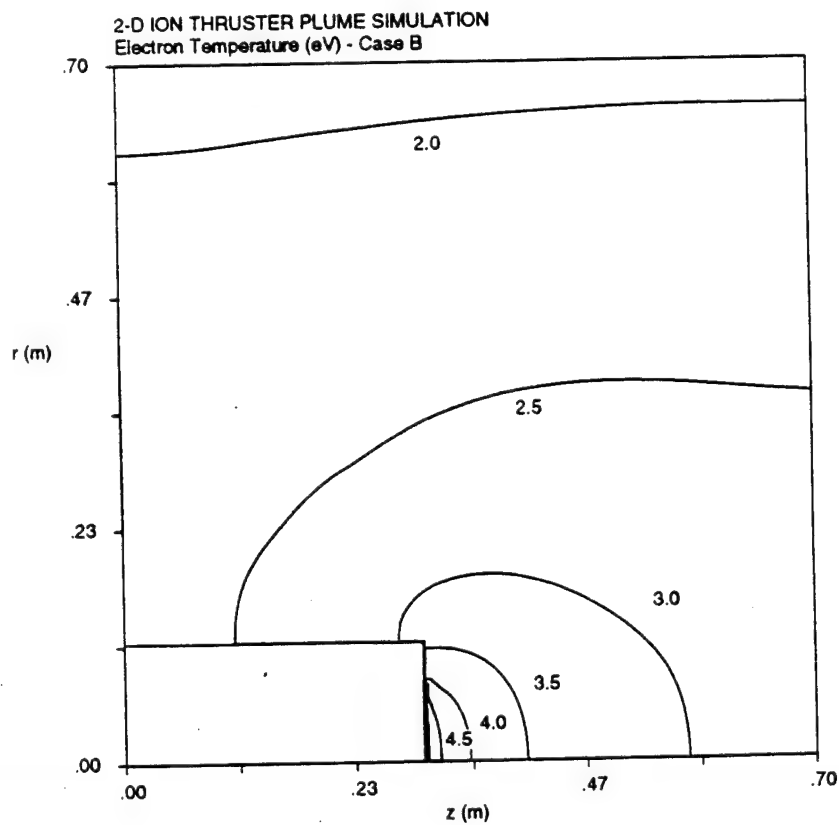


Figure 5.21 Contours of electron temperature computed for a) Case A and b) Case B



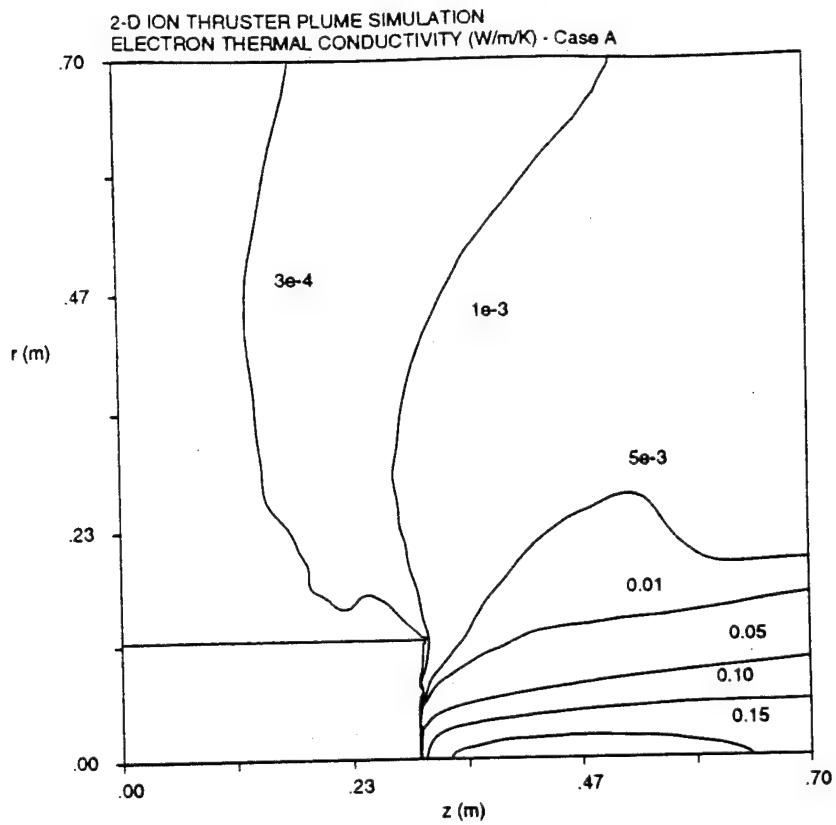
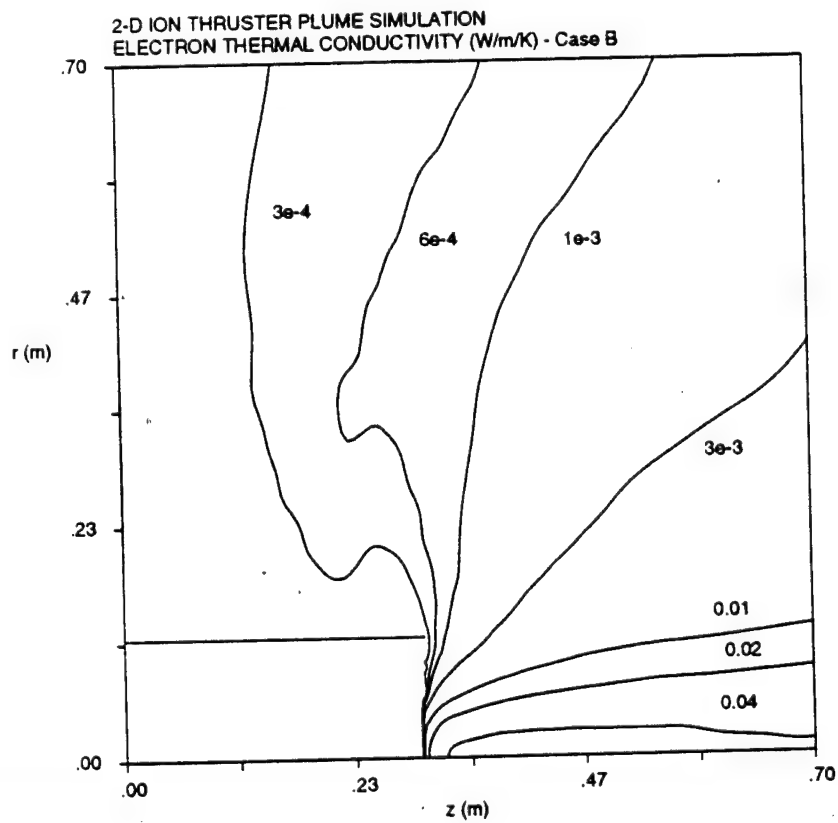


Figure 5.22 Contours of electron thermal conductivity for a) Case A and b) Case B



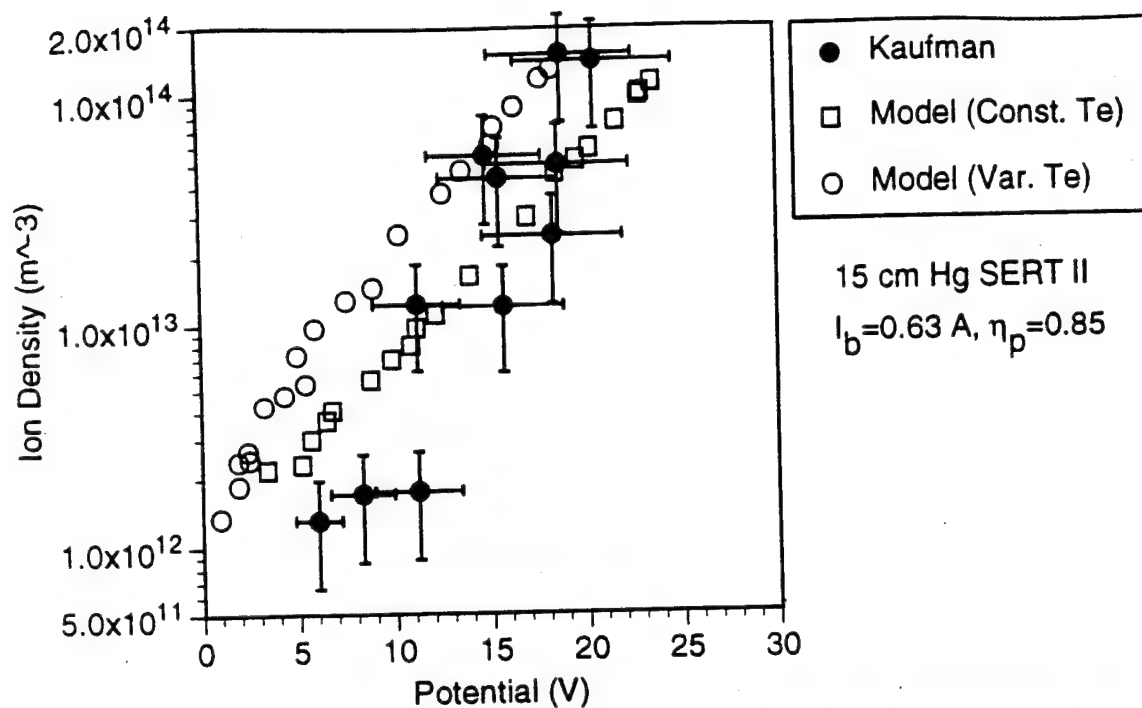


Figure 5.23a Plasma density vs. potential; comparison with data for *Kaufman* Case A

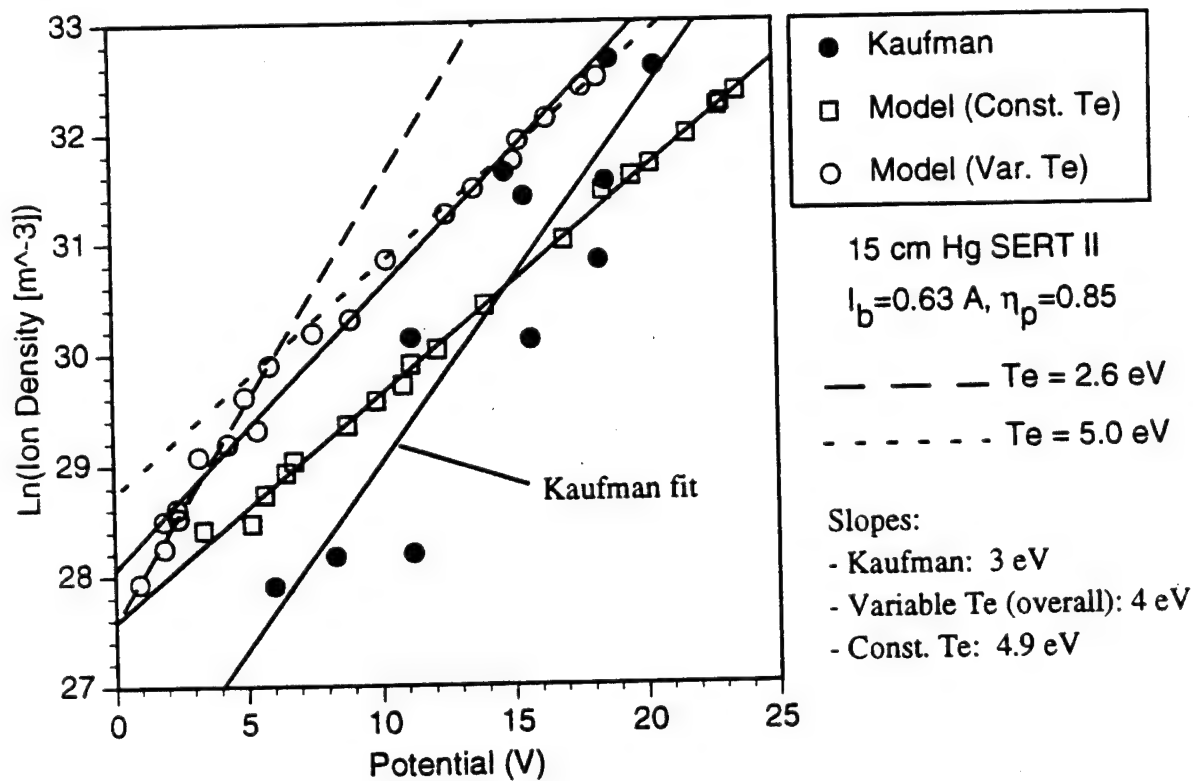


Figure 5.23b Same data as above; Ln plot for extracting electron temperature

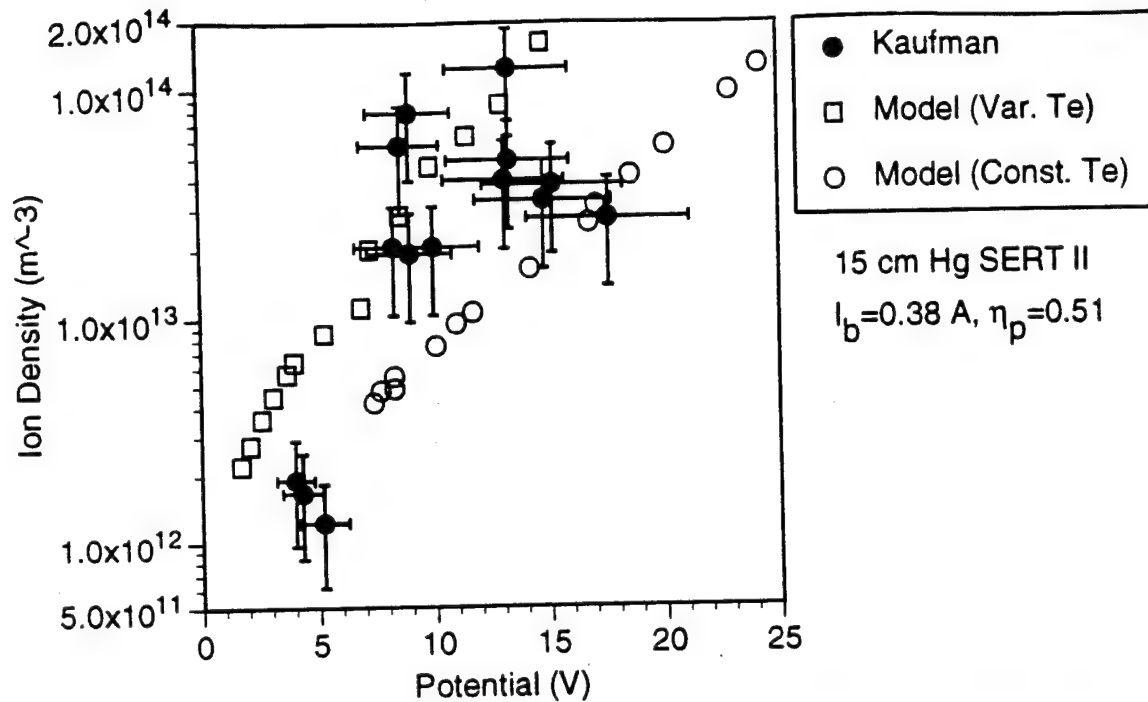


Figure 5.24a Plasma density vs. potential; comparison with data for *Kaufman* Case B

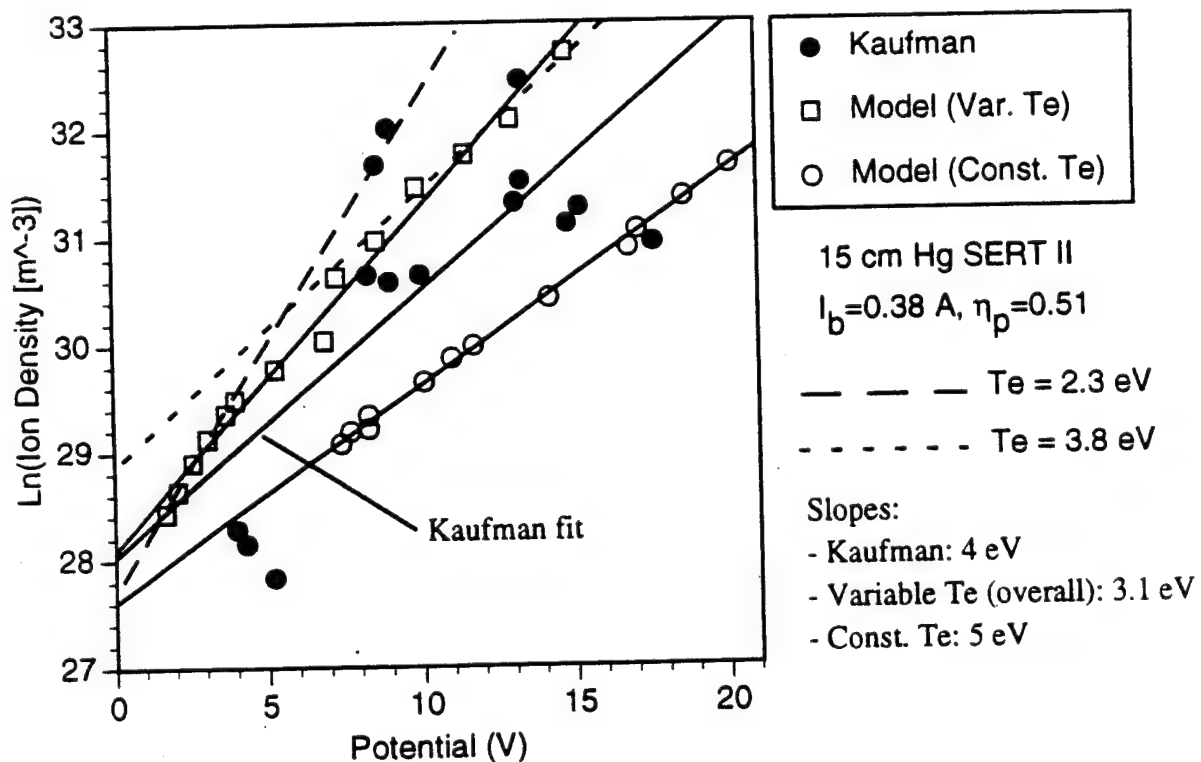


Figure 5.24b Same data as above; Ln plot for extracting electron temperature

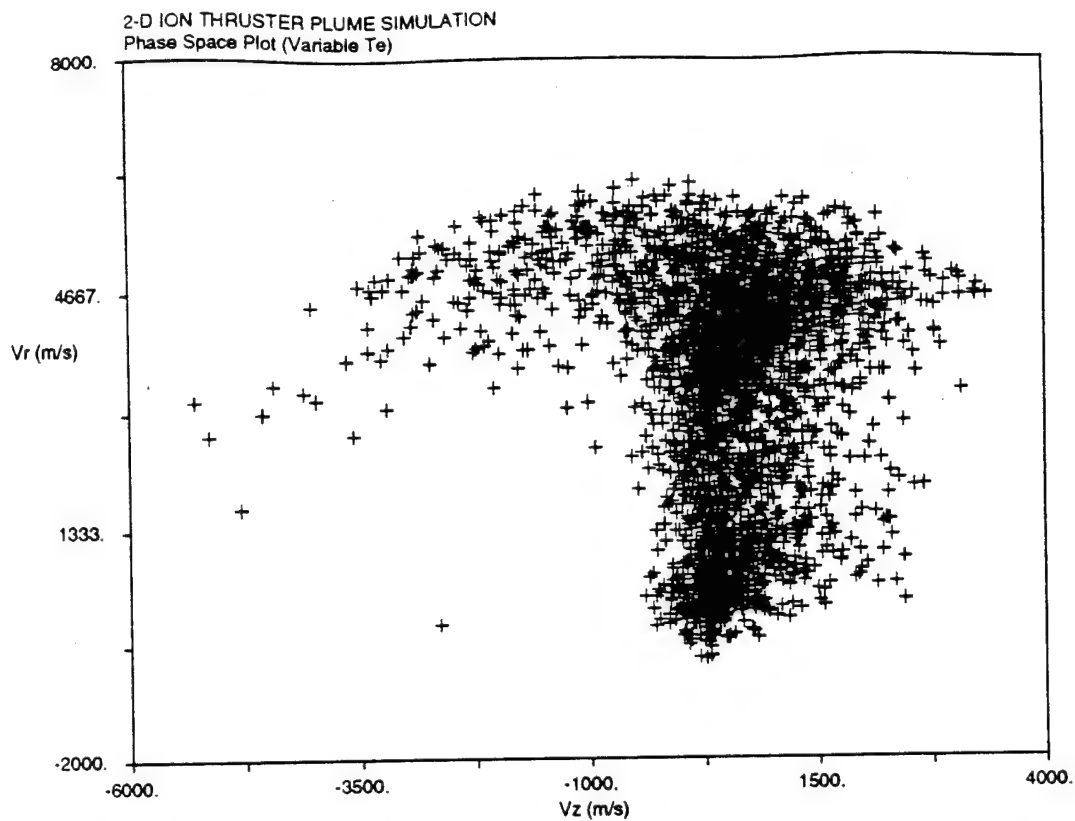
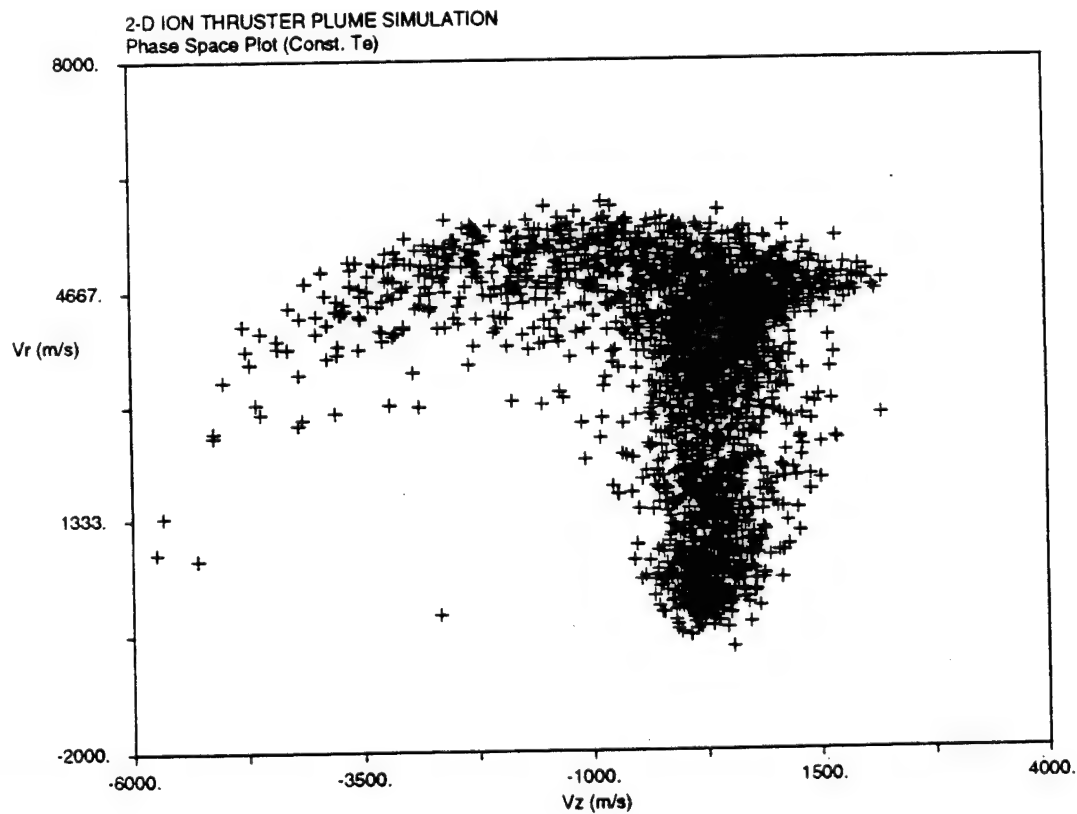


Figure 5.25 Phase phase plots of CEX ions: radial vs. axial velocity for *Kaufman* Case A, a) variable and b) constant temperature models



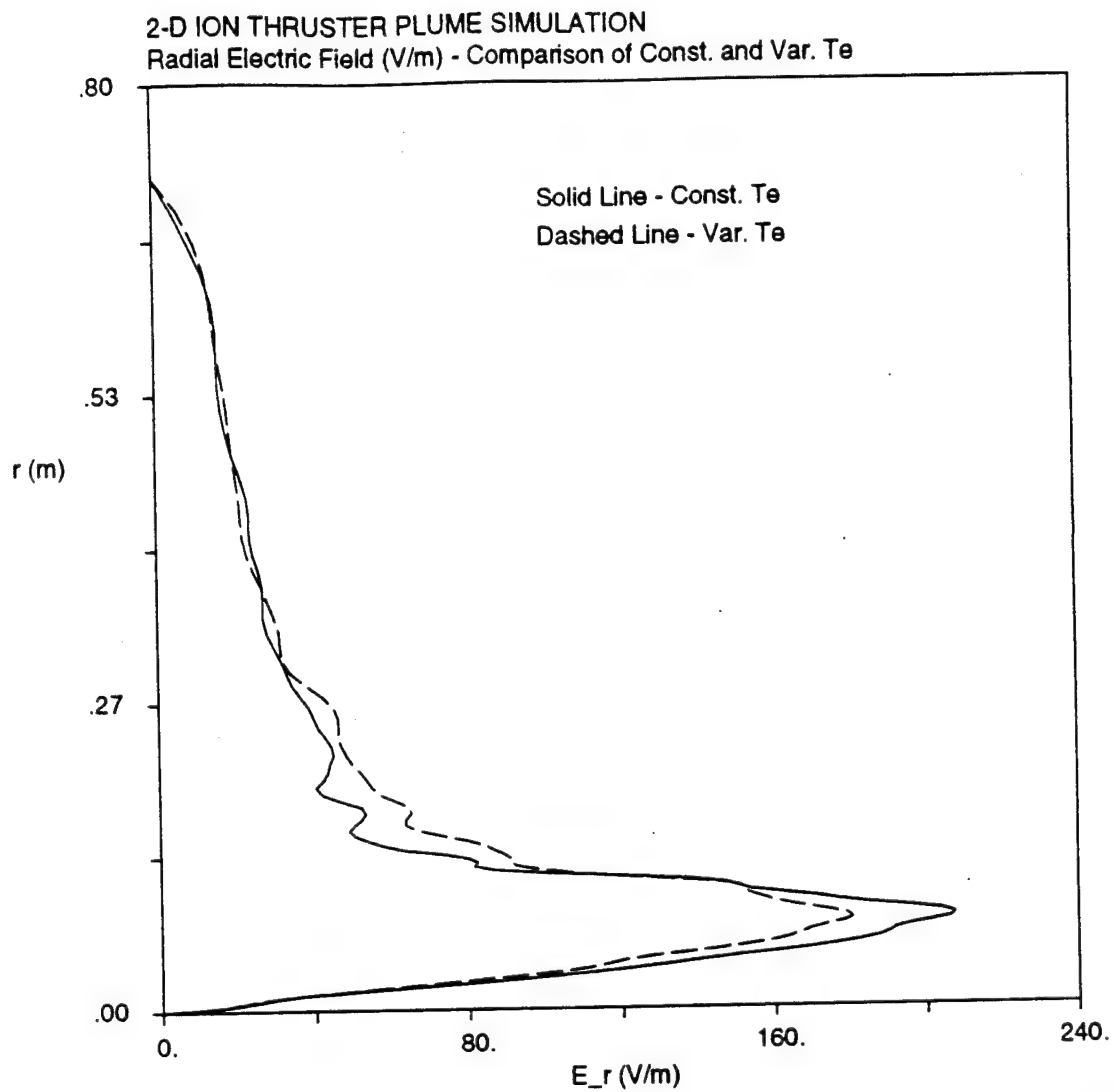


Figure 5.26 Comparison of radial electric fields for Case A from variable temperature and isothermal models

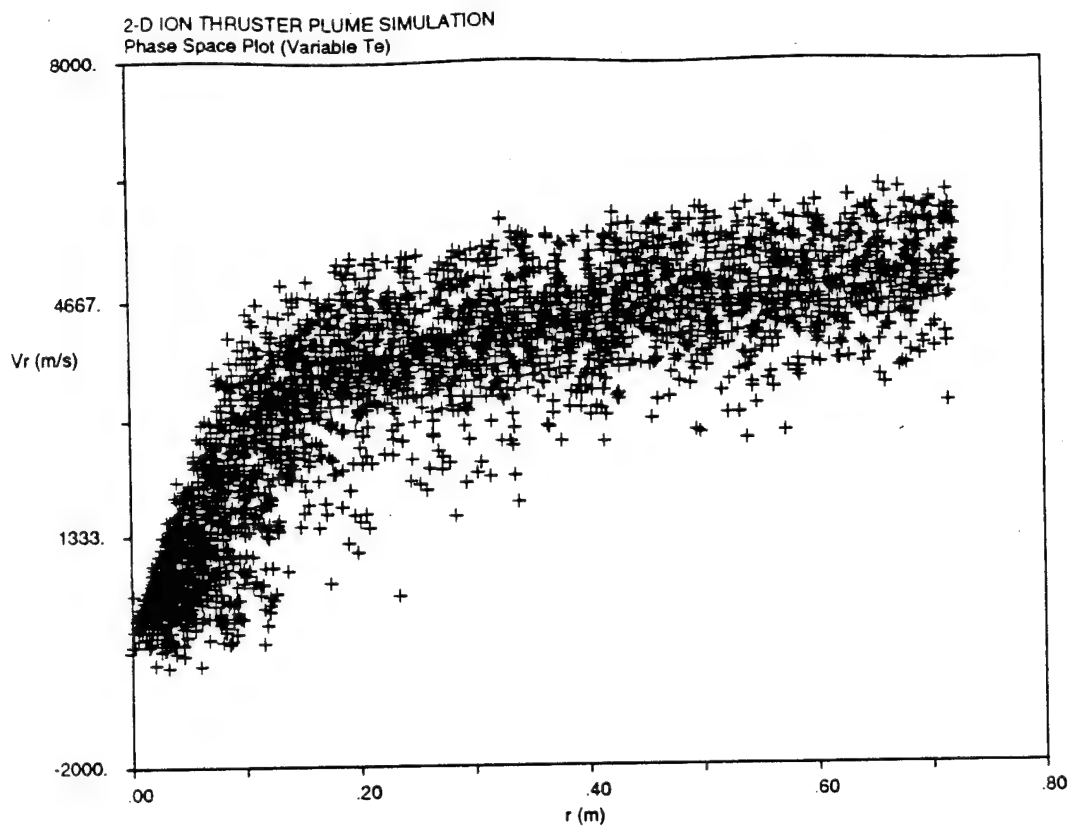
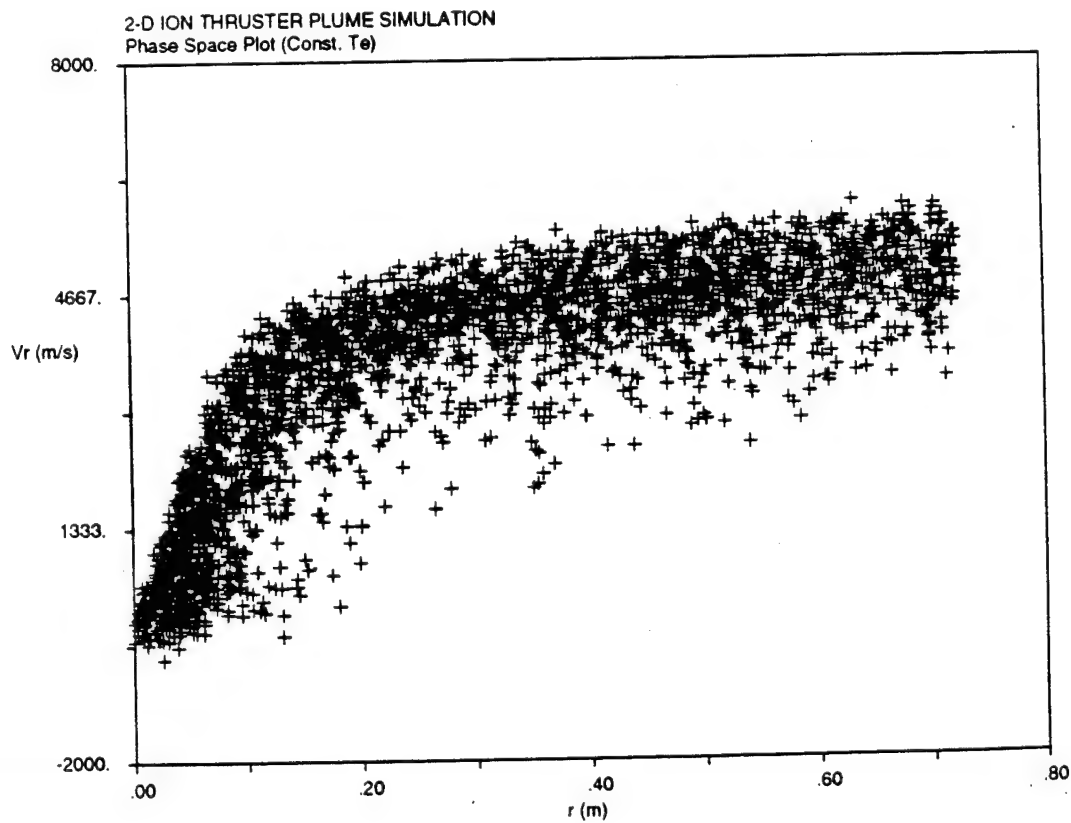


Figure 5.27 Phase phase plots of CEX ions: radial velocity vs. radial position for *Kaufman* Case A, a) variable temperature and b) isothermal models



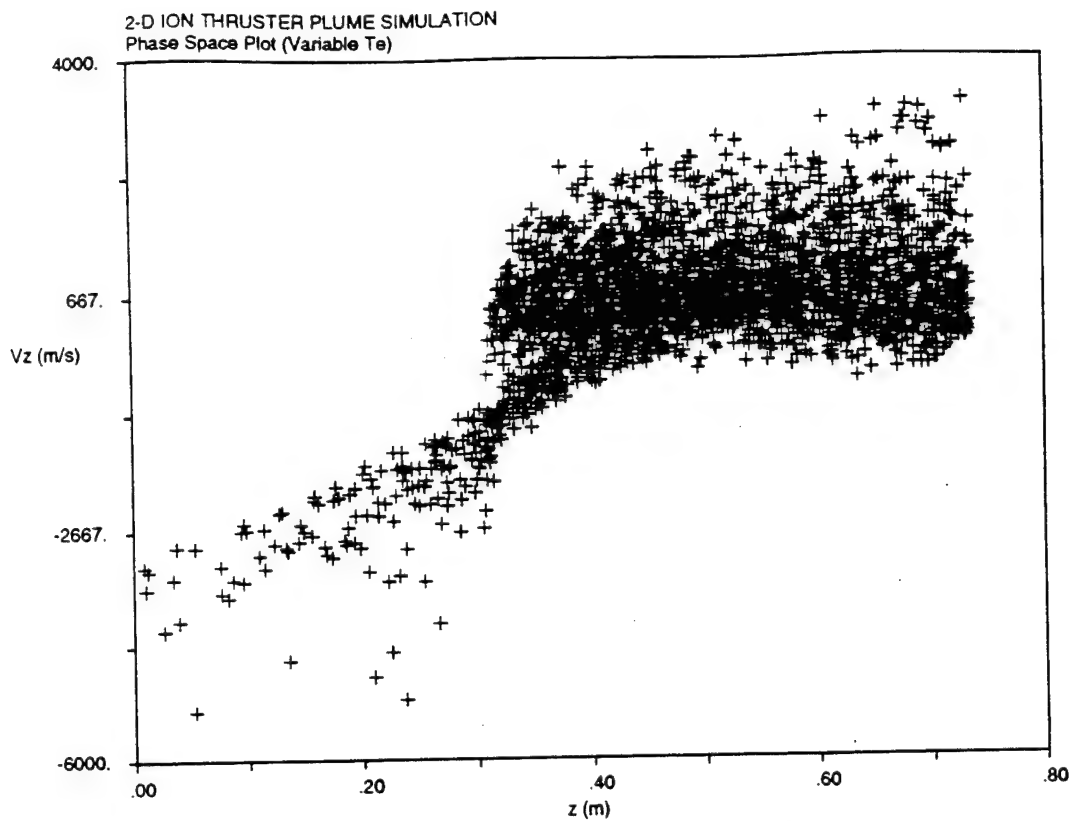
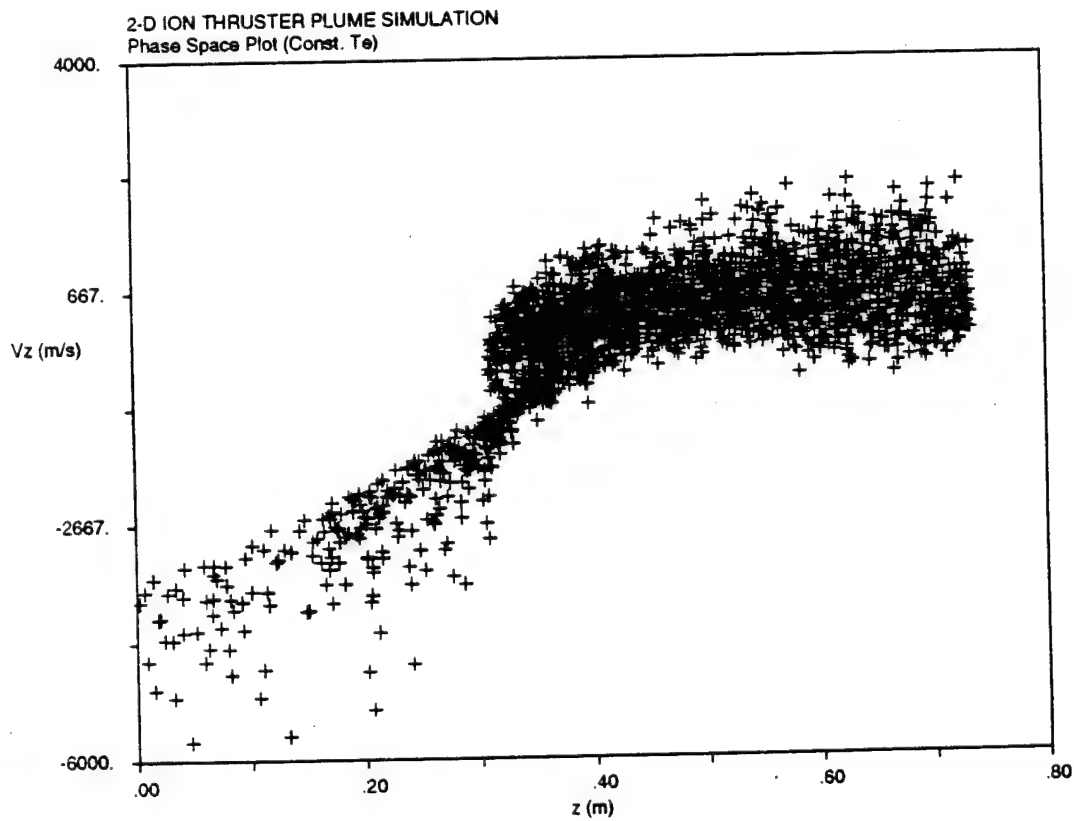


Figure 5.28 Phase phase plots of CEX ions: axial velocity vs. axial position for *Kaufman* Case A, a) variable temperature and b) isothermal models





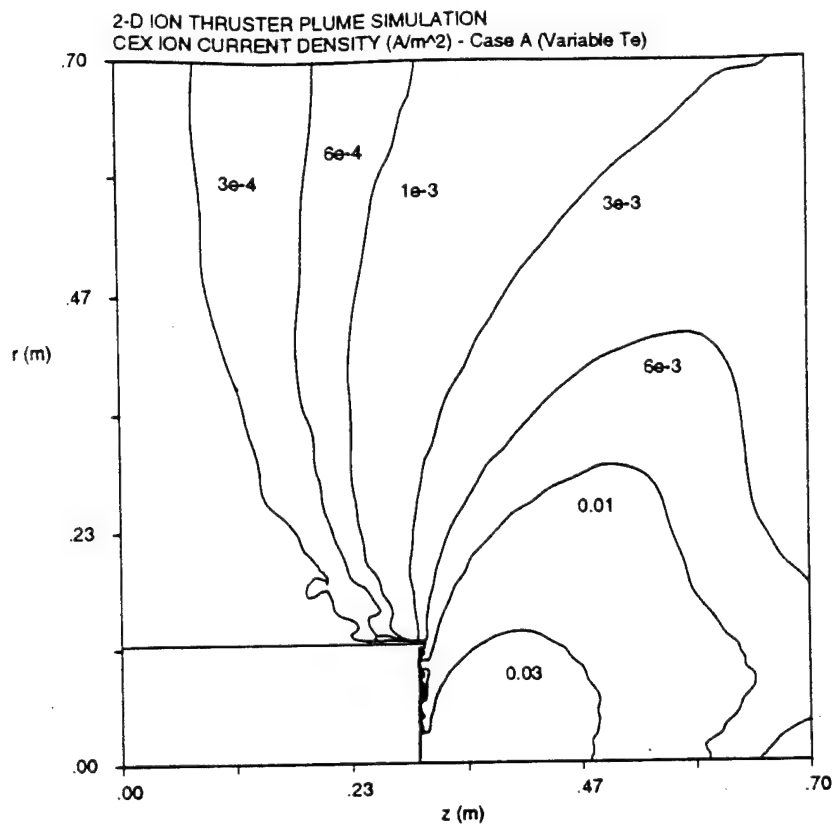
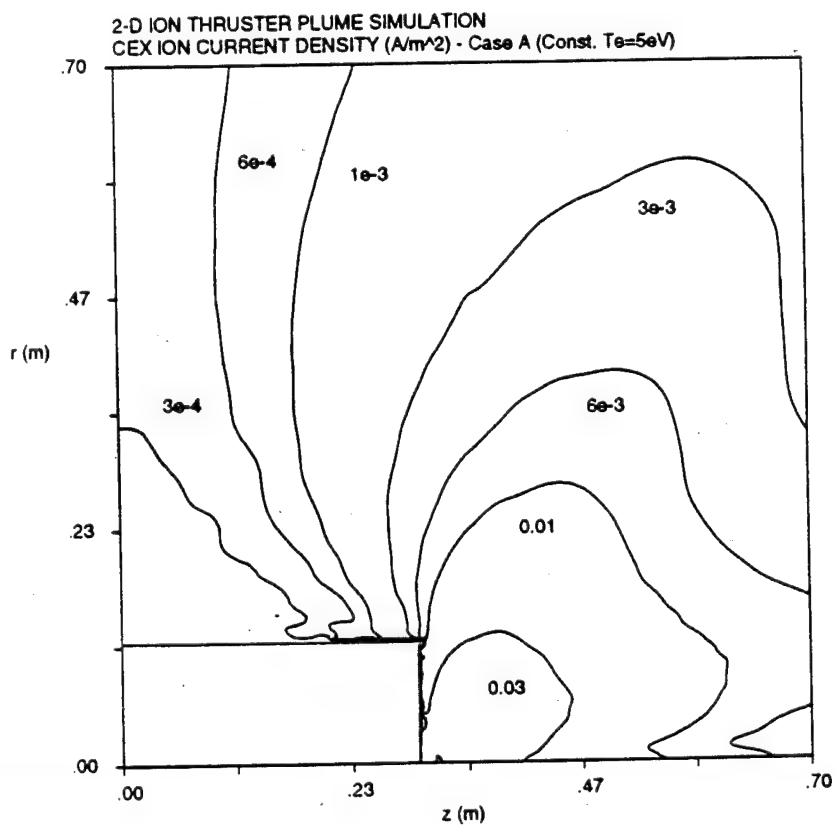


Figure 5.29 CEX ion current density contours for *Kaufman* Case A, a) variable temperature and b) isothermal models



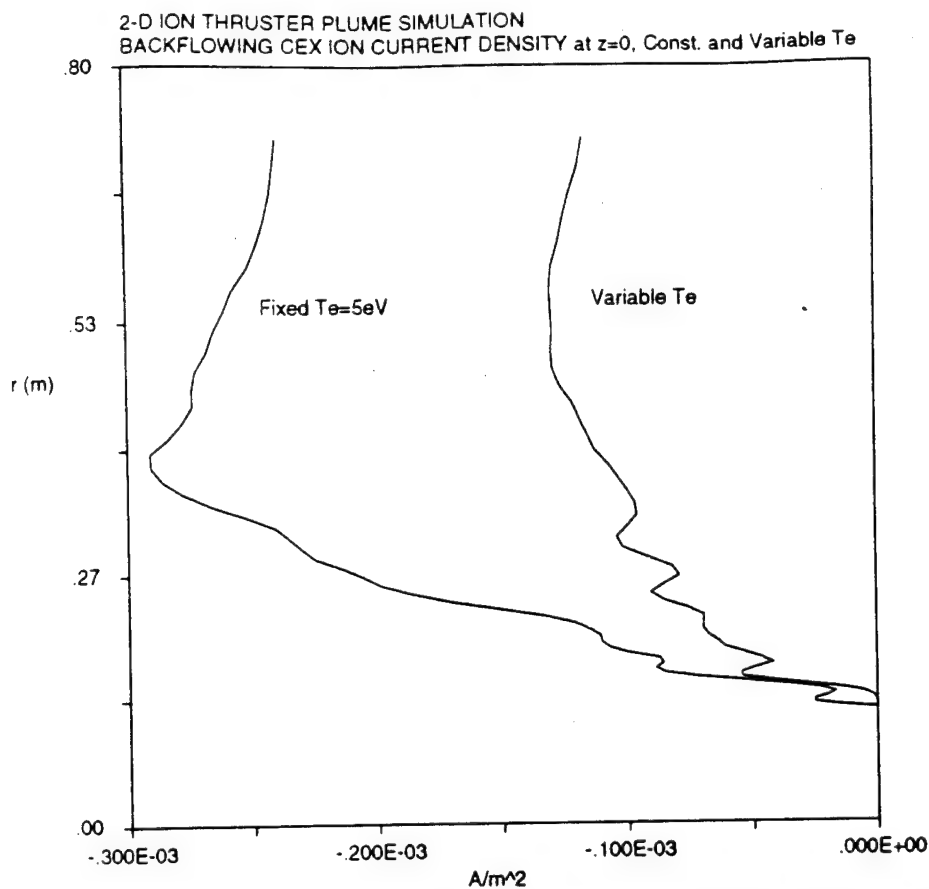


Figure 5.30 CEX ion current density at  $z=0$  for *Kaufman* Case A, variable temperature and isothermal model results

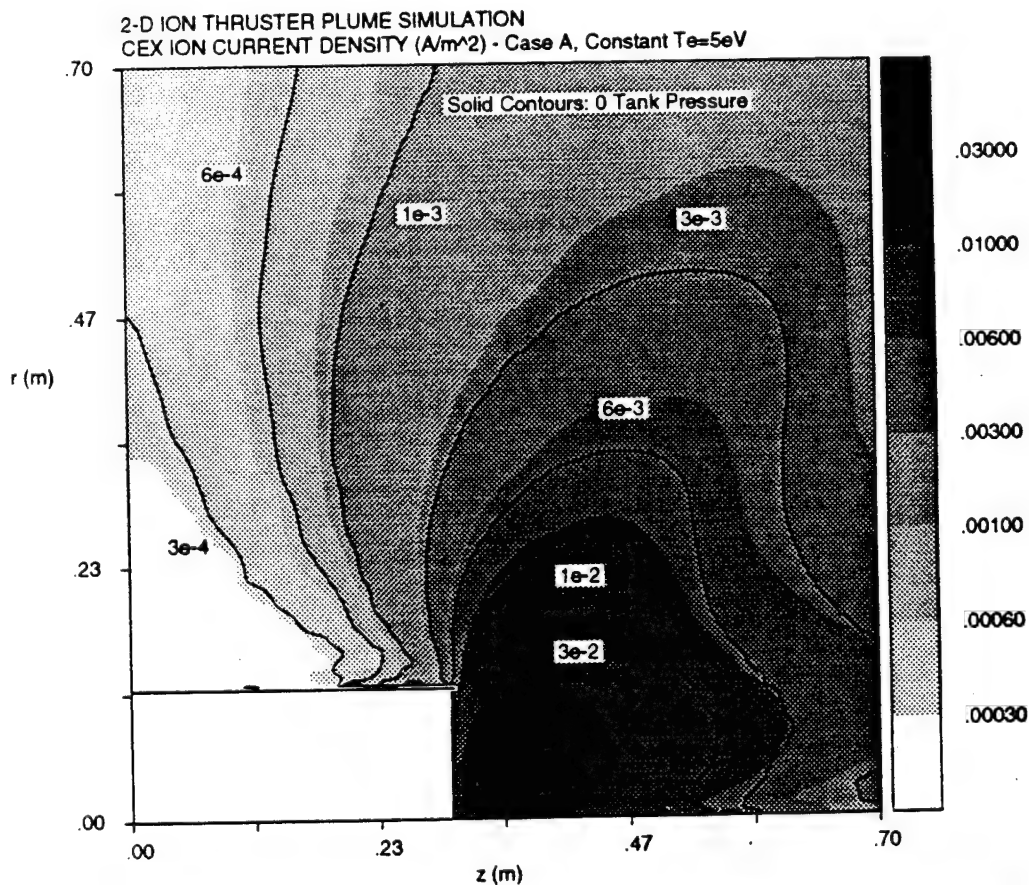


Figure 5.31 CEX ion current contours for *Kaufman* Case A, (isothermal) with background pressure (gray-scale) and without (solid line)

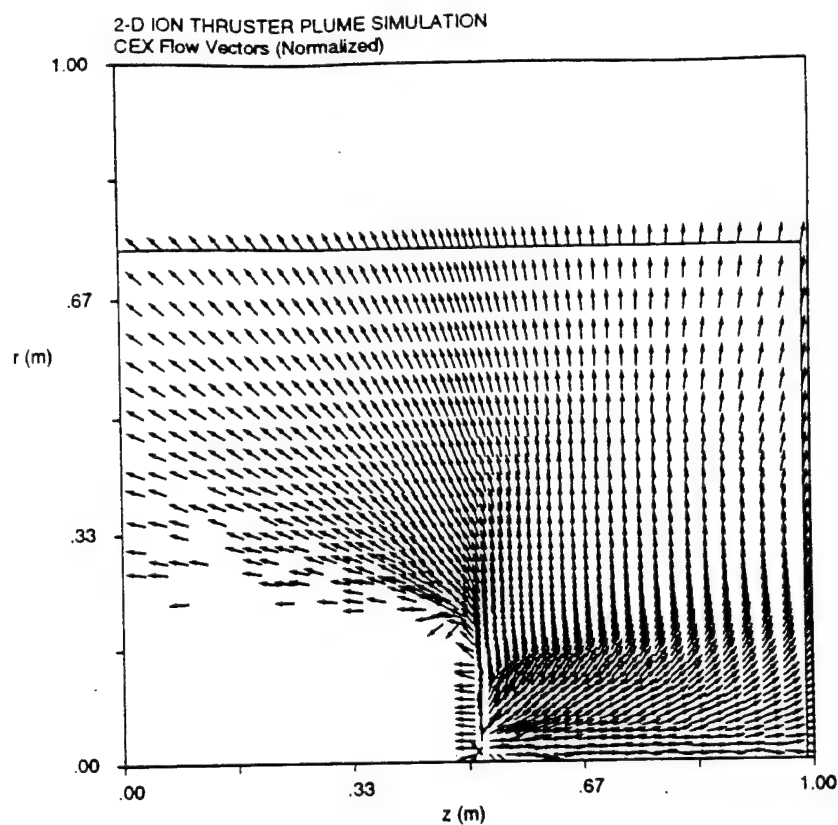


Figure 5.32 CEX ion current density vector field (normalized)

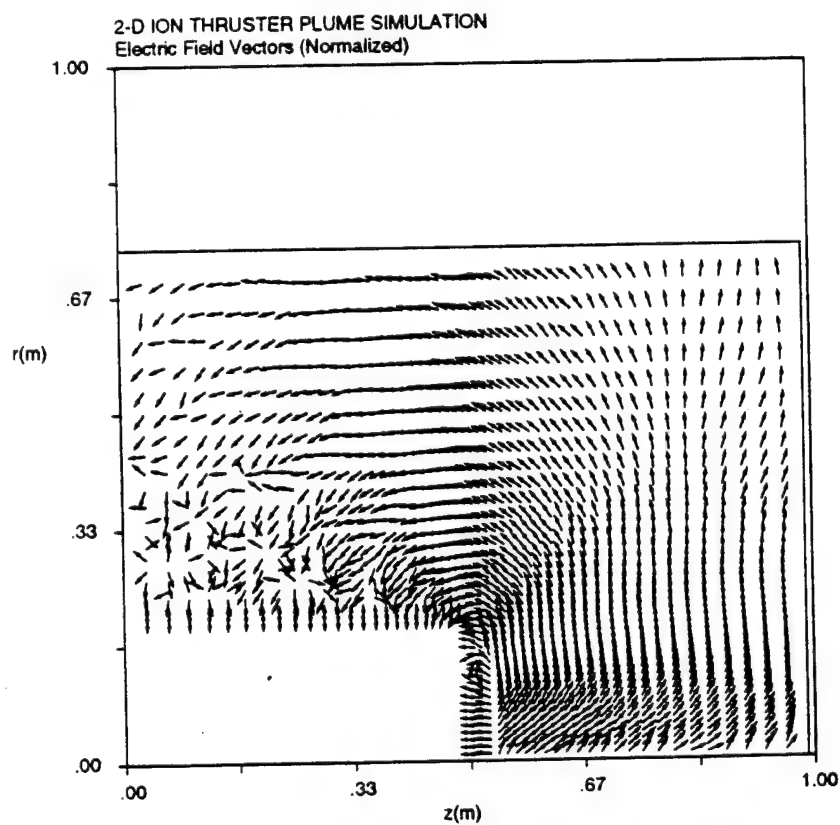


Figure 5.33 Electric field vector plot (normalized)

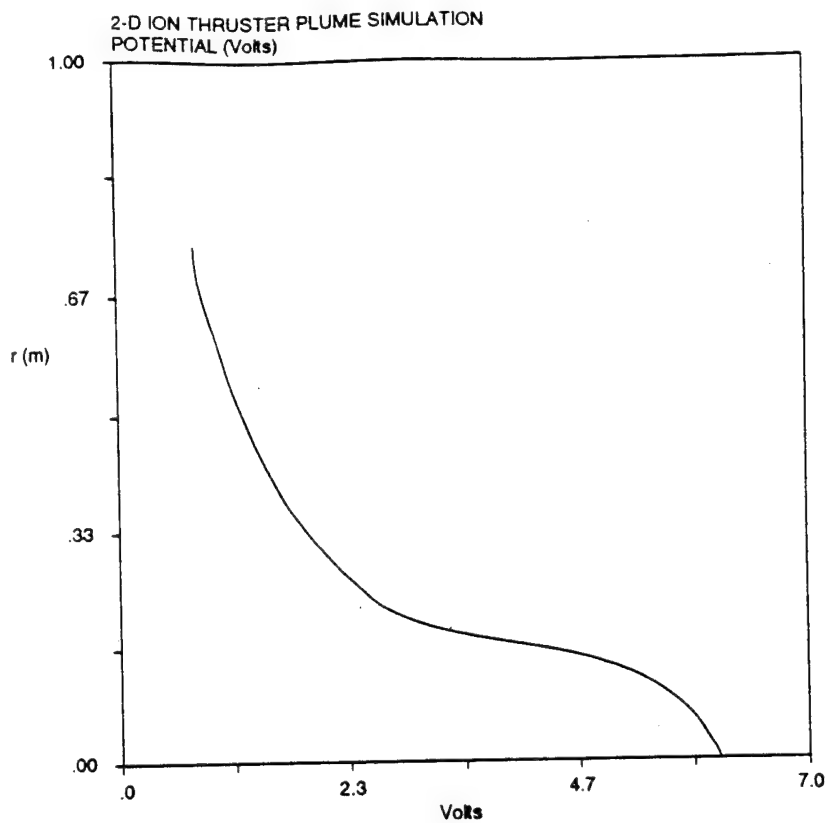
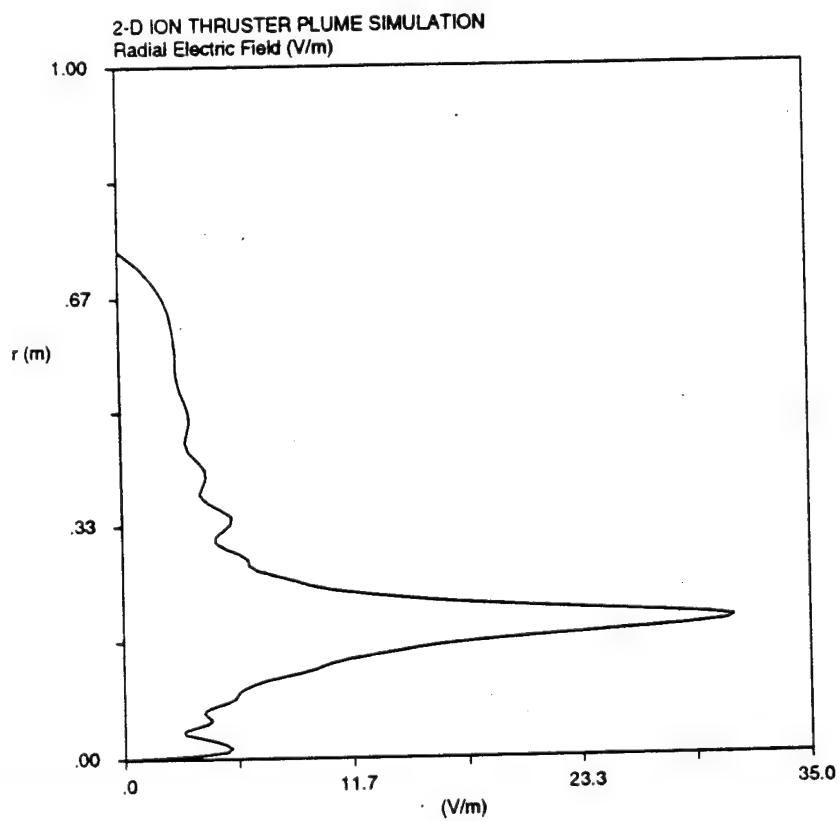


Figure 5.34 a) Radial potential and b) electric field cuts through the beam 10 cm downstream



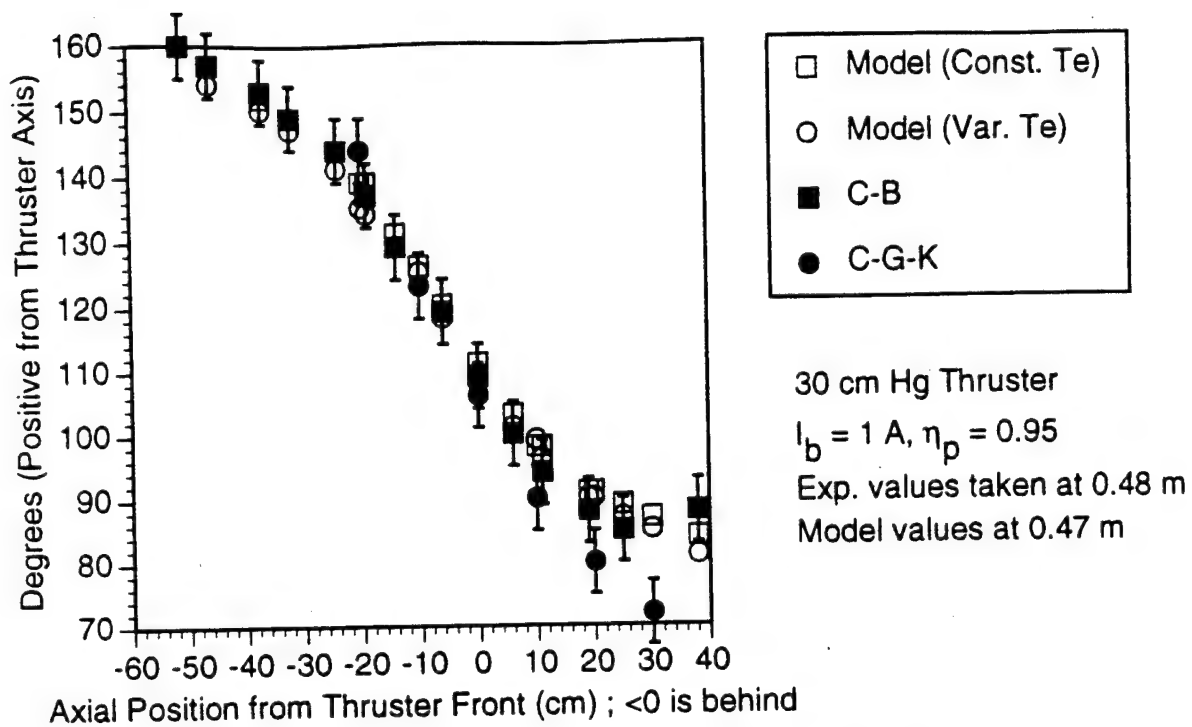


Figure 5.35a CEX ion flow angle at 48 cm from plume centerline

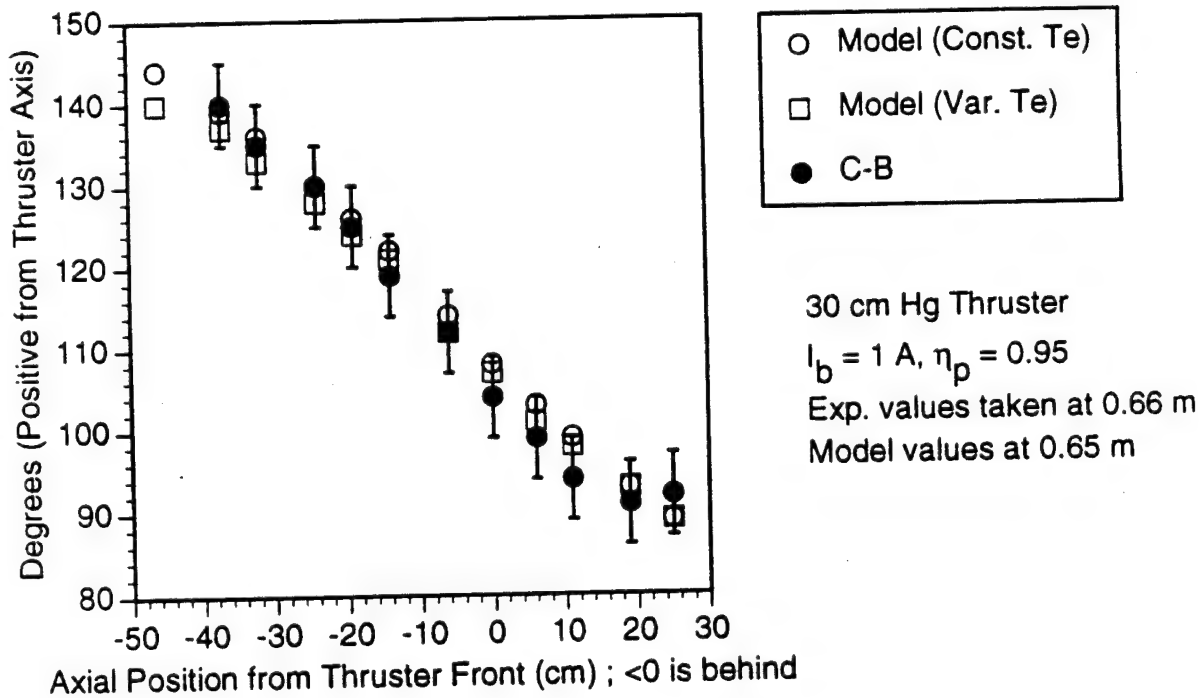


Figure 5.35b CEX ion flow angle at 66 cm from plume centerline

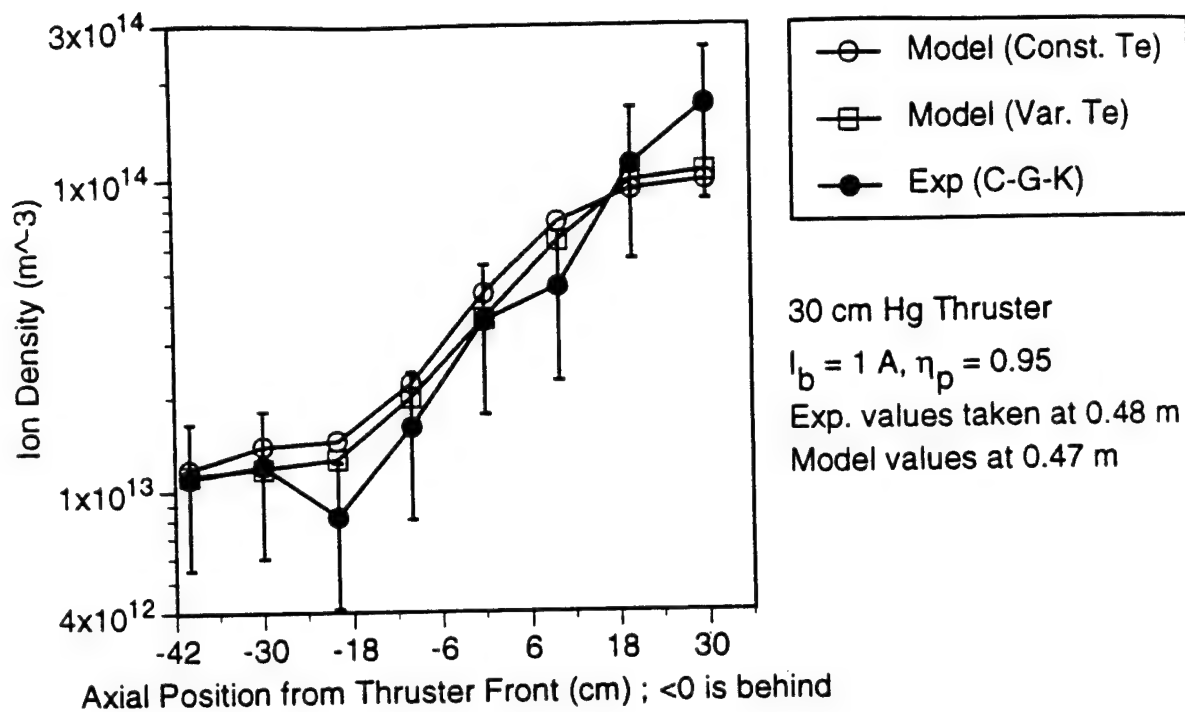


Figure 5.36 Comparison of ion density at 48 cm from plume centerline

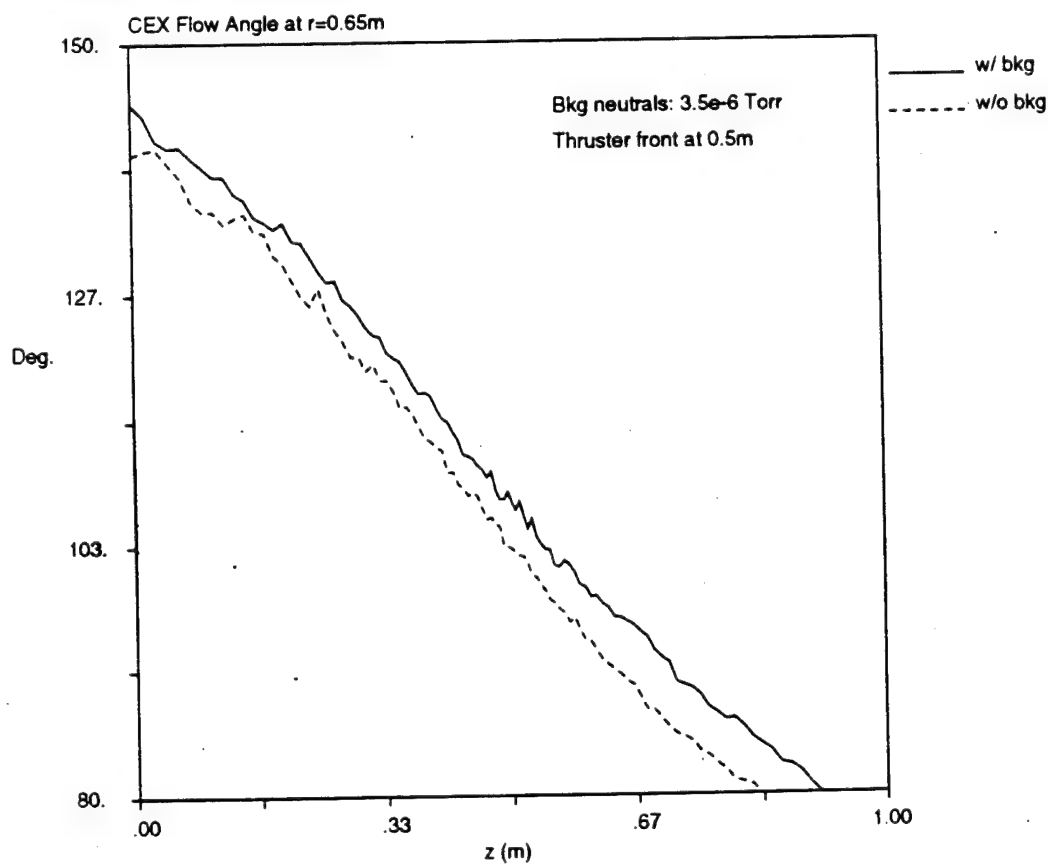


Figure 5.37 Comparison of CEX ion flow angle with and without neutral background pressure

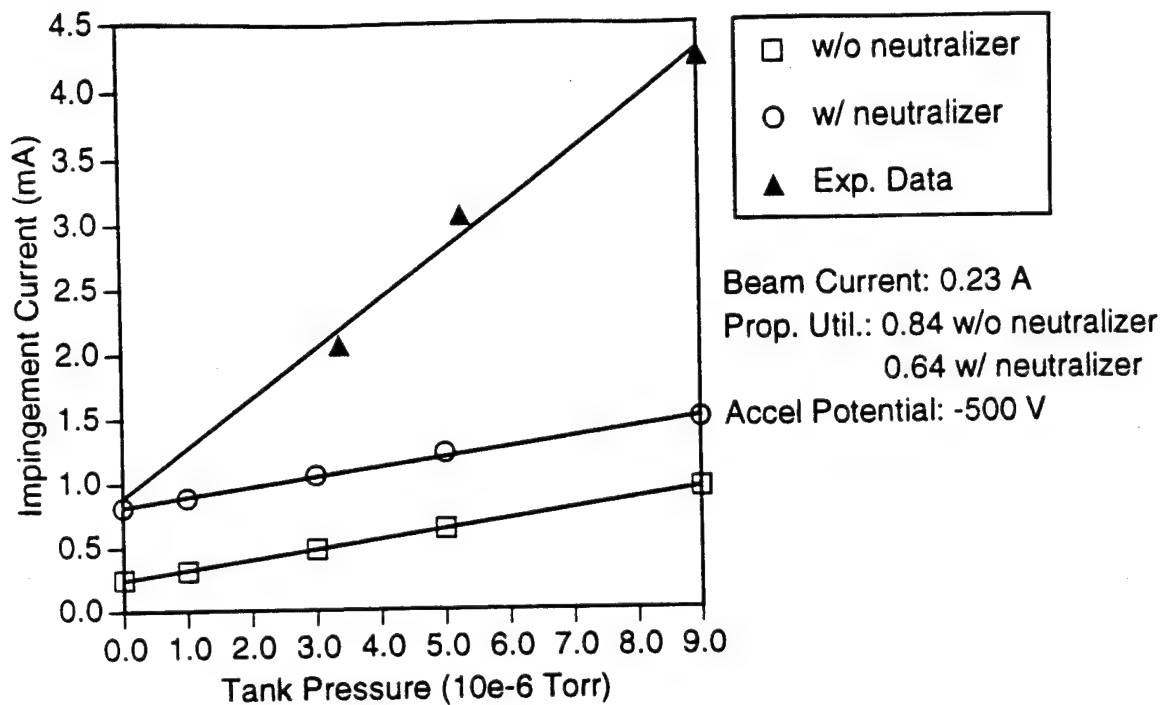


Figure 5.38 Grid impingement current vs. tank pressure for *Monheiser* modified SERT II 15 cm xenon thruster

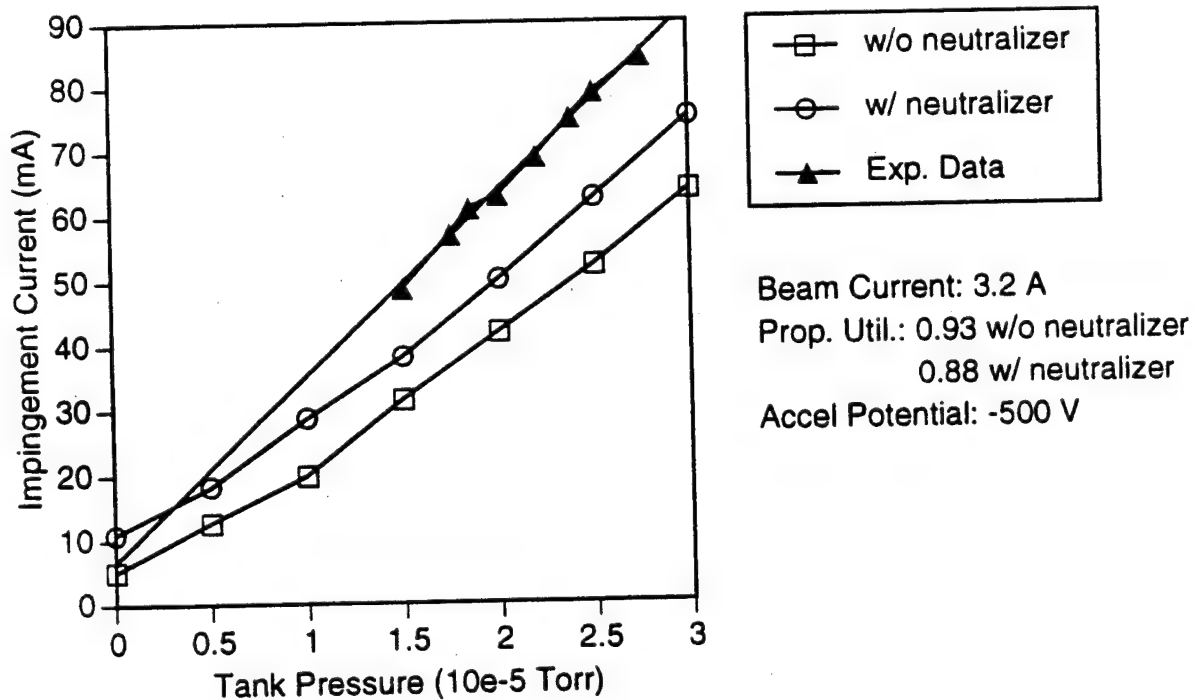


Figure 5.39 Grid impingement current vs. tank pressure for Hughes 30 cm xenon thruster  
 Data from Beattie and Matossian [1992]

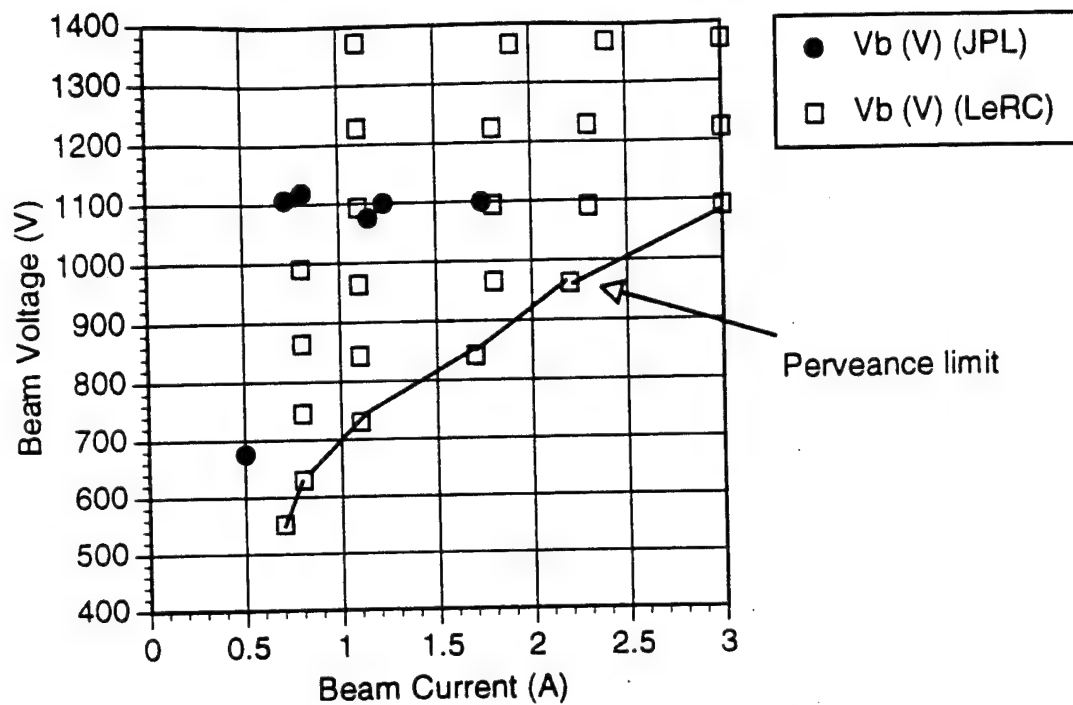


Figure 5.40 NASA 30 cm xenon ion thruster operating envelope

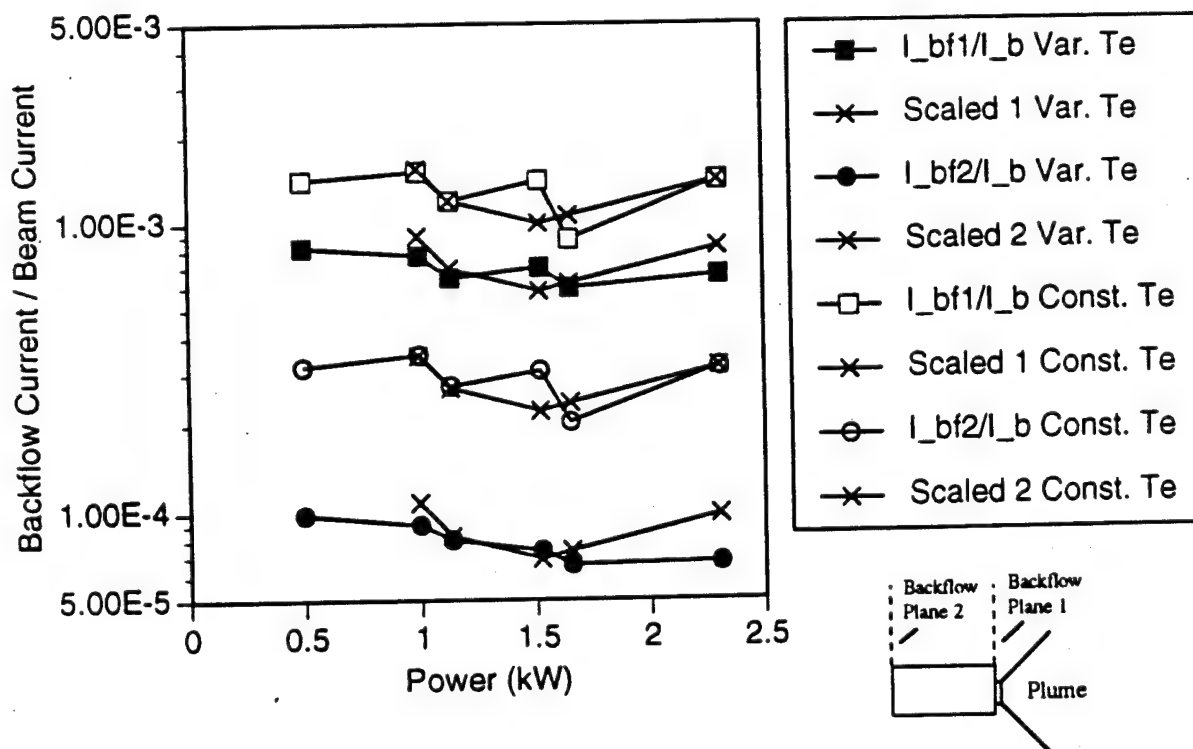


Figure 5.41 Ratio of backflow current to beam current for 30 cm NASA xenon thruster as a function of thruster power; model results and scaled predictions



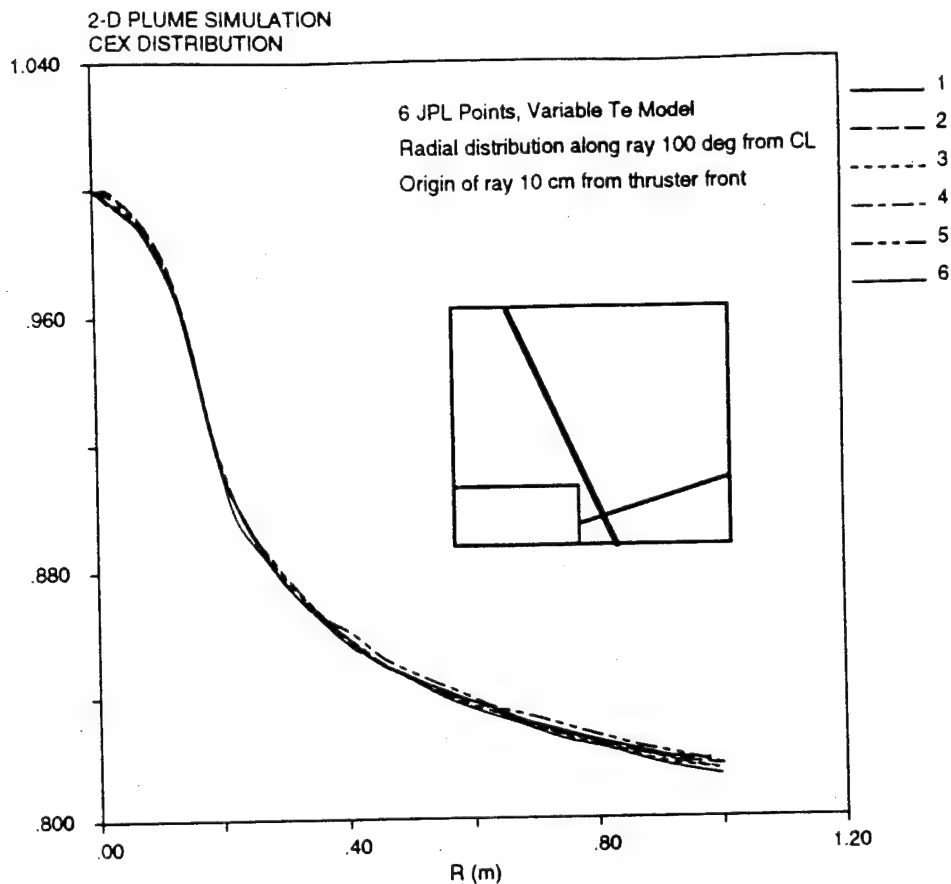
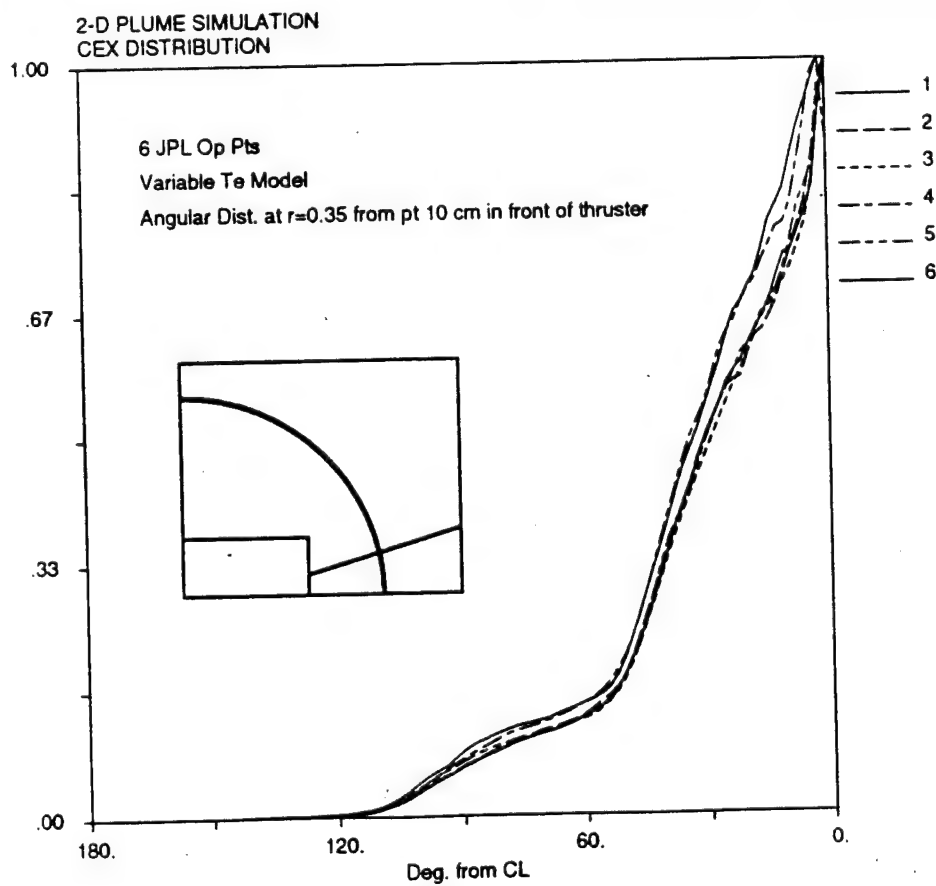


Figure 5.42 30 cm NASA Xe thruster CEX ion density distribution a) Radial ray 100° from centerline from point 10 cm downstream, b) Angular arc 35 cm from point 10 cm downstream; Variable temperature model



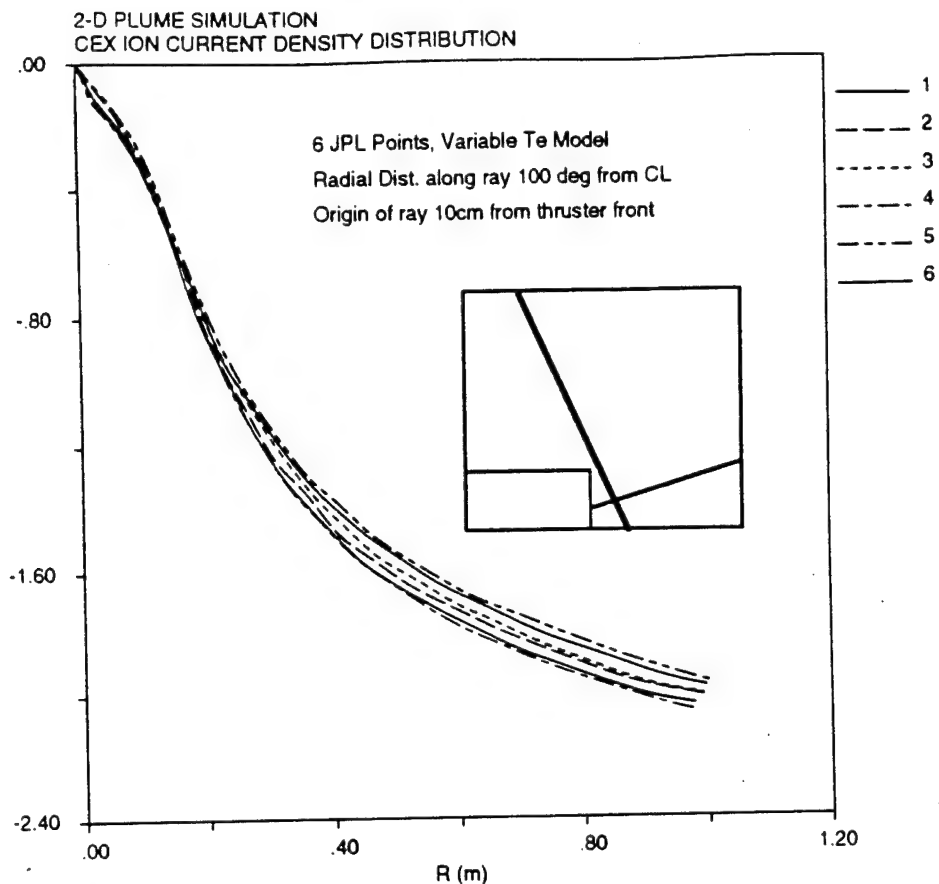
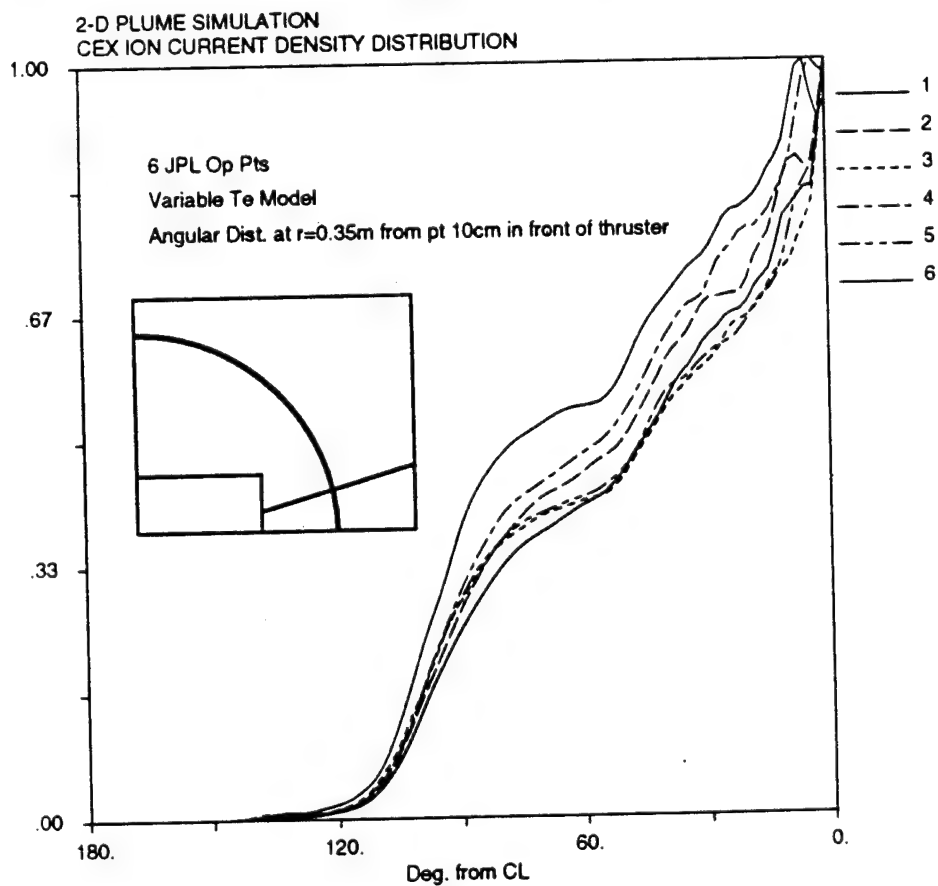


Figure 5.43 30 cm NASA Xe thruster CEX ion current density distribution a) Radial ray 100° from centerline from point 10 cm downstream, b) Angular arc 35 cm from point 10 cm downstream; Variable temperature model



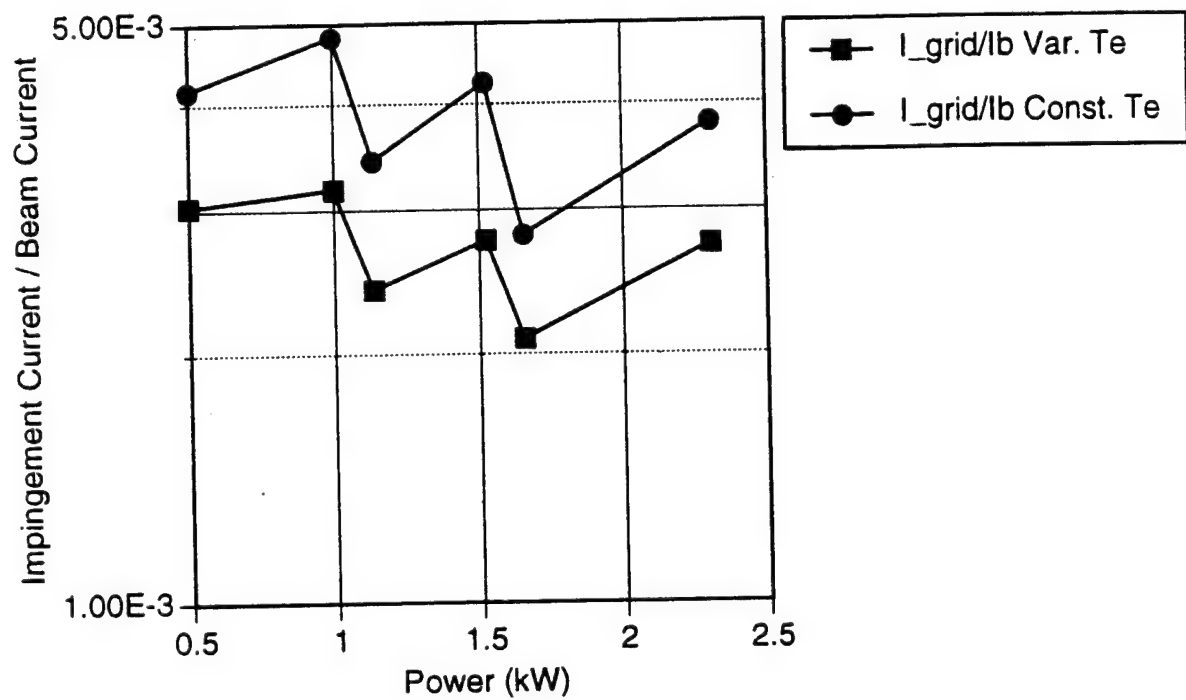


Figure 5.44 Ratio of accel grid impingement current to beam current for JPL operating points

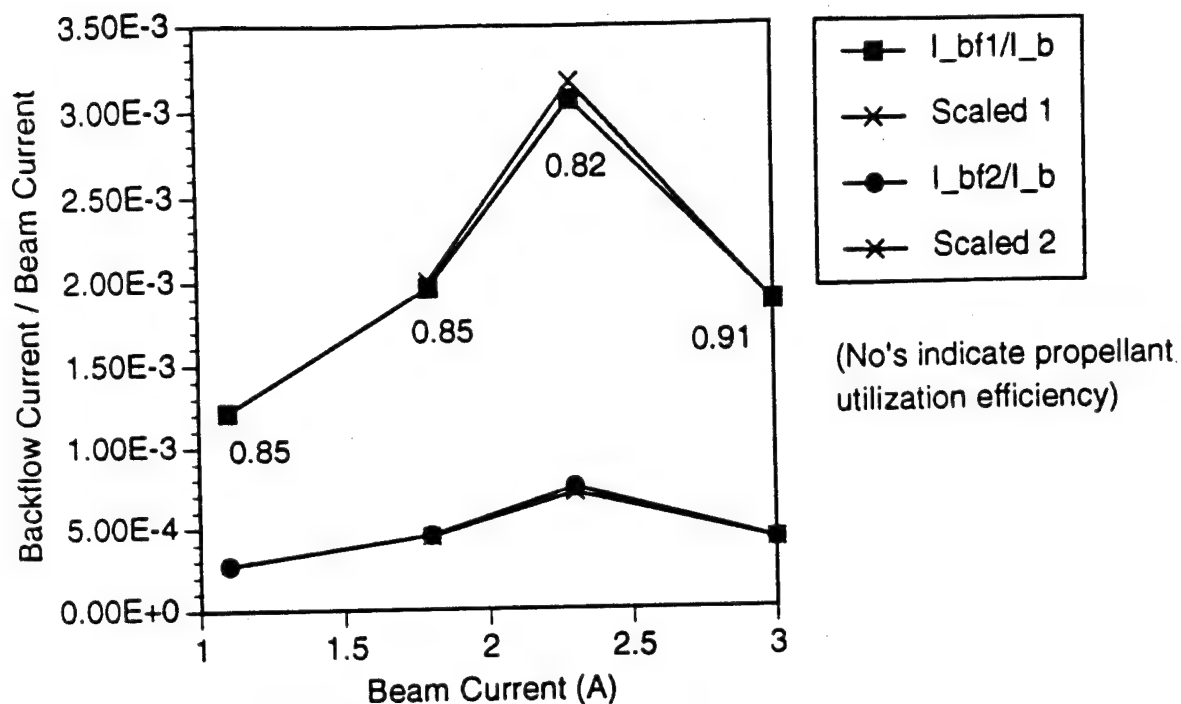


Figure 5.45 Ratio of backflow current to beam current as a function of beam current for constant beam voltage = 1090 V

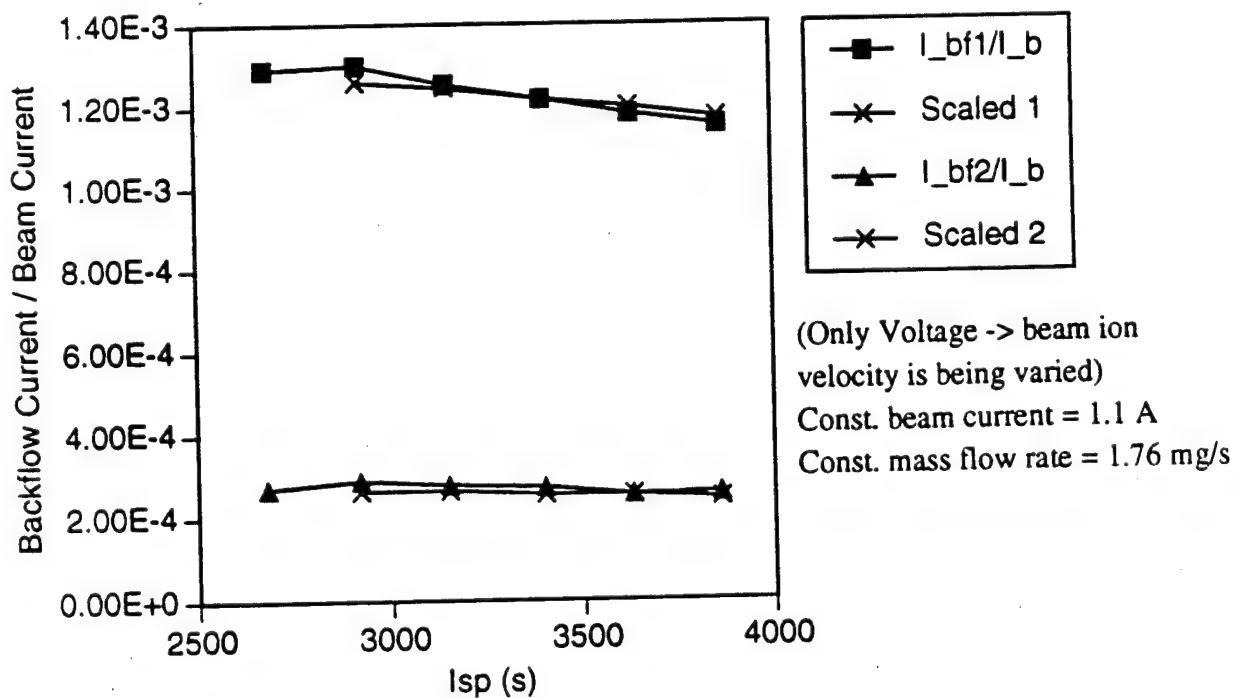


Figure 5.46 Ratio of backflow current to beam current as a function of beam voltage for constant beam current and mass flow rate

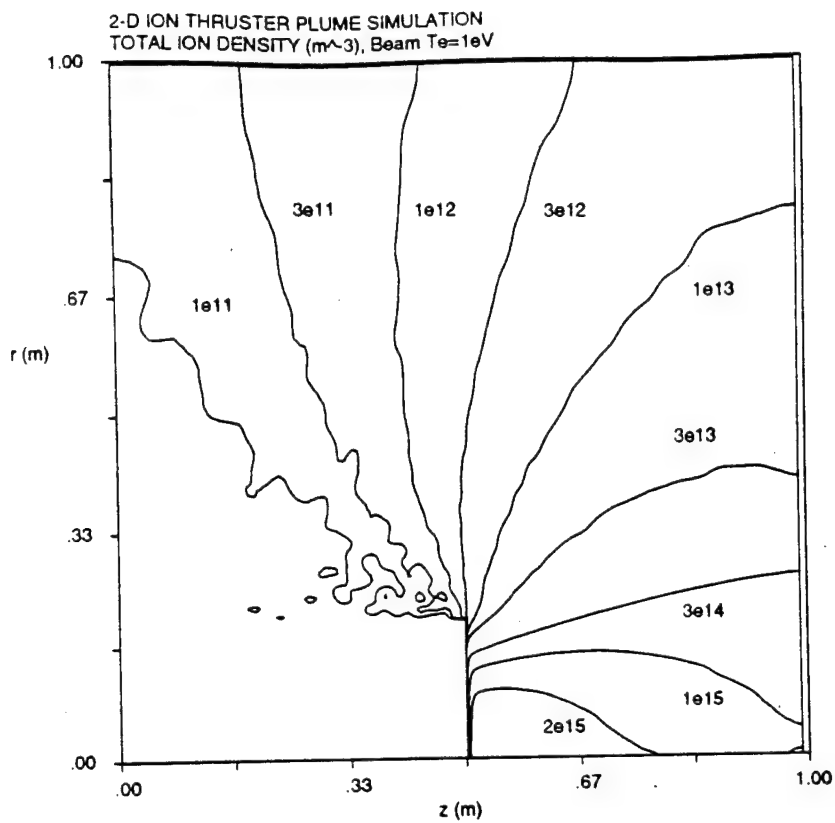
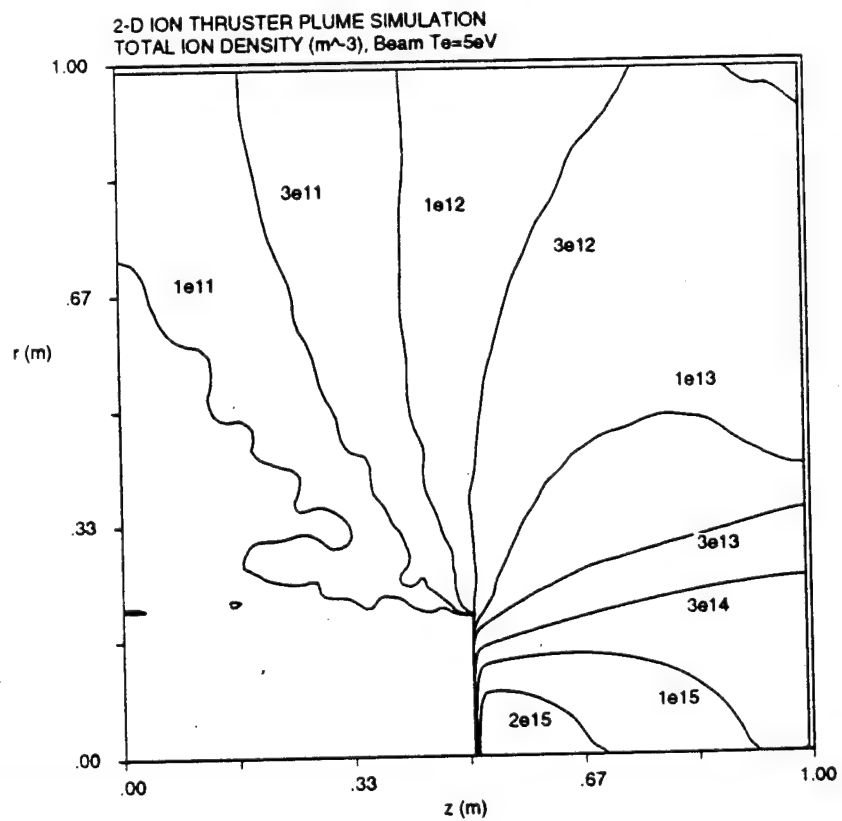


Figure 5.47 Contours of CEX ion density for a)  $T_{e0}=1\text{ eV}$ , b)  $T_{e0}=5\text{ eV}$



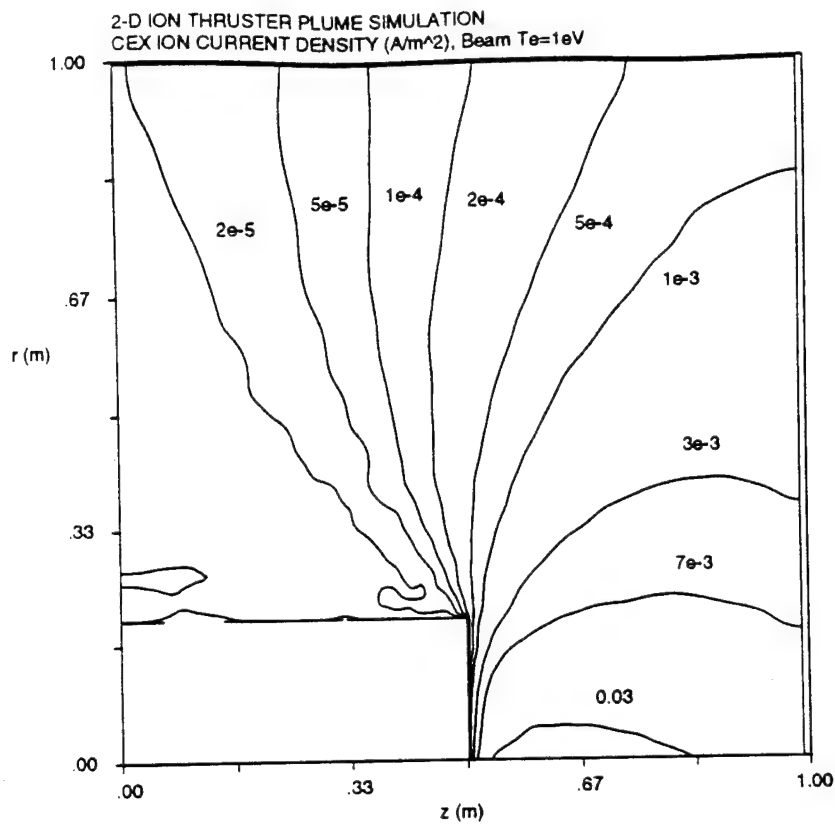
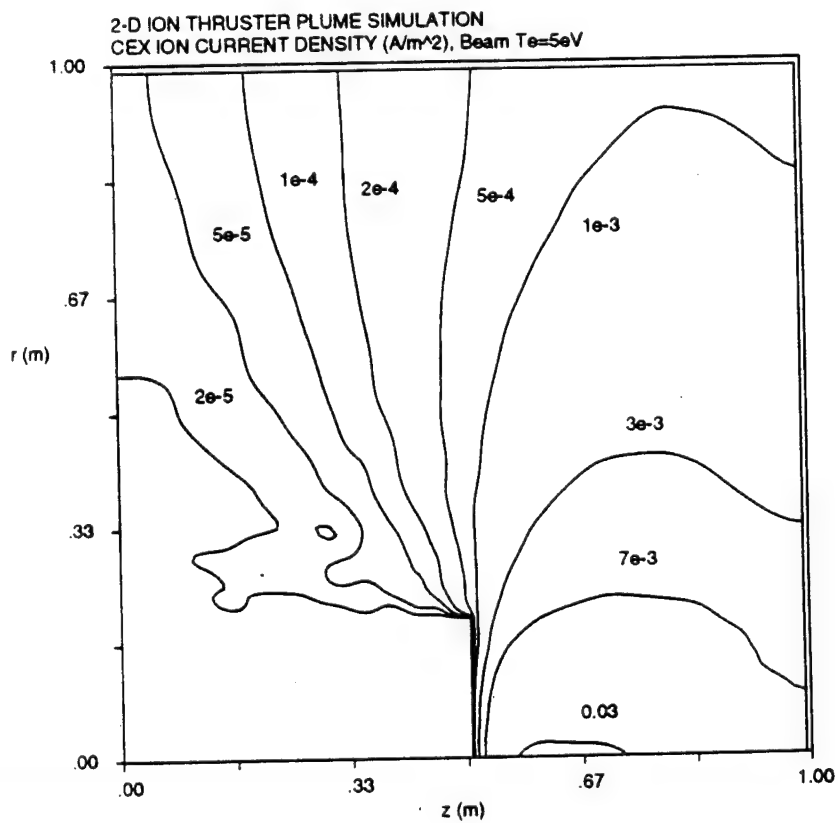


Figure 5.48 Contours of CEX ion current density for a)  $T_{e0}=1$  eV, b)  $T_{e0}=5$  eV



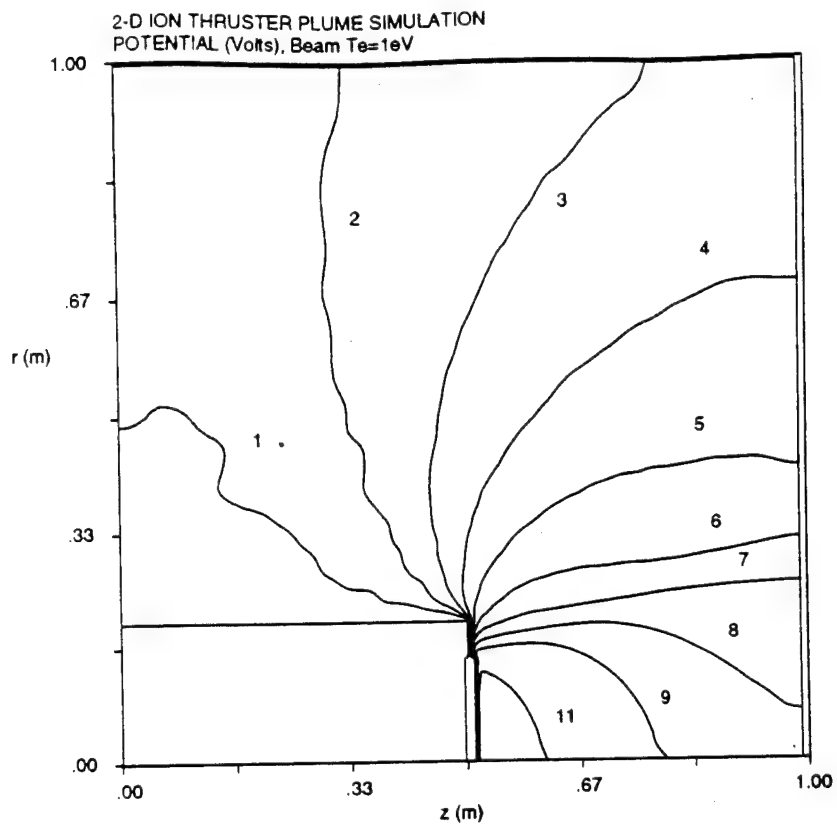
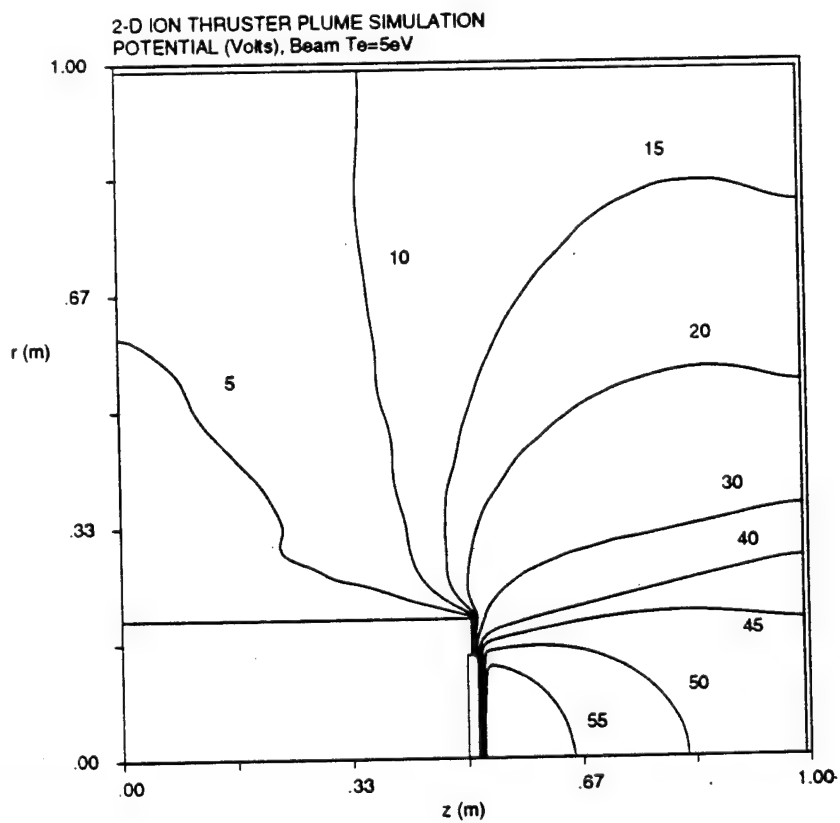


Figure 5.49 Contours of potential for a)  $T_{e0}=1\text{ eV}$ , b)  $T_{e0}=5\text{ eV}$



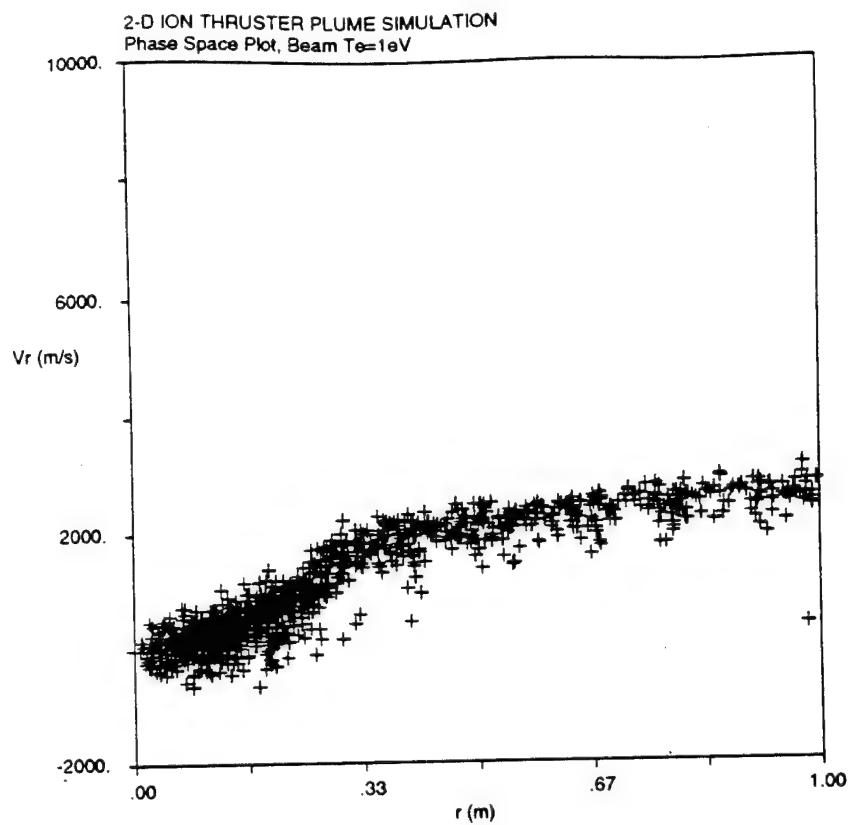
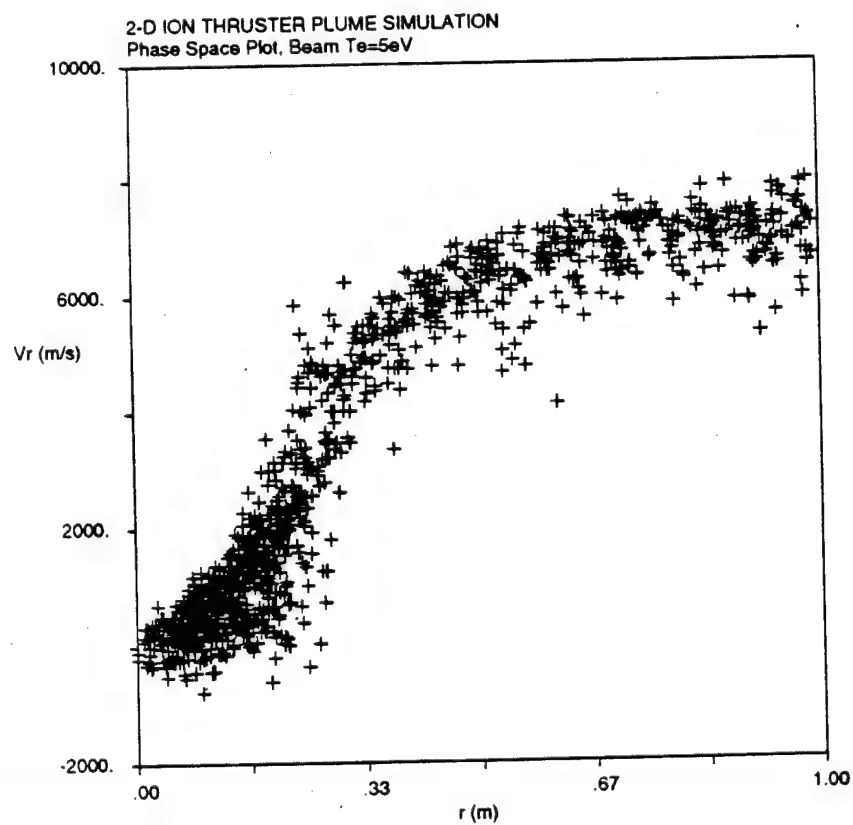


Figure 5.50 Radial velocity vs. radial position phase plots a)  $T_{e0}=1\text{ eV}$ , b)  $T_{e0}=5\text{ eV}$





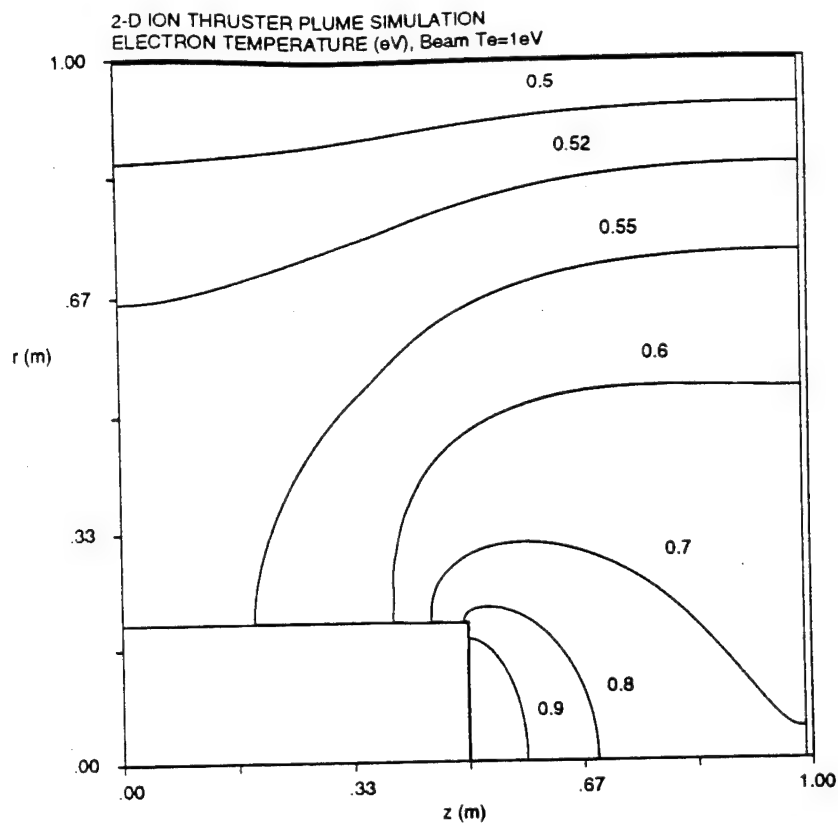
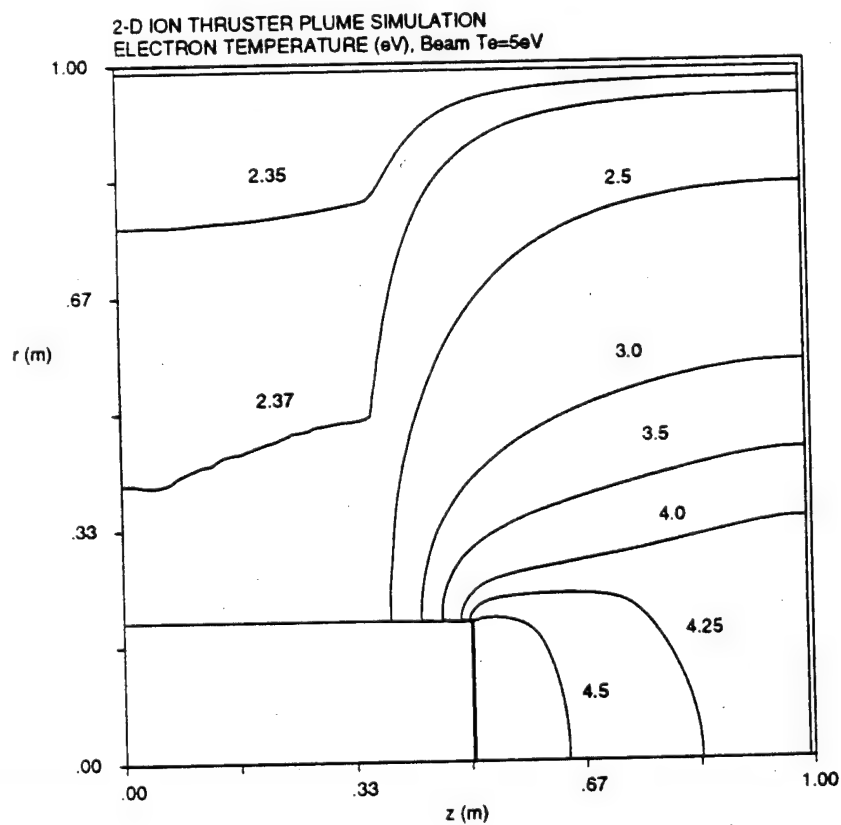


Figure 5.51 Contours of electron temperature for a)  $T_{e0}=1\text{ eV}$ , b)  $T_{e0}=5\text{ eV}$



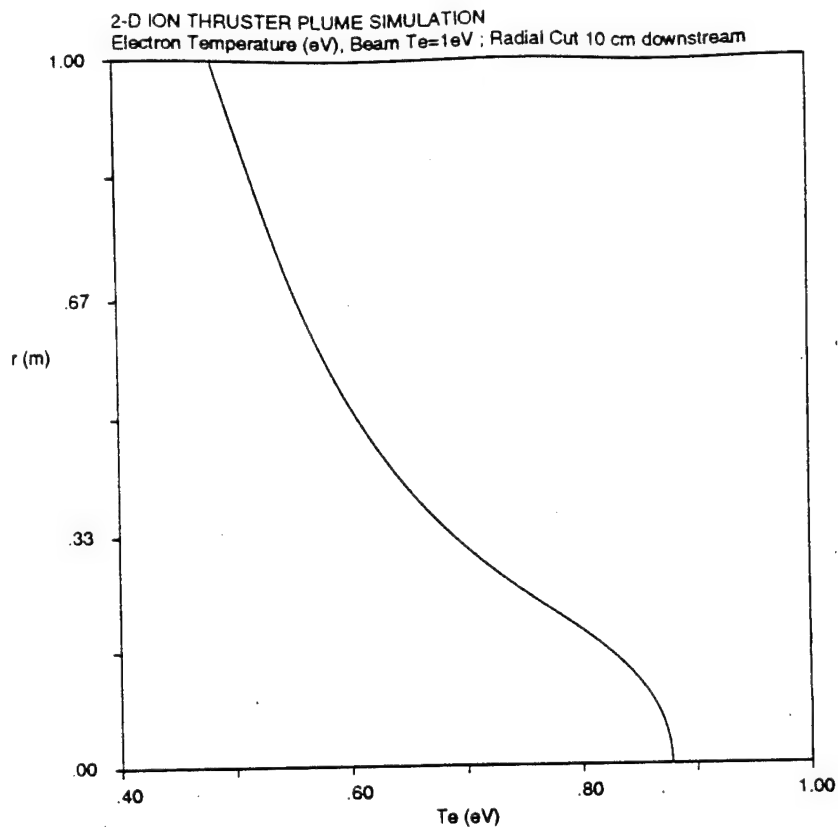
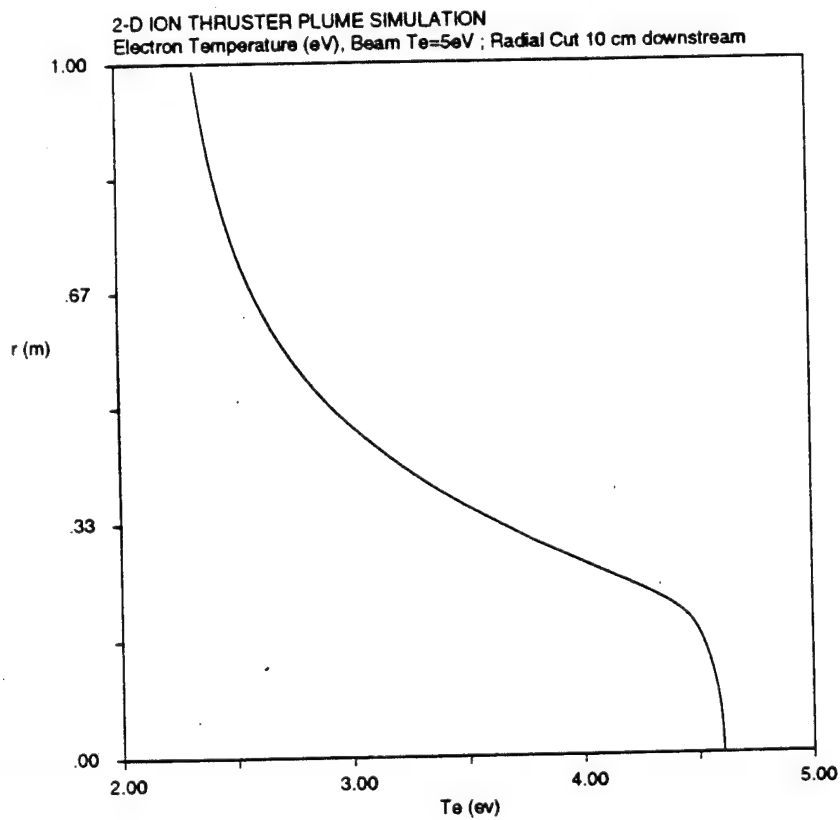


Figure 5.52 Radial cuts of electron temperature profiles for a)  $T_{e0}=1\text{ eV}$ , b)  $T_{e0}=5\text{ eV}$



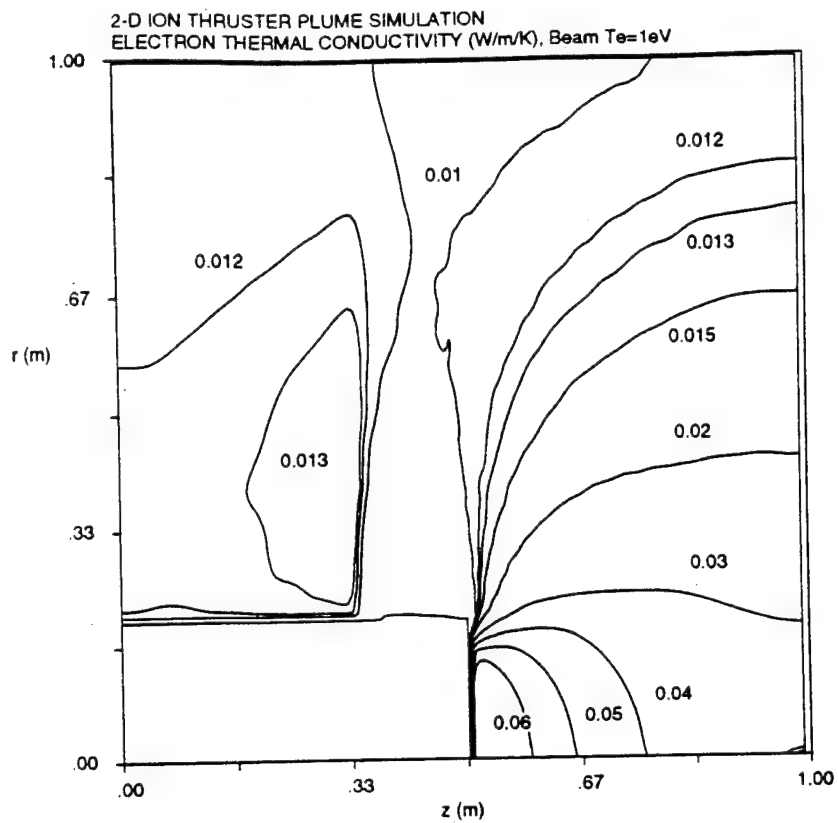
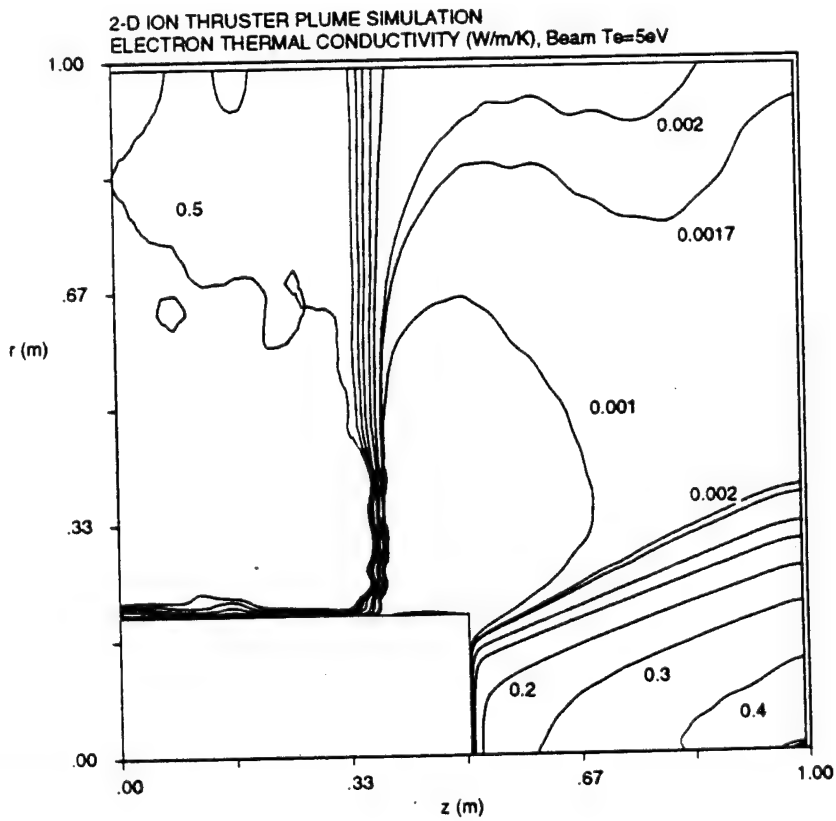


Figure 5.53 Contours of electron thermal conductivity for a)  $T_{e0}=1\text{ eV}$ , b)  $T_{e0}=5\text{ eV}$



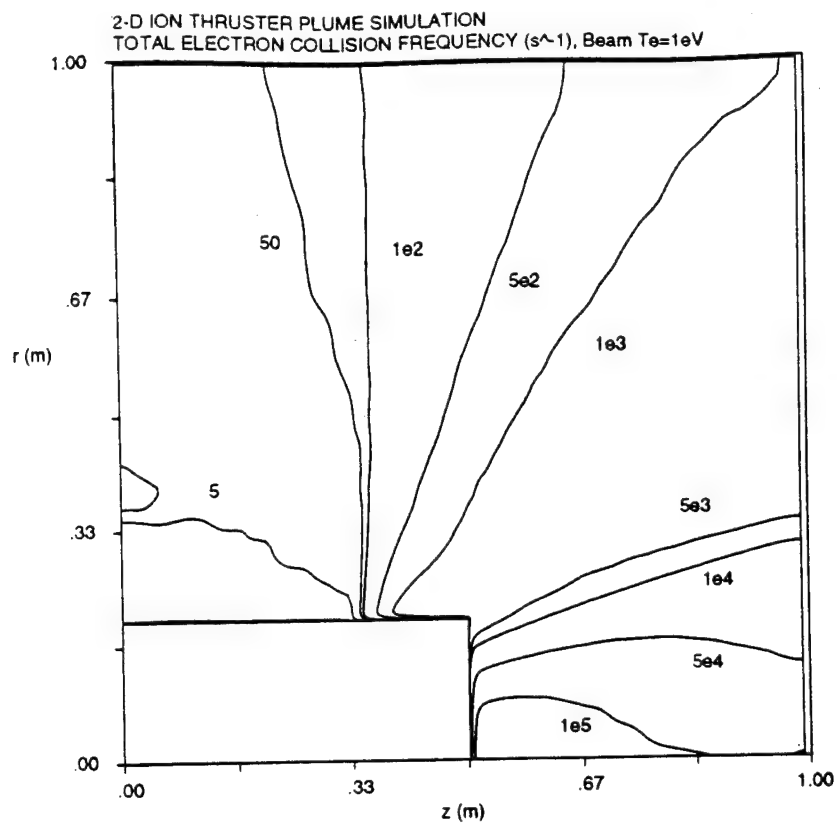
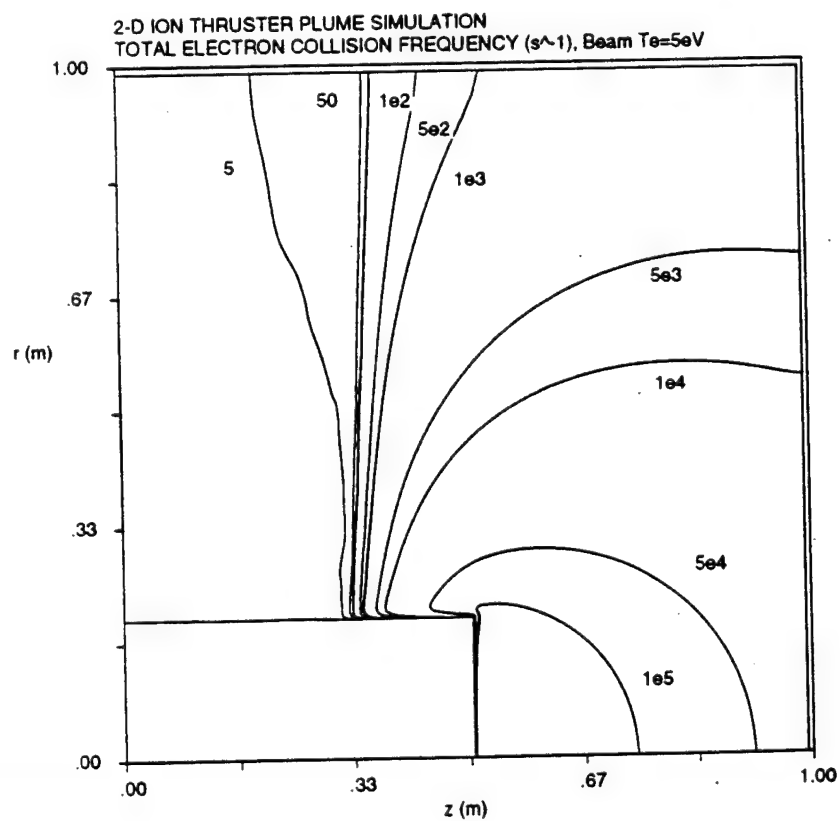


Figure 5.54 Contours of total electron collision frequency for a)  $T_{e0}=1 eV$ , b)  $T_{e0}=5 eV$



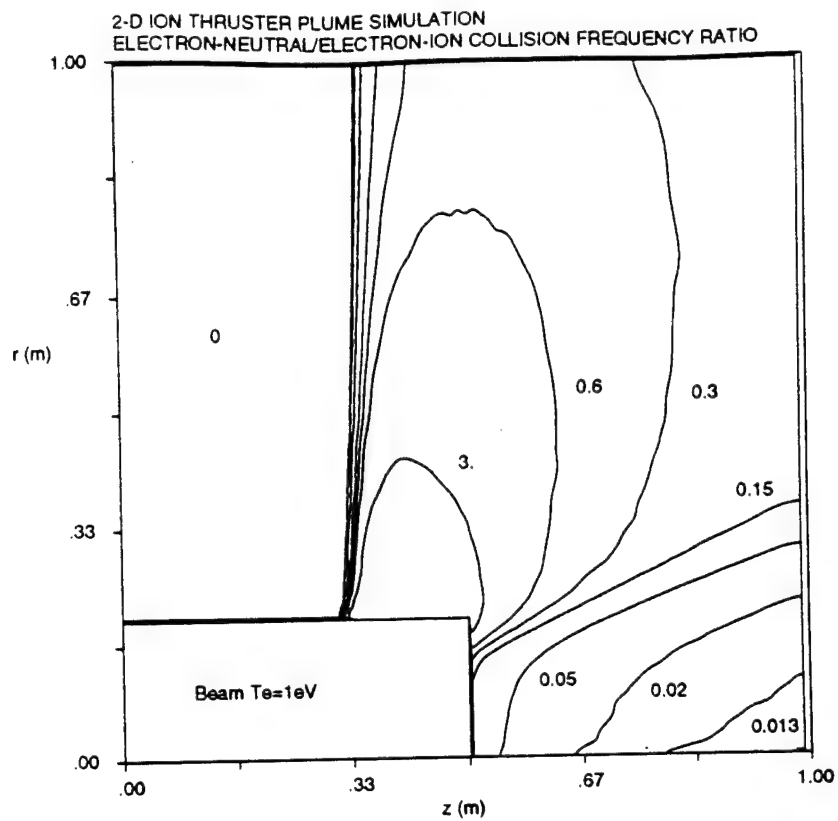
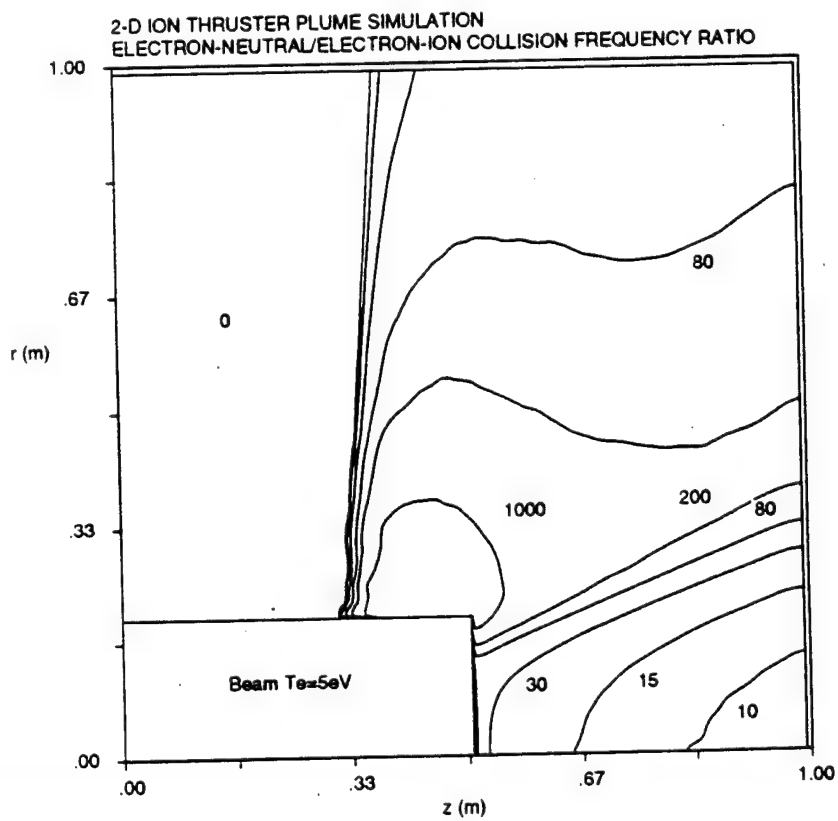


Figure 5.55 Contours of ratio of electron-neutral to electron-ion collision frequency for a)  $T_{e0}=1$  eV, b)  $T_{e0}=5$  eV



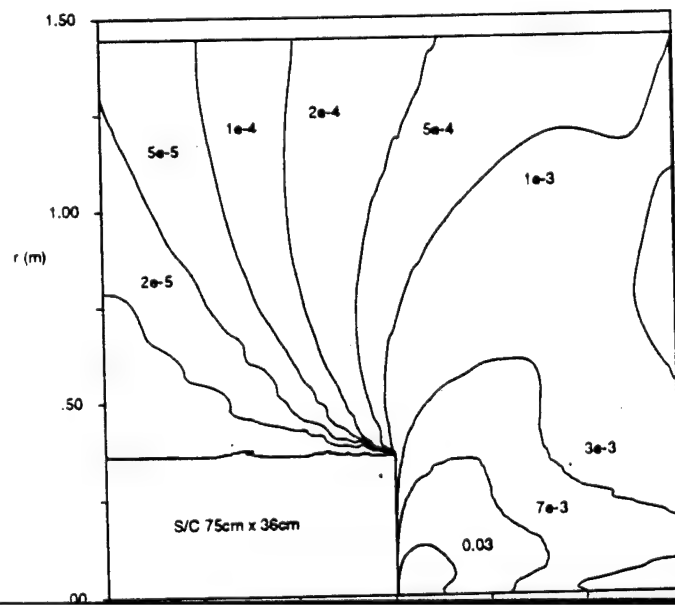
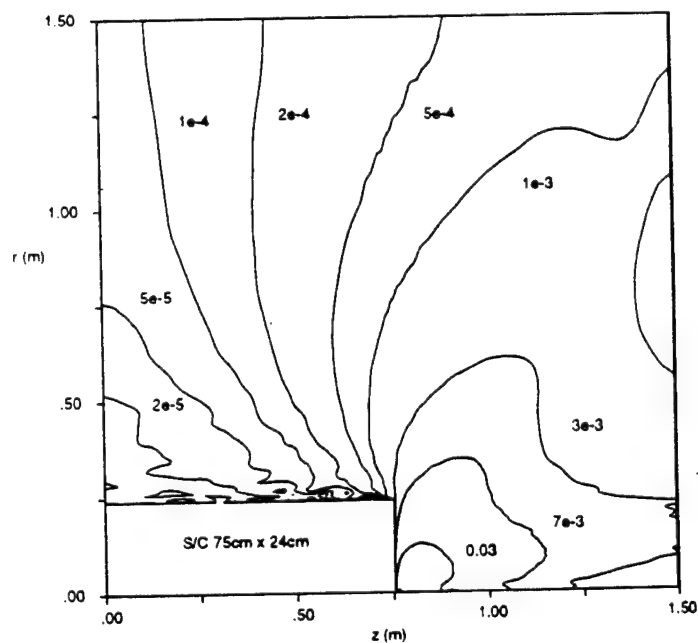
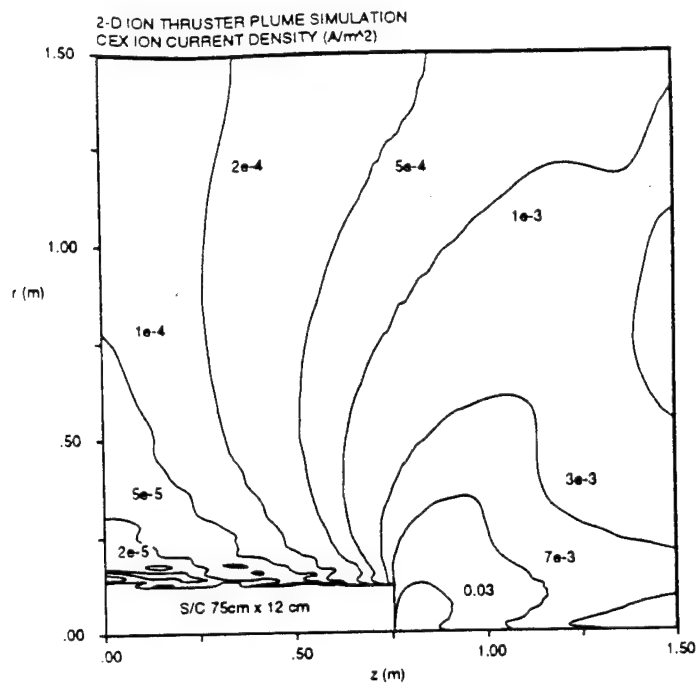


Figure 5.56 CEX ion current density contours for various spacecraft geometries; spacecraft widths: a) 12 cm, b) 24 cm, c) 36 cm

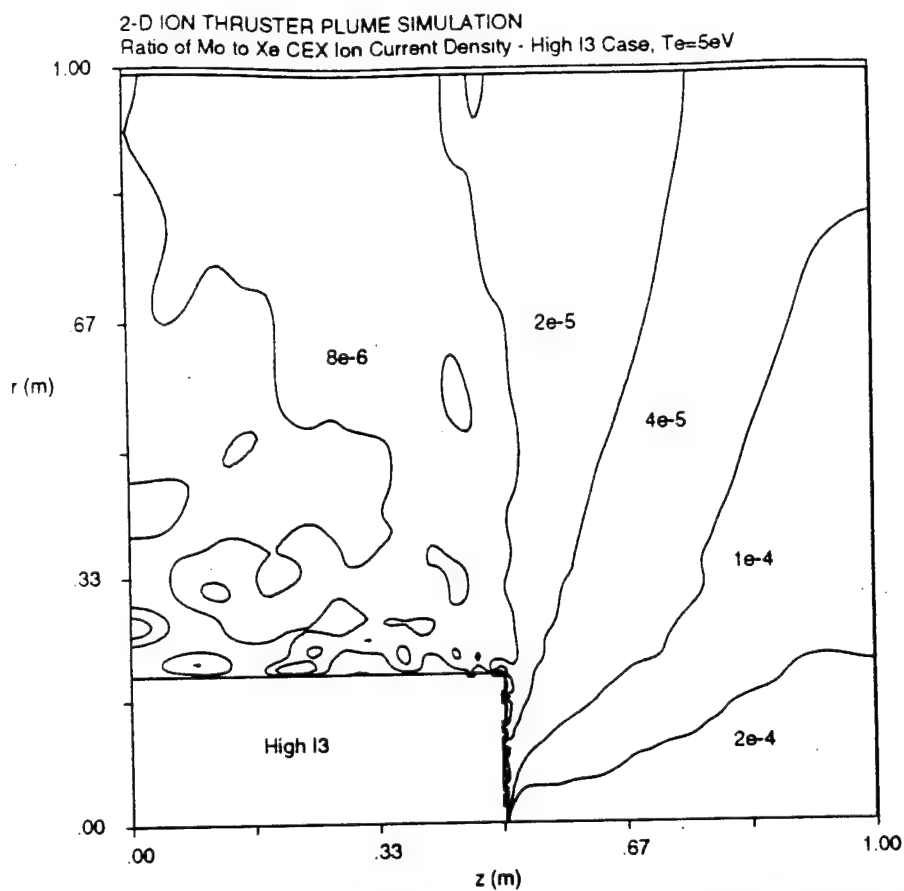


Figure 5.57 Ratio of Mo to Xe CEX ion current density for I3 high ion creation rate case

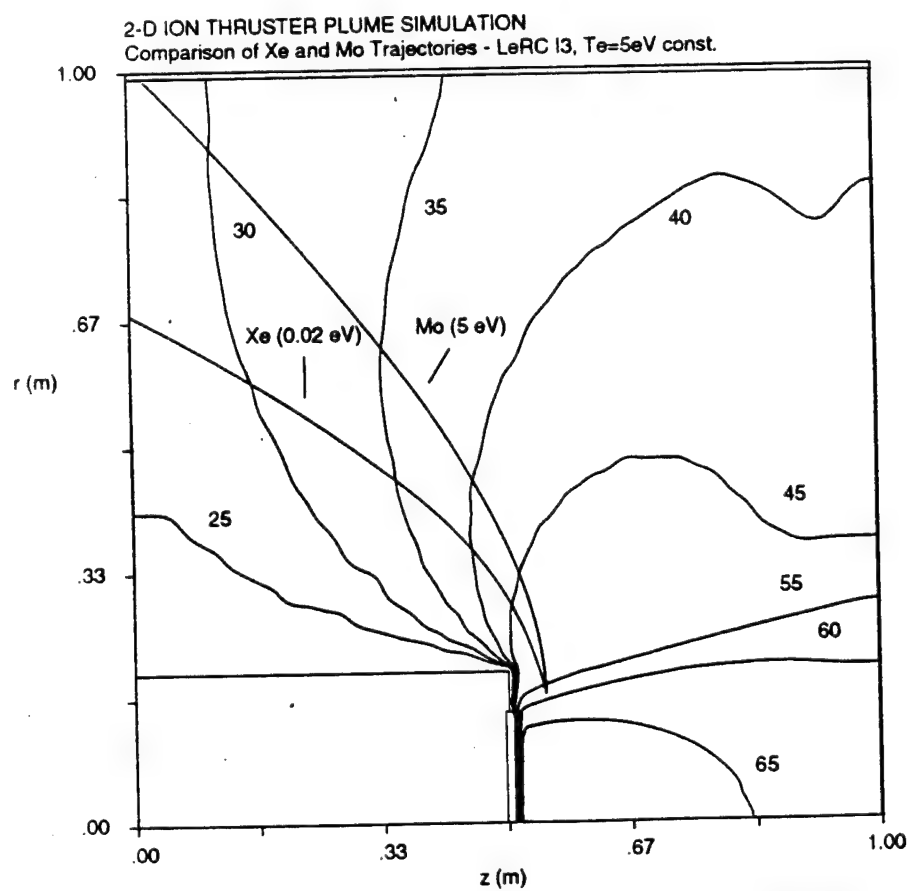


Figure 5.58 Trajectories of Mo and Xe ions in plume potential field

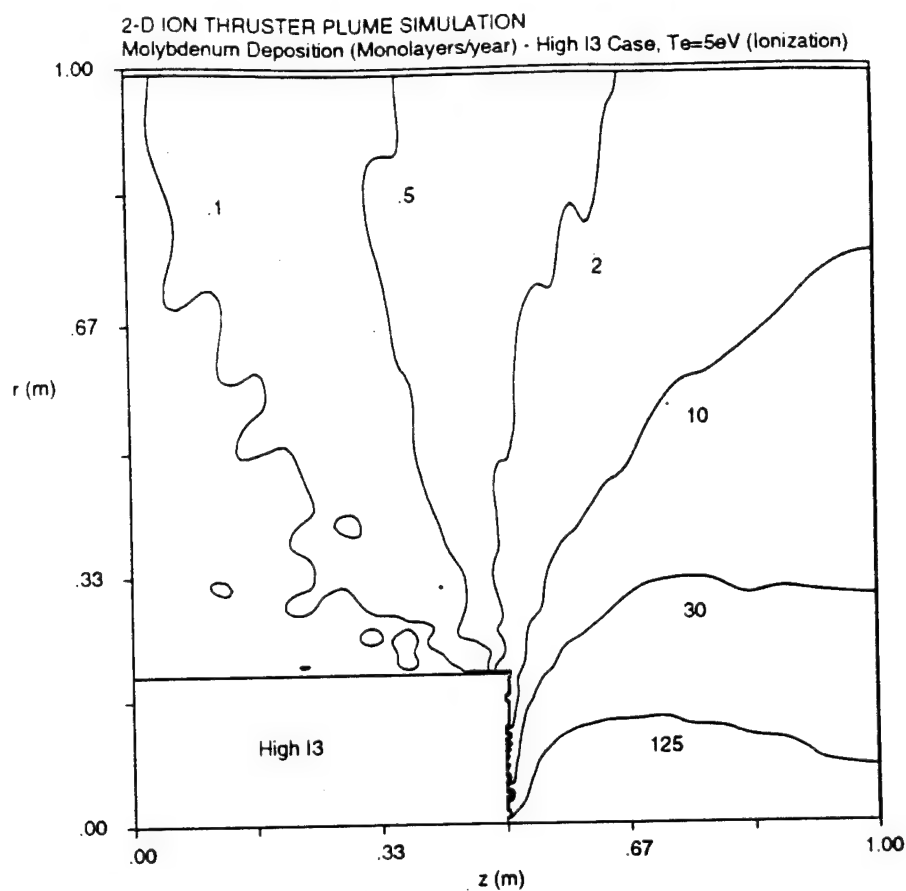


Figure 5.59 Contour map of Mo deposition for I3 case with high ion creation rate

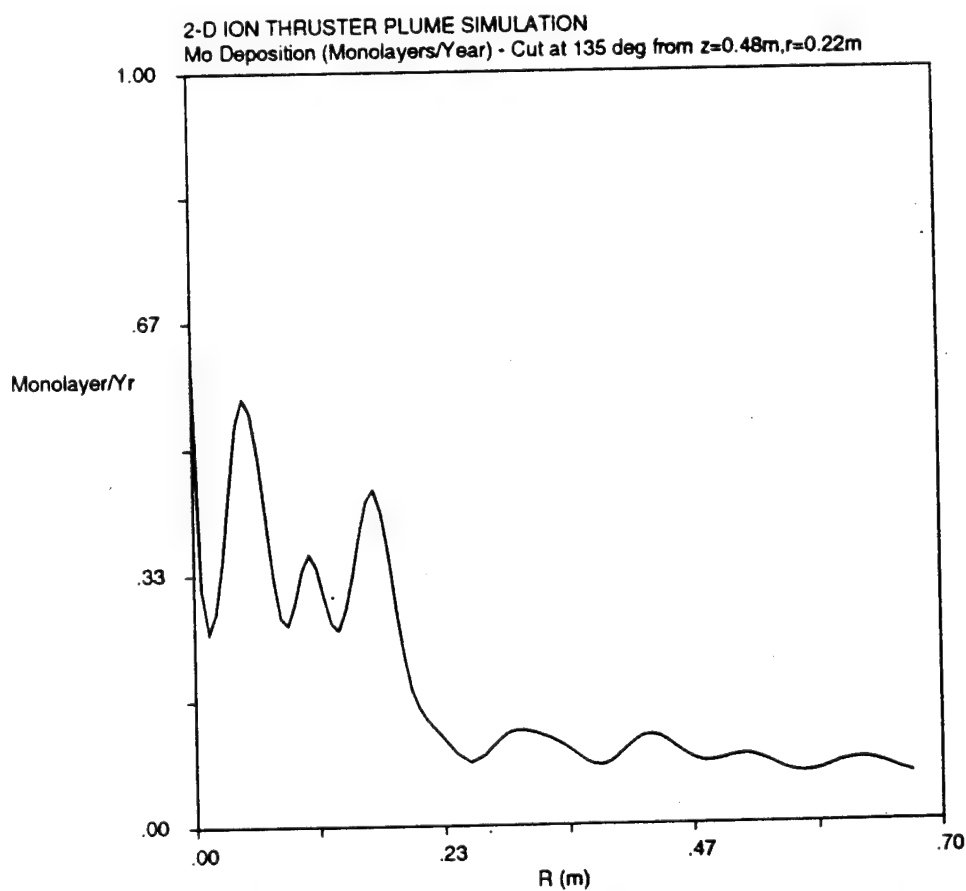


Figure 5.60 Mo deposition along ray 135° from a point at  $z=0.48m, r=0.22m$



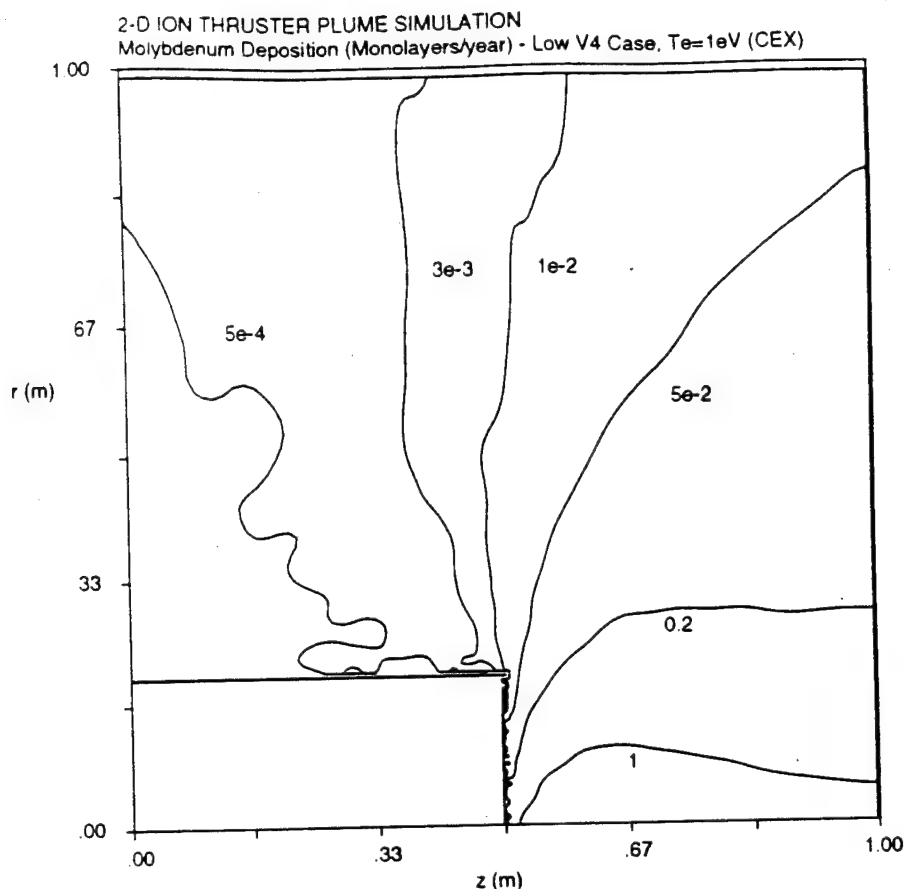


Figure 5.61 Contour map of Mo deposition for I1 case with low ion creation rate

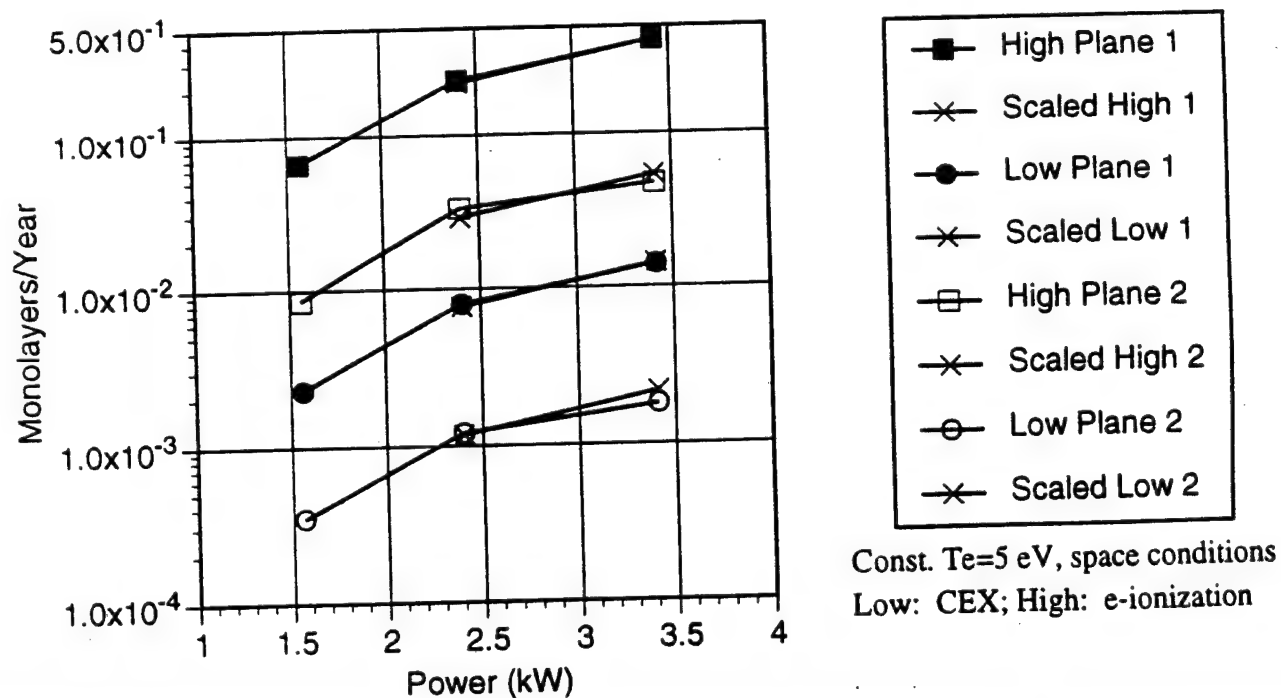


Figure 5.62 Mo deposition as a function of thruster power for NASA 30 cm xenon thruster; high and low ion creation rates along with predicted scaled values

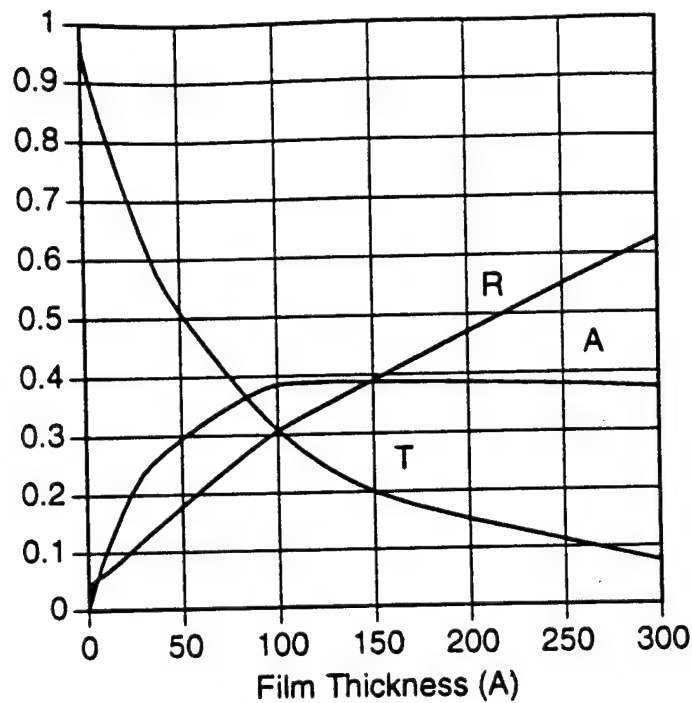


Figure 5.63 Film Properties of Mo on Solar Cell Coverglass including T-transmittance, R-reflectance, A-absorptance (from *Kemp et al* [1972]) (1 monolayer =  $2.8\text{\AA}$ )

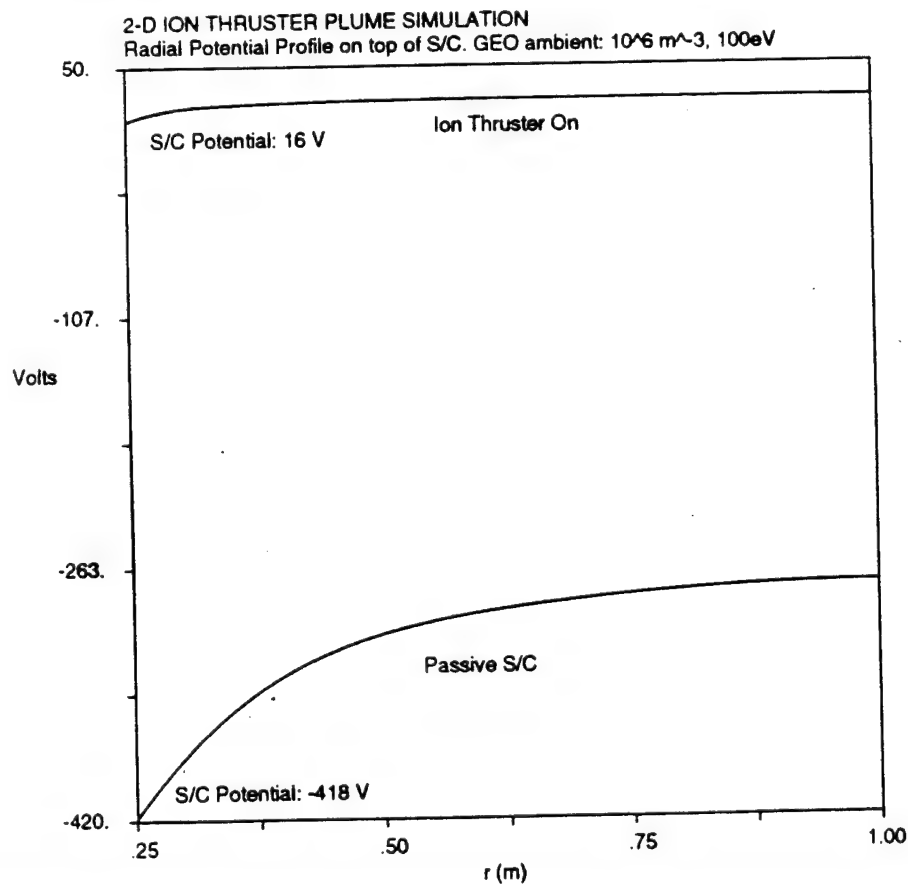


Figure 5.64 Radial potential profile on top of spacecraft showing effect of CEX plasma collapsing the sheath around the spacecraft and alleviating extreme negative bias

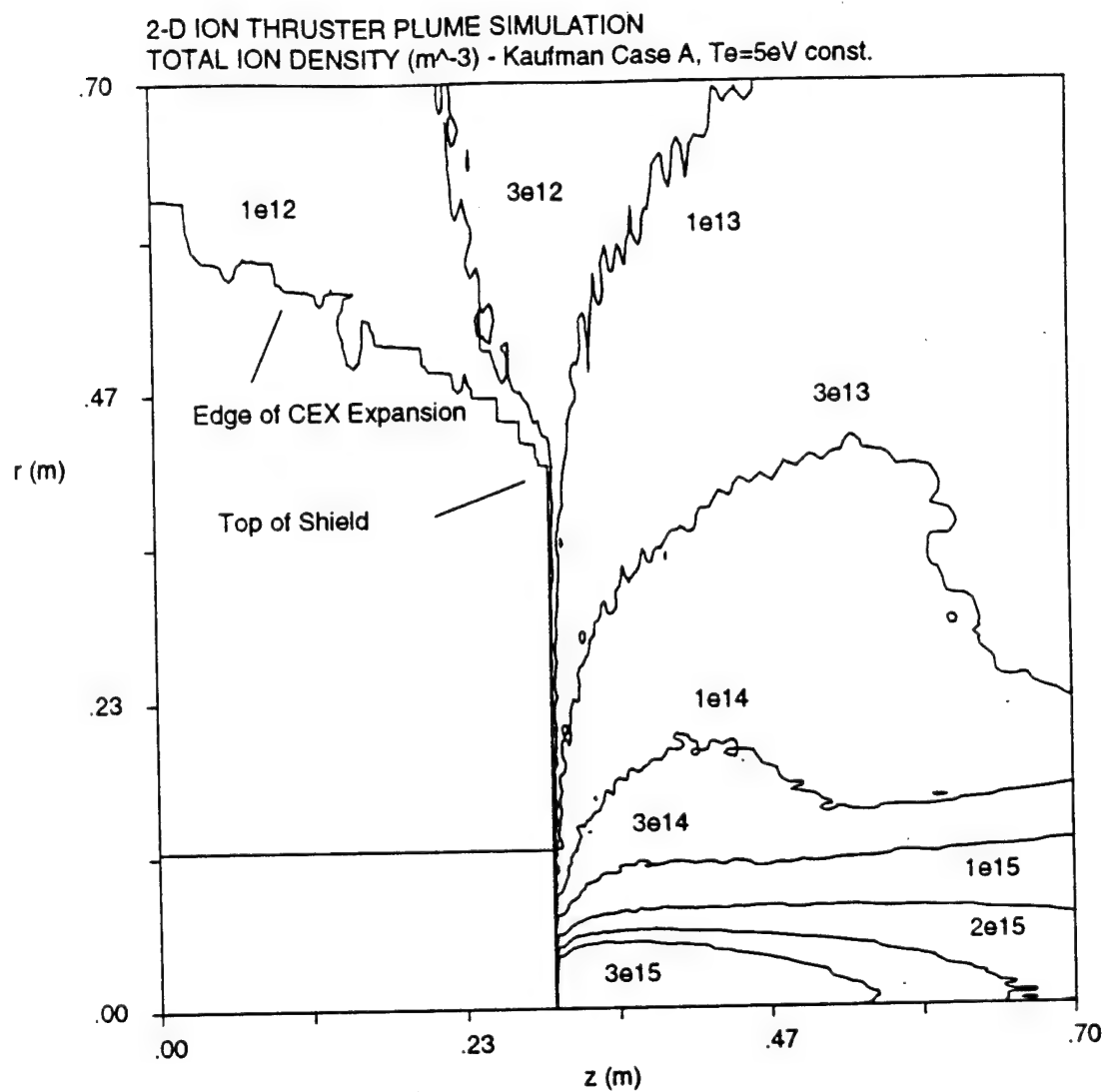


Figure 5.65 Total ion density contours from *Kaufman Case A* thruster with plume shield at thruster exit plane

## Chapter 6

### Numerical Plume Model and Methods (Three-Dimensional)

In Chapter 5, we investigated the plume backflow with a model that assumes complete axisymmetry. However, for a realistic assessment of plume backflow for an arbitrary spacecraft and thruster configuration, it is necessary to develop a fully three-dimensional model to take into account the true nature of the geometry. One of the important issues that can not be captured in an axisymmetric model, are three-dimensional geometrical influences on electric fields that can cause focusing of ion trajectories. Moreover, with a three-dimensional model, a spacecraft designer can investigate the distribution of the backflow over a realistic geometry, and make contamination assessments for the placement of sensitive spacecraft components such as thermal radiator surfaces. In addition, if the spacecraft dimensions are large enough ( $\sim 10$  m), the geomagnetic field becomes important for the CEX ions, particularly in LEO. Only a three-dimensional model can take in account the effects of an arbitrarily oriented magnetic field.

However, the computational resources required for a three-dimensional PIC model on a computational domain greater than a couple meters in each dimension are enormous. To encompass a typical spacecraft (or at least half), the domain must be at least 2-5 meters in each direction. Given the constraint on the grid cell size to be on the order of the local Debye length, the number of grid cells is easily on the order of  $10^7$ . In addition, to satisfy the requirement that there be roughly ten particles per cell, this requires at least  $10^8$  particles. Thus, the memory requirements ( $>2$  GB) are orders of magnitude beyond those of any current workstation or even most single processor supercomputers. Indeed, only in the last five years with the advent of massively parallel computers, has it been possible to contemplate the numerical solution of such a large-scale problem. Fortunately, massively parallel computers exist today upon which problems of this nature can be addressed. In

this chapter, we present the modifications necessary to the PIC plume model to extend it to three-dimensions. We then discuss the issues related to parallel computing and present a fully three-dimensional parallel PIC algorithm.

## 6.1 Three-Dimensional Additions to Model

For the fully three-dimensional model, we employ a reduced set of physics due to the complexities of programming on parallel architectures. Specifically, the electrons are treated as an isothermal Boltzmann distribution, and the solution of the electron temperature equation is eliminated. We have seen in Chapter 5 in comparisons between the isothermal and variable temperature models, that the isothermal model yields higher values of the CEX ion backflow current. Thus, the three-dimensional model will be conservative in its estimates of the backflow. All other aspects of the physical model remain the same as in the two-dimensional case. Below, we go through the various three-dimensional extensions of the numerical model.

### Computational Grid

The computational grid is Cartesian, and the grid is non-uniform as in the axisymmetric case with linear stretching based on the Debye length. The domain spans the  $x$  direction from 0 to  $L$ , in the  $y$  direction from  $-H$  to  $H$ , and in the  $z$  direction from  $-W$  to  $W$ . Figure 6.1 shows a general schematic of the computational domain and the model spacecraft configuration. As can be seen, the spacecraft is  $X_{sc}$  long in the  $x$ -axis direction (plume axis), has a half-height of  $Y_{sc}$ , and is  $2xZ_{sc}$  wide. Solar array panels extend from  $Y_{sc}$  to  $Y_{sa}$  above and below the spacecraft and are also  $2xZ_{sc}$  wide. While the model is completely three-dimensional, we usually only simulate a half domain (in the  $y$ -direction) due to symmetry about the  $y=0$  plane (without a geomagnetic field). The smallest grid cell is located at the thruster exit on the centerline and has dimensions  $X_c$  by  $Y_c$  by  $Z_c$ , each of which are a multiple of the Debye length of the CEX plasma at the thruster exit. As in the axisymmetric case, the  $x$  axis is partitioned into a section behind the thruster exit plane, and a region in front of the thruster exit. At  $x=0$ , the grid cell size in  $x$  is stretched by an amount  $\zeta_x^0 = (X_{sc}/r_T)$ ; and at  $x=L$ , by  $\zeta_x^L = (L-X_{sc})/r_T$ . In the  $y$  direction, the grid is partitioned into a region from the plume centerline ( $y=0$ ) to the top of the spacecraft,  $Y_{sc}$ , and from  $Y_{sc}$  to the upper boundary  $y=H$ , where the grid cell is stretched in  $y$  by an amount  $\zeta_y^H = (H/r_T)$  (and similarly in the negative  $y$ -direction). Lastly, in the  $z$  direction, the grid is partitioned into three sections from  $z=-W$  to  $-Z_{sc}$ , a section from  $-Z_{sc}$  to  $Z_{sc}$ , and from  $Z_{sc}$  to  $W$ . At  $z=-W$  and  $W$ , the grid cell size is stretched in  $z$  by an amount  $\zeta_z^W = (W/r_T)$ .

These stretching factors, as in the axisymmetric case, are based on the approximation that the plasma density decreases as  $(r_T/R)^2$  from the thruster exit.

The grid is generated by computing the grid coordinates in each direction by,

$$x_{i+1} = x_i + \Delta x(x_i) ; y_{j+1} = y_j + \Delta y(y_j) ; z_{k+1} = z_k + \Delta z(z_k) \quad (6.1)$$

where the linear variations of the grid cells are given by the following. In the x direction,

$$\begin{aligned} \Delta x(x_i) &= X_c \left(1 - \zeta_x^0\right) \frac{x}{X_{sc}} + \zeta_x^0 X_c, \quad 0 \leq x \leq X_{sc} \\ \Delta x(x_i) &= X_c \left(\zeta_x^L - 1\right) \frac{(x - X_{sc})}{(L - X_{sc})} + X_c, \quad X_{sc} \leq x \leq L \end{aligned} \quad (6.2)$$

Note that for  $x=0$ ,  $\Delta x = \zeta_x^0 X_c$ , for  $x=X_{sc}$ ,  $\Delta x = X_c$ , and for  $x=L$ ,  $\Delta x = \zeta_x^L X_c$ . For the y direction,

$$\begin{aligned} \Delta y(y_j) &= Y_c, \quad -Y_{sc} \leq y \leq Y_{sc} \\ \Delta y(y_j) &= Y_c \left(\zeta_y^H - 1\right) \frac{(|y| - Y_{sc})}{(H - Y_{sc})} + Y_c, \quad Y_{sc} \leq |y| \leq H \end{aligned} \quad (6.3)$$

where for  $y=H$ ,  $\Delta y = \zeta_y^H Y_c$ . Lastly, in the z direction,

$$\begin{aligned} \Delta z(z_k) &= Z_c, \quad -Z_{sc} \leq z \leq Z_{sc} \\ \Delta z(z_k) &= Z_c \left(\zeta_z^W - 1\right) \frac{(|z| - Z_{sc})}{(W - Z_{sc})} + Z_c, \quad Z_{sc} \leq |z| \leq W \end{aligned} \quad (6.4)$$

where for  $z=\pm W$ ,  $\Delta z = \zeta_z^W Z_c$ .

### Particle Weightings

For the particle weightings, we use Cartesian weighting factors similar to Eqn. (4.13), but applied in all three directions. Thus, weighting is done by volumes, rather than by areas as in two dimensions. Given a particle at  $(x_p, y_p, z_p)$ , located between x coordinate indices  $i$  and  $i+1$ , y coordinate indices  $j$  and  $j+1$ , and z coordinate indices  $k$  and  $k+1$ , the weighting factors of the neighboring eight grid points for the charge density, as well as for electric field extrapolation, are,

$$\begin{aligned} S_{i,j,k} &= (x_{i+1} - x_p)(y_{j+1} - y_p)(z_{k+1} - z_p)/(\Delta x \Delta y \Delta z) \\ S_{i+1,j,k} &= (x_p - x_i)(y_{j+1} - y_p)(z_{k+1} - z_p)/(\Delta x \Delta y \Delta z) \\ S_{i+1,j+1,k} &= (x_p - x_i)(y_p - y_j)(z_{k+1} - z_p)/(\Delta x \Delta y \Delta z) \\ S_{i,j+1,k} &= (x_{i+1} - x_p)(y_p - y_j)(z_{k+1} - z_p)/(\Delta x \Delta y \Delta z) \\ S_{i,j,k+1} &= (x_{i+1} - x_p)(y_{j+1} - y_p)(z_p - z_k)/(\Delta x \Delta y \Delta z) \\ S_{i+1,j,k+1} &= (x_p - x_i)(y_{j+1} - y_p)(z_p - z_k)/(\Delta x \Delta y \Delta z) \\ S_{i+1,j+1,k+1} &= (x_p - x_i)(y_p - y_j)(z_p - z_k)/(\Delta x \Delta y \Delta z) \\ S_{i,j+1,k+1} &= (x_{i+1} - x_p)(y_p - y_j)(z_p - z_k)/(\Delta x \Delta y \Delta z) \end{aligned} \quad (6.5)$$

where  $\Delta x = x_{i+1} - x_i$ ,  $\Delta y = y_{j+1} - y_j$ , and  $\Delta z = z_{k+1} - z_k$ .

### Poisson Field Solver

The elliptic solver that is used to solve Poisson's equation, is a Successive Over-Relaxation (SOR) method that is coupled with the Newton-Raphson scheme to handle the non-linearity due to the Boltzmann electron density term. The SOR scheme is used instead of the ADI scheme due to its ease in implementation. The issues dealing with parallelization will be discussed in Section 6.3.

Coupled with the Newton-Raphson scheme discussed in Section 4.4, Poisson's equation, Eqn. (4.7), in three dimensions on a non-uniform grid, is written in finite difference form with the stencil shown in Figure 6.2 as (with non-dimensional quantities),

$$\frac{2}{\Delta x_1 \Delta x} \phi_{i+1,j,k}^{t+1} + \frac{2}{\Delta x_2 \Delta x} \phi_{i-1,j,k}^{t+1} + \frac{2}{\Delta y_1 \Delta y} \phi_{i,j+1,k}^{t+1} + \frac{2}{\Delta y_2 \Delta y} \phi_{i,j-1,k}^{t+1} + \frac{2}{\Delta z_1 \Delta z} \phi_{i,j,k+1}^{t+1} + \frac{2}{\Delta z_2 \Delta z} \phi_{i,j,k-1}^{t+1} - \left[ 2 \left( \frac{1}{\Delta x_1 \Delta x_2} + \frac{1}{\Delta y_1 \Delta y_2} + \frac{1}{\Delta z_1 \Delta z_2} \right) + n_{\infty} \exp(\phi_{i,j,k}^t) \right] \phi_{i,j,k}^{t+1} = n_{\infty} (1 - \phi_{i,j,k}^t) \exp(\phi_{i,j,k}^t) - n_i \quad (6.6)$$

where  $\Delta x = x_{i+1} - x_{i-1}$ ,  $\Delta x_1 = x_{i+1} - x_i$ ,  $\Delta x_2 = x_i - x_{i-1}$ , and similarly for  $y$  and  $z$ . This can be written more generally as,

$$A_{i,j,k}^W \phi_{i+1,j,k}^{t+1} + A_{i,j,k}^E \phi_{i-1,j,k}^{t+1} + A_{i,j,k}^U \phi_{i,j+1,k}^{t+1} + A_{i,j,k}^L \phi_{i,j-1,k}^{t+1} + A_{i,j,k}^N \phi_{i,j,k+1}^{t+1} + A_{i,j,k}^S \phi_{i,j,k-1}^{t+1} + A_{i,j,k}^C(\phi_{i,j,k}^t) \phi_{i,j,k}^{t+1} = R_{i,j,k}(\phi_{i,j,k}^t) \quad (6.7)$$

Note that  $A_{i,j,k}^C$  is a function of the potential at a previous iteration due to the Newton-Raphson linearization.

The SOR scheme is defined as follows [Press et al, 1989]. At every grid point  $(i,j,k)$ , the potential is updated as,

$$\phi_{i,j,k}^{t+1} = \phi_{i,j,k}^t - \omega \frac{\Psi_{i,j,k}}{A_{i,j,k}^C} \quad (6.8)$$

where  $\Psi_{i,j,k}$  is the residual of Eqn. (6.7) that is driven to zero. The over-relaxation parameter,  $\omega$ , typically lies between 1 and 2. This value can be chosen optimally with the process of Chebyshev acceleration [Press et al, 1989]. In this scheme, given the Jacobi radius of convergence of the problem (or an estimate based on a reduced problem),  $\rho_J$ ,

$$\begin{aligned} \omega &= 1, & t=0 \\ \omega &= 1/(1 - \rho_J^2/2), & t=1 \\ \omega &= 1/(1 - \omega^{(t-1)} \rho_J^2/4), & t>1 \end{aligned} \quad (6.9)$$

## Particle Mover

Lastly, even though we showed that magnetic field effects can be neglected for CEX ion transport for length scales  $\leq 3$ -5 meters, we have included a magnetic field into the general three-dimensional equations of motion for the particles. The inclusion of the magnetic field requires changing the particle trajectory integrators [Birdsall and Langdon, 1991]. The time-centered finite difference form of the Lorentz equation for the particles is,

$$\frac{\mathbf{v}_{t+\Delta t/2} - \mathbf{v}_{t-\Delta t/2}}{\Delta t} = \frac{q}{m} \left[ \mathbf{E} + \frac{\mathbf{v}_{t+\Delta t/2} + \mathbf{v}_{t-\Delta t/2}}{2} \times \mathbf{B} \right] \quad (6.10)$$

The electric and magnetic field contributions can be separated by introducing two new variables,

$$\mathbf{v}^- = \mathbf{v}_{t-\Delta t/2} + \frac{q\mathbf{E}}{m} \frac{\Delta t}{2}; \quad \mathbf{v}^+ = \mathbf{v}_{t+\Delta t/2} - \frac{q\mathbf{E}}{m} \frac{\Delta t}{2} \quad (6.11a,b)$$

which upon substitution into Eqn. (6.10), eliminate the electric field term,

$$\frac{\mathbf{v}^+ - \mathbf{v}^-}{\Delta t} = \frac{q}{2m} (\mathbf{v}^+ + \mathbf{v}^-) \times \mathbf{B} \quad (6.12)$$

Thus, the velocity can be updated by computing  $\mathbf{v}^-$  from the old velocity using Eqn. (6.11a), performing the rotation due to the  $\mathbf{B}$  field and solving for  $\mathbf{v}^+$  from Eqn. (6.12), and lastly, obtaining the new velocity from  $\mathbf{v}^+$  using Eqn. (6.11b). The vector rotation through an angle  $\theta = (q|\mathbf{B}|/m)\Delta t$ , is performed by,

$$\begin{aligned} \mathbf{v}' &= \mathbf{v}^- + \mathbf{v}^- \times \boldsymbol{\tau}; \quad \boldsymbol{\tau} = \frac{q\mathbf{B}\Delta t}{2m} \\ \mathbf{v}^+ &= \mathbf{v}^- + \mathbf{v}' \times \mathbf{s}; \quad \mathbf{s} = \frac{2\boldsymbol{\tau}}{1 + |\boldsymbol{\tau}|^2} \end{aligned} \quad (6.13a,b)$$

## 6.2 Parallel Computing Concepts

As we have seen, the use of massively parallel computers is enabling for the three-dimensional simulation of the ion thruster backflow over a realistic spacecraft geometry. However, in order to use parallel computers effectively, careful attention is required for the development of algorithms that are suitable for  $N$  computers working simultaneously on a problem and that are communicating together.

Out of the many different types of parallelism that have emerged in high performance computing, there are two types that are most commonly employed now. One is *data parallelism* which is an approach where more or less, the same operation is executed on many elements of a data set. The data parallel approach formed the basis for SIMD (Single Instruction Multiple Data) computers where all the processors are controlled to execute one instruction at a time, but on many pieces of data simultaneously. This approach is valid for



data that are not heavily interconnected, and hence interprocessor communications is negligible. However, if large portions of the data are interrelated, this approach is not as flexible and efficient as the use of a MIMD (Multiple Instruction Multiple Data) computer which is able to do different operations on various subsets of the data. SIMD computers, such as the Thinking Machines CM2 and MasPar, comprise many computational processors that are controlled by a control processor. This control architecture presents a bottleneck in scalability, because as the number of computational processors increases, the workload of the control processor that provides synchronization is the limiting factor in performance. Another drawback is that since every processor is signaled to perform the same operation simultaneously, if the data on a particular processor does not have to be operated on (i.e. does not pass an if test), then that processor remains idle.

The second type of programming model is commonly referred to as *message passing*. In this paradigm, the data is decomposed among the processors, each of which can execute individual instructions on its own set of data. In addition, data is sent between the processors as required. This model is much more flexible, but is more complicated to program since the programmer must explicitly control all the flow of information between the processors. Since many different instructions can be executed at once, these computers are referred to as MIMD computers (as defined above). This type of computer has become the most common today, including the Intel parallel computers, the Cray T3D, IBM SP2, and Thinking Machines CM5 (which is actually a hybrid between a SIMD and MIMD machine).

Initially, the two-dimensional plume model was implemented on the CM5 in SIMD mode to measure performance improvements on a parallel computer. However, results were discouraging, and the message passing approach was adopted. There are three main parallel programming activities that must be taken into account: 1) *partitioning* a program and/or data into concurrent components, 2) adjusting the *granularity* of these components, and 3) *mapping* the components onto the  $N$  computers that form the parallel computing architecture. In addition, the *load balancing* of the parallel system is a very important aspect that must also be considered. Below, we elaborate on these concepts, following the work of Chandy and Taylor [1992] and Fox et al [1988] on these topics.

### Partitioning

The partitioning process involves the dividing of a problem into components that may execute concurrently. The two primary goals in partitioning are *scalability* and the concealing of *latency* and does not necessarily imply the division of a problem into  $N$  pieces where  $N$  is the number of computers available.

Scalability concerns how the performance of a given partitioning scales as a function of the number of computers available. Figure 6.3 shows a typical performance graph for a parallel program operating on a problem of fixed size. The computational time versus the number of computers working is shown. In addition, the time for execution on a single processor is displayed for comparison. For a small number of computers (if the problem can fit onto a small number), the execution time is actually longer than a single processor. This is due to the additional time incurred from communication and synchronization of the processors. As the number of processors increases, the execution time decreases as the speedup due to more processors overcomes the communications overhead costs. However, the execution time reaches a plateau eventually where increases in the number of computers do not result in decreased execution time. This is because there are so many computers, there is insufficient work to keep all the computers occupied, and the communications time is much greater than computational time.

The second goal, concealing latency, also affects the partitioning process. Latency is the time for messages to travel between computers. Instead of waiting for messages to arrive, a processor should have several work components so that it can continue computing while communication is in progress. This concept is called multiprocessing, and allows performance to be improved. Therefore, the partitioning should provide more components than processors available so that multiprocessing is possible.

The partitioning of the problem can refer to two major types: data/domain decomposition, or functional decomposition. Domain decomposition divides up the data - whether it be an array, or a computational grid - among the processors. Functional decomposition divides up the various functions, i.e. subroutines, of a program among the processors. A very complex problem for domain decomposition is when the domain changes dynamically in such a way that the computational load on each processor changes. In this case, dynamic load balancing techniques must be implemented to maintain an equal work load on each processor.

### **Granularity**

The granularity of a parallel computation is the ratio of the amount of computation to interprocessor communication. A proper algorithm should be designed to keep this ratio as small as possible. One way of achieving this is to exploit locality in the problem, i.e. to group partitions that share the same data together to minimize communication. Another important consideration for granularity is tied with domain decomposition. Computation generally scales with the volume of a partition (i.e. the total number of grid points), while communication scales with the surface area of the partition (i.e. only grid points on

partition boundaries are communicated). Thus the volume to surface area ratio of a partition should be kept as large as possible. Conversely, if communication is dominant in a certain direction in the domain, the partitions can be sized accordingly to minimize the amount of communication in that particular direction.

### **Mapping**

Lastly, after the problem has been partitioned, the components must be mapped, or laid out among the processors of the parallel computer. To reduce communications, it is important to place partitions that must exchange information as close together as possible within the parallel architecture. Since mapping concerns the use of a particular machine, the details of the computers' architecture may become important, particularly for higher performance gains. For instance communications strategies may be different in a simple two-dimensional mesh connection versus a hypercube or fat-tree architecture. However, at the general user level, current computer operating systems are growing increasingly sophisticated, and try to make message passing programming relatively independent of machine architecture. Details on the specific computers - the Intel Touchstone Delta and Cray T3D - that were used in this thesis, will be discussed in Chapter 7.

## **6.3 Parallel Implementation of 3-D PIC Model**

### **Partitioning**

Data decomposition is used for the partitioning of the problem. The computational domain described in Section 6.1 is partitioned into blocks according to a simple rule that each block face must be of a single type, i.e. a face is completely a spacecraft surface or an interior interblock face - it should not be a mixture in order to maintain simplicity in programming. The methodology of dividing a problem into blocks actually simplifies programming structure, and enables very general geometries to be handled, because each block can be individually initialized with or without particles, and with various boundary conditions.

Figure 6.4 shows a coarse decomposition of the domain in the x-y plane. The domain is partitioned into a minimum of two blocks in the x-direction: one behind the thruster plane, and another in front. There are seven in the y-direction for a full plane simulation, and four for a half plane simulation in order to accommodate thruster, spacecraft, solar array, and exterior boundary surfaces. Lastly, there are five in the z-direction. Thus, for a half plane simulation, there are a minimum of 40 blocks in the primary decomposition. Each block can then be decomposed into smaller blocks by a secondary decomposition, so

that depending on the total domain size, there are two to three blocks per available processor. The blocks are numbered as  $N = i + j N_x + k N_x N_y$ , where  $N_x$  and  $N_y$  are the number of blocks in the  $x$  and  $y$  direction, and  $i, j, k$  are the block indices which start from (0,0,0) in the lower south-east corner of the domain.

The faces of each block must be categorized for computing and communications purposes. It is important to know what types of boundary conditions to enforce for the Poisson solver, and how to treat particles that cross the boundaries of each block. The face types are identified in the following manner:

- Hole (Interior of spacecraft - no computation or communication)
- Interior interblock cut face
- Exterior boundary - Dirichlet or Neumann potential boundary condition
- Spacecraft surface - potential specified
- Thruster front - potential specified
- Top solar array - potential specified
- Bottom solar array - potential specified
- Reflecting boundary condition on  $y=0$  plane for upper half plane calculations - (Neumann condition on potential)

The reflecting boundary condition is used for the particles, i.e. a particle that hits this surface is reflected - just as on the plume centerline in the axisymmetric model. Physically, for every particle that leaves the upper half plane, there is another one that is entering from the lower half plane. On all other exterior and spacecraft boundaries, particles are absorbed. Particles are passed between processors if they share an interior interblock cut face.

The way that the global computational grid is divided at the boundary between two blocks is illustrated in Figure 6.5 (which is the same for every axis). Particles in Block  $N$  whose position is greater than or equal to  $x(\text{IXB})$  are passed to Block  $N+1$ . Similarly, particles that are less than  $x(1)$  in Block  $N+1$  are passed to Block  $N$ .

### Parallel PIC Algorithm

A pre-processing geometry code generates the global computational domain for a given problem, and interactively decomposes the domain into  $N_b$  blocks. Generally, if  $M$  is number of processors available,  $N_b = (2-3)M$ . An input file for each block is created that consists of the local grid, boundary conditions, and face types. The  $N_b$  input files are mapped onto the  $M$  processors, and the same PIC code operates on each block.

Appendix B gives a full flowchart of the parallel PIC algorithm. The main difference between the parallel algorithm and the serial one in Appendix A, is that the particle

operations are combined together for simplicity of programming. During the particle operations, the particles' charge is deposited to the grid and then they are moved based on the electric field computed at the previous time step. This offset in time does not pose a problem since we are interested in the steady-state solution. However, for time accurate behavior, one must be cautious.

Communication between the processors is necessary at two different locations as can be seen in the flowchart. After the particle operations, particles that have left a block need to be passed to neighboring blocks if necessary. In addition to the particles being passed between blocks, the densities at the grid points on the boundaries between neighboring blocks must be superimposed to get the right values. For instance, referring to Figure 6.5, a particle in Block  $N$  between  $x(IXB-1)$  and  $x(IXB)$  is weighted to those two points. However, Block  $N+1$  must know about the charge of that particle in order to have the proper density at its grid point  $x(1)$ . Thus these boundary density values must be added up between blocks.

Communication between blocks for the potential solver is also necessary. After an SOR sweep in all the blocks, the potentials must be passed between blocks that have common interior interblock faces. In essence, continuity of the potential must be enforced. The potential at grid points  $IXB$  in Block  $N$  are passed to grid points 1 in Block  $N+1$ , while grid points 2 in Block  $N+1$  are passed to grid points  $IXB+1$  in Block  $N$ . Thus, each block solves the potential from points 2 to  $IXB$ , holding points 1 and  $IXB+1$  fixed for each iteration. The process of an SOR sweep followed by boundary cell exchange is continued until global convergence is met.

The biggest challenge to parallel computing for simulations where the computational load is dynamically changing is the load balancing of all the processors. In our simulations, the CEX ions are created within the beam and expand outwards to surround the spacecraft. Initially, all the particles are within the beam, and processors that have blocks in that region are doing all the work. Processors outside of the beam do not have any particles and are only solving the potential field in their respective blocks. Thus, initially, there is a severe load imbalance on the machine. However, as the simulation progresses, the particles travel into other processors and the load becomes more distributed. To alleviate this problem somewhat, the blocks that are within the beam (where the particle densities are the highest) are made smaller than blocks outside so that more processors have portions of the beam. It may be noted that blocks outside are larger and hence have more grid points for the potential solver. Thus, processors outside of the beam may not have any particles, but will be busy solving the field. However, the field must be solved before the particle operations, so that there is no gain in this respect.

The most efficient approach is to balance the load dynamically while the simulation is in progress. There are two approaches: one is to change dynamically the size of the blocks, and another is to move the blocks that have the most particles to processors that have the least work. By load balancing dynamically, there is always the tradeoff between gains in computational efficiency and the cost associated with the repartitioning. The results of the three-dimensional calculations in this thesis do not incorporate any form dynamic load balancing. A static decomposition was used based on sizing the blocks so that those in the beam were about half the size of those outside. These results are the first of their kind in three-dimensional ion thruster plume simulations, but are quite elementary in terms of the complexity of the computer science issues. There is much room for increases in parallel efficiency, and is one area of future improvement beyond this thesis.

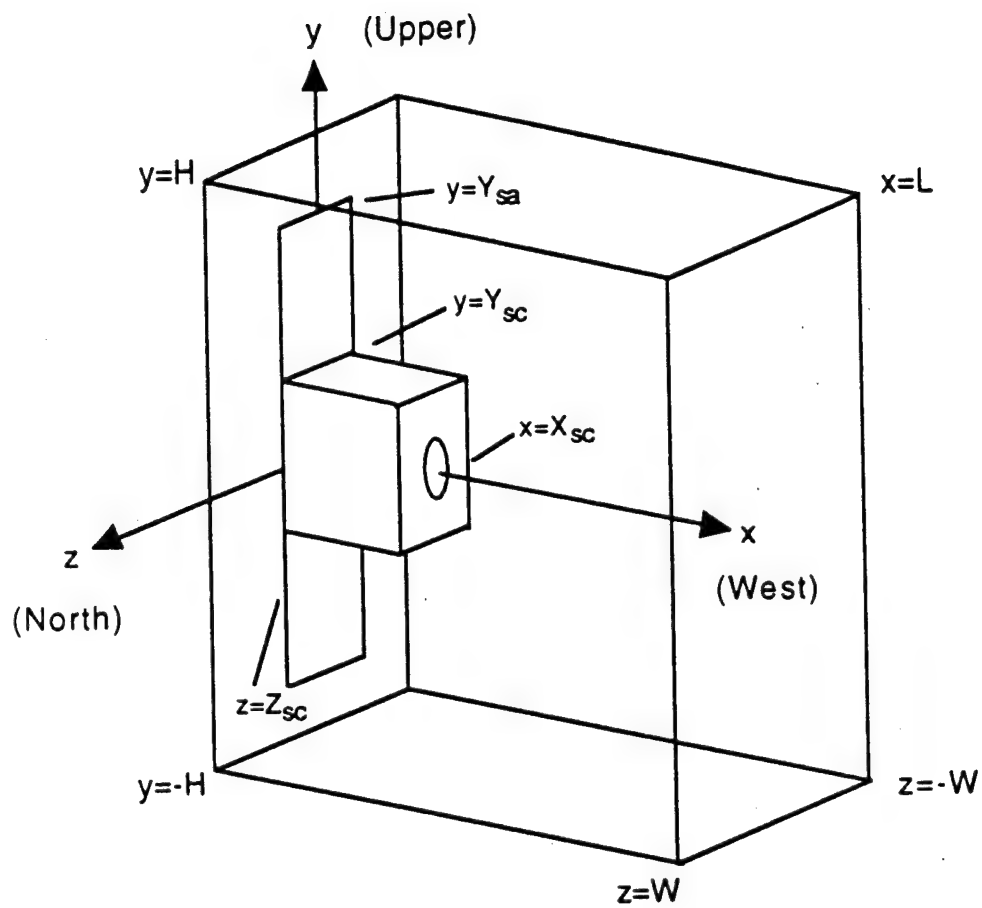


Figure 6.1 Three-dimensional domain geometry

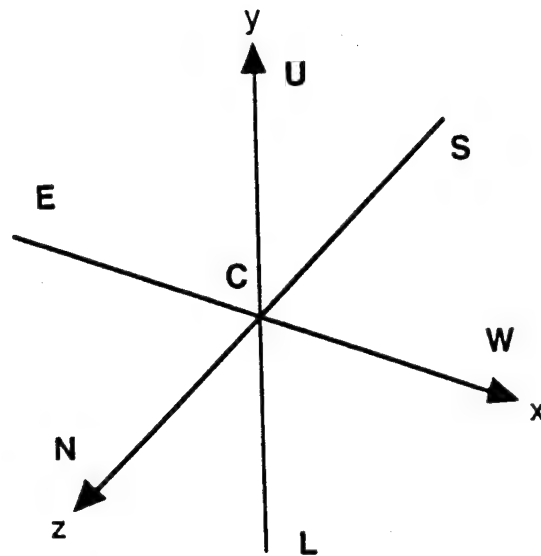


Figure 6.2 Three-dimensional Poisson equation solver stencil

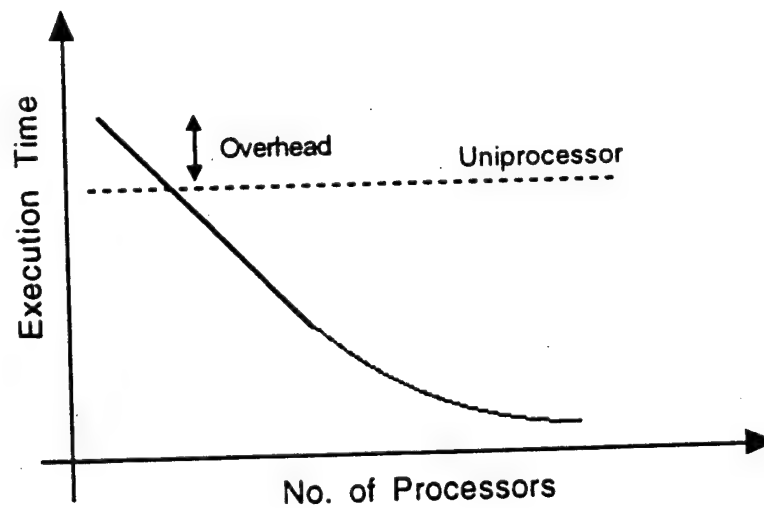


Figure 6.3 Typical parallel computing performance graph  
(adapted from *Chandy and Taylor* [1992])



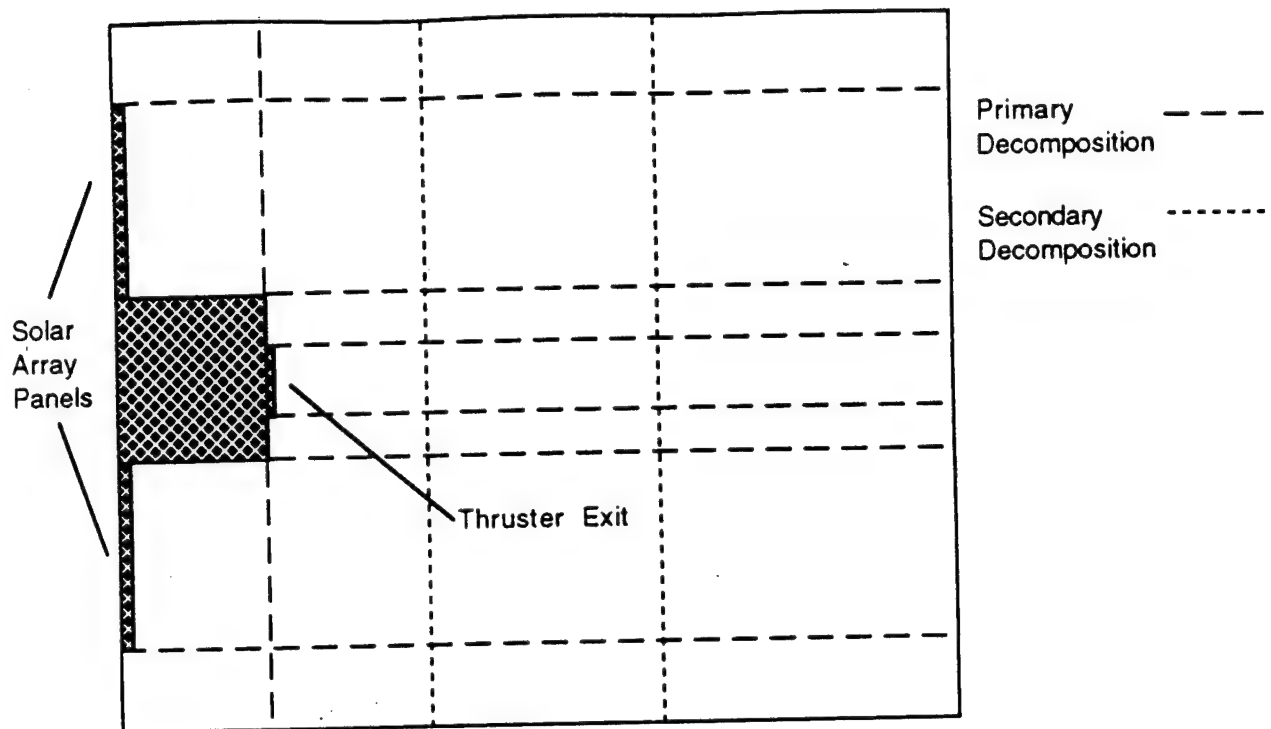


Figure 6.4 Example of domain decomposition (in a plane)

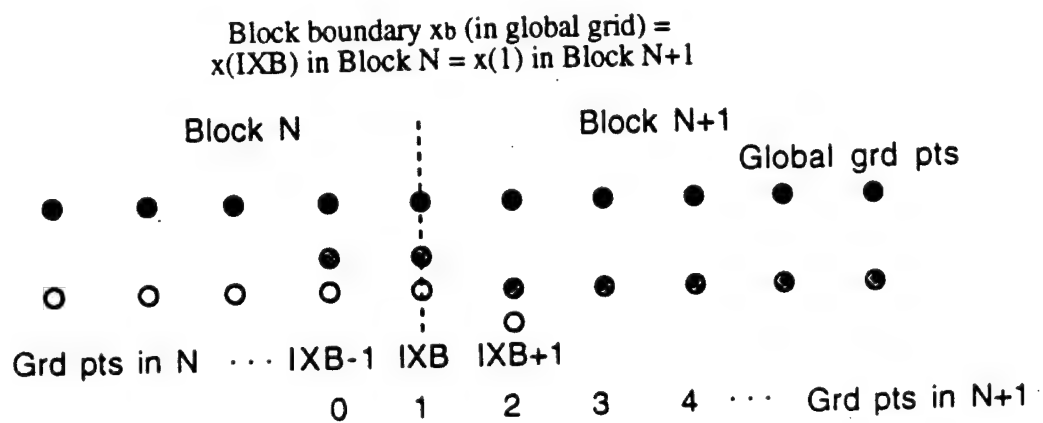


Figure 6.5 Detail of splitting computational grid between two neighboring blocks

# Chapter 7

## Three-Dimensional Simulation Results

In this chapter, we present and discuss the three-dimensional simulation results. The main goal of the three-dimensional model in this thesis is to investigate the CEX ion backflow structure and see whether geometrical effects due to a fully three-dimensional spacecraft are important. We will also compare the three-dimensional results with two-dimensional axisymmetric results. In the case considered in this thesis, it is shown that the two-dimensional model gives an upper bound on the CEX plasma density, and hence, the two-dimensional model can be used for estimates in situations that are not purely axisymmetric. This is highly desirable since the two-dimensional model offers vast computational savings over the three dimensional model.

### 7.1 Three-Dimensional Effects

We will examine the backflow from an ion thruster on a spacecraft that is similar in dimensions to the U.S. Air Force ARGOS spacecraft (Advanced Research and Global Observation Satellite). The launch of this spacecraft, scheduled in 1995, with the ESEX (Electric Propulsion Space Experiment) payload, will be the first USAF electric propulsion flight in over 25 years, and will demonstrate EP thruster operation at high power levels [Pollard *et al.*, 1993]. We simulate an ion thruster on this spacecraft, but in actuality, the thruster onboard will be a 26 kW ammonia arcjet. The arcjet will be fired for ten cycles of 15 minutes duration each using battery power. Instrumentation onboard will measure vehicle acceleration, surface contamination, thermal loads, radiated EMI in the 2-12 GHz range, and visible plume emissions. The goal of the flight is to understand aspects of high-power arcjet performance and spacecraft interactions that cannot be simulated on the ground. However, the brief testing of the thruster will not allow the assessment of long-

term surface contamination [Pollard *et al.*, 1993].

Following the geometry of Figure 6.1, the size of the model spacecraft in the simulation is 1.5 m long in the  $x$ -direction. This is only the distance from the solar array panels to the thruster exit; the entire spacecraft is not modelled. The model spacecraft has a half-height of 0.5 m in the  $y$ -direction, and a width of 1 m in the  $z$ -direction. A solar array panel extends 3.1 m from the top of the spacecraft 1.5 m behind the thruster exit, and is biased. The potential drop from the spacecraft to the end of the array is 28 volts, typical of most current systems, with the spacecraft grounded to the positive end. The simulation domain is a half-domain in the  $y$ -direction. The ion thruster simulated is based on a Hughes 13 cm beam diameter xenon thruster, and the operating conditions are a beam current of 0.404 A, a propellant utilization efficiency of 0.84, and a beam ion velocity of 33,200 m/s. A constant electron temperature of 1 eV is used, and no geomagnetic field was included. To encompass the spacecraft and the solar array panel, the dimensions of the computational domain are 3.2 m  $\times$  4.5 m  $\times$  3 m in the  $x$ ,  $y$ , and  $z$  directions respectively. The computational grid has 139 grid points in the  $x$ -direction, 241 in the  $y$ -direction, and 281 in the  $z$ -direction - a total of 9,413,219 grid points.

The problem was run initially on the massively parallel Intel Touchstone Delta at Caltech, and subsequently on the Cray T3D at the Jet Propulsion Laboratory. Inaugurated in 1991, the Delta consists of 512 processors each with 16 MB of memory and a peak speed of 80 Mflops. However, the amount of user available memory per node is closer to 12 MB, bringing the total machine capacity to over 6 GB. The processors are connected via a scalable two-dimensional mesh. The Cray T3D, installed in 1994, consists of 256 nodes, each with about 55 MB of usable memory - a total of 14 GB. The speed of each processor is about 150 Mflops peak, and they are connected via a three-dimensional torus topology which offers much better interprocessor communications. Message latency (time to send a message) on the Delta is about 150  $\mu$ s and the bandwidth (rate of information being transmitted) is about 10 MB/s. In contrast, the latency is around 10  $\mu$ s, and the bandwidth is 120 MB/s on the T3D.

Since the problem was initially targeted for the Delta, the domain was partitioned into 1575 blocks so that there would be three or more blocks per processor. The same partitioning was kept for the T3D, hence six or more blocks were allocated to each processor. It was found that the simulation code performed about six times faster on the T3D due to its more powerful processors, and faster communications network. The simulation was run until steady-state was reached with the particle population reaching 17.5 million. Due to the lack of dynamic load balancing, at the start of the simulation, only about 10% of the processors are utilized for particle operations. However, as the particles

expand from the beam region, the number of processors utilized increases. The ratio of the time spent in interprocessor communications to computation, is about 1.4%, and the overall speed of the code is about 30 s/timestep. Due to the high demand of the machines and the availability of only four hour slots on weekends, the simulation took nearly two months to complete.

Even with 17.5 million particles, there is a noticeable amount of numerical noise (even with smoothing applied) since there are not at least ten particles per cell in the backflow regions. However, the results are sufficient for identifying general three-dimensional aspects in the backflow structure. For better results, the number of particles in this simulation should be doubled - to at least 35 million. Figure 7.1 shows a picture of the spacecraft (gray surfaces) and two planes in the  $x$ - $y$  (vertical) and  $x$ - $z$  (horizontal) displaying the potential in the plume. A potential isosurface is also rendered. Since the isothermal Boltzmann model is used for the electrons, isopotential surfaces are also isodensity surfaces, and we can clearly see the expansion of the CEX plasma around the model spacecraft.

To show the plume structure more clearly, we show a contour plot of the total ion density in the  $x$ - $y$  plane cut directly through the center of the plume ( $z=0$ ) in Figure 7.2. The plasma density decays from  $10^{14} \text{ m}^{-3}$  in the beam at the thruster exit, to below  $2 \times 10^{10} \text{ m}^{-3}$ . The background plasma density is fixed at  $10^{10} \text{ m}^{-3}$ , typical of the LEO environment. In the region directly above the spacecraft, the CEX ions expand over the top of the spacecraft, and the density there is between  $1$ - $2 \times 10^{10} \text{ m}^{-3}$ . It should be pointed out that the valleys in the contours at right angles to the beam at  $x=1.5 \text{ m}$ , are due to few particles in the highly skewed grid cells in that region.

Figure 7.3 shows the same contour levels of the total ion density in the  $x$ - $z$  plane cut directly through the center of the plume ( $y=0$ ). It is important to compare this plane with the  $x$ - $y$  plane to see whether there are any differences. If the plume structure is truly axisymmetric, there should be no difference. In Figure 7.4, the total ion density along an arc 1.25 m from a point 5 cm in front of the thruster center is shown for both the  $x$ - $y$  and  $x$ - $z$  planes. Within the beam, the densities are the same as they must be since the beam is circular. However, outside of the beam from angles of  $30^\circ$  to  $105^\circ$ , the  $x$ - $y$  plane density is higher by a factor of about 1.5. However, in the backflow regions closer to the spacecraft ( $>110^\circ$ ), the densities are the same and fall to zero around  $155^\circ$  where the radial arc intersects the spacecraft surfaces. Even though there is a solar array panel in the  $x$ - $y$  plane, it does not affect the density near  $155^\circ$  since the solar array panel is about 30 cm away at that point, and the influence of the panel only extends a few cm away due to Debye shielding. However, the differences between the two planes near the thruster beam can not

be given too much significance with these particular results given the fair amount of noise and the fact that the  $x$ - $z$  plane is a computational boundary. It should be mentioned that since the thruster was located in the center of the spacecraft face, significant differences would not be expected. However, if the thruster was off-centered, there would definitely be a difference seen, with higher densities along the spacecraft side that was closer to the thruster.

The geometrical effect of the rectangular spacecraft on the backflow is apparent though, when we examine the  $z$ - $y$  plane that is perpendicular to the plume axis. Figures 7.5a,b,c are  $z$ - $y$  planes that are 3, 67, and 95 cm respectively behind the thruster exit plane. In Figure 7.5a, we can clearly see that the CEX ions flowing back around the spacecraft do not do so in a completely axisymmetrical fashion due to the rectangular geometry of the spacecraft. The CEX ions are essentially expanding around a plate that is the spacecraft face the thruster is located on, and the backflow is concentrated on the top and both sides. However, at the corners ( $45^\circ$  to the  $y$  axis), the density is much less. This "corner-effect" can also be seen in the three-dimensional potential structure in Figure 7.1. The potential surfaces on the top and sides of the spacecraft are roughly flat "planes" that angle back. Along the top corners, the potential has a ridge structure. However, as the plasma continues to expand back around the spacecraft, the CEX ion distribution becomes more uniform as seen in Figures 7.5b and c. Note the high level of noise above the spacecraft which is due to the small grid cells and small numbers of particles. In the planes farther behind the thruster exit, the ballooning of the CEX plasma in the negative  $x$  axis direction can be seen in the contour plots.

A clearer presentation of the asymmetry in the  $z$ - $y$  plane is shown in Figure 7.6, where the total ion density along an arc 0.75 m from the center of the plume is shown for three  $z$ - $y$  planes located 3, 24, and 95 cm upstream of the thruster exit plane. In the plane 3 cm upstream, the density falls by almost an order of magnitude at  $45^\circ$  and  $135^\circ$  - angles corresponding to the corners of the spacecraft. However, at planes further upstream, the density becomes more axisymmetric, until 95 cm upstream, there is no azimuthal distinction. At distances further from the plume center though, the structure of the CEX density still retains a distinctive asymmetric nature due to the rectangular spacecraft. Thus, this relatively simple calculation demonstrates that the three-dimensional geometry of the spacecraft influences the structure of the plume backflow.

## 7.2 Comparison of Two- and Three-Dimensional Results

To see how substantial the three-dimensional effects are in comparison, the

axisymmetric model was applied to the ARGOS spacecraft in the  $x$ - $y$  plane, including the solar array panel. The same number of grid points ( $139 \times 241$ ) and the same thruster operating conditions were used. Various numbers of particles were used ranging from 60,000 to 300,000. The "valleys" seen in the contours at  $x=1.5$  m above the beam in Figure 7.2 were recreated to a certain extent when the particle count was very low, verifying that the three-dimensional simulation did not have a satisfactory number of particles. The appeal of the axisymmetrical model is that low noise results could be obtained in two-dimensions with less than 200,000 particles. The two dimensional simulation could run 24 hours a day on a workstation, and depending on the number of particles, the overall performance was between 4-20 s/timestep. Thus, the axisymmetric code was much more cost effective in terms of producing quality results in a relatively short amount of time ( $<1$ -3 days).

Figure 7.7 compares the total ion density along a radial cut ( $90^\circ$  to plume centerline) 22 cm downstream of the thruster in the  $x$ - $y$  plane from both the three-dimensional and axisymmetric simulations. We can see that the comparison is very good. The plume radial expansion is axisymmetric as we expect. It is interesting to see what the decay rate in the density is due to the plume expansion. Recall in Chapter 2, that the simple backflow model models the CEX plasma with a constant velocity spherical expansion, and the density decays as  $1/R^2$ . From the density profile in Figure 7.7, we see that the density decays roughly with a rate of  $1/R^{2.4}$ , which is quite close. However, a difference is to be expected since the CEX ions are not expanding at constant velocity, but are still slowly gaining speed as they fall down the potential hill from the plume. It must be kept in mind that with the isothermal Boltzmann electron model, the plasma density and potential follow each other, and hence the potential is not completely flat outside of the beam.

It is important to see how the CEX plasma behaves, not only radially to the beam, but also along rays at angles greater than  $90^\circ$  that penetrate into the backflow region. In Figure 7.8, the total ion density along a ray  $120^\circ$  from the plume centerline and from a point 0.75 m in front of the thruster exit is shown. Again, we see that the agreement between the two models is very good, with the three-dimensional results falling slightly below the axisymmetric results at distances greater than two meters. This may possibly be due to an insufficient number of particles in the three-dimensional model, but nevertheless, the axisymmetric model yields larger densities. We note that the density decay in the backflow region along this ray is also about  $1/R^{2.23}$ , very similar to the behavior along a ray perpendicular to the plume axis.

In addition to radial comparisons, we compare the models along an arc of constant radius. In Figure 7.9, the total ion density along an arc a distance of 1.5 m from a point 5

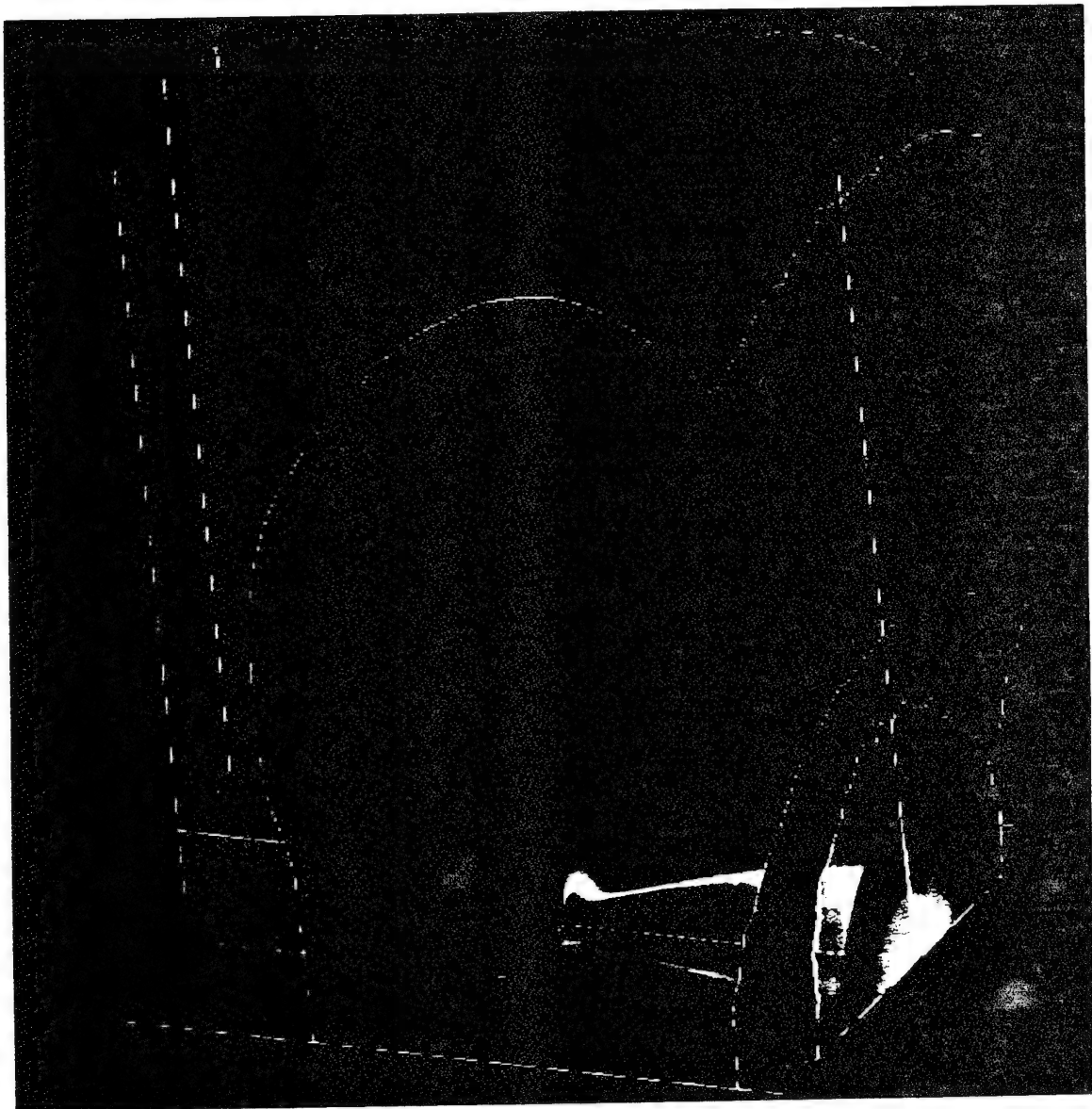
cm in front of the thruster is shown. In the backflow region at angles greater than  $90^\circ$ , the axisymmetric results are higher than the three-dimensional results again. Thus, we see that the axisymmetric model gives an upper bound on the CEX plasma density in the backflow regions.

Lastly, we investigate the influence of the solar array panel on the backflow with the axisymmetric model. Figure 7.10 shows the total ion density along an arc 1.25 m from a point 5 cm in front of the thruster, similar to Figure 7.4. Compared are a case with a solar array panel extending 3.1 m above the spacecraft, and a case without the solar array panel. The arc intercepts the surface of the spacecraft around  $155^\circ$  at a point about 30 cm from the solar array panels. Within numerical noise, there is no difference between the two cases. This is to be expected since the influence of the solar arrays is very localized to a few cm from its surface. Hence, the noticeable differences seen in Figure 7.4 are suspected to be not physical.

From the comparisons of this relatively simple geometry case, we conclude (at least for asymmetric cases similar to one explored here) that the axisymmetric model can be used to provide an upper bound on the CEX backflow in situations that are not too strongly asymmetric. For situations where asymmetry is stronger, the two-dimensional model can be used along various directions to at least provide an estimate. For example, if the thruster was not located in the center of the spacecraft face, but was located in a manner shown in Figure 7.11, the axisymmetric model could be run twice - once with dimension  $a$ , and again with dimension  $b$ , to estimate the CEX plasma at points  $A$  and  $B$  respectively. However, for more complex geometries, the fully three-dimensional model would have to be used. There are many computer science issues that need to be addressed such as dynamic load balancing that will improve the performance of the code. Nevertheless, routine three-dimensional calculations of this nature may have to wait for the next generation of massively parallel computers.



Figure 7.1 3-D simulation results showing potential on x-y and x-z planes and a potential isosurface





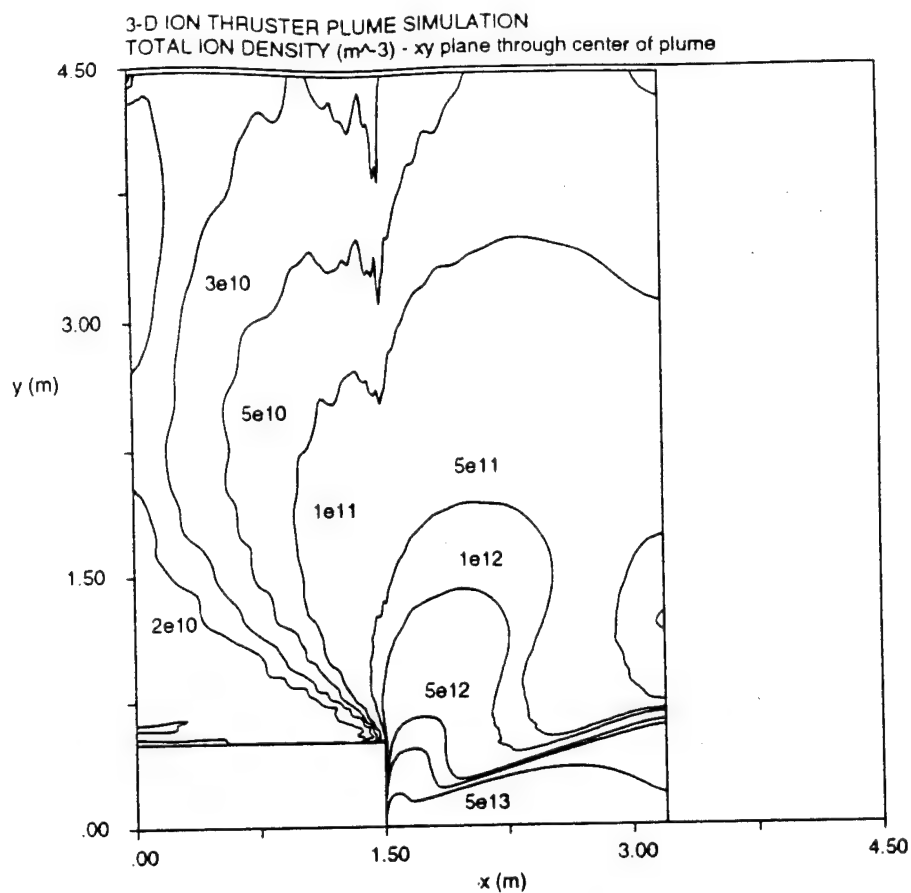


Figure 7.2 Total ion density in x-y plane through plume center ( $z=0$ )

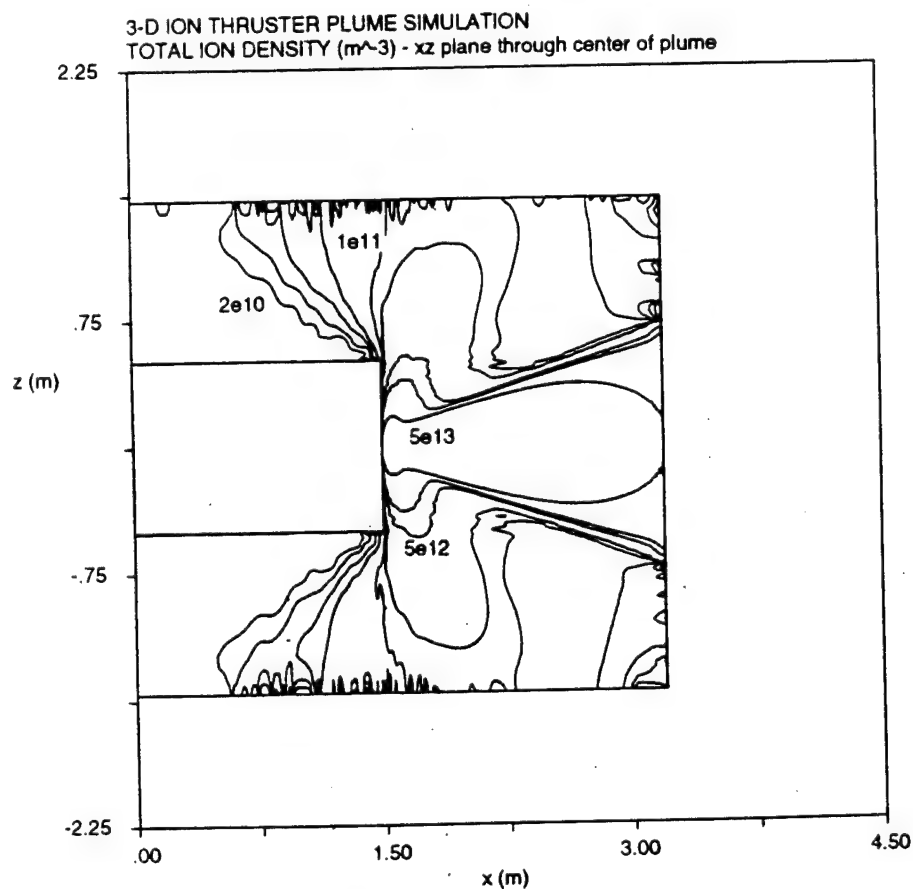


Figure 7.3 Total ion density in x-z plane through plume center ( $y=0$ )

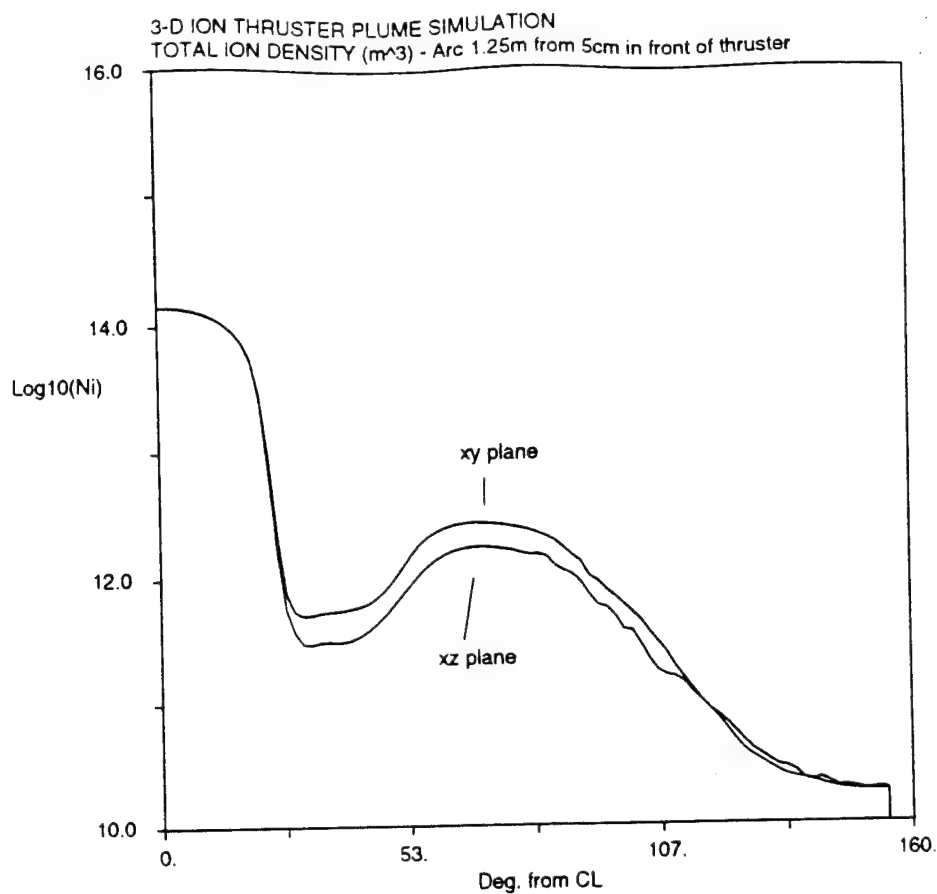


Figure 7.4 Comparison of total ion density in x-y and x-z planes along an arc 1.25 m from a point 5 cm in front of the thruster exit

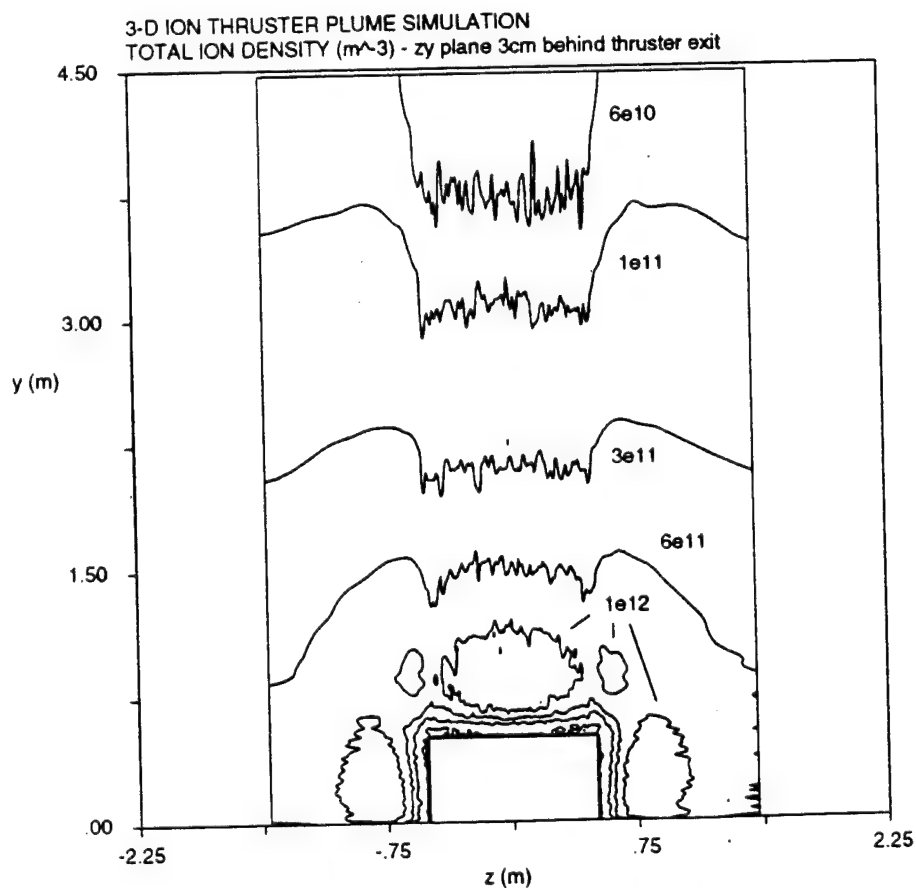


Figure 7.5 Total ion density in z-y plane for x position a) 3 cm upstream of thruster exit plane

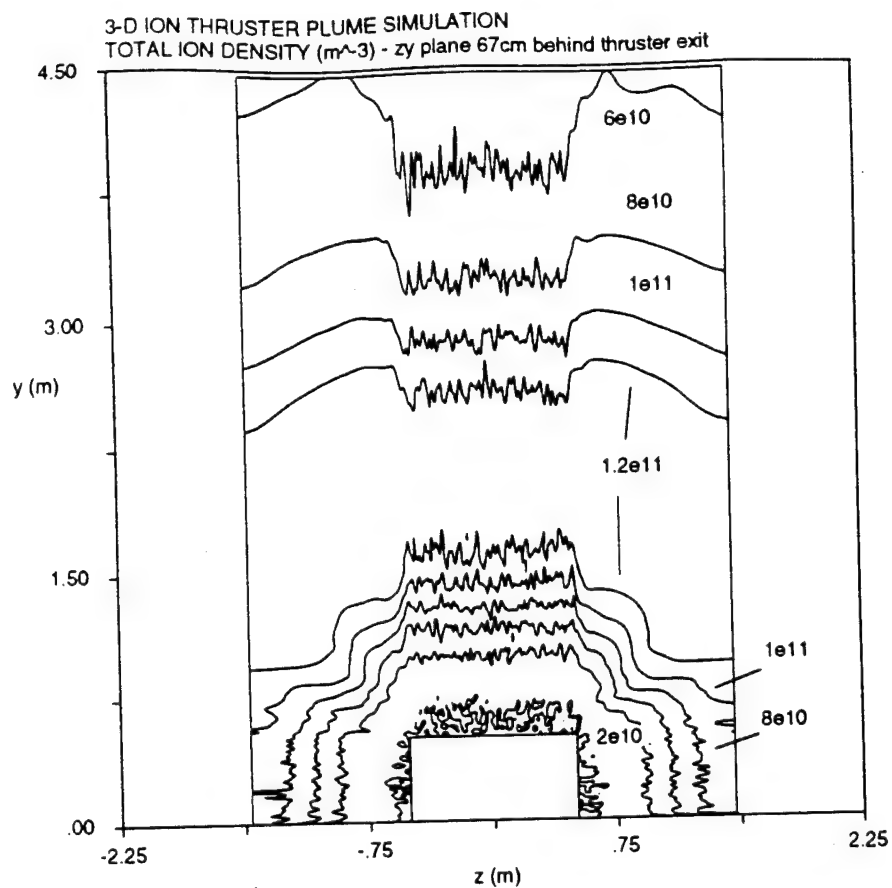
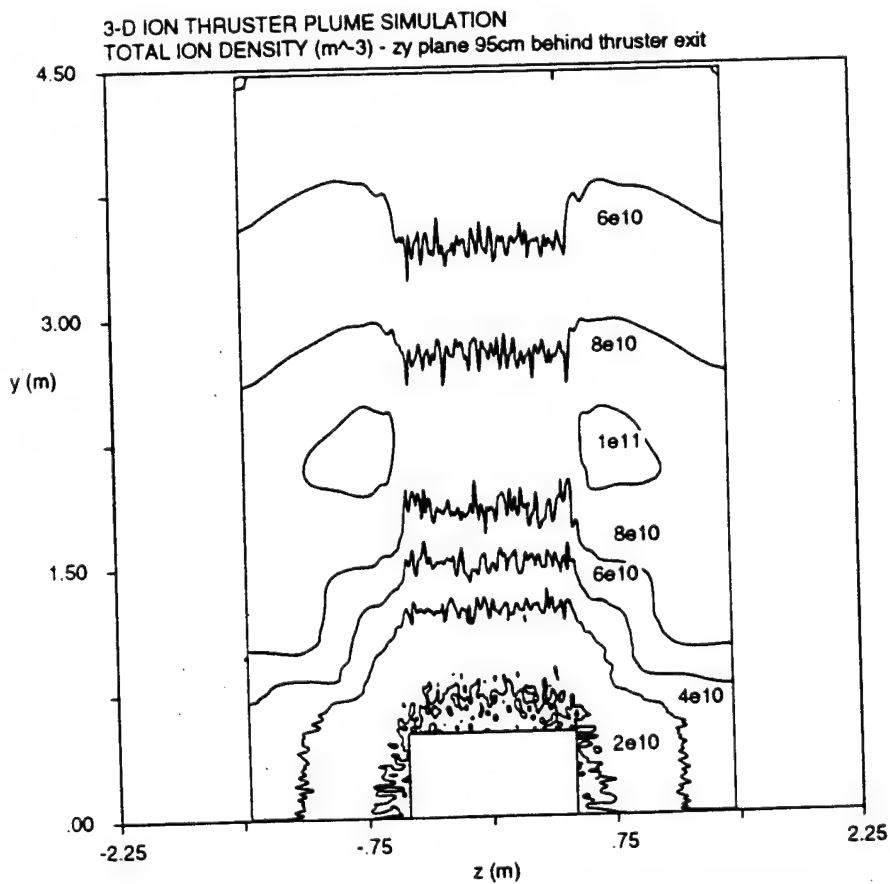


Figure 7.5 Total ion density in  $z$ - $y$  plane for  $x$  positions b) 67, and c) 95 cm upstream of thruster exit plane



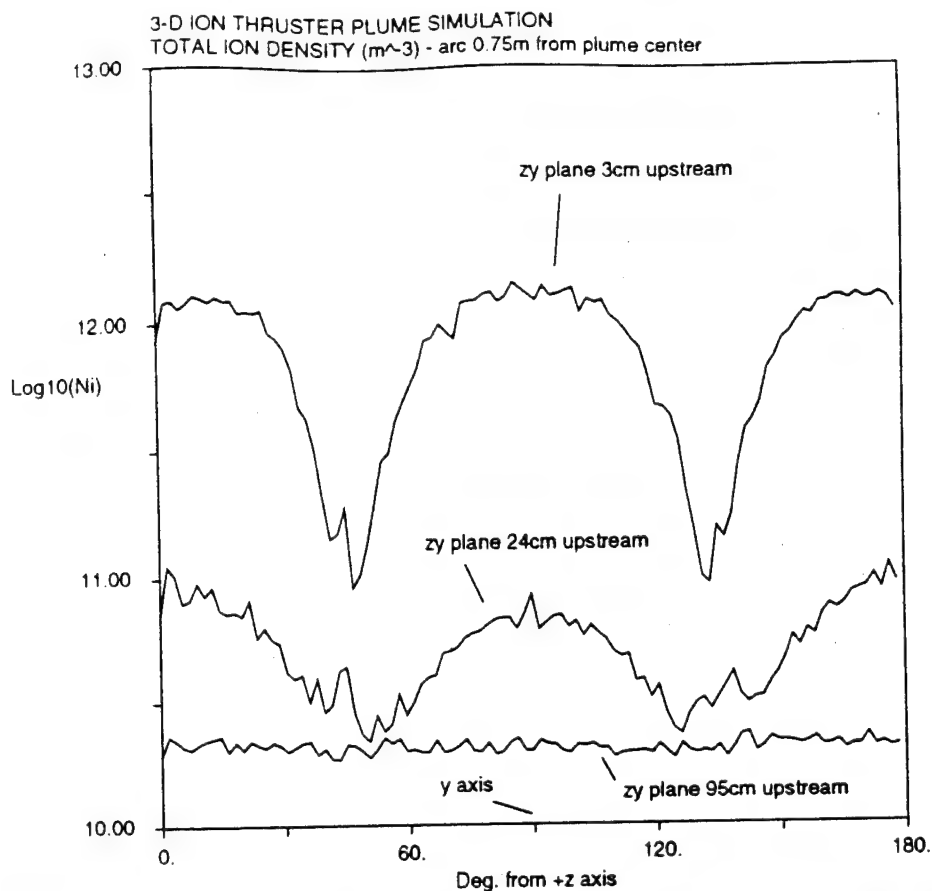


Figure 7.6 Comparison of total ion density along an arc in the z-y plane 0.75 m from the plume center in planes 3, 24, and 95 cm upstream of the thruster exit plane

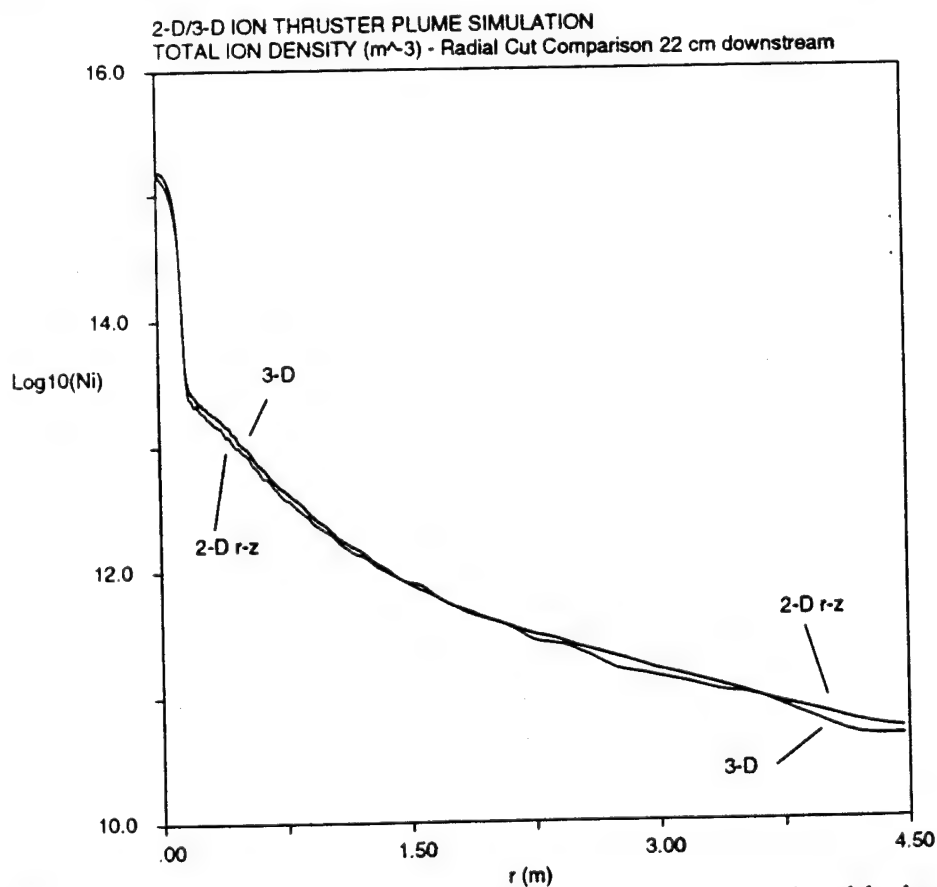


Figure 7.7 Comparison of total ion density from two and three-dimensional models along a cut  $90^\circ$  to plume 22 cm downstream from the thruster exit in x-y plane

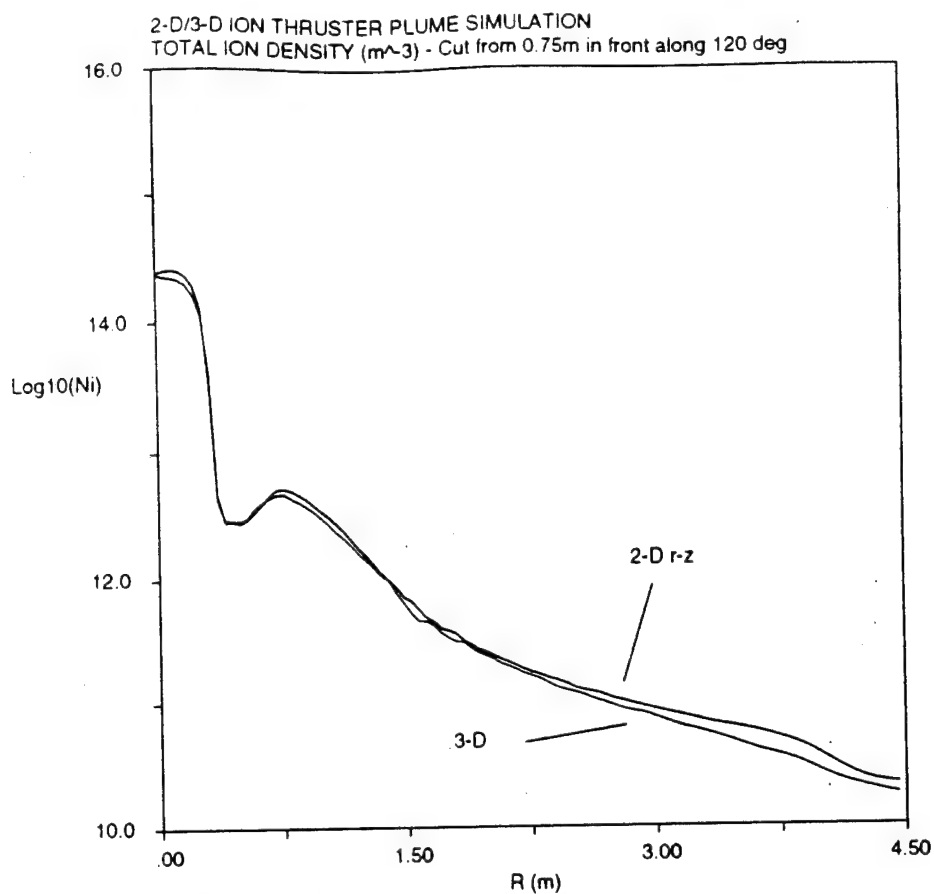


Figure 7.8 Comparison of total ion density from two and three-dimensional models along a cut 120° from plume and from a point 75 cm downstream of thruster exit in x-y plane

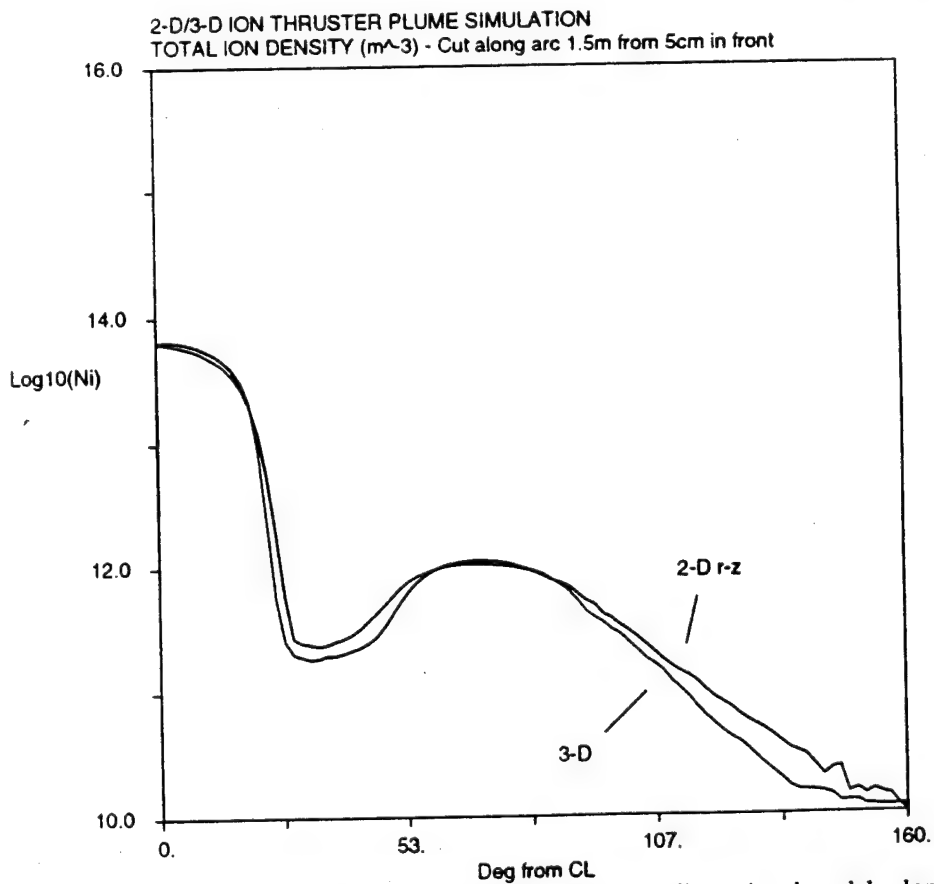


Figure 7.9 Comparison of total ion density from two and three-dimensional models along an arc 1.5 m from a point 5 cm in front of the thruster in the x-y plane

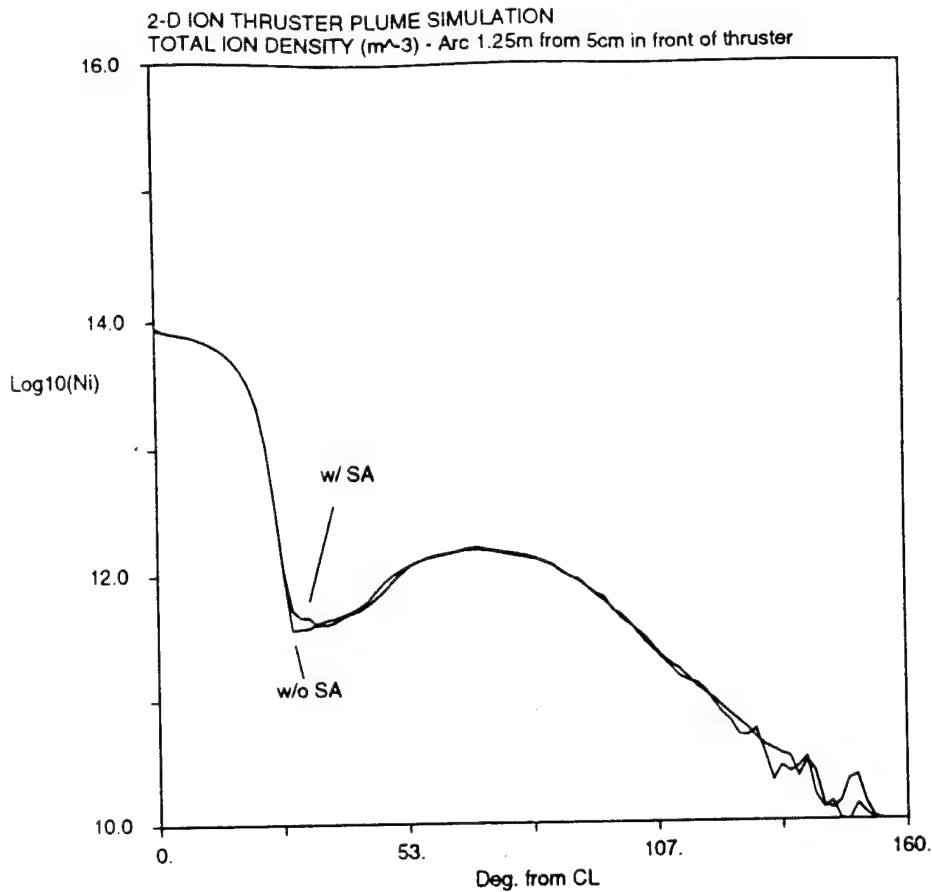


Figure 7.10 Comparison of total ion density with and without solar array panel along an arc 1.25 m from a point 5 cm in front of the thruster in the x-y plane

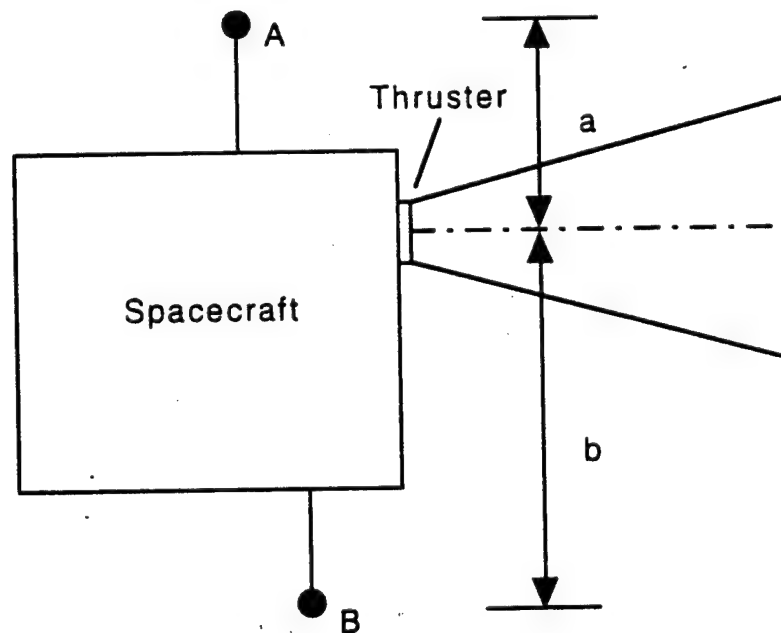


Figure 7.11 Geometry of a situation where axisymmetric code can be applied with two different dimensions

# Chapter 8

## Dual Thruster Simulation Results

### 8.1 Multiple Thruster Issues

Thus far, we have concentrated on investigating the plume backflow of single thrusters. In reality, thrusters will most likely be operated on spacecraft in multiples or at least in pairs for increased thrust, as well as reliability. In this chapter, we extend the previous single thruster models to examine the plumes and backflow from two thrusters operating simultaneously. The most important issue is whether the backflow from each individual thruster can be superimposed to give the total backflow from a group of thrusters. The aim of this chapter is to address this issue by showing that the backflow is indeed non-linear. It is shown that the potential structure in the combined plume yields enhanced backflow currents in certain directions. In addition, the grid impingement current on a thruster increases with multiple thruster operation. Of course, these results are dependent upon the separation distance and orientation between the thrusters.

An important modelling issue regarding multiple thruster operation is the interaction between the beams. In the axial direction, the beams are co-streaming, and in the radial direction, counter-streaming as they penetrate each other. The presence of streaming instabilities may give rise to fluctuating electric fields and turbulence that may affect the transport of slow thermal ions within the beam. In addition, beam instabilities will convert the kinetic energy of fast beam ions to thermal energy, and will cause the plume to spread over some length scale. However, these kinetic effects can not be dealt with rigorously with the present model due to the fluid nature of the electron model. Such issues must be addressed with a fully kinetic model of both the ions and electrons.

In the previous single beam modeling, the beam ion density was given by an analytical expression which agreed well with experimental data. To model multiple thrusters, an

important issue is whether the beam ion models can be superimposed for the multiple thrusters. This issue was addressed by comparing the CEX ion production rates based on adding the densities of two individual ion beams and a more rigorous method where the beam ions were treated as computational particles. In the later method, beam ions were injected each time step from two thrusters, until the beams fully developed, i.e. the first particles traversed the computational domain. The volumetric CEX ion creation rates from the two approaches compared well as shown in Figure 8.1. In this figure, the number of CEX ions created by the injection method rises to a steady state when the beam fully develops. Slight differences were noted at the beam edges; the particle beam had a divergence angle that was greater by 1-2°, but in these regions, the amount of CEX ions created was negligible. Thus, the approach of simply adding the beam ion densities for the two beams is reasonable. A numerical model was developed that could be applied to any number of thrusters in any arbitrary geometric configuration as long as they are oriented in the same direction and their exit planes are the same. However, in this study, we only considered two thrusters. Unfortunately, very little data has been taken from dual thruster operation, so detailed comparisons are not possible.

## 8.2 Dual Thruster Results

In this study, the plumes and backflow was investigated for two 8-cm beam diameter ion thrusters using xenon as propellant. The thrusters were oriented as in Figure 8.2 on a model rectangular spacecraft that was 10 cm long in the  $x$  direction, and 20 cm wide in both the  $y$  and  $z$  directions. The thrusters were aligned along the  $y$  axis, and were separated by 10 cm (from center to center). Each thruster had a beam current of 0.3 A, a beam velocity of 33,200 m/s, and a propellant utilization of 0.84. Ambient plasma conditions typical in low earth orbit were used. For the sputtered molybdenum grid material, a neutral density of  $3.25 \times 10^{13} \text{ m}^{-3}$  was used, a value from Table 5.6. The actual value used is irrelevant; the goal here was to see qualitatively the distributions with two thrusters operating, and not to predict the backflow for a given thruster and thruster-spacecraft configuration. The computational domain was 0.3 m along each side, and the total number of grid points (including empty ones within the spacecraft) was nearly 230,000.

### 8.2.1 Directional Orientation of Xenon CEX Backflow

Figure 8.3 shows a contour plot in the  $y$ - $z$  plane two cm behind the thruster exit plane showing the propellant CEX ion density. The contours clearly show the enhanced density



on the sides of the spacecraft perpendicular to the axis joining the two thruster centers. This clearly shows the directional nature of the backflow. Figure 8.4 shows an angular cut in the same  $y$ - $z$  plane of the CEX ion current density sweeping from  $-90^\circ$  ( $-y$  axis) to  $90^\circ$  ( $+y$  axis). At  $0^\circ$  ( $+z$  axis), the current density is almost a factor of five greater than along the axis that joins the thruster centers.

An examination of phase space clearly shows how the CEX ions are expelled from the beams. In Figures 8.5a and 8.5b,  $v_y$ - $v_z$  phase plots are shown for both single and dual thruster operation respectively. The single thruster is the lower thruster, and the velocity distribution is symmetric as would be expected. With dual thruster operation, there is a noticeable asymmetry. Firstly, the thermal region in the center is elongated in the  $v_z$  axis direction. Secondly, the side regions along the  $v_z$  axis are more populated.

The physical reason for the directional backflow is the potential structure within the beam that leads to trapping of the thermal propellant CEX ions. CEX ions from both beams that are transported into the potential well between the two beams, are forced to leave where the potential hill falls down, and that is in the direction perpendicular to the axis joining the thruster centers. Figure 8.6 shows cuts of the potential in the  $y$ - $z$  plane four cm downstream of the thruster exits along both the  $y$  and  $z$  axes that demonstrates that the potential structure is basically a saddle point. Since the thrusters are aligned along the  $y$  axis, there is a potential well between the two beams which traps CEX ions. Along the  $z$  axis there is only a potential hill. That is why in this direction, more CEX ions leave leading to the directional component of the backflow.

### 8.2.2 Effect on Grid Impingement Current

In addition to CEX ions being expelled along the  $z$ -axis, a number of the CEX ions are attracted back towards the spacecraft, and actually increase the grid impingement current. For a single thruster operation, the grid impingement current was  $6 \times 10^{-5}$  A. When the second thruster was turned on, the grid impingement current increased to  $8 \times 10^{-5}$  A. Figure 8.7 shows a vector plot in the  $x$ - $y$  plane ( $z=0$ ) of the propellant CEX ion current density, and the increased flow to the spacecraft from the region between the two beams where CEX ions are trapped is apparent.

### 8.2.3 NPE Sputtered Grid Material Backflow

Lastly, the backflow structure of sputtered grid material was examined with dual thruster operation. Figure 8.8 shows a  $v_y$ - $v_z$  phase plot of the sputtered molybdenum ions. It is interesting to note that the elongation of the particle population along the  $v_z$  axis is no

longer present. Since the molybdenum ions are of much higher energy compared to the xenon ions, they are not as affected by the potential well between the beam. In fact, looking at the potential structure in Figure 8.6, one sees that the net potential drop along the z axis is greater than along the y axis. Therefore, the velocity along that direction is higher for the molybdenum ions.

Lastly, it is interesting to look at the ratio of the molybdenum to xenon ion current density. In Figure 8.9, this ratio is shown along an arc in the y-z plane two cm upstream of the thruster exits from  $-90^\circ$  (-y axis) to  $+90^\circ$  (+y axis). This ratio is on the order of  $10^{-5}$  at  $0^\circ$  where the xenon is the largest, and molybdenum is the smallest, to over  $10^{-4}$  at  $\pm 90^\circ$  where the opposite is true. These results indicate that minimum molybdenum deposition will take place along the axis where maximum propellant CEX ion backflow is expected.

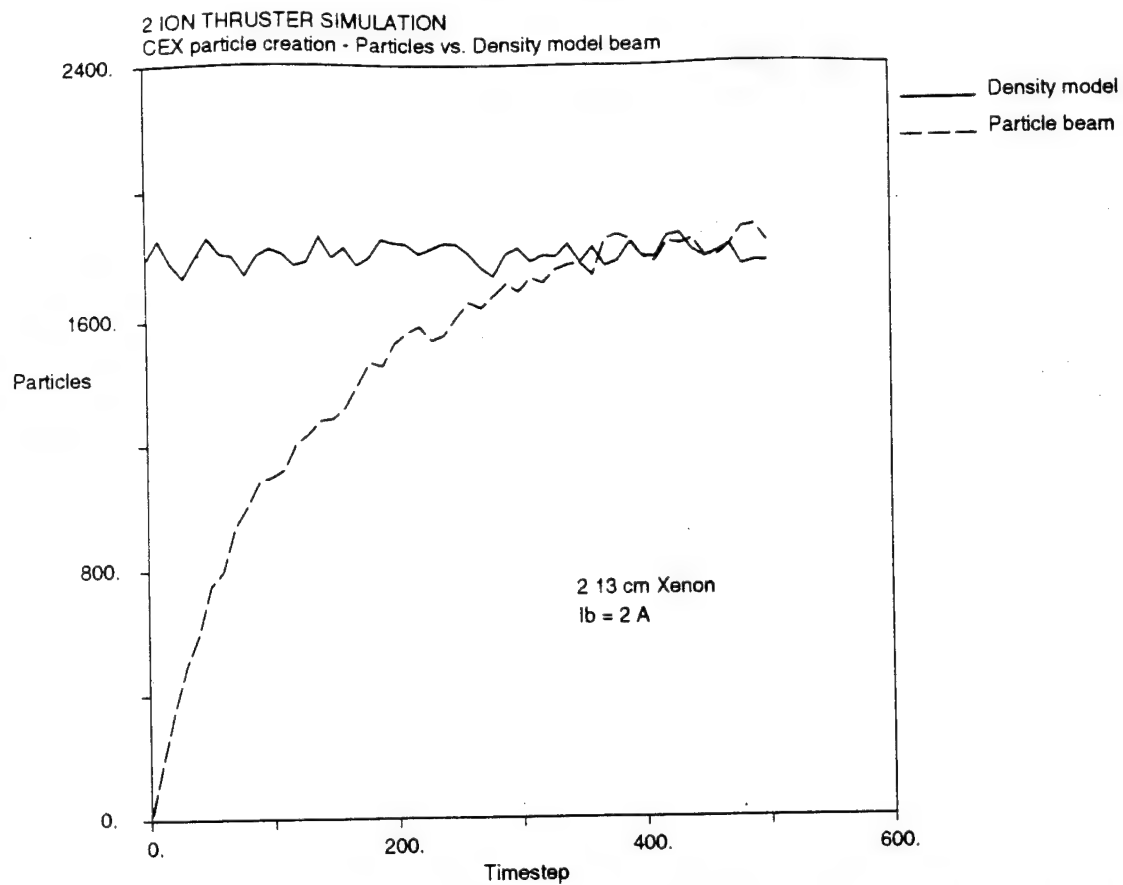


Figure 8.1 Comparison of propellant CEX ion production rates between beam ion model and beam ion particle injection

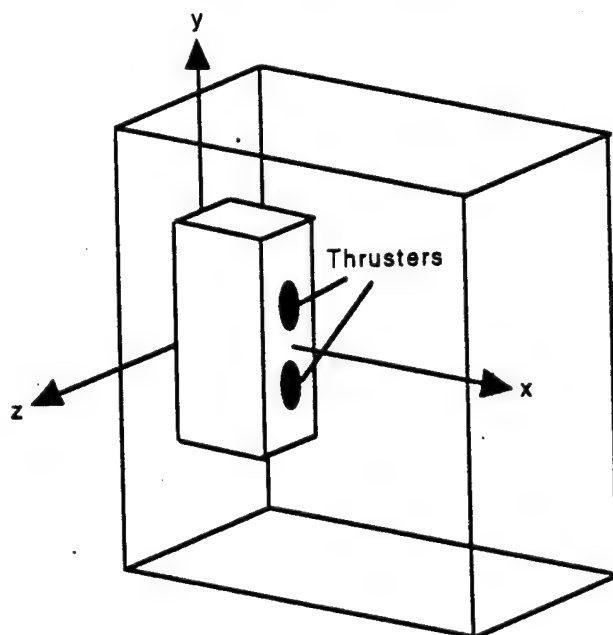


Figure 8.2 Three-dimensional domain geometry with dual thrusters

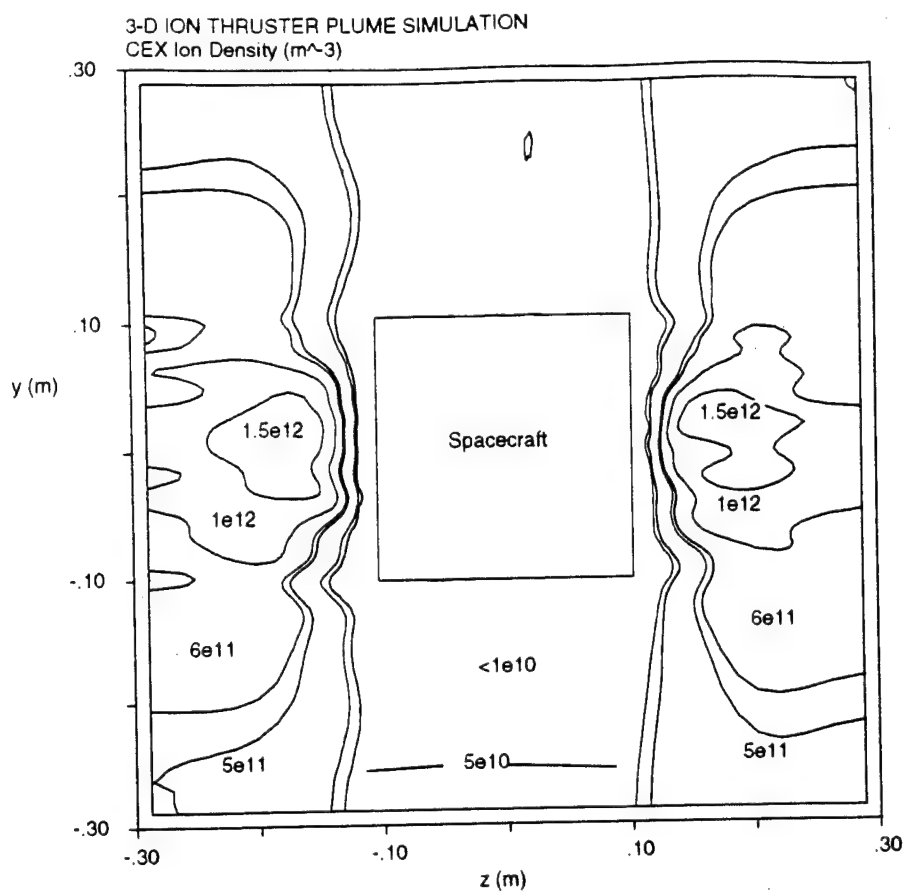


Figure 8.3 CEX ion density in  $y$ - $z$  plane 2 cm upstream of thruster exit

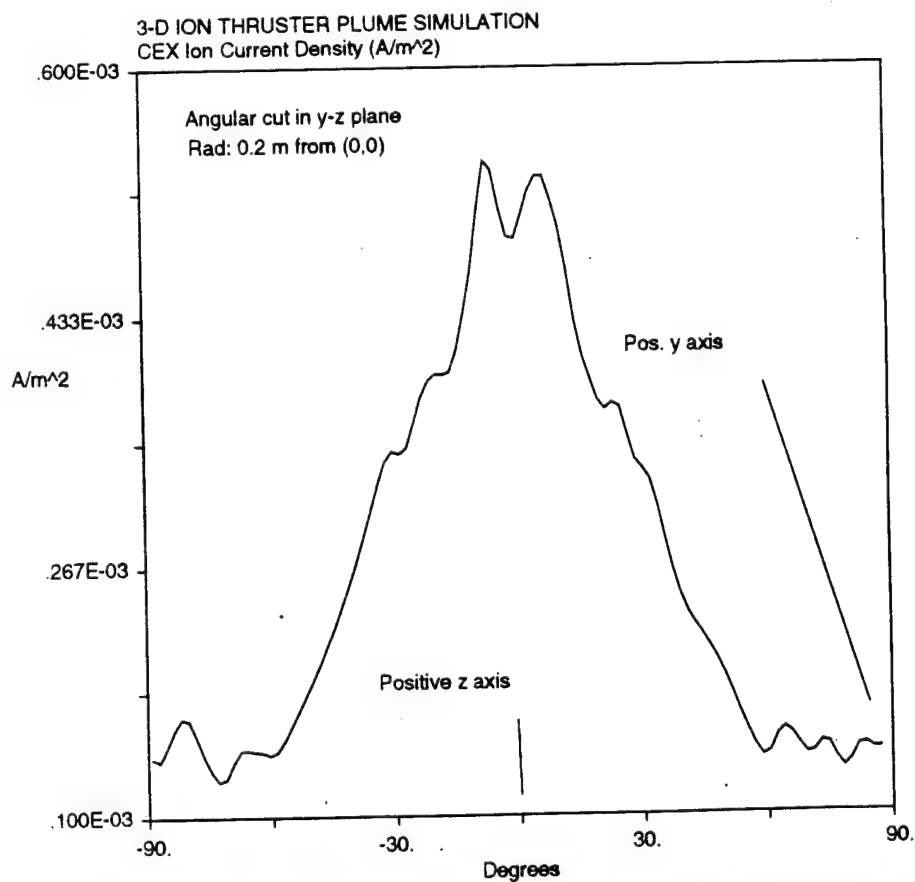


Figure 8.4 CEX ion current density along arc 0.2 m from spacecraft center in  $y$ - $z$  plane (2 cm upstream) from  $-y$  to  $+y$  axis

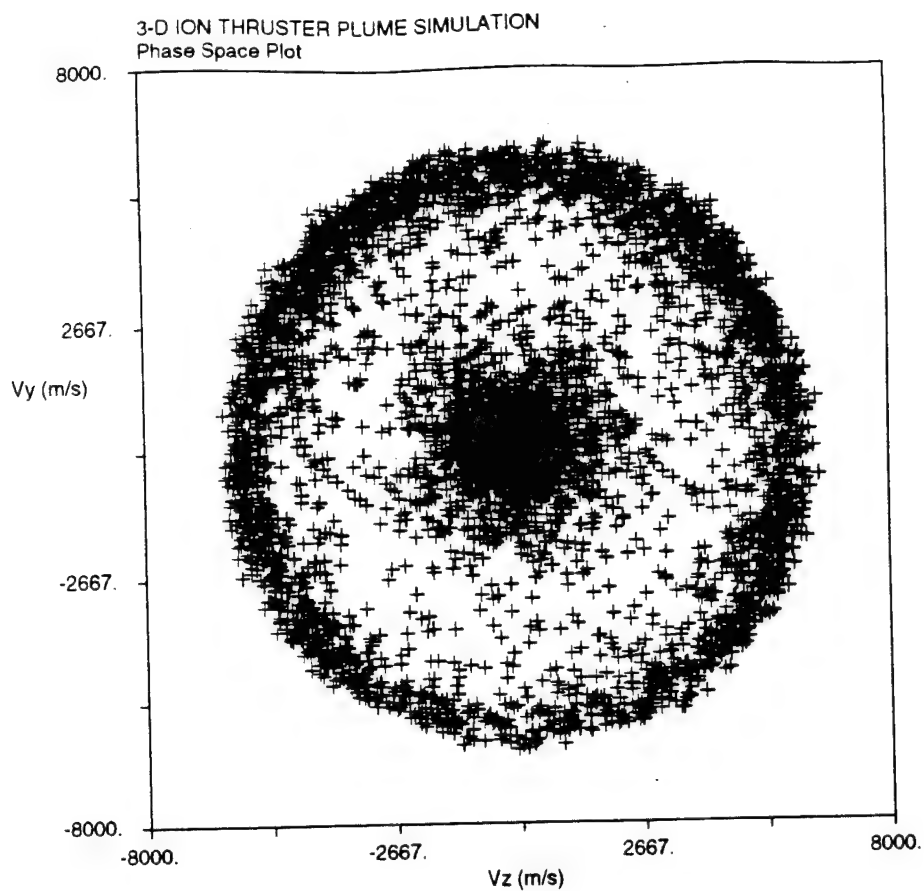


Figure 8.5a Phase plot ( $v_y$ - $v_z$ ) of Xe CEX ions for single thruster

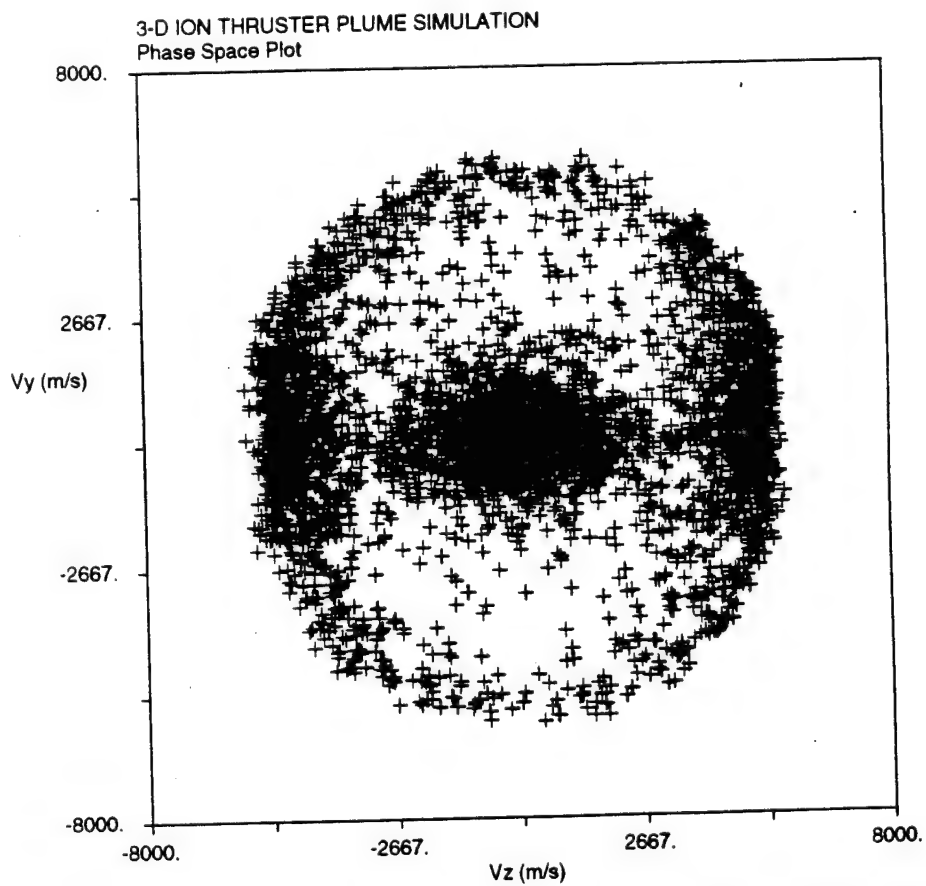


Figure 8.5b Phase plot ( $v_y$ - $v_z$ ) of Xe CEX ions for dual thrusters

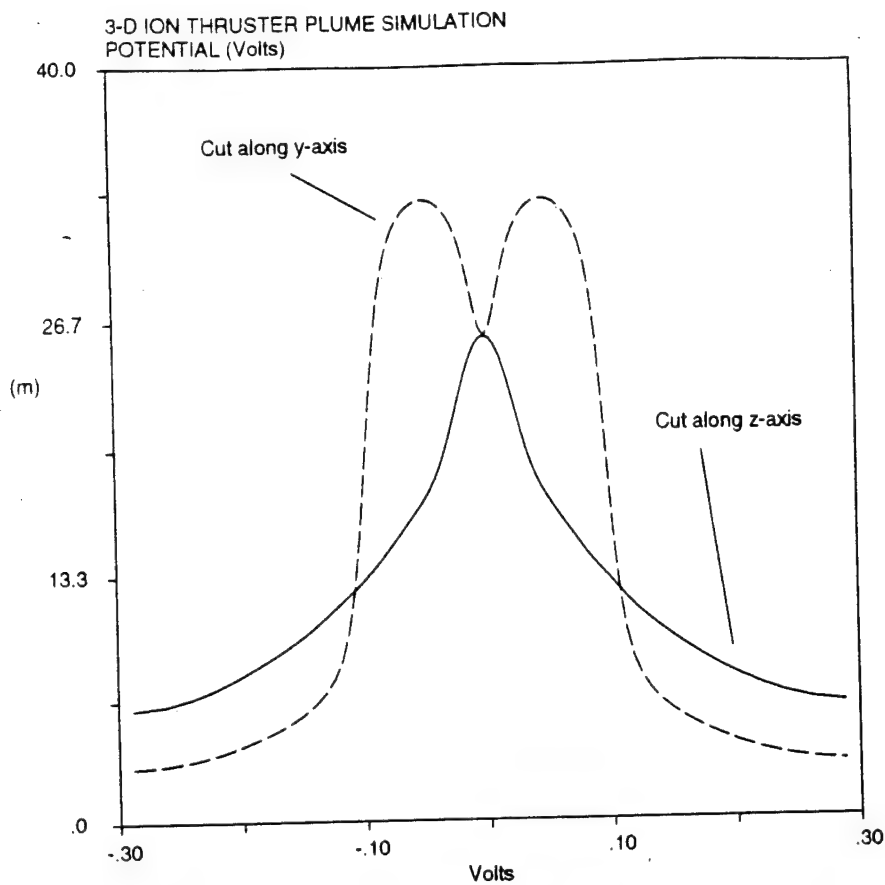


Figure 8.6 Potential cuts through beam 4 cm down stream along y and z axes

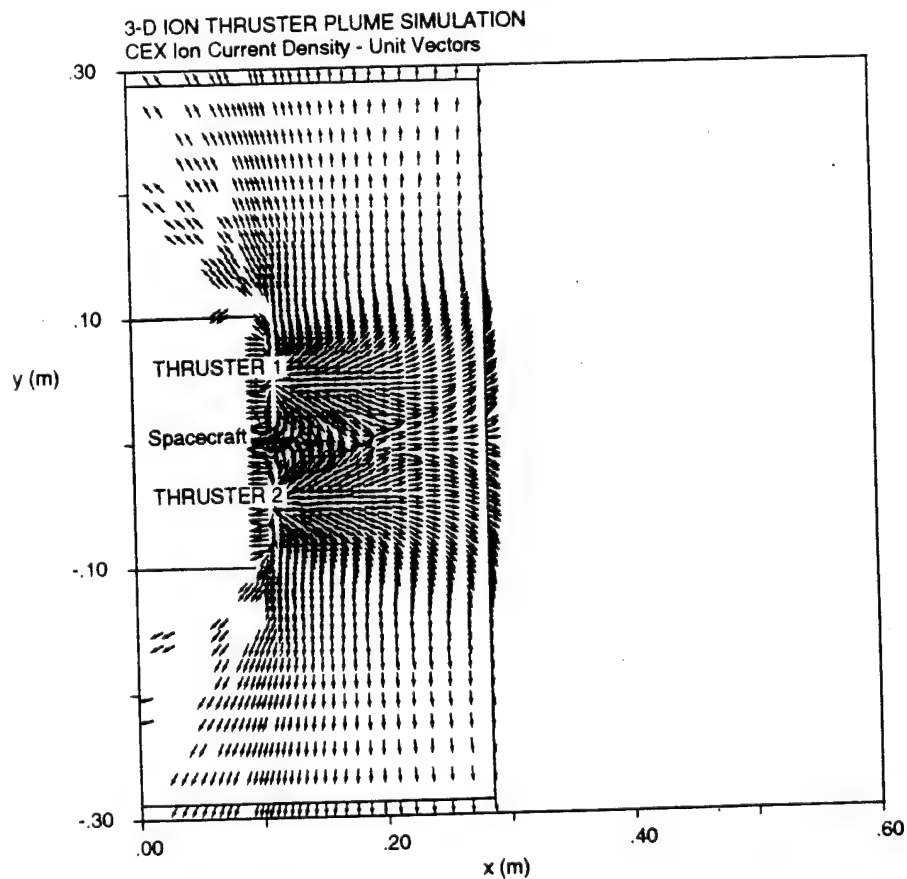


Figure 8.7 Propellant CEX ion current density vector plot in x-y plane ( $z=0$ )

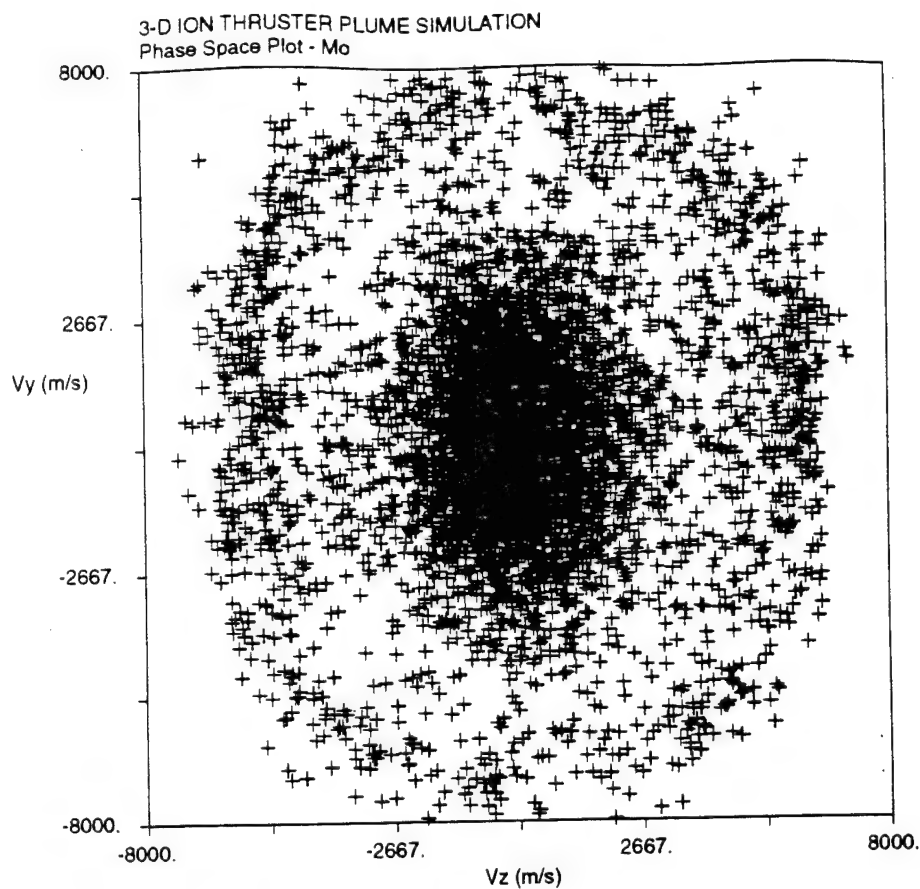


Figure 8.8 Phase plot ( $v_y$ - $v_z$ ) of Mo CEX ions (dual thrusters)

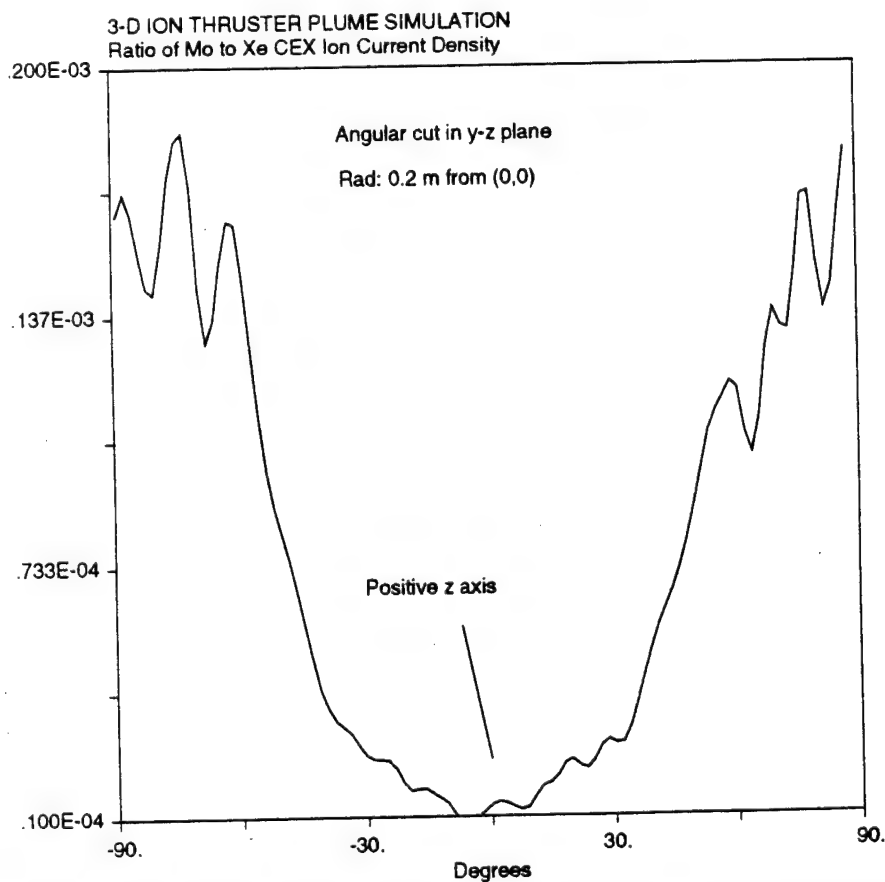


Figure 8.9 Ratio of Mo to Xe current density along arc 0.2 from spacecraft center in y-z plane (2 cm upstream) from -y to +y axis

# Chapter 9

## Conclusions

### 9.1 Review of Results

We have developed a physical and numerical model of the backflow contamination of an ion thruster plume. Detailed models for all the thruster effluents and plume components were developed and integrated into a comprehensive numerical model for axisymmetric geometry. In addition, a fully three dimensional model was also implemented on massively parallel computers - the first such model for ion thruster plumes. Physical aspects of the plume backflow were elucidated, comparisons with data were made, and predictions of backflow for the current NASA 30 cm xenon ion thruster were computed. This is the first comprehensive study of an ion thruster plume that accurately includes the dominant physical processes involved. Moreover, the model is of great usefulness to spacecraft designers since no other predictive capability for ion thruster plume contamination exists. We review the contributions and findings of this thesis below with respect to the physics, numerical aspects, and applications issues.

#### 9.1.1 Contributions to Ion Thruster Plume Backflow Modelling

A general physical model of the effluents of an ion thruster was developed. The specific components included were the beam ions, neutral propellant, thermal propellant ions created predominantly from charge-exchange (CEX) collisions, sputtered grid material, and neutralizing electrons. The overall framework of the model is sufficiently flexible so that each of the specific components can be changed for a particular ion thruster. For instance, a radial parabolic profile beam ion model compared well with measurements from modern thrusters. However, an examination of older thrusters showed that a radial



Gaussian profile provided a better fit. A simple point source model used for the neutral propellant effusing from the thruster compared well with a detailed numerical model. Collisional processes were examined within the plume. In addition to CEX collisions that had been previously identified as the mechanism for thermal ion production, electron impact ionization was assessed. Ionization becomes important for xenon at electron temperatures of 5 eV and above. However, most current thrusters operate at the 1-2 eV level, and hence ionization is subdominant to CEX collisions for xenon. On the other hand, previous generations of ion thrusters used mercury as a propellant, for which ionization rates become higher than CEX collision rates around 4 eV. Recombination of ions of both propellants and electrons is orders of magnitude less than ion creation rates within the plume. A model of the sputtered grid material was developed based on experimentally measured grid mass loss data. It was shown that for the typical grid material, molybdenum, ionization is an important mechanism for creating charged grid metal ions. A fluid model of the neutralizing electrons was derived taking into account the momentum and energy equations. A scaling of the dominant terms in the momentum equation showed that the electric fields are balanced by the pressure gradients. Hence, a generalized Boltzmann relationship for the electrons with a slowly varying spatial temperature distribution was derived. A similar scaling of the electron energy equation showed that conduction is the dominant mechanism, compared to convection, ohmic heating, and electron-ion collisional transfer, since the thermal velocity of the electrons is much greater than drift velocities. Far-field temperature models for the boundary conditions on the electron temperature were developed. Both electron-ion and electron-neutral collisions were included in calculations of the electron thermal conductivity.

All these elements were incorporated into a numerical simulation model that was used to study the plume backflow. The plasma particle-in-cell (PIC) method was employed that rigorously treats a plasma based on first principles, and computes self-consistent electric fields taking into account charged spacecraft surfaces. The main focus was on the creation and transport of the CEX propellant ions, and charged grid material. Volumetric production rates were used for both the propellant and sputtered grid ions. The underlying physics of the CEX ion backflow was identified in the simulations. CEX ions created within the beam are accelerated radially outwards by the strong radial electric fields at the beam edge. An examination of phase space plots showed the existence of two populations of ions: thermal ions within the beam, and energetic ions that were accelerated out of the beam and into the backflow regions.

Comparisons between simulation results and experimental data were made, and reasonably good agreement was found in general. The CEX ion density distributions were

compared for two different ground tests, and better agreement was found with the test that was conducted in a larger test chamber. Overall, computational results of CEX ion density and experimental values do not deviate more than by a factor of two. Comparisons of potential distributions in the plume are more difficult and it is thought this is due to the presence of test facility walls. The model developed in this thesis is for space based thruster operation, and can not take into account the complex processes in ground tests due to chamber walls. However, experimental values of the electron temperature of the CEX plasma agree with the model. The flow angle of the CEX ions expanding from the beam was compared with experiment, and excellent agreement was found. In addition, the influence of tank background pressure in ground tests was investigated by comparing results with and without the background pressure. For example, backflowing CEX ion current densities were 20% less when a background pressure of  $5 \times 10^{-6}$  Torr was removed. The accelerator grid impingement current that causes grid erosion, the main life-limiting mechanism in ion thruster operation, was computed and compared to experimental and numerical studies. Calculations of the impingement current for ground operation agree within a factor of five with ground experimental data. Comparisons with another numerical model created specifically for computing impingement currents, agree within 6% for space based operation. Even though the details of the grid apertures are not modelled, nor was the model intended to focus on the impingement current, the model gives reasonable results since the CEX ions created directly downstream of the thruster are responsible for the bulk of the accel grid current. In addition, it was found that the neutrals from the neutralizer appear to play an important role in determining the impingement current.

An isothermal model of the electrons was considered since the reduced physics decreased the computational time for a solution, thus allowing the model to be used more effectively for parametric studies. Comparisons between the full temperature model and isothermal model show that the backflow CEX ion density and current density in the backflow regions differ by about a factor of two, with the isothermal model giving higher results. The differences between the two models were explained in terms of the effect of the electron temperature on the potential structure in the plume. Thus, the isothermal model gives conservative estimates for backflow contamination. The role of the electron temperature in the plume was studied with the variable temperature model. Simulations with beam electron temperatures of 1 and 5 eV were computed. Little difference in the CEX ion density was found, but significant differences in the ion current density were found since the potential structure in the plume scales with the electron temperature. In addition, the electron temperature strongly influences the dominance of either electron-ion or electron-neutral collisions. At higher temperatures, electron-neutral collisions are

dominant, whereas, electron-ion collisions are dominant at lower temperatures. The differences in collisional behavior have a strong impact on the temperature structure in the plume, since the electron thermal conductivity is a function of the total electron collision frequency.

### 9.1.2 Contributions to Large-Scale Plasma Simulations

In order to investigate geometrical effects on the backflow structure due to the three-dimensional spacecraft, a fully three-dimensional numerical model was developed. Due to the extremely large computational resources required for the large spatial domains involved encompassing a realistic spacecraft, the use of massively parallel computers was necessary and enabling. A PIC algorithm for a message-passing multi-computer environment was developed and implemented on two massively parallel computers that had sufficient memory to handle up to 2 GB memory requirements.

The propellant CEX ion backflow from a Hughes 13 cm xenon ion thruster was computed on a model spacecraft with dimensions similar to the U.S. Air Force ARGOS spacecraft. The computational domain contained over 9.4 million grid points, and the simulation employed 17.5 million particles. This is the first calculation ever conducted of ion thruster plume backflow on such a large scale. In addition, the computational model created can be used as a testbed tool with which many computer science issues such as dynamic load balancing can be explored.

The plume backflow was examined for three-dimensional effects since the spacecraft's geometry could not be captured with an axisymmetric model. Since the spacecraft was a box shape, a "corner-effect" where the CEX plasma flowed over the front face of the spacecraft was identified. This led to an asymmetry in the backflow around the spacecraft, that could produce significant decreases in CEX ion density up to an order of magnitude, particularly close to the thruster exit plane.

The three-dimensional results were compared with the axisymmetric model applied in a plane through the plume. Comparisons of CEX ion densities along radial and angular cuts throughout the backflow region away from the "corner-effect" regions did not show significant differences. It was shown that the axisymmetric model can be used to give a conservative upper bound on the backflow, at least for geometries that are not highly asymmetric, as was the case in this thesis. In addition, the effect of the solar array panel on the spacecraft, which produced a strong asymmetry to the geometry, did not have a major impact due to Debye shielding.

### 9.1.3 Contributions to Ion Thruster Backflow Predictions

The plume backflow model developed in this thesis is a useful tool for spacecraft designers and propulsion system integrators to assess ion thruster backflow. To demonstrate this capability, both the propellant and sputtered grid material backflow was predicted for the NASA 30 cm xenon thruster over the entire range of the operating envelope for space-based operation. Backflow currents from the propellant CEX ions, and surface deposition estimates of sputtered molybdenum were computed as a function of thruster operating conditions. Operating points specified by both JPL and NASA LeRC were used. In addition to using the nominal operating conditions that correspond to a power throttling profile, the backflow for thruster operation at fixed beam current and fixed beam voltage was investigated. Scaling relationships between thruster backflow and thruster operating conditions were studied, and a previously identified scaling relationship was verified. It was shown that the backflow current scaled with the CEX ion production rate which varied with the beam current, propellant utilization efficiency, and beam ion velocity as,

$$\dot{N}_{cex} \sim I_b^2 \left( \frac{1 - \eta_p}{\eta_p} \right) \sigma_{cex}(v_{bi}) = \chi \quad (9.1)$$

In addition, it was shown that the CEX ion density and current density distributions remained constant over the thruster operating envelope; only the magnitude varied according to Eqn. (8.1). From the lowest to the highest power settings (a factor of seven) the backflow current increased by a factor of 5.56. The ratio of the backflow current over a 75 cm high plane 50 cm behind the thruster exit to the beam ion current ranged from  $3.2 \times 10^{-4}$  to  $4.05 \times 10^{-4}$ . In other words, for every 10,000 ions leaving the thruster providing thrust, three to four ions travel in a direction completely opposite to the thrust direction. Based on extrapolated ground measurements of grid sputtering, calculations were made of charged molybdenum deposition rates in the backflow regions. Depending on the electron temperature in the beam, which would influence whether ionization or CEX is the dominant mechanism for creating charged molybdenum, the deposition rates 50 cm behind the thruster exit ranged from  $5 \times 10^{-4}$  monolayers/year for low current, low temperature operating conditions, to 0.1 monolayers/year for high beam current, high temperature operating conditions. Molybdenum deposition is not as high as previous estimates showed, which were based on models that assumed that the molybdenum density structure followed the propellant CEX ion density. In our simulations, molybdenum ions were less likely than xenon CEX ions to be influenced by the potentials in the backflow

region due to their higher energies.

Specific spacecraft design issues were also addressed. The effect of spacecraft size on the backflow structure was looked at in axisymmetric geometry. In addition, the effect of thruster operation on spacecraft floating potential was examined. The principle of the CEX plasma cloud acting as a plasma "bridge" with the ambient plasma environment was demonstrated, and it was shown that large negative spacecraft potentials encountered in geostationary orbits can be alleviated. Lastly, the use of a plume shield to mitigate backflowing plume contamination was studied. A shield at a constant voltage was shown to be very effective in eliminating any contamination in the region directly behind its location. Currently, no other ion thruster plume model exists that is capable of addressing the large scope of issues that were investigated in this thesis, and thus this work is a significant advancement in this field.

## **9.2 Recommendations for Ion Thruster/Spacecraft Operation**

As a result of the studies of plume contamination presented in this thesis and the identification of physical trends, a number of suggestions can be made for thruster operation and spacecraft integration that will reduce any harmful effects of ion thruster plume contamination. Among some of the recommendations are the following:

- The ion thruster should be operated with as high a propellant utilization efficiency as possible to reduce the amount of neutrals that will be able to create the thermal CEX ions. However, there is a power cost associated with higher discharge chamber performance that must be weighed in.
- The thruster should be operated in such a manner that the electron temperature in the beam be as low as possible. Since the electron temperature is directly related to the beam potential drop, lower temperatures will mean lower energy backstreaming ions.
- To reduce erosion of the thruster grids, the sputter yield, which is a function of the energy of the impinging ions, can be decreased by not biasing the accel grid too negative or using a third decel grid. There will still be a minimum bias necessary, however, to prevent electron back-streaming. In addition, current research on sputter-resistant grids is promising and offers the possibility of drastically reducing this contamination risk.

- Grid metal deposition is not as high as previously thought. However, to protect sensitive spacecraft surfaces, a plume shield should be used, although there is mass penalty involved.

### 9.3 Recommendations for Future Research

In spite of the advances made in this work, there remain a host of other issues to be addressed. In addition, there are many improvements to the numerics and physics that can be made to the current model, as well as future directions of research. Recommended improvements on the numerics of the model include:

- *Speed up electron temperature solution.* A large fraction of time is spent solving for the electron temperature. More advanced direct solvers can be attempted.
- *More efficient computational grid structure.* The current grid is inefficient in terms of highly skewed grid cells in regions where high resolution is not necessary. An adaptive grid, or a multiblock approach (even with a Cartesian grid) would be useful. More importantly, the ability to model completely arbitrary spacecraft surfaces with unstructured grids will be very useful, as well as having the ability to model thrusters that are placed at angles to spacecraft surfaces. In addition, these gridding techniques will allow assessment of plume shields that are conical in shape instead of flat surfaces.
- *Speed up the three-dimensional parallel model.* Substantial improvements can be made by implementing dynamic load balancing based on the diffusion of work among processors.

In terms of the physics of the model, there are a number of issues that need to be further explored:

- *Improve the electron fluid model and model the neutralizer.* A full fluid model of the electrons that includes the solution of the continuity, momentum, and energy equations should be included to give a clearer picture of the electrons. The geomagnetic field must be included and its influence on the electrons fully explored. The electron drift velocity, including  $\mathbf{E} \times \mathbf{B}$  drifts in the CEX plasma cloud on larger length scales, must be investigated. However, these are fully three-dimensional effects with an arbitrary magnetic field. The physics perhaps can be studied initially in a simple two-dimensional Cartesian system in a plane perpendicular to the



geomagnetic field. The electron temperature model can be improved by addressing the question of what determines the electron temperature at the thruster exit, and by including variable temperature for the ions and ionization. Ionization of the neutrals would also have to be included for ion production. This will be important only for cases where the electron temperature in the beam is high.

It should be mentioned that with a full fluid model that determines the electron density, Poisson's equation for the potential becomes linear. A full fluid approach was attempted during the course of work in this thesis, but was fraught with numerical difficulties due to instabilities in the Poisson equation created by noise from the solution of the electron continuity equation. In addition, attention must be given to the issue of the timestep of the electron fluid solution. The solution of the electron fluid equations is constrained by a CFL condition. If the same grid is used as for the PIC ions, the grid cell size is on the order of the Debye length, and with the electron velocity a fraction of the thermal velocity, the timestep becomes a fraction of the electron plasma frequency which can be quite restrictive for ion timescale behavior. A full fluid model of the electrons would be a step forward towards including a model of the neutralizer - a future direction of research.

- *Role of plasma turbulence on transport.* Instabilities and turbulence must be examined in the plume to develop transport coefficients such as the thermal conductivity, and electrical conductivity for a fully fluid model. Only classical collisions were used in this thesis. Investigations in this area may necessitate the need of studying the electrons with a fully kinetic model.
- *Better model of spacecraft floating potential.* Ambient environment parameters such as the electron temperature should be more closely examined, as well as global current closure. The issue of the balance of the ion beam and neutralizer emission currents and the impact on spacecraft potential and the neutralizer coupling voltage must be investigated.
- *Better ground testing modelling capability.* To model the results of ground tests, efforts should be aimed at understanding in detail the interactions and effects of the ground testing chambers. Models on massively parallel computers can be used to model the entire test chamber.
- *Study multiple thruster arrays.* Most thruster configurations on spacecraft involve multiple thrusters. The approach taken in this thesis is not suitable for modelling the

complex interactions that will occur at the boundaries of two ion thruster beams. A fully particle treatment of the beam ions will most likely be necessary. The backflow contamination structure from multiple thrusters must be examined for nonlinear effects.

Future research efforts can also be broadened to include the following issues:

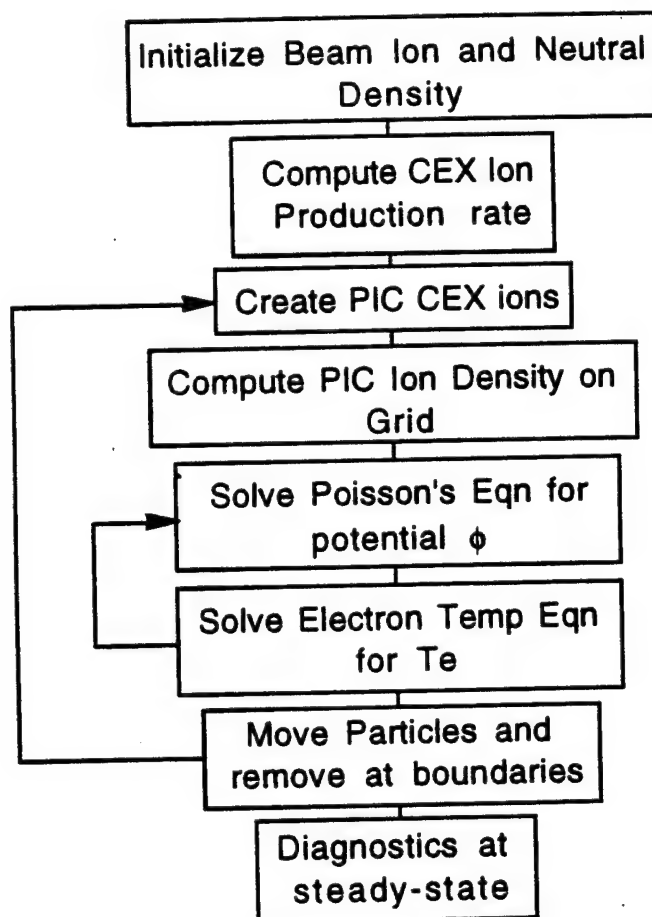
- *Plume contamination from SPT thrusters.* Many of the same processes in ion thruster plumes are present in SPT thrusters as well. However, the level of collisionality is higher. In addition, the modelling challenges are greater since a large amount of CEX ion production occurs within the thruster itself, and hence a model of the thruster must be included for a rigorous analysis.
- *Examine surface contamination effects.* As was mentioned in Chapter 1, the last phase of contamination assessment is to investigate the effects of the plume deposits. Surface property modifications due to thin film deposition by the sputtered molybdenum needs to be thoroughly studied.
- *Examine systems issues associated with nuclear electric propulsion.* If future EP thrusters will be powered by nuclear reactors, the presence of the reactor and its effluents such as ionizing radiation must be examined and quantified for a complete EP system contamination analysis.

Above all, what is most important is a modern experimental effort to characterize ion thruster plume backflow. Most of the data available today was taken during a major effort during the 1970's and 80's. However, all this data was for mercury. What is needed is a similar effort for xenon with modern diagnostic techniques to provide a complete database of the plume densities, current densities, electron temperatures, and potentials in the backflow regions that can be used to validate plume contamination models. These models will enable spacecraft designers and integrators to more confidently assess, and control if necessary, EP thruster contamination and will thus help EP emerge as a commonly accepted form of spacecraft propulsion.



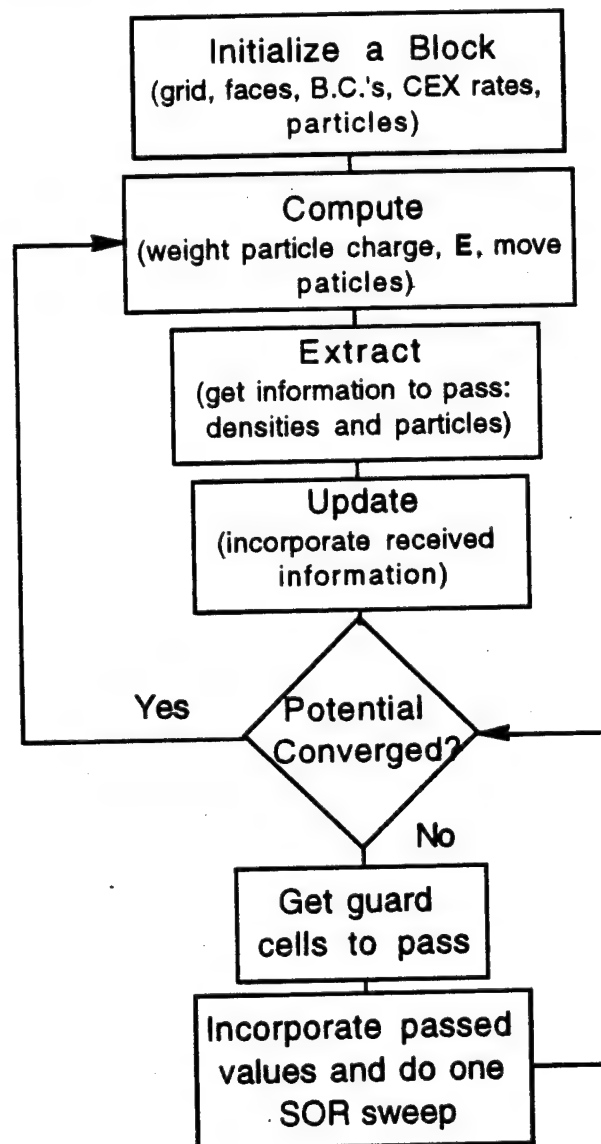
## Appendix A - Serial Computer Model Flowchart

This is a flowchart of the serial plume model.



## Appendix B - Parallel Computer Model Flowchart

This is a flowchart of the parallel plume model.



## Bibliography

- [1] Absalamov, S.K., Andreev, V.B., Colbert, T., Day, M., Egorov, V.V., Gnizdor, R.U., Kaufman, H., Kim, V., Korakin, A.I., Kozubsky, K.N., Kudravzev, S.S., Lebedev, U.V., Popov, G.A., and Zhurin, V.V., "Measurement of Plasma Parameters in the Stationary Plasma Thruster (SPT-100) Plumes and its Effect on Spacecraft Components", AIAA Paper 92-3156, 1992.
- [2] Agrawal, B.N., *Design of Geosynchronous Spacecraft*, Prentice-Hall, NJ, 1986.
- [3] Albini, F.A., "Approximate Computation of Underexpanded Jet Structure", *AIAA J.*, Vol. 3, No. 8, Aug. 1965, pp. 1535-1537.
- [4] Anderson, D.A., Tannehill, J.C., and Pletcher, R.H., *Computational Fluid Mechanics and Heat Transfer*, Hemisphere Publishing Corporation, NY, 1984.
- [5] Auweter-Kurtz, M., Glocker, B., Kurtz, H.L., Loesener, O., Schrade, H.O., Tubanos, N., Wegmann, T., Willer, D., and Polk, J.E., Cathode Phenomena in Plasma Thrusters, AIAA Paper 90-2662, 1990.
- [6] Banks, P., "Collision Frequencies and Energy Transfer - Electrons", *Planet. Space Sci.*, Vol. 14, pp. 1085-1103, 1966.
- [7] Banks, P., "Collision Frequencies and Energy Transfer - Ions", *Planet. Space Sci.*, Vol. 14, pp. 1105-1122, 1966.
- [8] Baum, H., "The interaction of a transient exhaust plume with a rarefied atmosphere", *J. Fluid Mech.*, Vol. 58, Part 4, 1973, pp. 795-815.
- [9] Beattie, J.R. and Matossian, J.N., "High Power Ion Thruster Technology", NASA Report CR 187161, 1992.
- [10] Bettinger, R.T. and Chen, A.A., "An End-Effect Associated with Cylindrical Langmuir Probes Moving at Satellite Velocities", *J. Geophys. Res.*, Vol. 73, No. 7, 1968, pp. 2513-2528.
- [11] Bird, G.A., *Molecular Gas Dynamics*, Clarendon Press, Oxford, 1976.
- [12] Birdsall, C.K. and Langdon, A.B., *Plasma Physics via Computer Simulation*, Adam Hilger, Bristol, 1991.

- [13] Bishaev, A.M., Kalashnikov, V.K., and Kim, V., "Numerical Modelling of Rarefied Plasma Plume Entering Neutral Environment Gas", IEPC Paper 93-137, 1993.
- [14] Bogorad, A., Lichtin, D.A., Bowman, C., Armenti, J., Pencil, E., and Sarmiento, C., "The Effects of 1kW Class Arcjet Thruster Plumes on Spacecraft Charging and Spacecraft Thermal Control Materials", *IEEE Trans. on Nuclear Sci.*, Vol. 39, No. 6, Dec. 1992, pp. 1783-1789.
- [15] Book, D.L., *NRL Plasma Formulary*, Naval Research Laboratory Publication 0084-4040, Washington, D.C., 1987.
- [16] Borisov, B.S., Garkusha, V.I., Kozyrev, N.V., Korsun, A.G., Sokolov, L.Yu., and Strashinsky, V.A., "The Influence of Electric Thruster Plasma Plume on Downlink Communication in Space Experiments", AIAA Paper 91-2349, 1991.
- [17] Boyd, I.D. and Stark, J.P.W., "Modelling of Small Hydrazine Thruster Plumes Using Discrete Particle and Continuum Methods", AIAA Paper 88-2631, 1988.
- [18] Boyd, I.D., Cappelli, M.A., and Beattie, D.R., "Monte Carlo and Experimental Studies of Nozzle Flow in a Low-Power Hydrogen Arcjet", AIAA Paper 93-2529, 1993.
- [19] Boynton, F.P., "Highly Underexpanded Jet Structure: Exact and Approximate Calculations", *AIAA J.*, Vol. 5, No. 9, Sept. 1967, pp. 1703-1704.
- [20] Brewer, G.R., *Ion Propulsion: Technology and Applications*, Gordon and Breach Science Publishers, NY, 1970.
- [21] Brophy, J., "Ion Thruster Performance Model", NASA CR-174810, December 1984.
- [22] Brophy, J.R., Polk, J.E., and Pless, L.C., "Test-to-Failure of a Two Grid 30 cm-dia. Ion Accelerator System", IEPC Paper 93-172, 1993.
- [23] Brophy, J., Personal Communication, 1994.
- [24] Brukhty, V.I. and Kirdyashev, K.P., "The Effect of Alkali Metal Electric Rocket Engines on Spacecraft", IEPC Paper 93-149, 1993.
- [25] Byers, D.C., "Electron Bombardment Thruster Field and Particle Interfaces", *J. Spacecraft*, Vol. 16, No. 5, Sept.-Oct. 1979, pp. 289-301.
- [26] Carney, L.M., "Evaluation of the Communications Impact of a Low Power Arcjet Thruster", AIAA Paper 88-3105, 1988.
- [27] Carruth, M.R. and Brady, M.E., "Measurement of the Charge-Exchange Plasma Flow from an Ion Thruster", *J. Spacecraft*, Vol. 18, No. 5, Sept.-Oct. 1981, pp. 457-461.
- [28] Carruth, M.R., Ed., "Experimental and Analytical Evaluation of Ion Thruster /Spacecraft Interactions", JPL Publication 80-92, 1981.
- [29] Carruth, M.R., "A Review of Studies on Ion Thruster Beam and Charge-Exchange Plasmas", AIAA Paper 82-1944, 1982.

- [30] Carruth, M.R., Gabriel, S.B., and Kitamura, S., "Ion Thruster Charge-Exchange Plasma Flow", AIAA Paper 82-0403, 1982.
- [31] Carruth, M.R., Personal Communication, 1994.
- [32] Chakarov, I.R., Cherepin, V.T., Karpuzov, D.S., Kosyachkov, A.A., and Vichev, R.G., "Angle and Energy Distributions of Sputtered Particles from Molybdenum (110) Surfaces", *Nuclear Instruments and Methods in Physics Research*, Vol. B39, 1989, pp. 81-85.
- [33] Chandy, K.M. and Taylor, S., *An Introduction to Parallel Programming*, Jones and Bartlett, Boston, 1992.
- [34] Chang, R., *Chemistry*, Random House, NY, 1988.
- [35] Crofton, M.W., "Spectral Irradiance of the 1kW Arcjet Thruster from 80 to 500 nm", AIAA Paper 92-3237, 1992.
- [36] Cruciani, G. and Deininger, W.D., "A 300-Hour Endurance Test of an Arcjet Thruster at 1kW", AIAA Paper 93-1900, 1993.
- [37] Cuffel, R.F., "Mathematical Model of the Current Density for the 30-cm Engineering Model Thruster", AIAA Paper 75-431, 1975.
- [38] Deininger, W.D., "Electric Propulsion Produced Environments and Possible Interactions with the SP-100 Power System", AIAA Paper 85-2046, 1985.
- [39] Dettleff, G., "Plume Flow and Plume Impingement in Space Technology", *Prog. Aerospace Sci.*, Vol. 28, 1991, pp. 1-71.
- [40] Ducati, A.C, et al, "Experimental Results in High Specific Impulse Thermoionic Acceleration", *AIAA J.*, Vol. 2, No. 8, Aug. 1964, p. 1452.
- [41] Elgin, J.B., Cooke, D.C., Tautz, M.F., and Murad, E., "Modeling of Atmospherically Induced Gas Phase Optical Contamination for Orbiting Spacecraft", *J. Geophys. Res.*, Vol. 95, No. A8, Aug. 1, 1990, pp. 12197-12208.
- [42] Fearn, D.G., "Ion Thruster Lifetime Limitations Imposed by Sputtering Processes", IEPC Paper 93-177, 1993.
- [43] Fearn, D.G., Martin, A.R., and Smith, P., "Ion Propulsion Development in the UK", AIAA Paper 93-2603, 1993.
- [44] Fox, G., Johnson, M., Lyzenga, G., Otto, S., Salmon, J., and Walker, D., *Solving Problems on Concurrent Processors*, Prentice Hall, New Jersey, 1988.
- [45] Gabriel, S.B. and Kaufman, H.R., "A Comparison of Experimental and Computer Model Results on the Charge-Exchange Plasma Flow from a 30 cm Mercury Ion Thruster", AIAA Paper 82-1946, 1982.
- [46] Garner, C.E., Polk, J.E., Goodfellow, K.D., and Brophy, J.R., "Performance Evaluation and Life Testing of the SPT-100", IEPC Paper 93-091, 1993.

- [47] Gatsonis, N.A., *Electrodynamics of the Plasma Environment Induced Around Spacecraft in Low Earth Orbit: Three-Dimensional Theory and Numerical Modeling*, MIT Ph.D. Thesis, 1991.
- [48] Gatsonis, N.A., Mauk, B.H., and Bythrow, P.F., "Modelling Induced Environments and Spacecraft Interactions for the Nuclear Electric Propulsion Space Test Program (NEPSTP)", AIAA Paper 93-2533, 1993.
- [49] Giannini, G.M., "The Plasma Jet and Its Application", *Office Sci. Res. Tech. Note* 57-520, 1957.
- [50] Grier, N.T., "Back Flow from Jet Plumes into Vacuum", NASA TN D-4978, Jan. 1969.
- [51] Hall, D.F. and Kelley, L.R., "Experimental Techniques to Determine Electrostatic Rocket Exhaust Effects on Spacecraft Surfaces", AIAA Paper 70-1144, 1970.
- [52] Hall, D.F., Newnam, B.E., and Womack, J.R., "Electrostatic Rocket Exhaust Effects on Solar-Electric Spacecraft Subsystems", *J. Spacecraft*, Vol. 7, No. 3, March 1970, pp. 305-312.
- [53] Hall, D.F. and Green, H.E., "Erosive and Chemical Effects of Energetic Mercury Ions Bombarding Spacecraft Surface Material", AIAA Paper 72-446, 1972.
- [54] Hamel, B.B. and Willis, D.R., "Kinetic Theory of Source Flow Expansion with Application to the Free Jet", *Phys. Fluids*, Vol. 9, No. 5, May 1966, pp. 829-841.
- [55] Hayakawa, Y., Miyazaki, K., and Kitamura, S., "Ion Beam Characteristics of a 14 cm Xenon Ion Thruster", AIAA Paper 94-2852, 1994.
- [56] Hester, S.D. and Sonin, A.A., "Ion Temperature Sensitive End-Effect in Cylindrical Langmuir Probe Response at Ionospheric Satellite Conditions", *Phys. Fluids*, Vol. 13, No. 5, 1970, pp. 1265-1274.
- [57] Hill, J.A., and Draper, J.S., "Analytical Approximation for the Flow from a Nozzle into a Vacuum", *J. Spacecraft*, Vol. 3, No. 10, October 1966, pp. 1552-1554.
- [58] Hockney, R.W. and Eastwood, J.W., *Computer Simulation using Particles*, Adam Hilger, Bristol, 1988.
- [59] Hoffman, R.J., Webber, W.T., Oeding, R.G., and Nunn, J.R., "An Analytical Model for the Prediction of Liquid Rocket Plume Contamination Effects on Sensitive Surfaces", AIAA Paper 72-1172, 1972.
- [60] Hruby, V., Martinez-Sanchez, M., Bates, S., and Lorents, D., "A High Thrust Density C60 Cluster Ion Thruster", AIAA Paper 94-2466, 1994.
- [61] Jahn, R.G., *Physics of Electric Propulsion*, McGraw-Hill, NY, 1968.
- [62] Jenkins, R., Ciucci, A., and Cochran, J., "A Simplified Model for Calculation of Backflow Contamination from Rocket Exhausts in Vacuum", AIAA Paper 90-1846, 1990.

- [62] Jones, S.G., Staskus, J.V., and Byers, D.G., "Preliminary Results of SERT II Spacecraft Potential Measurements using Hot Wire Emissive Probes", AIAA Paper 70-1127, 1970.
- [63] Jursa, A.S., Ed., *Handbook of Geophysics and the Space Environment*, Air Force Geophysics Laboratory, 1985.
- [64] Katz, I., Parks, D.E., Mandell, M.J., Harvey, J.M., and Wang, S.S., "NASCAP, a Three-Dimensional Charging Analyzer Program for Complex Spacecraft", *IEEE Trans. on Nuclear Science*, Vol. 6, Dec. 1977, pp. 2276-2280.
- [65] Katz, I., Parks, D.E., Mandell, M.J., and Schnuelle, G.W., "Parasitic Current Losses Due to Solar Electric Propulsion Generated Plasmas", AIAA Paper 81-0740, 1981.
- [66] Katz, I., Lilley, J.R. Jr., Jongeward, G.A., Mandell, M.J., and Luu, T.T., "Polar Code Validation", Air Force Geophysics Laboratory Report GL-TR-89-0276, 1989.
- [67] Kaufman, H.R., "Technology of Electron-Bombardment Ion Thrusters", in *Advances in Electronics and Electron Physics*, Vol. 36, Academic Press, NY, 1974.
- [68] Kaufman, H.R., "Charge-Exchange Plasma Generated by an Ion Thruster", NASA CR-134844, June 1975.
- [69] Kaufman, H.R., "Plasma Physics Analysis of SERT II Operation", NASA CR-159814, January 1980.
- [70] Kaufman, H.R., Personal Communication, 1994.
- [71] Kemp, R.F., Leudke, E.E., Hall, D.F., and Miller, W.D., "Effects of Electrostatic Rocket Material Deposited on Solar Cells", AIAA Paper 72-447, 1972.
- [72] Kerslake, W.R. and Ignaczak, L.R., "Development and Flight History of SERT II Spacecraft", AIAA Paper 92-3516, 1992.
- [73] Komatsu, G.K. and Sellen, J.M., "Beam Efflux Measurements for a 30-cm Mercury Ion Thruster", AIAA Paper 76-1052, 1976.
- [74] Komatsu, G.K., Cole, R.K., Hoffmaster, D.K., Sellen, J.M. Jr., "Charge Exchange Ion Formation and Motion in Mercury Ion Engine Thrust Beams", AIAA Paper 75-428, 1975.
- [75] Lathem, Walter C., "Particle and Field Measurements on Two J-Series 30-cm Thrusters", NASA Technical Memorandum 81741, 1981.
- [76] Leifer, S. and Saunders, W., "Electrostatic Propulsion Using C60 Molecules", IEPC Paper 91-154, 1991.
- [77] Lichtin, D., Personal Communication, 1995.
- [78] Liebeskind, J.G., Hanson, R.K., and Cappelli, M.A., "Plume Characteristics of an Arcjet Thruster", AIAA Paper 93-2530, 1993.

- [79] Macie, T.W. and Whittlesey, A.C., "Electromagnetic Interference Onboard an Electrically Propelled Spacecraft", AIAA Paper 73-1128, 1973.
- [80] Manzella, D.H., "Stationary Plasma Thruster Plume Emissions", IEPC Paper 93-097, 1993.
- [81] Masek, T.D. and Womack, J.R., "Experimental Studies with a Clustered Ion Engine System", AIAA Paper 67-698, 1967.
- [82] Massey, H.S.W. and Burhop, E.H.S., *Electronic and Ionic Impact Phenomena*, Clarendon Press, Oxford, 1952.
- [83] Massey, H.S.W., Burhop, E.H.S., and Gilbody, H.B., *Electronic and Ionic Impact Phenomena*, Vol. III - Slow Collisions and Heavy Particles, Clarendon Press, Oxford, 1971.
- [84] Meadows, G.A. and Free, B.A., "Effect of Decel Electrode on Primary and Charge-Exchange Ion Trajectories", AIAA Paper 75-427, 1975.
- [85] Messerole, J.S. and Hedges, D.E., "Comparison of Erosion Rates of Carbon-Carbon and Molybdenum Ion Optics", IEPC Paper 93-111, 1993.
- [86] Messerole, J.S., "Measurement of Relative Erosion Rates of Carbon-Carbon and Molybdenum Ion Optics", AIAA Paper 94-3119, 1994.
- [87] Mitchner, M. and Kruger, C.H. Jr., *Partially Ionized Gases*, John Wiley and Sons, NY, 1973.
- [88] Monheiser, J.M., "Advanced Electric Propulsion Research - 1990", NASA Report CR-187103, 1991.
- [89] Myers, R.M. and Manzella, D.H., "Stationary Plasma Thruster Plume Characteristics", IEPC Paper 93-096, 1993.
- [90] Nakanishi, S. and Pawlik, E.V., "Experimental Investigation of a 1.5 m Diameter Kaufman Thruster", AIAA Paper 67-725, 1967.
- [91] Noller, H.G., "Approximate Calculation of Expansion of Gas from Nozzles into High Vacuum", *J. of Vacuum Sci. and Tech.*, Vol. 3, No. 4, July/Aug. 1966, pp. 202-207.
- [92] Olsen, R.C., "Operations of the ATS-6 Ion Engine and Plasma Bridge Neutralizer at Geosynchronous Altitude", AIAA Paper 78-663, 1978.
- [93] Oppe, T.C., Joubert, W.D., and Kincaid, D.R., "A Package for Solving Large Sparse Linear Systems by Various Iterative Methods", Center for Numerical Analysis, Univ. of Texas, Austin, 1988.
- [94] Parks, D.E., Mandell, M.J., and Katz, I., "Fluid Model of Neutralized Ion Beams", AIAA Paper 81-0141, 1981.
- [95] Patterson, M., Haag, T., Rawlin, V., and Kussmaul, M., "NASA 30 cm Ion Thruster Development Status", AIAA Paper 94-2849, 1994.



- [96] Patterson, M.J. and Verhey, T.R., "5 kW Xenon Ion Thruster Lifetest", AIAA Paper 90-2543, 1990.
- [97] Patterson, M.J., Haag, T.W., and Hovan, S.A., "Performance of the NASA 30 cm Ion Thruster", IEPC Paper 93-108, 1993.
- [98] Peng, X., Keefer, D., and Ruyten, W., "Plasma Particle Simulation of Electrostatic Ion Thrusters", AIAA Paper 90-2647, 1990.
- [99] Peng, X., Ruyten, W., and Keefer, D., "Monte Carlo Simulation of Ion-Neutral Charge Exchange Collisions and Grid Erosion in an Ion Thruster", AIAA Paper 91-0607, 1991.
- [100] Peng, X., Ruyten, W., and Keefer, D., "Further Study of the Effect of the Downstream Plasma Condition on Accelerator Grid Erosion in a Ion Thruster", AIAA Paper 92-3829, 1992.
- [101] Peng, X., Ruyten, W., and Keefer, D., "Charge-Exchange Grid Erosion Study for Ground-Based and Space-Based Operations of Ion Thrusters", IEPC Paper 93-173, 1993.
- [102] Peracchio, A.A., "Kinetic Theory Analysis for the Flowfield of a Two-Dimensional Nozzle Exhausting to Vacuum", *AIAA J.*, Vol. 8, No. 11, November 1970, pp. 1965-1972.
- [103] Polk, J.E. and Pivrotto, T.J., "Alkali Propellants for MPD Thrusters", AIAA Paper 91-3572, 1991.
- [104] Pollard, J.E., Jackson, D.E., Marvin, D.C., Jenkin, A.B., and Janson, S.W., "Electric Propulsion Flight Experience and Technology Readiness", AIAA Paper 93-2221, 1993.
- [105] Pollard, J.E., "Plume Measurements with the T5 Xenon Ion Thruster", Aerospace Corporation Report No. TR-94(4507)-2, 1994.
- [106] Press, W.H., Flannery, B.P., Teukolsky, S.A., and Vetterling, W.T., *Numerical Recipes*, Cambridge University Press, Cambridge, 1989.
- [107] Rapp, D. and Francis, W.E., "Charge Exchange between Gaseous Ions and Atoms", *J. of Chemical Physics*, Vol. 37, No. 11, December 1962, pp. 2631-2645.
- [108] Rawlin, V., Banks, B.A., and Byers, D.C., "Design, Fabrication, and Operation of Dished Accelerator Grids on a 30-cm Ion Thruster", AIAA Paper 72-486, 1972.
- [109] Rawlin, V., "Internal Erosion Rates of a 10-kW Xenon Ion Thruster", AIAA Paper 88-2912, 1988.
- [110] Reynolds, T.W. and Richley, E.A., "Propellant Condensation on Surfaces near an Electric Rocket Exhaust", *J. Spacecraft*, Vol. 6, No. 10, October 1969, pp. 1155-1161.
- [111] Reynolds, T.W., "Mathematical Representation of Current Density Profiles from Ion Thrusters", AIAA Paper 71-693, 1971.

- [112] Robinson, R.S., Kaufman, H.R., and Winder, D.R., "Plasma Propagation Simulation Near an Electrically Propelled Spacecraft", *J. Spacecraft*, Vol. 19, No. 5, Sept.-Oct. 1982, pp. 445-450.
- [113] Rosenberg, D. and Wehner, G.K., "Sputtering Yields for Low Energy He<sup>+</sup>, Kr<sup>+</sup>, and Xe<sup>+</sup>-Ion Bombardment", *J. Applied Physics*, Vol. 33, No. 5, May 1962, pp. 1842-1845.
- [114] Roux, J.A. and McCay, T.D., Eds., *Spacecraft Contamination: Sources and Prevention*, Progress in Aeronautics and Astronautics Series, Vol. 91, 1984.
- [115] Rutherford, J.A. and Vroom, D.A., "Charge transfer cross sections for Hg<sup>+</sup>, Xe<sup>+</sup>, and Cs<sup>+</sup> in collision with various metals and carbon", *J. Chem. Phys.*, Vol. 74, No. 1, Jan. 1981, pp. 434-441.
- [116] Ruyten, W.M., Burtner, D. and Keefer, D., "Spectroscopic Investigation of a Low-Power Arcjet Plume", AIAA Paper 93-1790, 1993.
- [117] Ruyten, W.M., "Density-Conserving Shape Factors for Particle Simulations in Cylindrical and Spherical Coordinates", *J. Comp. Phys.*, 105, 224-232, 1993.
- [118] Samanta Roy, R.I., Hastings, D.E., and Gatsonis, N.A., "A Review of Contamination from Electric Propulsion Thruster", AIAA Paper 94-2469, 1994.
- [119] Sanmartin, J.R., "End-Effect in Langmuir Probe Response Under Ionospheric Satellite Conditions", *Phys. Fluids*, Vol. 15, No. 6, June 1972, pp. 1134-1143.
- [120] Sellen, J.M., Bernstein, W., and Kemp, R.F., "Generation and Diagnosis of Synthesized Plasma Streams", *The Review of Scientific Instruments*, Vol. 36, No. 3, March 1965, pp. 316-322.
- [121] Simons, G., "Effect of Nozzle Boundary Layers on Rocket Exhaust Plumes", *AIAA J.*, Vol. 10, No. 11, Nov. 1972, pp. 1534-1535.
- [122] Sovey, J., "Improved ion confinement using a ring-cusp ion thruster", AIAA Paper 82-1928, 1982.
- [123] Sovey, J.S. and Mantenieks, M.A., "Performance and Lifetime Assessment of MPD Arc Thruster Technology", AIAA Paper 88-3211, 1988.
- [124] Sovey, J.S., Carney, L.M., and Knowles, S.C., "Electromagnetic Emission Experiences Using Electric Propulsion Systems", *J. Propulsion*, Vol. 5, No. 5, Sept.-Oct. 1989, pp. 534-547.
- [125] Staggs, J.F., Gula, W.P., and Kerslake, W.R., "Distribution of Neutral Atoms and Charge-Exchange Ions Downstream of an Ion Thruster", *J. Spacecraft*, Vol. 5, No. 2, Feb. 1968, pp. 159-164.
- [126] Staskus, J.V. and Burns, R.J., "Deposition of Ion Thruster Effluents on SERT II Spacecraft Surfaces", AIAA Paper 70-1128, 1970.
- [127] Stavisskii, Y.Y., Bondarenko, I.I., Krotov, V.I., Lebedev, S.Y., Pupko, V.Y., and Stumbur, E.A., "Experiment to Obtain Reaction Thrust in a Laboratory Model of an Ion Engine", *Soviet Phys. Tech.*, Vol. 4, No. 8, 1958, p. 875.

- [128] Stuart, R.V., Wehner, G.K., and Anderson, G.S., "Energy Distribution of Atoms Sputtered from Polycrystalline Metals", *J. Applied Physics*, Vol. 40, No. 2, Feb. 1969, pp. 803-812.
- [129] Stuhlinger, E., *Ion Propulsion for Spaceflight*, McGraw-Hill, NY, 1964.
- [130] Tajima, T., *Computational Plasma Physics: With Applications to Fusion and Astrophysics*, Addison-Wesley, NY, 1989.
- [131] Takegahara, H., Kasai, Y., Gotoh, Y., Miyazaki, K., Hayakawa, Y., Kitamura, S., Nagano, H., and Nakamaru, K., "Beam Characteristics Evaluation of ETS-VI Xenon Ion Thruster", IEPC Paper 93-235, 1993.
- [132] Tokmakoff, A., Haynes, D.R., and George, S.M., "Desorption Kinetics of C<sub>60</sub> Multilayers from Al<sub>2</sub>O<sub>3</sub>(0001)", *Chemical Physics Letters*, Vol. 186, No. 4,5, Nov. 1991, pp.450-455.
- [133] Torres, E.R., *Prediction of the Performance of an Ion Thruster using Buckminsterfullerene as Propellant*, MIT S.M. Thesis, 1993.
- [134] Tribble, A.C., Searing, R., Scheps, R., and Underwood, D., "Analysis of Spacecraft Thruster Interactions for the SPT-70 and SPT-100 Stationary Plasma Thrusters", AIAA Paper 94-0330, 1994.
- [135] Wang, J., Brophy, J. Liewer, P., and Murphy, G., "Modeling Ion Thruster Plumes", AIAA Paper 95-0596, 1995.
- [136] Weast, R.C., Ed., *Handbook of Chemistry and Physics*, Chemical Rubber Co., 1990.
- [137] Wehner, G.K. and Rosenberg, D., "Angular Distribution of Sputtered Material", *J. Applied Physics*, Vol. 31, No. 1, Jan. 1960, p. 177-179.
- [138] Wehner, G.K. and Anderson, G.S., "The Nature of Physical Sputtering", in *Handbook of Thin Film Technology*, Eds. Maissel, L.I. and Glang, R., McGraw-Hill Book Co., 1970.
- [139] Weigand, A.J. and Mirtich, M.J., "Measurement of Sputtered Efflux from 5-, 8-, and 30-cm diameter Mercury Ion Thrusters", AIAA Paper 75-358, 1975.
- [140] Weijsenfeld, C.H. and Hoogendoorn, A., "Cathode Sputtering by Rare Gas Ions of Low Energy", in *Proc. 5th Conf. Ion. Phenom. Gases*, Vol. 1, No. 124, Munich, 1961.
- [141] Wetch, J.R., Lawless, J.L., and Koroteev, A.S., "Review of the Development of the Closed Drift Hall Thruster", IEPC Paper 91-149, 1991.
- [142] Worlock, R.M., James, E.L., Hunter, R.E., and Barlett, R.O., "The Cesium Bombardment Engine North-South Stationkeeping Experiment on ATS-6", AIAA Paper 75-363, 1975.
- [143] Woronowicz, M.S. and Rault, D.F.G., "On Plume Flowfield Analysis and Simulation Techniques", AIAA Paper 94-2048, 1994.

- [144] Zafran, S., "Arcjet System Integration Development", NASA Contract Report NAS 3-25603, August 1990.
- [145] Zana, L.M., Hoffman, D.J., Breyley, L.R., and Serafini, J.S., "An Analytical and Experimental Investigation of Resistojet Plumes", AIAA Paper 87-0399, 1987.
- [146] Zhang, Q., Peng, X., and Keefer, D., "Particle Simulation of Grid Erosion for a Three-Grid Ion Thruster", IEPC Paper 93-178, 1993.